Element Redistribution in Hydrothermal Systems: From Formation to Supergene Weathering

Dissertation

der Mathematisch-Naturwissenschaftlichen Fakultät

der Eberhard Karls Universität Tübingen

zur Erlangung des Grades eines

Doktors der Naturwissenschaften

(Dr. rer. nat.)

vorgelegt von

M.Sc. Maximilian Keim

aus Aalen

Tübingen

2018

Gedruckt mit Genehmigung der Mathematisch-Naturwissenschaftlichen Fakultät der Eberhard Karls Universität Tübingen.

Tag der mündlichen Qualifikation:	04.06.2018
Dekan:	Prof. Dr. Wolfgang Rosenstiel
1. Berichterstatter:	Prof. Dr. Gregor Markl
2. Berichterstatter:	Prof. Dr. Marcus Nowak

Danksagung

Mein erster und besonderer Dank gebührt Prof. Dr. Gregor Markl für die Vergabe der Promotion und sein mir damit entgegengebrachtes Vertrauen. Auch für die Finanzierung im ersten Promotionsjahr bin ich ihm zu Dank verpflichtet. Erst durch unsere zahlreichen Diskussionen und seine Anregungen konnten viele Ideen, die in diese Arbeit eingeflossen sind, entstehen. Besonders dankbar bin ich auch für die stets zeitnahe Begutachtung der Manuskripte.

Für die Übernahme der Zweitbetreuung meiner Promotion sowie für die Diskussionen und Anregungen, möchte ich Prof. Dr. Marcus Nowak herzlich danken.

Weiter schulde ich PD. Dr. Thomas Wenzel großen Dank für die Betreuung der Mikrosondenmessungen, die Übernahme der Projektkoordination, das Korrekturlesen von Manuskripten sowie für erheiternde und hilfreiche Gespräche, auch außerhalb dieser Promotionsarbeit.

Bei Dr. Udo Neumann möchte ich mich für seine Hilfe bei der Mikroskopie, das Bereitstellen von Literatur sowie dem Korrekturlesen von Manuskripten bedanken.

Dr. Sebastian Staude, Manuel Scharrer und Stefan Bruder möchte ich ganz herzlich für das Korrekturlesen der Zusammenfassung danken.

Für die Hilfe und Unterstützung bei der Analytik möchte ich mich bei PD. Dr. Michael Marks, Dr. Melanie Keuper, Dr. Tobias Kiemle, Dr. Mathias Burisch, Dr. Benjamin Walter, Dr. Mathias Burisch, Dr. Joachim Opitz, Dr. Katharina Marquardt, Dr. Sabine Gilbricht, Kai Bachmann sowie Gabriele Stoschek bedanken. Für die hervorragende Probenpräparation bedanke ich mich bei Simone Schafflick. Für das zur Verfügung stellen von Unterlagen und Probenmaterial bin ich insbesondere Jens Burch, Richard Bayerl und Bernd Gassmann zu Dank verpflichtet.

Den Koautoren meiner Publikationen Prof. Dr. Gregor Markl, Dr. Udo Neumann, Dr. Sebastian Staude, Dr. Benjamin Walter, Dr. Katharina Marquardt, Dr. Joachim Opitz, Stefan Kreißl, Kai Bachmann, Rafael Vaudrin, Bernd Gassmann und Richard Bayerl danke ich für die gute Zusammenarbeit.

Auch bei meinen Kollegen und ehemaligen Kollegen Manuel Scharrer, Tatjana Epp, Anja Allabar, Marguerita Duchoslav, Rainer Babiel, Mathias Burisch, Johannes Giebel, Petya Atanasova, Stefan Kreißl und Dr. Sebastian Staude möchte ich mich für die vielen hilfreichen Diskussionen und die gute Arbeitsatmosphäre bedanken.

Mein ganz besonderer Dank gilt meiner Familie, meinen Freunden und insbesondere meiner Freundin. Sie alle haben mich stets unterstützt und immer an mich geglaubt.

Kurzzusammenfassung

Die treibende Kraft für die Elementumverteilung in hydrothermalen Ganglagerstätten bei der Bildung sowie der supergenen Verwitterung ist die thermodynamische Stabilität von Mineralphasen. Elementumverteilungsprozesse führen nicht nur zur Veränderung des Wertpotentials von Lagerstätten, sondern auch zur Freisetzung und Mobilisierung von Schwermetallen. Der Schwarzwald in SW-Deutschland stellt ein ideales Studiengebiet dar, um Umverteilungsprozesse zu studieren, da hier eine Vielzahl polymetallischer, hydrothermaler Gangvererzungen mit Primär-, Oxidations- und Zementationszone aufgeschlossen sind.

Die Grube Clara bietet ein einmaliges, über 850 m aufgeschlossenes, vertikales, hydrothermales Gangprofil einer silberreichen Sulfidvererzung, welches mehrfach von Umlagerungsprozessen beeinflusst, jedoch bislang keiner intensiven wissenschaftlichen Untersuchung unterzogen wurde. Diese Arbeit zeigt, basierend auf Stabilitätsdiagrammen, unter Berücksichtigung der Fluid- und Mineralchemie, dass eine großmaßstäbliche Silberzonierung durch unterschiedliche Redoxpotentiale der Bildungsfluide angelegt und später von mindestens vier weiteren hydrothermalen Phasen sowie einer Alterationsphase überprägt wurde, wobei die generelle Silberzonierung erhalten geblieben ist.

Kommen die hydrothermalen Gänge durch Hebung und Erosion in oberflächennahe Bereiche, sind die Sulfide thermodynamisch nicht mehr stabil und es bilden sich neue, stabilere, Mineralphasen oder aber die Elemente gehen in Lösung und werden abtransportiert und/oder repräzipitiert. Es wurde die Umverteilung von Silber bei der Verwitterung von silberhaltigem Galenit und von bismuthaltigem Fahlerz als wichtige Träger von Wert- aber auch Schwermetallen untersucht, da bisherige Studien nur Teilaspekte derselben betrachten. Durch Spurenelementanalytik und Stabilitätsberechnungen zeigt sich, dass Silber bei der Verwitterung von Bleiglanz im Gegensatz zu Blei mobil ist, nur im geringen Maße in Bleisekundärminerale eingebaut wird und stattdessen in anderen Gangteilen durch Redoxprozesse als eigenständige Mineralphasen wie ged. Silber und Akanthit repräzipitiert wird. Bismut hingegen verhält sich bei der Verwitterung von bismuthaltigem Fahlerz immobil, wobei durch die Bildung von Bi-Sb-Phasen, die Mobilität von Antimon kontrolliert wird. Zudem zeigt sich, dass die Arsenmobilität, sowie die generierten Verwitterungstexturen wesentlich vom Oxidationspotential der Verwitterungsfluide abhängen.

Verwitterungsprozesse sind nicht nur rein auf natürliche Vorgänge zurückzuführen, sondern unterliegen auch anthropogenem Einfluss. Die komplexe Vergesellschaftung von basischen Bleimineralen, deren Bildung im Zusammenhang mit mittelalterlichem Feuersetzen steht, wurde genutzt, um mit Hilfe von thermodynamischen Fluidpfadmodellierungen das Vorkommen basischer Bleiminerale auch in anderen anthropogen beeinflussten Umgebungen zu erklären. Zudem konnte durch Verwitterungsexperimente gezeigt werden, dass basische Bleiminerale die Mobilität von Blei unter oxidierenden Bedingungen kontrollieren können.

Wie sich reduzierende Thermalfluide auf eine Oxidationszone auswirken, ist bislang nicht bekannt. Um dies zu untersuchen, wurden Galenit Pseudomorphosen nach Pyromorphit aus der Kautenbachmine in Rheinland-Pfalz (Deutschland) erstmals wissenschaftlich untersucht, da sie den mehrfachen Wechsel oxidierender und reduzierender Fluide eingefangen haben. Anhand eines thermodynamischen Genesemodells, basierend auf neuen Wasseranalysen konnte gezeigt werden, dass sich diese Pseudomorphosen durch calcium- und fluorreiche Fluide, bei relativ hohen pH-Werten gebildet haben wobei sich Blei immobil verhält.

Abstract

The driving force for elemental redistribution in hydrothermal vein-type deposits during their formation and subsequent supergene weathering is the thermodynamic stability of mineral phases. Elemental redistributional processes will not only influence the economic potential of ore deposits but also lead to the mobilization of (toxic) heavy metals. The Schwarzwald in SW-Germany provides an ideal area to study redistribution processes, as numerous polymetallic hydrothermal veins with their primary-, oxidation- and cementation zones are exposed near to the surface.

The Clara mine offers a unique, vertical profile of a silver-rich, hydrothermal sulfide mineralization that is exposed over 850 m vertically. This vertical profile has been influenced by redistribution processes several times, but has not yet undergone intensive scientific investigation. Based on mineral textures and stability diagrams, this work reveals, that a large scale silver zonation was caused by different redox potentials of the formation fluids. The original mineralization was overprinted subsequently by at least four further hydrothermal phases and an additional alteration phase, whereby the general silver zonation has been preserved.

If the hydrothermal veins are exposed to near-surface environments by uplift and erosion, the sulfides are thermodynamically no longer stable and new, more stable, mineral phases form or the contained elements go into solution and are removed and/or re-precipitate. The redistribution of silver during the weathering of argentiferous galena and bismuth-bearing fahlore as important carriers of precious as well as heavy metals was investigated, since only partial aspects are considered by previous studies. Trace element analysis and stability calculations show that silver in contrast to lead is mobile during the weathering of galena and is re-precipitated in other parts of the vein by redox processes as discrete mineral phases such as native silver and acanthite. Bismuth, on the other hand, is immobile during the weathering of Bi-containing fahlore, whereby the mobility of antimony is controlled by the formation of Bi-Sb phases. Furthermore, it is shown that the mobility of arsenic and the produced weathering textures depend on the oxidation potential of the weathering fluids.

Supergene weathering is not only caused by natural processes, but is also influenced by anthropogenic processes. With the help of thermodynamic fluid path modelling, the complex association of basic lead minerals (their formation is related to medieval fire setting), was used to explain their occurrence also in other anthropogenically influenced environments. In addition, weathering experiments have shown that the basic lead minerals are able to control the mobility of lead under oxidizing conditions.

How reducing thermal fluids affect an oxidation zone is not yet known. In order to investigate this unusual effect, galena pseudomorphoses after pyromorphite from the Kautenbach mine in Rhineland-Palatinate (Germany) were investigated for the first time, since they have captured the alternation of oxidizing and reducing fluids. Using a thermodynamic model based on new water analyses, it was shown that these pseudomorphs were formed by calcium and fluorine rich fluids at relatively high pH values, in which lead is immobile.

Inhaltsverzeichnis

1 Einleitung

Die vorliegende Arbeit wurde im Fachbereich Geowissenschaften der Universität Tübingen angefertigt und untersucht die Elementumverteilung in Hydrothermalssystemen während deren primärer Bildung bis hin zur Modifikation durch natürliche aber auch anthropogen beeinflusste Verwitterungsprozesse. Neben der Elementumverteilung fokussiert sich diese Arbeit auf das generelle Prozessverständnis, um Verwitterungsprozesse besser verstehen und durch thermodynamische Modelle zu quantifizieren.

1.1 Allgemeine Einleitung

Wird eine Mineralphase gebildet, steht diese im Idealfall im thermodynamischen Gleichgewicht mit den umgebenden physikochemischen Bedingungen (PARK UND MACDIARMID 1975; SATO 1992; HUDSON-EDWARDS ET AL. 2011). Im hydrothermalen System sind hierfür wichtige Parameter: Temperatur, pH-Wert, Ionenaktivität und Gasfugazitäten (z. B. VAUGHAN UND CRAIG 1997; WILLIAMS-JONES UND HEINRICH 2005 und Referenzen darin). Ändern sich die physikochemischen Randbedingungen für eine Mineralphase, wird sich diese unter Bildung einer neuen Phase und/oder Anpassung ihres Chemismus anpassen, bzw. auflösen und in wässrige Spezies übergehen (z. B. THORNBER 1992; CRANE ET AL. 2001; ARROYO UND SIEBE 2007; ROPER ET AL. 2012; BETHKE UND YEAKEL 2015). Bei diesen Prozessen können Elemente in unterschiedlichem Ausmaß mobilisiert und in den neu gebildeten Mineralparagenesen absolut bzw. relativ angereichert oder aber verarmt werden (LEYBOURNE ET AL. 2005; MARKL ET AL. 2014A; YESARES ET AL. 2014). Durch diese Umverteilung kann es zur relevanten Anreicherung strategisch wichtiger Elemente wie Bismut, Antimon und Silber kommen. Weiter können solche Prozesse zur Mobilisierung toxischer Elemente wie Arsen, Blei, Quecksilber, Cadmium und Antimon führen, welche dadurch in die Biosphäre gelangen (z. B. DUDKA UND ADRIANO 1997; MONCUR ET AL. 2009; JAMIESON 2011; PLUMLEE UND MORMAN 2011; FÖRSTNER UND WITTMANN 2012; CALLENDER 2014). Deshalb ist es von großer Bedeutung, Prozesse, die zur (Re-)Mobilisierung von Elementen und ihrer damit einhergehenden Umverteilung führen können, zu verstehen und bestenfalls zu quantifizieren.

Ganz allgemein lassen sich Umverteilungsprozesse zunächst am effektivsten durch eine detaillierte Beobachtung von Phasenbeziehungen in makroskopischen Proben sowie im Dünnschliff evaluieren. Durch die quantitative Bestimmung von Haupt- und Spurenelementen können Schlüsse über die Umverteilung einzelner Elemente in Mineralassoziationen im Meter- bis Nanometerbereich getroffen werden.

Zur Mobilisierung/Umverteilung von Elementen werden meist Fluide benötigt, da unter tieftemperierten, oberflächennahen Bedingungen die Festkörperdiffusion sehr langsam ist (PUTNIS 2014). Um Fluide zu charakterisieren, die zur Elementumverteilung führen, können diese in den Verwitterungszonen direkt beprobt werden (z. B. MAGALHÃES ET AL. 1985; INGWERSEN, 1990; BUCHER ET AL. 2009; GÖB ET AL. 2011, 2013A, B; MARKL ET AL. 2014A). Im Hydrothermalssystem hingegen ist solch eine direkte Beprobung in den allermeisten Fällen nicht mehr möglich und es muss auf die indirekte Beprobung der Fluide anhand von Flüssigkeitseinschlüssen zurückgegriffen werden (z. B. SHEPERD ET AL. 1985; GOLDSTEIN UND REYNOLDS 1994). Anhand der Fluidchemie in Kombination mit thermodynamischen Daten und der bekannten Mineralparagenese können die Umverteilungsprozesse nun modelliert werden. Moderne hydrogeochemische Modellierungsprogramme (wie z. B. „Phreeqc“ und „The Geochemist Workbench“) beruhen auf der Minimierung der Gibbs´schen freien Enthalpie und berechnen somit Gleichgewichtszustände unter vorgegebenen Parametern (PARKHURST UND APPELLO 1999; BETHKE UND YEAKEL 2015). Ganz konkret können so Sättigungsberechnungen, Prädominanzgrenzen sowie Stabilitätsbereiche und Reaktionspfade berechnet werden. Diese Berechnungen können dazu genutzt werden, texturelle Beobachtungen und Wasserchemie zu koppeln, um so Modelle zu erstellen, welche die Elementumverteilung nachvollziehen bzw. voraussagen können.

Wie bereits eingangs erwähnt, lassen sich im Hydrothermalsystem Umverteilungsprozesse zum einen während dessen Bildung unter reduzierenden Bedingungen (Primärzone) (z. B. KRUPP 1989; MELCHER ET AL. 2006; BURISCH ET AL. 2017; KREISSL ET AL. IN PRESS), zum anderen während dessen supergener Verwitterung unter oxidierenden Bedingungen (Oxidationszone Zementationszone) beobachten (PARK UND MACDIARMID 1975; VERHAERT ET AL. 2017). Folgend soll kurz auf wichtige Faktoren und Prozesse eingegangen werden, die in diesen Zonen bei Umverteilungsprozessen von Bedeutung sind.

1.2 Elementumverteilung in der Primärzone

Minerale in der Primärzone von Hydrothermalsystemen werden durch heiße, zum Teil salinare, metallreiche Lösungen gebildet (BARNES 1997; HEINRICH UND CANDELA 2014 und Referenzen darin). Da diese Fluide zumeist reduziert sind, bilden sich vornehmlich Sulfide und Sulfosalze, die in Gangarten wie Baryt [$BaSO_4$], Quarz [SiO_2], Fluorit [CaF_2] und Karbonaten [z. B. $CaCO_3$] eingeschlossen sind. Die Ausfällung der Minerale ist dabei beispielsweise durch die Änderung des Redoxzustandes, des pH-Werts, der Ionenkonzentration oder der Temperatur möglich (z. B. BARNES 1997; SEWARD UND BARNES 1997; SEWARD ET AL. 2014).

Hydrothermalsysteme sind in aller Regel über längere Zeiträume aktiv, wobei durch Änderungen der Fluidparameter (z. B. Abkühlung oder pH-Wert-Änderung) die zuvor

gebildeten Minerale verdrängt oder aufgelöst und die darin enthaltenen Elemente mobilisiert oder aber repräzipitiert werden können (z. B. HILMY UND OSMAN 1989; YOSHIMURA ET AL. 2004; SACK ET AL. 2005; BURISCH ET AL. 2017; SCHARRER ET AL. IN PREP). Texturell ist dieser Prozess nachweisbar, wenn zuvor gebildete Sulfide nahezu vollständig aufgelöst werden, jedoch Relikte der früheren Phasen in ihnen eingeschlossen erhalten bleiben. Solche Verdrängungstexturen lassen sich in einer Vielzahl hydrothermaler Lagerstätten beobachten (z. B. STAUDE ET AL. 2010B; REPSTOCK ET AL. 2015; APOPEI ET AL. 2016; MARUSHCHENKO ET AL. IN PRESS).

1.3 Elementumverteilung in der Oxidations- und Zementationszone

Kommt ein hydrothermaler Erzgang beispielsweise durch Hebungsprozesse und einhergehender Erosion in oberflächennnahe Bereiche, steht dieser zunehmend in Kontakt mit oxidierenden Fluiden (PARK UND MACDIARMID 1975; WEBSTER 1984). Hierbei kommt es aufgrund des massiven Ungleichgewichts zwischen den Verwitterungsfluiden und den primär gebildeten sulfidischen Erzmineralen zu deren Auflösung bzw. zur Präzipitation stabilerer Sekundärminerale (z. B. DRAHOTA UND FILIPPI 2009; HUDSON-EDWARDS ET AL. 2011; REICH UND VASCONCELOS 2015). Hierbei bilden sich eine Vielzahl von neuen, unter diesen Bedingungen stabileren, sauerstoffhaltigen Mineralphasen wie Carbonate, Sulfate, Hydroxide, Oxide, Phosphate, Arsenate, Silikate, Wolframate, Vanadate aber auch gediegene Elemente (z. B. MARKL 2015, 2016, 2017A, B; KEIM UND MARKL 2015; VERHAERT ET AL. 2017). Bis in welche Tiefe die oxidierenden Fluide vordringen können, ist im Wesentlichen vom Klima und der lokalen Geologie abhängig (PARK UND MACDIARMID 1975).

Im obersten Bereich der Lagerstätte überwiegen Auflösungsprozesse und es bildet sich häufig ein sogenannter Eiserner Hut aus, der sich durch das Vorhandensein von schwer löslichen Eisenoxiden und Hydroxiden auszeichnet. Darunter schließt sich die eigentliche Oxidationszone an, in der die Primärerze zu sauerstoffhaltigen Verbindungen umgesetzt bzw. aufgelöst und durch Verwitterungslösungen in Richtung des Grundwasserspiegels abtransportiert werden. Der Bereich unterhalb des Grundwasserspiegels wird als Zementationszone bezeichnet. Hier werden die in der Oxidationszone gelösten Metalle durch Redoxprozesse als sekundäre Sulfide und Sulfosalze ausgefällt (PARK UND MACDIARMID 1975). Generell sind in der Oxidations- und Zementationszone drei grundlegende Prozesse für die Elementmobilität und Umverteilungsvorgänge von Bedeutung (REICH UND VASCONCELOS 2015):

I. Die elektrochemische Oxidation von Elementen, die in den primären Erzmineralen enthalten sind (z. B. $Ag^0 \rightarrow Ag^+$; $S^{2-} \rightarrow S^{6+}$; $Fe^{2+} \rightarrow Fe^{3+}$ oder $As^{3+} \rightarrow As^{5+}$), die im Wesentlichen von deren spezifischen Redoxpotentialen und dem Oxidationszustand

des Fluides abhängt. Auch bakterielle Aktivität kann ein wichtiger Faktor sein, der die Oxidation von Elementen katalysiert.

II. Der Transport der Elemente als Komplexe oder Ionen, abhängig von den physikochemischen Randbedingungen (z. B. pH-Wert, Temperatur, fO_2, zur Verfügung stehende Liganden). Wichtige Komplexbildner sind dabei Wasser bzw. Hydroxidionen (z. B. $MeOH^+$), Chlor (z. B. $MeCl_2^-$) und Schwefel (z. B. $Me(HS)_2$).

III. Die Ausfällung der gelösten Spezies durch Übersättigung, pH-Wert-Änderung, Ionenaustauschreaktionen, Adsorption und/oder Änderung des Redoxzustandes. Hervorgerufen werden diese Änderungen beispielsweise durch Fluidmischung oder Wasser-Gesteins-Wechselwirkung.

Diese Prozesse führen dazu, dass bei der Evaluierung von Elementumverteilungsprozessen stets möglichst viele dieser Faktoren miteinbezogen werden müssen. Um diese komplexen Prozesse besser zu verstehen, kann einerseits auf einen experimentellen Ansatz (z. B. ZHANG UND RYAN 1999; HARVEY ET AL. 2006; QIAN ET AL. 2013), andererseits auf die thermodynamische Fluidpfadmodellierung bzw. die Berechnung von Stabilitätsdiagrammen zurückgegriffen werden (z. B. MAGALHÃES UND WILLIAMS 1985; INGWERSEN, 1990; REED UND PALANDRI 2006; REICHERT UND BORG 2008; GÖB ET AL. 2011, 2013A; LOGES ET AL. 2012A; MARKL ET AL. 2014A; HOUWERS 2015; KEIM UND MARKL 2015). Häufig steht bei den Studien der Umweltaspekt im Vordergrund, um Voraussagen zu treffen, inwieweit toxische Elemente mobilisiert werden und so in die Biosphäre gelangen können (z. B. JAMIESON 2011). Zum Teil wird neben den thermodynamischen Berechnungen auch noch der kinetische Aspekt (z. B. LICHTNER UND BIINO 1992; PÉREZ ET AL. 2000) und/oder bakterielle Aktivität miteinbezogen (BAKER UND BANFIELD 2003; LU UND WANG 2012).

Neben den natürlich gesteuerten Prozessen, die zur Elementumverteilung führen, spielen auch anthropogen beeinflusste Verwitterungsprozesse eine wichtige Rolle, wie beispielsweise das Ausbringen von Erzen auf Halden (z. B. ROMERO ET AL. 2006; HUDSON-EDWARDS ET AL. 2011) oder bergbauliche Aktivität, die zur Bildung von Fluidwegsamkeiten in tiefe Bereiche einer Lagerstätte führt (z. B. BOWELL 2014). Die Interaktion von Sulfiden und Fluiden generiert zumeist saure Lösungen, die große Mengen an Schwermetallen mobilisieren können und wird gemeinhin als „acid mine drainage“ bezeichnet (JAMIESON 2011; NORDSTROM 2011).

Einerseits können Verwitterungs- und einhergehende Umverteilungsprozesse den wirtschaftlichen Wert von Lagerstätten durch das (teilweise) Lösen und Abtransportieren von Wertmetallen schmälern. Anderseits kommt es beispielsweise bei der Verwitterung von porphyrischen Kupferlagerstätten, verglichen zu dem Primärerzkörper, zur Anreicherung von Kupfer (z. B. HARTLEY UND RICE 2005; SILLITOE 2005). Weiter entsteht der wirtschaftliche Wert von beispielsweise lateritischen Lagerstätten oder nichtsulfidischen Zinklagerstätten erst durch Verwitterungs- und Umverteilungsprozesse (REICH UND VASCONCELOS 2015 und Referenzen darin).

2 Zielsetzung

Das Ziel dieser Arbeit ist es, die komplexen Prozesse, die zur Umverteilung in einem Hydrothermalsystem während seiner Bildung und seiner anschließenden Modifizierung durch natürliche und anthropogen beeinflusste Verwitterungsprozesse, besser zu verstehen und gegebenenfalls durch thermodynamische Stabilitäts- und Fluidpfadberechnungen zu untermauern.

Die Umverteilung von Silber in der Primärzone eines Hydrothermalsystems kann hervorragend an der Grube Clara studiert werden, da hier ein hydrothermales, silberreiches Gangsystem über mehrere hundert Meter vertikal aufgeschlossen ist und mehrfach reaktiviert und überprägt wurde. Die Genese sowie die Umverteilungsprozesse sind jedoch unzureichend verstanden. Deshalb fokussiert sich die erste Studie (*Kapitel 4.1*) auf:

- die räumliche und zeitliche Unterscheidung der hydrothermalen Stadien sowie das Aufdecken von Umverteilungsprozessen anhand von Texturen und Mineralchemie;
- die Charakterisierung der erzbildenden Fluide;
- das Erstellen eines Genesemodells mit Hilfe von berechneten Stabilitätsdiagrammen;
- das Einbinden der Ergebnisse in den regionalgeologischen Kontext.

Weiter wird in dieser Arbeit lokalitätsübergreifend auf die Elementumverteilung von primär hydrothermal gebildeten Sulfiden und Sulfosalzen bei der supergenen Verwitterung eingegangen. Hierbei wurden mit Galenit [PbS] und Fahlerz [$(Cu,Ag)_{10}(As,Sb,Bi)_4(Fe,Zn)_2S_{13}$] zwei der in Lagerstätten am weitesten verbreiteten Sulfide ausgewählt. Die Umverteilung von Wertmetallen wie Silber (aus silberhaltigem Galenit) und Schwermetallen wie Antimon, Arsen und Bismut (aus Fahlerz) ist bislang nur teilweise verstanden. Deshalb fokussiert sich der zweite Teil dieser Arbeit in Studie 2 (*Kapitel 4.2.1*) und Studie 3 (*Kapitel 4.2.2*) auf:

- die Akkumulation von Haupt- und Spurenelementen in Sekundärphasen (Studie 2 & 3);
- die Quantifizierung der freigesetzten Elemente bei der Verwitterung (Studie 2 & 3);
- die räumliche Umverteilung innerhalb der Oxidationszone (Studie 2 & 3);
- die thermodynamische Modellierung der Verwitterungsprozesse (Studie 2);
- die Erstellung einer Massenbilanzrechnung (Studie 3);
- den physikochemischen Prozess der Verwitterung (Studie 3).

Nachdem die Studien 1-3 sich auf Prozesse in der Primär- bzw. der Oxidations- und Zementationszone fokussiert haben, wurde in Studie 4 (*Kapitel 4.3*) die Schnittstelle zwischen diesen beiden Zonen untersucht, da sich bisher keine wissenschaftliche Studie dieser Thematik angenommen hat. Der mehrmalige Wechsel zwischen einem Hydrothermalsystem und der Oxidationszone ist eindrucksvoll in den Galenitpseudomorphosen nach Pyromorphit

$[Pb_5(PO_4)_3Cl]$ aus der Kautenbachmine zu erkennen, wobei es das Ziel war, folgende Aspekte mit einzubeziehen:

- die texturelle Beschreibung der Pseudomorphosen;
- die Eingrenzung der hydrogeochemischen Randbedingungen mittels Wasseranalysen;
- die thermodynamische Fluidpfadmodellierung und Entwicklung eines Genesemodells;
- der Vergleich mit weiteren europäischen Vorkommen.

Die vorangegangenen Studien 1-4 dieser Arbeit bearbeiten ausschließlich natürliche Verwitterungsprozesse. Deshalb wurde in Studie 5 (*Kapitel 4.5*) der anthropogene Einfluss auf die Verwitterung untersucht. Die Entstehung von basischen Bleimineralen im Zusammenhang mit mittelalterlichem Feuersetzen eignet sich ideal, um die Entstehung basischer Bleiminerale auch in anderen anthropogen beeinflussten Umgebungen zu erklären. Ziel dieser Studie war es, folgende Aspekte mit einzubeziehen:

- die texturelle Beschreibung der Feuersetzparagenese zur Erstellung eines Genesemodells;
- die thermodynamische Berechnung von Stabilitätsdiagrammen sowie die Fluidpfadmodellierung, um das Vorkommen der basischen Bleiminerale auch in anderen anthropogen beeinflussten Umgebungen zu erklären;
- die Temperaturabschätzung des Feuersetzprozesses;
- die Evaluierung der Bleimobilität durch Verwitterungsexperimente.

3 Auswahl der Studiengebiete

In Mitteleuropa ist eine Vielzahl hydrothermaler Gangmineralisationen auf Variszische Gesteinseinheiten und assoziierte sedimentäre Deckgebirgsschichten beschränkt, die sich von Nordafrika über Südeuropa und Mitteleuropa bis nach Osteuropa erstrecken (MURPHY ET AL. 2016 und Referenzen darin). In Deutschland ist Variszisches Grundgebirge im Schwarzwald, Erzgebirge, Odenwald, Harz, Spessart, Bayerischen Wald und dem Rheinischen Schiefergebirge aufgeschlossen (FRANKE 1989). Der überwiegende Teil der bearbeiteten Proben stammt aus dem Schwarzwälder Erzrevier (Studien 1, 2, 3 und 5). Die Studie 4 bildet dabei eine Ausnahme, da die benötigte Art der Proben nicht im Schwarzwald verfügbar ist und somit auf Proben des Rheinischen Schiefergebirges, genauer dem Hunsrück, zurückgegriffen wurde. Auf die Geologie sowie die hydrothermalen Mineralisationen des Schwarzwaldes wird im folgenden *Kapitel 3.1* kurz eingegangen. Auf eine detaillierte Beschreibung der Geologie sowie der Mineralisationen des Hunsrücks in einem eigenen Kapitel wird verzichtet. Details hierzu werden in Einzelstudie 4 (*Kapitel 4.3*) kurz beschrieben.

Der Schwarzwald eignet sich hervorragend als Untersuchungsgebiet, um Umverteilungs- und Verwitterungsprozesse zu untersuchen, da die Entstehung der Hydrothermalgänge und ihre chemischen Parameter (z. B. BEHR UND GERLER 1987; BEHR ET AL. 1987; STAUDE ET AL., 2009; 2012A; FUSSWINKEL ET AL. 2013; BONS ET AL. 2014; BURISCH ET AL. 2016A; WALTER ET AL. 2015; 2016, 2017A, B, 2018), die Mineralchemie von primären Sulfiden (z. B. STAUDE ET AL. 2010A, B; PFAFF ET AL. 2011; HARSCH 2015; EPP 2016; SCHARRER UND VAUDRIN 2016) sowie die Wasserchemie oberflächennaher Verwitterungsfluide (BUCHER ET AL. 2009; LOGES ET AL. 2012B; GÖB ET AL. 2011; 2013A, 2013B; MARKL ET AL. 2014A) gut bekannt sind. Dieses Vorwissen wurde dazu genutzt, um eine sinnvolle Auswahl an Proben für die Einzelstudien treffen zu können, die sich für die Einzelstudien in *Kapitel 4* eignen.

3.1 Regionale Geologie und hydrothermale Mineralisationen des Schwarzwalds

Der Schwarzwald ist ein etwa 50 x 120 km großes in SW-Deutschland gelegenes Mittelgebirge und besteht geologisch aus kristallinem, Variszischem Grundgebirge, welches diskordant von jüngeren Sedimentschichten überlagert wird (GEYER UND GWINNER 2011). Kollisionstektonik während des Karbons führte zur Akkretion und metamorphen Überprägung der einzelnen Krustenbereiche bis hin zur Granulitfazies (GEYER UND GWINNER 2011). Die präkarbonischen Gesteine liegen heute hauptsächlich als Para- und Orthogneise vor und wurden zum Teil migmatisiert (KALT ET AL. 2000). Großräumige Krustendehnung im mittleren bis späten Karbon führten zur post-kollisionalen Intrusion saurer Magmatite, welche ihren Ursprung in Meta-Sedimenten der Unterkruste hatten (ALTHERR ET AL. 2000). Während des Perms wird die

Kruste großräumig geschert und das Variszische Gebirge erodiert, wobei sich innerhalb der entstandenen pull-apart Becken, Sedimente des Rotliegend ablagerten. Folgend kam es zur diskordanten Ablagerung von terrestrischen, fluviatilen und marinen Sedimenten während der Atlantiköffnung, welche heute als triassische bis jurassische Deckgebirgsschichten vorliegen. Die Alpine Gebirgsbildung induzierte die Öffnung des Oberrheingrabens im Paläogen. Durch dessen Öffnung und einhergehende Absenkungsprozesse wurden die Grabenschultern asymmetrisch gehoben, wobei diese anschließend der Erosion ausgesetzt wurden. Durch die asymmetrische Hebung sind die Deckgebirgsschichten im Nordschwarzwald erhalten geblieben, wobei sie im Süden bis zu einer Tiefe von etwa 2 km unter der Grundgebirgs-Deckgebirgs-Diskordanz erodiert sind (RUPF UND NITSCH 2008; GEYER UND GWINNER 2011).

Innerhalb des Schwarzwalds sind über 1000 hydrothermale Erzgänge aufgeschlossen (METZ ET AL. 1957), welche sich mehr oder weniger kontinuierlich über die letzten 310 Millionen Jahren bis heute gebildet haben (PFAFF ET AL. 2009; STAUDE ET AL. 2009; WALTER ET AL. 2016; BURISCH ET AL. 2018) und sowohl im Grundgebirge als auch im Deckgebirge aufgeschlossen sind. Die hydrothermalen Gänge bestehen aus Quarz, Fluorit, Baryt und Karbonaten, die von Sulfiden, Arseniden und Oxiden begleitet werden, welche im Wesentlichen Pb, Zn, Cu, Ag, Co, Ni, U, Fe, Mn und Sb führen (METZ ET AL. 1957; BLIEDTNER UND MARTIN 1986; MARKL 2015 und Referenzen darin). Die hydrothermalen Maxima im Schwarzwald fanden zwischen 200-100 Millionen Jahren durch die Öffnung des Nordatlantiks und zwischen 40-20 Millionen Jahren während der Oberrheingrabenbildung statt (STAUDE ET AL. 2009; BURISCH ET AL. 2018). Basierend auf Fluideinschluss- und Isotopenstudien wird davon ausgegangen, dass die Gänge während der maximalen hydrothermalen Aktivität (Trias-Tertiär) durch Fluidmischung eines heißen, metallreichen, hochsalinaren Grundgebirgsfluids mit einem ebenfalls hochsalinaren, zumeist metallarmen, sedimentären Fluid gebildet wurden (BEHR UND GERLER 1987; BEHR ET AL. 1987; STAUDE ET AL. 2009, 2010A, 2011, 2012A, B; PFAFF ET AL. 2009, 2010; MARKL 2015; WALTER ET AL. 2015, 2016, 2017A, 2017B, 2018; BURISCH ET AL. 2016A, 2016B). Basierend auf strukturgeologischen- und mineralogischen Studien sowie Fluideinschlussstudien werden die hydrothermalen Gänge im Schwarzwald in fünf Hauptphasen unterteilt: (i) Karbonische Quarz-Turmalin-Gänge mit W-Sn Vererzungen; (ii) permische Quarzgänge mit Sb- und Au Vererzungen; (iii) triassisch-jurassische Quarzgänge mit Hämatitvererzung; (iv) jurassisch-kretazische Fluorit-Baryt-Quarz-(Karbonat)-Gänge mit Pb-Zn-Cu-Ag- und Ag-Bi-Co-Ni-U-Vererzungen; (v) post-kretazische Quarz-Baryt-Fluorit oder Karbonat Gänge mit Pb-Zn-Cu-Ag und Cu-Ni-Bi-Ag Vererzungen (Walter et al. 2016 und Referenzen darin).

Die Hebung der hydrothermalen Gänge und die folgende Erosion der darüberliegenden Gesteinsschichten ist auf etwa 20 Millionen Jahre zu datieren (BURISCH ET AL. 2018). Durch die Hebung wurden die Gänge in oberflächennahe Bereiche gebracht, wobei sie folgend der supergenen Verwitterung ausgesetzt waren. Die ältesten Sekundärminerale im Schwarzwald

sind auf etwa 15 Millionen Jahre zu datieren (HAUTMANN UND LIPPOLT 2000). Mit den Bildungsbedingungen und der Genese von Sekundärmineralvergesellschaftungen befassen sich im Schwarzwald die Arbeiten von HAUTMANN UND LIPPOLT (2000), LOGES ET AL. (2012A), BURMANN ET AL. (2013), GÖB ET AL. (2013) HAßLER ET AL. (2014), MARKL ET AL. (2014A, B), KEIM UND MARKL (2015) MARKL (2015), (2016), (2017A, B).

4 Einzelstudien

4.1 Mehrphasige Silberumverteilung im Hydrothermalsystem der Grube Clara

Hinsichtlich des Bergbaus blickt der Schwarzwald auf eine bewegte Geschichte zurück, die mindestens bis 5000 v. Chr. zurückreicht (MARKL 2015). Die Fluss- und Schwerspatgrube Clara im oberen Rankachtal stellt den letzten noch aktiven Abbau dieses Schwarzwälder Erzreviers dar. Hier wird neben Schwer- und Flussspat seit 1997 zusätzlich ein Silber-Kupfer-Konzentrat gefördert (BAUMGÄRTL UND BUROW 2002; MARKL 2015). Das Gangsystem, auf dem die Grube Clara abbaut, wird in Fluoritgang, Barytgang, und Diagonaltrum unterteilt, wobei genetisch ersterer die älteste und letzterer die jüngste Mineralisationsphase darstellt (LIST 1969; ZIRNGAST 1978; MAUS ET AL. 1979; HUCK 1984). Das Silber-Kupfer-Konzentrat entstammt den sulfidreichen Partien des Barytganges und wird als Silberspat bezeichnet (HUCK 1984). Bisherige Arbeiten am Silberspat beschränkten sich vornehmlich auf die mineralogische Beschreibung und Bestandsaufnahme der darin vorkommenden Mineralphasen (SCHMELTZER 1983; WALENTA 1984; REHREN 1985; BLASS UND GRAF 2001; BAUMGÄRTL UND BUROW 2002), befassen sich jedoch nicht mit deren Petrographie und Genese. Die Arbeit von VAN DER HEYDE (2002) stellt hier eine Ausnahme dar, wobei diese nur einen kleinen Ausschnitt des Silberspats betrachtet, nämlich den der 14ten Abbausohle. Aus den bisherigen Arbeiten kann geschlossen werden, dass mit der Tiefe der Sulfidanteil deutlich zunimmt. Zudem scheinen eigenständige Silberphasen (hauptsächlich Polybasit-Pearceit [$(Ag,Cu)_{16}(As,Sb)_2S_{11}$]) erst ab etwa der 10ten Abbausohle aufzutreten, wobei die Gründe hierfür bislang unbekannt waren. Die Studie im *Anhang 1* versucht deshalb, ein Genesemodell des Silberspats basierend auf detaillierten mikroskopischen Beobachtungen, Mineralchemie mittels Elektronenstrahl-Mikrosonde und Fluideinschlussmessungen zu erstellen, wofür Proben eines Vertikalprofils des Silberspats von über 850 m herangezogen wurden. Die Ergebnisse sollen in die bisherigen Arbeiten über Hydrothermalsysteme im Schwarzwald eingegliedert werden und diese gegebenenfalls erweitern. Die Studie zeigt, dass sich der Silberspat in mindestens fünf hydrothermale Phasen sowie eine Alterationsphase unterteilen lässt (Phase 1-6), welche Einfluss auf die Verteilung von Silber innerhalb der Vererzung haben.

1. Phase: Während der ersten Phase wurde eine großmaßstäbliche Silberzonierung im Gang angelegt. In den unteren Teufenbereichen (bis zur 10ten Sohle; 450 m ü.NN) bildete sich silberhaltiges Fahlerz (bis zu 22 Gew.% Ag) zusammen mit Chalkopyrit [$CuFeS_2$], wobei darüber Enargit [Cu_3AsS_4] an die Stelle von Fahlerz tritt. Berechnete Prädominanzdiagramme zeigen, dass Enargit unter höheren Sauerstoff- und/oder Schwefelfugazitäten als Fahlerz stabil ist. Die Erhöhung dieser Parameter wird auf den gesteigerten Einfluss eines

oberflächennahen Fluidaquifers zurückgeführt, der in den oberen Teufen durch veränderte Mischungsverhältnisse an Bedeutung gewinnt und somit die mineralogische Zweiteilung bzw. die primäre Silberzonierung hervorruft. Fluideinschlüsse zeigen, dass sich die erste Phase bei Temperaturen zwischen 70 und 125°C und Salinitäten zwischen 23.1 und 26.5 Gew.% $NaCl+CaCl_2$ gebildet hat, was typisch für die jurassisch-kretazischen Gangsysteme ist, zu denen die Grube Clara auch durch Datierungen an Gangarten und Nebengesteinen gezählt wird (PFAFF ET AL. 2009 UND REFERENZEN DARIN).

2. Phase: Während der zweiten Phase bildet sich durch das Zuströmen von kupfer- und eisenreichen Fluiden in den an Silber vorangereicherten Bereichen (unterhalb von 450 m ü.NN) durch die Verdrängung von silberreichem Fahlerz eine Paragenese aus Chalkopyrit, Polybasit-Pearceit und Fahlerz mit niedrigen bis mittleren Silbergehalten. Häufig umwächst dieses neu gebildete Fahlerz, Polybasit-Pearceit mit hohen Kupfergehalten. Mit Hilfe von Prädominanzdiagrammen lassen sich die beobachteten Texturen während dieser Hauptsuflidphase erklären. Sie zeigen, dass bei erhöhter Kupferaktivität silberreiches Fahlerz nicht mehr stabil ist und sich stattdessen (bei konstanten Silberaktivitäten) kupferreicher Polybasit bildet. Durch die Präzipitation von Polybasit nimmt im Folgenden die Silberaktivität im Fluid ab, wodurch sich silberarmes Fahlerz bildet. In den Gangbereichen oberhalb von 450 m ü.NN wird Enargit verdrängt, wobei sich silberarmes Fahlerz und Chalkopyrit bilden. Messungen an Fluideinschlüssen zeigen, dass sich die zweite Phase bei Temperaturen zwischen 90 und 160°C und Salinitäten zwischen 24.2 und 26.7 Gew.% $NaCl+CaCl_2$ gebildet hat.

3. Phase: Während der dritten Phase wird der zuvor gebildete kupferreiche Polybasit-Pearceit sowie das Fahlerz wiederum lokal von Pyrargyrit-Proustit [$Ag_3(As,Sb)S_3$] und Galenit verdrängt. Diese Paragenese ist auf den Influx eines Fluides mit hohen Silber- und Bleiaktivitäten zurückzuführen. Stabilitätsdiagramme zeigen, dass durch den Anstieg der Silberaktivität kupferreicher Polybasit und Fahlerz nicht mehr stabil sind und sich stattdessen silberreicher Polybasit bildet. Die Herkunft des mineralisierenden Fluides wird unten (5. Phase) kurz diskutiert. Messungen an Fluideinschlüssen konnten für diese Phase nicht durchgeführt werden.

4. Phase: Die vierte Phase ist durch die lokale Auflösung der zuvor gebildeten Sulfide und Sulfosalze durch vornehmlich Fluorit und Quarz gekennzeichnet. Fluideinschlussmessungen an Fluorit und Quarz zeigen, dass es sich hierbei um die höchsten Temperaturen (bis 250°C) und niedrigsten Salinitäten (19 bis 21 Gew.% $NaCl+CaCl_2$) handelt, die bisher im Schwarzwald für jurassisch-kretazische Gangsysteme in der Literatur beschrieben wurden. Jurassische Gänge liegen typischerweise in einem Temperaturbereich von 60 bis 180°C und besitzen eine Salinität zwischen 23 und 26 Gew.% $NaCl+CaCl_2$ (WALTER ET AL. 2016 und Referenzen darin).

Da angenommen wird, dass Grundgebirgsfluide im Schwarzwald typischerweise 300 bis 350°C (SCHWINN ET AL. 2006) und Salinitäten um 21 Gew.% NaCl+$CaCl_2$ besitzen (WALTER ET AL. 2016 und Referenzen darin), ist es wahrscheinlich, dass ein solches Fluid zur Auflösung der Sulfide geführt hat. Entweder handelt es sich dabei um ein reines Grundgebirgsfluid oder ein Fluid mit einem niedrigen Mischungsverhältnis.

5. Phase: Während der fünften Phase kommt es zur lokalen Verquarzung der Gangminerale und es werden As-Bi-reiche Paragenesen gebildet. Bringt man diese Beobachtung zusammen mit der dritten Phase, ist auffällig, dass die Elementassoziation (Pb-Ag-Bi-As) in quarzreicher Gangart der von Lagerstätten wie der Friedrich-Christian-Mine und der Herrensegen-Mine (Pb-Ag-Bi-As-Pb) ähnelt, die wie die Grube Clara an die Nordkinzigtalstörung gebunden sind (STAUDE ET AL. 2010A). Somit ist es wahrscheinlich, dass die dritte und fünfte Phase durch Fluide gebildet wurde, die über dieses Störungssystem mobilisiert wurden.

6. Phase: Zuletzt kommt es zur Alteration der gebildeten Ag-Sulfosalze und Chalkopyrit, wobei sich typische Alterationsphasen wie Famatinit-Luzonit [$Cu_3(As,Sb)S_4$] und Covellin [CuS] bilden. Die Bildung von Famatinit-Luzonit lässt auf ein oxidierteres, kupferreiches Milieu schließen. Mikrosondenmessungen zeigen, dass Silber nur zu einem geringen Anteil in Famatinit-Luzonit eingebaut wird und somit häufig als Akanthit [Ag_2S] und/oder ged. Silber [Ag] (mindestens zum Teil) repräzipitiert wird, was in Übereinstimmung mit den texturellen Beobachtungen ist.

Zusammenfassend konnte die Studie zeigen, wie Silber über mehrere hydrothermale Phasen hinweg durch sich ändernde Fluidchemie umverteilt wird, jedoch die vorangelegte Zonierung erhalten bleibt und die darauffolgende Mineralisation definiert. Betrachtet man Fahlerzzusammensetzungen des gesamten Schwarzwalds ist festzustellen, dass deren Silbergehalt im Süden generell höher ist als im Mittleren und Nordschwarzwald (STAUDE ET AL. 2010B). Diese Studie zeigt jedoch, dass im Mittleren Schwarzwald hohe Silbergehalte im Fahlerz in größeren Tiefen ebenfalls anzutreffen sind, im Falle der Grube Clara etwa 450 m unter der Geländeoberkante. Da der Mittlere und Nordschwarzwald nicht so tief erodiert wurden (etwa 1-1.5 km) wie der Südschwarzwald, kann darüber spekuliert werden, dass in zahlreichen Hydrothermalgängen des Mittleren und Nordschwarzwalds silberreiche Assoziationen in größeren Teufen anzutreffen sind.

4.2 Umverteilung von Silber und Bismut innerhalb der Oxidationszone

Nachdem die vorangegangene Studie die Umverteilung von Silber im hydrothermalen System unter reduzierenden Bedingungen fokussierte, wurde in zwei separaten Studien das Verhalten von Silber und Bismut bei der oxidativen Verwitterung von Galenit beziehungsweise Bi-reichem Fahlerz untersucht.

4.2.1 Silberumverteilung bei der Verwitterung von Bleiglanz

Galenit gilt als eines der ökonomisch wichtigsten Silbererze, was darin begründet liegt, dass durch gekoppelte Substitution mit Antimon und Bismut bis zu 9.8 Gew.% Silber eingebaut werden (RENOCK UND BECKER 2011) und er ein typisches Durchläufermineral in einer Vielzahl von Lagerstätten ist. Neben gekoppelter Substitution sind hohe Silbergehalte auf das Vorhandensein von µm- bis nm-großen Einschlüssen, silberhaltiger Sulfide und Sulfosalze, wie Akanthit, Pyrargyrit und Polybasit-Pearceit zurückzuführen (SHARP UND BUSECK 1993). Die Mobilität von Blei bei der Verwitterung unter verschiedenen physikochemischen Bedingungen ist gut verstanden (z. B. INGWERSEN 1990; BASTA UND MCGOVEN 2004; MIKHLIN ET AL. 2006; REICHERT 2007; LARA ET AL. 2011; KEIM UND MARKL 2015). Kommt Bleiglanz mit oxidierenden Fluiden in Kontakt, bildet sich abhängig von der Fluidzusammensetzung Anglesit, Cerussit, Pyromorphit, Mimetesit [$Pb_5(PO4)_3Cl$] oder Vanadinit [$Pb_5(VO4)_3Cl$] (KEIM UND MARKL 2015). Dies führt dazu, dass sich Blei innerhalb von Oxidationszonen (relativ) immobil verhält (PARK UND MACDIARMID 1975). Bisherige Studien zeigen, dass Bleisekundärminerale mitunter relativ hohe Silbergehalte aufweisen können. So wurden Silbergehalte in Pyromorphit von bis zu 500 ppm (MARKL ET AL. 2014B) und in Cerussit von bis zu 2000 ppm (STAVINGA 2014) dokumentiert. Bisher nicht systematisch untersucht bleibt, wieviel Prozent des freigesetzten Silbers vom ursprünglichen Galenit in die Bleisekundärminerale eingebaut werden. Um diese Fragestellung zu beantworten, wurden in Studie 2 (*Anhang 2*) 34 Proben von verwittertem Galenit zusammen mit Cerussit, Anglesit, Pyromorphit und Mimetesit von 15 Lokalitäten im Nord- und Südschwarzwald mittels LA-ICP-MS untersucht.

Der untersuchte Galenit zeigt deutlich unterschiedliche Silbergehalte zwischen 30 und 9700 ppm. Silbergehalte von Anglesit liegen stets unterhalb der Nachweisgrenze (<0.01 ppm). Cerussit hat maximale Silbergehalte von 0.4 ppm, Mimetesit von 6 ppm und Pyromorphit von maximal 56 ppm (durchschnittlich 20 ppm). Alle Analysepunkte wurden so gewählt, dass keine mikroskopischen Einschlüsse anderer Mineralphasen vorhanden waren und somit Mischmessungen ausgeschlossen werden konnten. Die in der Literatur berichteten, hohen Silbergehalte in Cerussit sind somit auf das Vorhandensein von Galenitrelikten zurückzuführen. Dies scheint sehr wahrscheinlich, da die in der Literatur analysierten Cerussite eine dunkelgraue Färbung aufweisen, welche für gewöhnlich auf das Vorhandensein von µm-großen Galenitrelikten zurückzuführen ist.

Vergleicht man nun die Silbergehalte der verwitternden Galenite direkt mit den Bleisekundärmineralen zeigt sich, dass maximal 13% des darin enthaltenen Silbers eingebaut werden, wobei der Wert zumeist zwischen 7 und 0% liegt. Folglich wird bei der Verwitterung von Galenit Silber freigesetzt, wobei sich die Frage stellt, ob das Silber als eigenständige Phasen repräzipitiert oder durch Fluide abtransportiert wird. Betrachtet man zunächst die untersuchten Lokalitäten hinsichtlich des Vorkommens von eigenständigen Silberphasen, ist

festzustellen, dass dort verbreitet sekundärer Akanthit und ged. Silber vorkommen. In nur einem Fall, dem der Grube Clara, kommt zusätzlich sekundärer Chlorargyrit vor. Das Vorkommen von eigenständigen Silberphasen, speziell an Lokalitäten, bei denen keine weiteren silberhaltigen primären Sulfosalze vorhanden sind, zeigt, dass Silber, welches bei der Verwitterung von Bleiglanz freigesetzt wird, innerhalb der Oxidationszone repräzipitiert wird und somit (zumindest zum Teil) als Wertmetall erhalten bleibt. Mit Hilfe von berechneten Stabilitätsdiagrammen in Kombination mit Wasseranalysen aus der Literatur (GÖB ET AL. 2011, 2013A, 2013B; MARKL ET AL. 2014A) wurde ein Modell erstellt, um Voraussagen darüber treffen zu können, wie sich Silber unter den heute vorherrschenden hydrogeochemischen Bedingungen in den Oxidationszonen des Schwarzwaldes verhält und umverteilt wird und warum Chlorargyrit nur an einer Probenlokalität auftritt.

Berechnete Stabilitätsdiagramme zeigen, dass unter oxidierenden Bedingungen Silberionen und Silberchloridkomplexe sowie Chlorargyrit stabil sind und unter reduzierenden Bedingungen ged. Silber und Akanthit. Die Größe des Chlorargyritfelds ist im Wesentlichen von der Silber- und Chloridaktivität abhängig. Durch die Verknüpfung von heutigen Minenwasseranalysen mit den Stabilitätsdiagrammen konnten folgende Schlüsse für die Verwitterung von silberhaltigem Galenit in Oxidationszonen des Schwarzwalds gezogen werden:

- Silber wird als Silberionen und nicht als Silberkomplexe freigesetzt.
- Freigesetzte Silberionen werden durch lokale Redoxprozesse überwiegend als ged. Silber und Akanthit repräzipitiert.
- Chlorargyrit kann nur entstehen, wenn verwitternder Galenit hohe Silbergehalte (um 1000 ppm) aufweist, weitere silberhaltige Minerale verwittern oder die Chloridgehalte der Wässer erhöht sind (z. B. durch Auflösen von Evaporitlagen oder dem anthropogenen Einbringen von Streusalz).

Zusammenfassend kann das entwickelte thermodynamische Modell in Lagerstätten dazu verwendet werden, um anhand der Chemie von Verwitterungsfluiden (Chloridaktivität und Sauerstofffugazitäten) und gemessenen Silbergehalten im Galenit Voraussagen zu treffen, ob Silber bei der Verwitterung von Galenit vornehmlich in Lösung geht und als welche Silberphasen es repräzipitiert werden kann.

4.2.2 Bismutumverteilung bei der Verwitterung von Fahlerz

Ebenso wie Galenit ist Fahlerz in einer Vielzahl von Lagerstätten verbreitet (z. B. LEACH ET AL. 1988; VAVELIDIS UND MELFOS 2004; STAUDE ET AL. 2010B; MUELLER UND MUHLING 2013; KOZUB 2014; PLOTINSKAYA ET AL. 2015; REPSTOCK ET AL. 2015; WOHLGEMUTH-UEBERWASSER ET AL. 2015; GEORGE ET AL. 2017) und ein bedeutendes Silber- und Kupfererz (WU UND PETERSON

1977). Im Gegensatz zu Galenit ist Fahlerz deutlich komplexer zusammengesetzt und kann große Mengen toxischer Schwermetalle, wie Sb, As, Cu und Hg akkumulieren, die potentiell bei der Verwitterung freigesetzt werden können und so in die Umwelt gelangen. Trotz dieser Problematik sind Studien über den Verwitterungsprozess und die Elementumverteilung während der Verwitterung von Fahlerz rar. Die Studien von NICKEL ET AL. (2007) und PETRUNIC ET AL. (2009) beschreiben die Mineralogie bei der Verwitterung im Kontakt zu W- bzw. Pb-reichen Fluiden. Beide Studien zeigen, dass sich verbreitet Arsenatphasen bilden. Erst kürzlich untersuchte die Studie von BORČINOVÁ RADKOVÁ ET AL. (2017) die Verwitterung von Sb-dominierten Fahlerzen, wobei der Fokus auf der Mobilisierung der toxischen Elemente Sb, As und Cu lag. Der allgemeine Verwitterungsprozess sowie eine Quantifizierung der mobilisierten toxischen Elemente wurden in den genannten Studien nicht untersucht. Weiter bleibt unbekannt, welchen Einfluss Bismut auf die Verwitterung von Fahlerz nimmt, da natürlich gebildete Fahlerze bis zu 22 Gew.% Bismut einbauen können (STAUDE ET AL. 2010B). Um die offenen Fragen zu klären, wurden in Studie 3 (*Anhang 3*) der Verwitterungsprozess sowie die quantitative Mobilisierung von toxischen Elementen und Schwermetallen anhand von verwittertem Bi-haltigem Fahlerz aus dem Schwarzwald untersucht. Hierzu wurden 17 Proben von 4 Lokalitäten mittels EMS, REM, TEM, LA-ICP-MS, µXRD, Raman und MLA untersucht. Basierend auf den beobachteten Texturen wurde die Verwitterung von Fahlerz in vier Verwitterungsstufen unterteilt:

1. Verwitterungsstufe: Verdrängung von Fahlerz entlang von unregelmäßig angeordneten, fingerartigen Adern. Die Adern bestehen aus einer engen Verwachsung einer Kupferoxidphase, einer Kupfersulfidphase und, je nach Fahlerzzusammensetzung, Roméitgruppenmineralen (RGM) bzw. Tripuhyit.

2. Verwitterungsstufe: Verdrängung des Fahlerzes durch amorphe bis nanokristalline Kupferarsenate, vornehmlich entlang von Verwitterungsfronten. Die erste Stufe bleibt dabei zumeist unbeeinflusst.

3. Verwitterungsstufe: Lokal beschränkte Prozesse, die vom generellen Verwitterungsprozess unabhängig sind. Es kommt zur Auflösung der ersten Verwitterungsstufe bzw. zur Bildung amorpher, neuer Phasen.

4. Verwitterungsstufe: Bildung von kristallinen Kupferkarbonaten und Bi-, Cu-, Ba-, Ca-, Al-Arsenaten entlang von Rissen und in Hohlräumen. Zum Teil werden ältere Verwitterungsstufen aufgelöst und/oder verdrängt.

Massenbilanzrechnungen basierend auf Rückstreuelektronenbildern zeigen, dass während der ersten Verwitterungsphase große Teile des im Fahlerz enthaltenen Arsens, Zinks und zum Teil Schwefel mobilisiert und abtransportiert werden. Im Gegensatz dazu verhält sich Bismut immobil. Sind die Bismutgehalte im Fahlerz hoch, so sind Antimon und Eisen ebenfalls

immobil. Ist hingegen das Fahlerz Bi-arm, werden Eisen und Antimon teilweise mobilisiert. Kupfer wird während der ersten Phase extern hinzugefügt. Weiter zu beobachten ist, dass sich, wenn das Fahlerz Bi- und Sb-reich ist, Bi-Sb RGM gebildet werden. Ist das Fahlerz Sb-arm aber Bi-reich, bilden sich Bi-Fe RGM, im umgekehrten Fall Tripuhyite/Hydroxyferroroméite.

Die gebildete Paragenese während der Verwitterungsstufe 1 lässt darauf schließen, dass die Sauerstoffaktivität und somit das Oxidationspotential der beteiligten Fluide zu gering war, um Schwefel (Vorhandensein von Sulfiden) und Arsen (Fehlen von Arsenaten) zu oxidieren. Die Studie von JANSSEN ET AL. (2010) an Ilmenit zeigt, dass sich fingerartige Verwitterungs-/Alterationstexturen unter der Beteiligung von Fluiden mit geringem chemischen Potential zwischen dem Verwitterungsfluid und Ilmenit durch Diffusion ausbilden. Für die Verwitterung von Sulfiden ist das wohl wichtigste chemische Potential die Sauerstoffaktivität der Fluide. Folglich spiegeln neben der gebildeten Paragenese auch die fingerartigen Texturen die Verwitterung bei relativ geringer Sauerstoffaktivität wider, was typisch für Zementationszonen ist. Typischerweise werden in dieser Zone primäre Sulfide durch sekundäre Cu-Sulfide verdrängt (z. B. REICH UND VASCONCELOS 2015). Fingerartige Texturen bei der Verwitterung von Fahlerz wurden auch von BORČINOVÁ RADKOVA ET AL. (2017) dokumentiert. Ähnliche fingerartige Texturen sind auch bei der Alteration von Basaltglas (Dultz et al. 2014) und bei der Verdrängung von Galenit durch Quarz, Gold und Akanthit zu beobachten (Kamenov et al. 2013). Zudem wurden sie in den untersuchten Proben auch in Pyrit [FeS_2], Gersdorffit [NiAsS], Wittichenit [Cu_3BiS_3], Emplektit [$CuBiS_2$] und Nickelin [NiAs] beobachtet. Diese Beobachtungen zeigen, dass diffusive Prozesse wohl typisch für Verwitterungsprozesse in Systemen sind, in welchen ein geringer chemischer Potentialunterschied zwischen Verwitterungsfluid und Mineral herrscht.

Während der zweiten Verwitterungsstufe bilden sich vornehmlich Kupferarsenate, wobei Kupfersulfide fehlen. Massenbilanzberechnungen zeigen, dass Arsen immobil ist und Eisen extern zugeführt wurde. Die Bi-Gehalte der amorphen Phase spiegeln die des primären Fahlerzes wider. Es bilden sich Bi-reiche Arsenate, wenn auch das Fahlerz Bi-reich ist, wobei Bismut nicht mobilisiert wird. Ist das Fahlerz hingegen Bi-arm, wird Bismut teilweise mobilisiert. Die Elemente Kupfer, Zink, Schwefel und Antimon verhalten sich mobil und werden zum Teil, oder nahezu vollständig abtransportiert. Die verbreitete Bildung von Kupferarsenaten spricht für höhere Sauerstoffaktivitäten, als bei der ersten Verwitterungsstufe, was interessanterweise für eine geringe Mobilität von Arsen sorgt. Die Verdrängung entlang von Fronten konnte bei der Studie von JANSSEN ET AL. (2010) an Ilmeniten ebenfalls beobachtet werden. Dieser Typ der Verdrängung tritt dabei in Experimenten auf, die bei einem höheren chemischen Potentialunterschied zwischen Fluid und Ilmenit durchgeführt wurden. Die Bildung von Arsenaten, das Fehlen von Sulfiden sowie die Verdrängung entlang von Fronten bei der

Fahlerzverwitterung spiegeln somit ein oberflächennahes Milieu mit hohem Oxidationspotential wider, typisch für Bedingungen innerhalb der Oxidationszone. Die Bildung amorpher Arsenate bei der Verwitterung von Fahlerz kann beispielsweise auch an folgenden Orten beobachtet werden: Grube Clara, SW-Deutschland (WALENTA 1992); Cínovec, Tschechien (PAULIŠ ET AL. 2008); Mt. Pleasant, Canada (PETRUNIC ET AL. 2009); Mt. Cernvandone, Italien (GUSTEANI ET AL. 2006). Dieses weit verbreitete Auftreten zeigt, dass die Bildung amorpher Arsenate bei der Verwitterung von Fahlerz ein typisches Phänomen in einer Vielzahl von Oxidationszonen mit unterschiedlichem geologischen Kontext darstellt.

Die dritte Verwitterungsstufe kann nur an zwei Lokalitäten ausgemacht werden. Sie repräsentiert nicht, wie die Verwitterungsstufen 1 und 2 einen generellen, lokalitätsübergreifenden Verwitterungsprozess, sondern Prozesse, welche lokal unterschiedlich Einfluss auf die Verwitterung nehmen. Diese Prozesse beinhalten zum einen die Auflösung früherer Verwitterungsstufen (Verwitterungsstufe 1) und somit die Mobilisation von Elementen, zum anderen die Präzipitation neuer Verwitterungsphasen. Die Auflösung von Verwitterungsstufe 1 betrifft die Kupferoxid- und die Kupfersulfidphase, wobei Kupfer und Schwefel mobilisiert werden. Die RGM bleiben hingegen stabil und verhindern eine Mobilisierung von Antimon und Bismut.

Die vierte Verwitterungsstufe unterscheidet sich nicht nur texturell von den vorherigen Verwitterungsstufen, sondern zeigt auch einen chemischen Wechsel der Sekundärphasen, da nun verbreitet Kupferkarbonate sowie Bi-, Cu-, Ca-, Fe-, Ba- und Al-Arsenate gebildet werden (z. B. Mixitgruppenminerale). Fahlerz wird in dieser Stufe nicht mehr in-situ in Sekundärphasen umgewandelt, sondern es findet ein Elementtransport auf Zentimeter- bis Meterebene statt, wobei Sekundärphasen entlang von Rissen und in Hohlräumen kristallisieren. Eine solch hohe Mobilität von Elementen findet typischerweise oberflächennah statt und zeigt wohl den Übergang von der Oxidationszone zum Eisernen Hut. Eine weitläufige Elementumverteilung bei der Verwitterung von Fahlerz kann beispielsweise auch in Tsumeb, Namibia (BOWELL 2014) und Bou Skour, Marokko (DIETRICH ET AL. 1969) beobachtet werden. Das Elementinventar der Sekundärphasen zeigt, dass neben Fahlerz und Verwitterungsprodukten der ersten beiden Verwitterungsstufen (Cu, As, Bi, Fe) auch Gangarten und Nebengesteine vermehrt aufgelöst werden, wobei Ba, Ca, Al, und C mobilisiert werden und als kristalline Sekundärphasen (zumindest zum Teil) repräzipitieren. Da während dieser Phase keine sekundären Antimonphasen gebildet werden, wird es wohl mobilisiert und abtransportiert.

Zusammenfassend zeigt sich, dass je nach Oxidationspotential der Verwitterungsfluide Schwermetalle bei der Verwitterung von Fahlerz in unterschiedlichem Maße mobilisiert werden. Bismut verhält sich in der Zementationszone und der Oxidationszone immobil und wird erst im Übergang zum Eisernen Hut mobilisiert und zum Teil als Mixitgruppenminerale

repräzipitiert. Zudem zeigt sich, dass das Vorhandensein von Bi im Fahlerz die Mobilität von Antimon kontrollieren kann, indem es in RGM eingebaut wird.

4.3 Blaubleierze – Einblick in die Schnittstelle zwischen Oxidationszone und Hydrothermalsystem

In aller Regel liegen zwischen der primären Bildung einer hydrothermalen, sulfidischen Vererzung und der supergenen Verwitterung mehrere Hunderttausend oder Millionen Jahre. Die allermeisten Hydrothermalgänge werden in Tiefen von einigen hundert Metern bis wenigen Kilometern gebildet (BURISCH ET AL. 2018) und in Folge von Hebung und Erosion in oberflächennahe Bereiche gebracht. Ist das Hydrothermalsystem weiterhin aktiv, bilden sich im Fall des Schwarzwalds aus hydrothermalen Lösungen vornehmlich Karbonate und Sulfate, jedoch keine Sulfide, was mit der chemischen Zusammensetzungsänderung der vertikalen Fluidstratigraphie zusammenhängt (BURISCH ET AL. 2018).

Innerhalb der eigentlichen Oxidationszone treten neben den normalen, meteorischen Verwitterungsfluiden zum Teil niedrigtemperierte Tiefenfluide als Thermalquellen in den Gängen oberflächennah auf, wie z. B. im Prospergang nahe Bad Rippoldsau (BLIEDTNER UND MARTIN 1986). Jedoch ändern sie die gebildete supergene Mineralogie bezüglich der Bildung neuer Sulfidphasen nicht, da die Fluide nicht reduziert sind. Dies gilt nicht für das Hydrothermalsystem der Kautenbachmine am Hunsrück in Rheinland-Pfalz, in dem supergen gebildeter Pyromorphit durch Galenit pseudomorphisiert wird und folglich ein Wechselspiel zwischen reduzierenden (Thermalfluide) und oxidierenden Fluiden stattgefunden haben muss (MARKL 2014C). Diese weltbekannten Pseudomorphosen werden als Blaubleierze bezeichnet (WERNER UND HOFFMANN 1789). Sie sind bislang nur von sechs Lokalitäten weltweit bekannt: Kautenbach, Rheinland-Pfalz; Wheal Hope, Cornwall; Huelgoat, Bretagne; Zschopau und Freiberg, Sachsen sowie Tsumeb, Namibia (MARKL, 2014C UND REFERENZEN DARIN). Die Verdrängung eines typischen Oxidationszonenminerals (Pyromorphit) durch ein typisches hydrothermales Sulfidmineral (Galenit) zeigt, wie oben schon angesprochen, dass die durch oxidierende Wässer gebildeten Pyromorphite mit sulfidreichen, reduzierenden Fluiden in Kontakt gekommen sein müssen (NÖGGERATH 1846; MARKL 2014C). Die Seltenheit der Pseudomorphosen beweist, dass ein solcher Wechsel von Fluidsystemen ein in der Natur seltenes Phänomen ist. Bisherige Arbeiten (BLUM 1843; NÖGGERATH 1846; GERGENS 1856; MARKL 2014C; JAHN 2016) beschränken sich auf die makroskopische Beschreibung der Pseudomorphosen, wobei die Texturen in Dünnschliffen bislang nicht untersucht wurden. Ebenfalls sind der genaue Entstehungsmechanismus und die hydrogeochemischen Randbedingungen weitestgehend unbekannt. NÖGGERATH (1846) und MARKL (2014C) bringen die Entstehung mit den bisulfidreichen Thermalquellen in Verbindung, die an mehreren Stellen

in der Kautenbachmine aufgefahren worden sind (JAHN 2016 und Referenzen darin). Um zu klären, ob diese Quellen zur Bildung der Blaubleierze geführt haben, wurden in Studie 4 (*Anhang 4*) die Wässer beprobt und durch die Kombination mit Texturbeobachtungen und berechneten Stabilitätsdiagrammen die Genese der Blaubleierze quantifiziert. Zudem wurde ein textureller Vergleich mit den anderen europäischen Blaubleierzvorkommen aufgestellt und bestimmt, ob Blei während der Entstehung der Pseudomorphosen mobilisiert wurde.

Die hydrothermalen Gänge der Kautenbachmine sind postvarizischen Alters und liegen in devonischen, niedrig metamorphen Schiefern (KRONZ 2005). Die Schiefer zeigen lokal Einschaltungen von Siltsteinen und Quarziten und überlagern prädevonisches, kristallines Grundgebirge (ONCKEN ET AL. 1999). Zudem sind sie häufig angereichert an diagenetischem Pyrit (TIBBS 2003). Die hydrothermalen Gänge der Kautenbachmine bestehen im Wesentlichen aus Quarz als Gangart zusammen mit Galenit, Sphalerit [ZnS], Chalkopyrit, Pyrrhotin [FeS] und Fahlerz (KRONZ 2005; JAHN 2016). Die Blaubleierze stammen aus einem etwa 60 cm mächtigen Gangbereich, der bis etwa 60 m unterhalb der Geländeoberkante große Mengen (häufig idiomorphen) Pyromorphit aufweist. Die wichtigsten makroskopischen Beobachtungen (BLUM 1843; NÖGGERATH 1846; GERGENS 1856; MARKL 2014C; JAHN 2016) an Blaubleierzen können wie folgt zusammengefasst werden:

- Pseudomorphosen häufig unvollständig; Pyromorphit als reliktischer Kern erhalten;
- teilweise (mehrfacher) Wechsel zwischen Pyromorphit und Galenit;
- Pseudomorphosen von dünnen Krusten aus Pyrit, Covellin oder Goethit [FeOOH] überzogen;
- Galenit zeigt im Bruch einen blassen Glanz;
- Verwachsungen mit traubig ausgebildetem Pyrit.

Die in Studie 4 untersuchten Dünnschliffe von drei Blaubleierzproben zeigen, dass Pyromorphit durch eine enge, schwammartige Verwachsung aus Galenit und Apatit [$Ca_5(PO_4)_3(Oh,F,Cl)$] pseudomorphisiert wurde, was den beschriebenen blassen Glanz des Galenits erklärt. Mikrosondenmessungen ergaben, dass es sich dabei um Fluorapatit [$Ca_5(PO_4)_3F$] handelt.

Weiter stellt sich die Frage, ob die heute in der Kautenbachmine auftretenden Thermalquellen zur Bildung der Pseudomorphosen geführt haben können. Es zeigte sich, dass die analysierten Thermalwässer Na^+-HCO_3^--SO_4^{2-}-dominiert sind und relativ hohe pH-Werte (~8) sowie Fluorgehalte zeigen (bis zu 460 ppm). Berechnete Stabilitätsdiagramme auf Basis der Wasseranalysen zeigen, dass die Paragenese aus Fluorapatit und Galenit nur in einem pH-Bereich von 6.6 bis 9.2 unter reduzierenden Bedingungen $<\log f_{O2} = -68$ stabil ist. In diesen pH-Bereich fallen auch die analysierten Thermalwässer, jedoch sind sie zu oxidiert ($\log f_{O2}$~-40). Die relativ hohen Sauerstofffugazitäten der Fluide sind auf die Equilibrierung mit Luftsauerstoff bei Quellaustritt zurückzuführen und sind wohl vor ihrem Austreten weitaus niedriger. Somit ist

es sehr wahrscheinlich, dass die heutigen Thermalwässer in der Kautenbachmine auch zur Bildung der Pseudomorphosen führen können. Basierend auf den texturellen Beobachtungen, den Wasseranalysen und den Stabilitätsdiagrammen, kann die Genese der Blaubleierze in drei Schritte eingeteilt werden.

I. Bildung von Pyromorphit durch die supergene Verwitterung von Galenit durch oxidierte, phosphatreiche Fluide mit einem $\log f_{O2} > \sim -60$.
II. Verdrängung des in Schritt I gebildeten Pyromorphits unter der Kopräzipitation von Galenit und Fluorapatit durch reduzierte ($\log f_{O2} < \sim -60$) sulfid-, fluor- und calciumreiche, thermale Fluide (Bildung der Blaubleierze).
III. Erneute Präzipitation von Pyromorphit durch die supergene Verwitterung der gebildeten Blaubleierze.

Die Wechsellagerungen zwischen Galenit und Pyromorphit zeigen, dass der Wechsel zwischen Schritt II und Schritt III in manchen Proben mehrere Male vollzogen wurde. Erklärt werden kann der mehrfache Wechsel zwischen einem Thermalsystem und supergener Fluide beispielsweise durch tektonische Aktivität, welche zur wiederholten Reduzierung bzw. dem Schließen von Fluidwegsamkeiten führen kann, wodurch sich die Dominanz des vorherrschenden Fluidsystems ändert.

Die geochemische Signatur der Thermalwässer lässt darauf schließen, dass sie ihre Quellen in den Gneisen des Grundgebirges haben. Hierfür sprechen die relativ hohen pH-Werte sowie die Cl/Br Verhältnisse um 100, die typisch für gneisische bzw. granitische Grundgebirgsfluide sind (z. B. BUCHER 2010; FUSSWINKEL ET AL. 2013).

Blaubleierzproben von Wheal Hope und Zschopau zeigen im Dünnschliff sehr ähnliche Texturen, wobei keine schwammartige Verwachsung mit Fluorapatit zu beobachten ist, sondern stattdessen Hohlräume vorhanden sind. Das Fehlen von Apatit in den Proben von Zschopau und Wheal Hope lässt entweder auf die Bildung unter der Beteiligung Ca- bzw. F-armer Fluide schließen, oder die Bildung bei pH-Werten, unter denen Apatit nicht stabil ist.

Das Vorhandensein von Hohlräumen bei der Pseudomorphisierung ist auf die unterschiedlichen Dichten von Galenit und Pyromorphit zurückzuführen. Massenbilanzrechnungen an Proben aus Kautenbach, Zschopau und Wheal Hope zeigen, dass Blei aus dem Pyromorphit nahezu 1:1 in Galenit umgesetzt wurde und folglich bei der Bildung der Pseudomorphosen nicht freigesetzt und mobilisiert wurde.

Die Texturen der Blaubleierze aus Huelgoat unterscheiden sich von den anderen Lokalitäten. Galenit tritt hier nicht schwammartig, sondern massiv auf. Dies bedeutet, dass bei der Bildung von Galenit, Blei bzw. Sulfid extern zugeführt werden musste. Zudem sind die Blaubleierze von Plumbogummit [$PbAl_3(PO_4)_2(OH)_5 \cdot H_2O$)] umwachsen und überwachsen massiven Pyrit. Die Bildung dieser ungewöhnlichen Textur kann wie folgt erklärt werden: Der supergen

gebildete Pyromorphit wird zunächst von Plumbogummit umwachsen. Anschließend wird Pyromorphit vollständig aufgelöst, wobei Plumbogummit davon unbeeinflusst bleibt und sich hohle Paramorphosen bilden. Später werden die Paramorphosen von Galenit gefüllt, wobei Blei durch ein externes Fluid und Sulfid durch das Auflösen des assoziierten Pyrits hinzugefügt werden. Ein Transport von Schwefel und Blei im selben Fluid ist aufgrund der geringen Löslichkeit nicht möglich.

Zusammenfassend zeigt die Studie, dass die Blaubleierze den zum Teil mehrmaligen Wechsel von reduzierenden und oxidierenden supergenen Fluiden aufzeichnen, wobei Blei nicht mobilisiert wird. Die Immobilität von Blei gilt nicht nur für das Vorkommen an der Kautenbachmine, sondern ist auch auf Wheal Hope und Zschopau übertragbar. Die gebildete Paragenese aus Galenit und Fluorapatit grenzt die Bildungsbedingungen für die Blaubleierze an der Kautenbachmine ein und zeigt, dass sie durch calcium- und fluorreiche Fluide bei relativ hohen pH-Werten gebildet wurden.

4.4 Anthropogener Einfluss auf die Verwitterung und Umverteilung

Seitdem der Mensch metallische Rohstoffe für sich nutzt, nimmt er durch deren Abbau Einfluss auf Verwitterungsprozesse und folglich auch auf die Mobilisierung und Umverteilung von Elementen. Durch den Abbau der Erze in Tagebauen und Bergwerken werden bis heute andauernd Wegsamkeiten für oxidierende, meteorische Fluide geschaffen, welche somit in tiefe Bereiche der Erzkörper vordringen können und dort zu Verwitterungsprozessen führen (e.g. BUCHER ET AL. 2009; DILL 2010; BOWELL 2014). Weiter werden Primärerze und ihre Verhüttungsprodukte seit mehreren tausend Jahren in großem Stil auf Halden gebracht, wo sie folgend meteorischen Fluiden ausgesetzt sind (e.g. ETTLER ET AL. 2009A, B; TYSZKA ET AL. 2014; EGLI ET AL. 2017). Auch verarbeitete Metalle und Metallverbindungen gelangen zum Teil in die Umwelt und können dort Verwitterungsprozessen ausgesetzt werden (e.g. LIN 1996; ESSIGNTON ET AL. 2004; LI ET AL. 2015).

In diesem Kontext spielen Bleiverbindungen (bzw. metallisches Blei) eine große Rolle, da sie in vielen Erzlagerstätten, auf Halden und als Nutzmetall omnipräsent sind. Aufgrund seiner bekannten Toxizität (CALLENDER 2014) ist es von großer Wichtigkeit, Prozesse bei der Verwitterung von Bleiverbindungen zu verstehen. Betrachtet man in diesem Zusammenhang Bleioxide bzw. ged. Blei, ist festzustellen, dass sich bei deren Verwitterung basische Bleiminerale wie Hydrocerussit [$Pb_3(CO_3)_2(OH)_2$], Leadhillit [$Pb_4(SO_4)(CO_3)_2(OH)_2$], Claedonit [$Pb_5Cu_2(CO_3)(SO_4)_3(OH)_6$], Lanarkit [$Pb_2OSO_4$], Elyit [$CuPb_4O_2SO_4(OH)_4 \cdot H_2O$], Chenit [$Pb_4Cu(SO_4)_2(OH)_6$] und andere bilden (KARUP-MØLLER, 1975; LIVINGSTONE 1993; WITTERN 1988; 1994; TREIMANN 1999). Diese sind beispielsweise bei der Verwitterung von Galenit, dem

in Erzlagerstätten am häufigsten vorkommenden Bleimineral, nicht anzutreffen. Hier bilden sich vornehmlich Anglesit, Cerussit, Pyromorphit und/oder Mimetesit und/oderVanadinit (KEIM UND MARKL 2015), welche die Bleilöslichkeit unter oxidierenden Bedingungen kontrollieren (RUBY ET AL. 1994).

Die wohl komplexeste Vergesellschaftung basischer Bleiminerale ist auf die mittelaltterliche Bergbautechnik des Feuersetzens zurückzuführen und wurde von WITTERN (1988, 1994) als Feuersetzparagenese bezeichnet. Hierbei handelt es sich zwar nur um sehr kleine, lokale Vorkommen, jedoch eignen sich diese aufgrund der komplexen Vergesellschaftung basischer Bleiminerale sehr gut, um deren generellen Entstehungsprozess und die Stabilitätsbeziehungen besser zu untersuchen. Bisherige Studien bearbeiten die Stabilitätsbeziehung einzelner basischer Bleiminerale (ABDUL-SAMAD ET AL. 1982A, B; TREIMANN 1999; ESSIGNTON ET AL. 2004), jedoch nicht deren Stabilitätsbeziehungen zueinander. Zudem zeigt keine Studie, wie sich Fluide bei der Entstehung von basischen Bleimineralen entwickeln und es ist wenig darüber bekannt, ob und wenn ja, unter welchen Bedingungen die basischen Bleiminerale die Bleilöslichkeit kontrollieren können. Auch über den Feuersetzprozess ist, bis auf die Studie von WITTERN (1988, 1994), bisher wenig bekannt. Es fehlen beispielsweise Informationen über die Temperaturen unter denen das Feuersetzen stattgefunden hat, bzw. wie schnell die Bildung von basischen Bleimineralen vonstatten geht. Deshalb wurde in Studie 5 (*Anhang 5*) die Feuersetzparagenese detailliert untersucht und die gewonnenen Erkenntnisse dazu genutzt, den Prozess des Feuersetzens sowie die Entstehung basischer Bleiminerale auch in anderen anthropogen beeinflussten aber auch natürlichen Paragenesen besser zu verstehen.

Beim Feuersetzen handelt es sich um eine der ältesten Methoden, um hartes Gestein mangels geeigneter Werkzeuge abbauen zu können (AGRICOLA 1556). Hierzu wurde Holz direkt am Stoß aufgestapelt und entzündet. Durch die starke Temperaturerhöhung wurde das Gestein mürbe gemacht. Wichtig in diesem Zusammenhang ist die Umwandlung von Hoch- zu Tiefquarz unterhalb von etwa 570°C, die zu einer Volumenänderung von etwa 5% führt. Um den thermischen Effekt noch zusätzlich zu verstärken, wurde das heiße Gestein in manchen Fällen mit Wasser abgeschreckt (CRADDOCK 1992). Nach dem Herausbrechen des nun brüchigen Gesteins wurde das Erz von der Gangart getrennt und verhüttet. Die Resterze sowie die Gangart wurden auf die Halde gebracht. Hiervon entstammen auch die bearbeiteten Proben. Die Texturen der Proben zeigen, dass die Entstehung der Feuersetzparagenese in drei Stufen eingeteilt werden kann:

I. Zunächst bilden sich Cerussit, Anglesit und Covellin durch die supergene Verwitterung von Galenit.

II. Beim Feuersetzen wird dem supergen gebildeten Cerussit CO_2 thermisch entzogen und es bilden sich die Bleioxide Minium [$Pb^{4+}Pb_2^{2+}O_3$], Lithargit [PbO] und Massicotit [PbO] sowie Bleioxycarbonate [$Pb_{10}(CO_3)_6(OH)_6O$]. Welche dieser Phasen sich bildet, ist abhängig von der Temperatur und der Dauer der thermischen Einwirkung (YAMAGUCHI ET AL. 1980; CIOMARTAN ET AL. 1996). In den untersuchten Proben sind bis auf Massicotit zumeist alle Bleioxide anzutreffen, was den Schluss zulässt, dass sich die Temperaturen beim Feuersetzen zumeist unter 540°C befunden haben müssen, da sich ansonsten die Hochtemperaturmodifikation Massicotit gebildet hätte. Weiter war in den Proben zu beobachten, dass Anglesit vom Feuersetzen nicht beeinflusst worden ist. Dies ist dadurch zu erklären, dass ein Austreiben des Sulfats erst bei Temperaturen über 880°C stattfindet (SAJADI 2011). Selten findet man in den Proben auch Bereiche, welche eine ehemalige Schmelze darstellen. Chemische Untersuchungen zeigten, dass es sich dabei um zwei Arten von ehemaligen Schmelzen handelt. Zum einen Bleisilikat- und zum anderen Blei-Zink-Silikatschmelzen. Durch grafische Integration können in Schmelzdiagrammen Abschätzungen darüber getroffen werden, bei welchen Temperaturen die Schmelzen erstarrt sind und somit auch, welche Temperaturen dabei mindestens erreicht worden sind. Die Ergebnisse zeigen, dass die Bleisilikatschmelzen bei Temperaturen um 760°C und die Blei-Zink-Silikatschmelzen bei Temperaturen um 950°C erstarren.

III. Nach dem Feuersetzen gelangten die gebildeten Bleioxide zum Teil auf die Halde. Hier kommen sie mit meteorischen Fluiden in Kontakt und werden hydratisiert, wobei sich die basischen Bleiminerale Hydrocerussit, Leadhillit, Claedonit, Lanarkit, Elyit, Chenit und Linarit bilden. Die Bleioxide werden hierbei verdrängt. Berechnete Prädominanzdiagramme zeigen, dass die basischen Bleiminerale Leadhillit, Hydrocerussit und Lanarkit bei relativ niedrigen CO_2-Partialdrücken und unter neutralen bis basischen pH-Bedingungen stabil sind. Bei höheren CO_2-Partialdrücken ist im sauren bis neutralen pH-Bereich Anglesit und im neutralen bis basischen pH-Bereich Cerussit stabil.

Texturell zeigt sich, dass die Genese der basischen Bleiminerale auf die beim Feuersetzen gebildeten Bleioxide zurückzuführen ist. Um die Bildung erklären und quantifizieren zu können, wurden thermodynamische Fluidpfadmodellierungen durchgeführt. Es zeigt sich, dass durch die Auflösung von Bleioxiden durch Verwitterungsfluide Protonen verbraucht (der pH-Wert steigt) und Bleiionen freigestezt werden. Da unter hohen pH-Werten Cerussit stabil ist, präzipitiert dieser aus der Verwitterungslösung sobald dessen Sättigung erreicht ist. Durch das Ausfällen sinkt (in geschlossenen Systemen) der CO_2-Partialdruck, wobei Hydrocerussit stabilisiert wird. Ist die Verwitterungslösung beispielsweise durch die Auflösung von Galenit schwefelhaltig, bilden sich hingegen Leadhillit und Lanarkit. Sind die Verwitterungslösungen

durch die Auflösung von Chalkopyrit oder Covellin kupferhaltig, bilden sich Cu-haltige basische Bleiminerale wie Elyit und Caledonit. Das thermodynamische Modell erklärt auch, warum sich basische Bleiminerale in anderen anthropogen beeinflussten Umgebungen bilden, in denen Bleioxide zu finden sind. Es erklärt ebenso die wenigen natürlichen Vorkommen von basischen Bleimineralen, bei denen Bleioxide supergener Verwitterung ausgesetzt sind (z. B. KARUP-MØLLER 1975). Jedoch gibt es auch natürliche Vorkommen, in denen basische Bleiminerale in Assoziation mit Galenit (ohne Bleioxide) vorgefunden werden (INGWERSEN 1990; BOWELL UND CLIFFORD 2014). Dieser Umstand kann durch die Verwitterung unter erhöhten Temperaturen erklärt werden, da sich die Stabilitätsfelder der basischen Bleiminerale hin zu geringeren CO_2-Partialdrücken vergrößern. So kann beispielsweise das Vorkommen von Hydrocerussit und Leadhillit in Tsumeb, Namibia erklärt werden, wo erhöhte Verwitterungstemperaturen anhand von Fluideinschluss-Messungen nachgewiesen wurden (GILG ET AL. 2003).

Weiter wurde das Vorkommen von basischen Bleimineralen (Hydrocerussit, Elyit, Leadhillit) bei der Verwitterung von Bleiverbindungen im Kontakt mit Zement beobachtet (KOLITSCH 2000; LEE 2007). Dieses Vorkommen kann dadurch erklärt werden, dass bei der Reaktion von Verwitterungslösungen mit Zement (genauer: Portlandit [$Ca(OH)_2$]) sowie der einhergehenden Ausfällung von Kalzit, CO_2 und Protonen verbraucht werden. Ist die ursprüngliche Verwitterungslösung beispielsweise durch die vorherige Auflösung von Galenit bleihaltig, werden unter der Voraussetzung eines lokal geschlossen Systems basische Bleiminerale stabilisiert.

Neben den Bildungsbedingungen der basischen Bleiminerale ist es wichtig zu evaluieren, inwiefern diese Minerale bei der Verwitterung von Bleioxiden die Bleilöslichkeit kontrollieren. Hierzu wurden Verwitterungsexperimente bei zwei verschiedenen pH-Werten und Mineralvergesellschaftungen über einen Zeitraum von 50 Tagen durchgeführt. In allen Experimenten bildete sich Hydrocerussit in Kontakt zu Bleioxid. Waren zusätzlich Cu-haltige Minerale enthalten, so bildete sich Elyit bzw. Chenit. Mineralpräzipitation wurde schon nach wenigen Stunden beobachtet.

Die Analyse der Verwitterungsfluide, kombiniert mit Löslichkeitsdiagrammen, zeigte, dass in allen Experimenten die Bleilöslichkeit durch die Bildung von Hydrocerussit limitiert und damit kontrolliert wird. Die Bleilöslichkeit ist deutlich geringer als bei der Bildung der häufigsten Bleisekundärminerale Cerussit und Anglesit. Einzig in Verwitterungssystemen in denen Phosphat, Arsenat oder Vanadat beteiligt sind, bilden sich mit Pyromorphit, Mimetesit und Vanadinit noch unlöslichere Mineralphasen (RUBY ET AL. 1994; BAJDA 2010; KEIM UND MARKL 2015).

Zusammenfassend lässt sich festhalten, dass für die Bildung von basischen Bleimineralen niedrige CO_2-Partialdrücke und neutrale bis basische pH-Bedingungen nötig sind. Diese

werden generiert, wenn Bleioxide in Kontakt mit Verwitterungsfluiden kommen oder bleihaltige Verwitterungslösungen in Kontakt zu Zement stehen. Weiter werden basische Bleiminerale bei Temperaturerhöhung stabilisiert, was deren Vorkommen ohne die Assoziation zu Bleioxiden erklärt. Zudem konnten Experimente zeigen, dass die Löslichkeit von Blei durch Hydrocerussit kontrolliert wird.

5 Schlussfolgerung

Diese Arbeit leistet einen Beitrag, um Umverteilungsprozesse während der Bildung hydrothermaler Lagerstätten sowie bei ihrer Modifikation innerhalb der Oxidations- und Zementationszone durch supergene Fluide besser zu verstehen. Es zeigte sich, dass die Umverteilung von Schwermetallen bei der primären Bildung und Verwitterung von Sulfiden und Sulfosalzen maßgeblich von der lokalen Fluid- und Mineralchemie beeinflusst wird, welche durch thermodynamische Modellierung häufig eingegrenzt bzw. quantifiziert werden konnten.

Somit konnte festgestellt werden, dass die großmaßstäbliche Silberzonierung an der Grube Clara mit silberreichem Fahlerz in Teufen unterhalb von 450 m ü.NN und Enargit in Teufen darüber durch unterschiedliche Sauerstofffugazitäten hervorgerufen wird, wobei Änderungen dieses Parameters auf unterschiedliche Mischungsverhältnisse eines aufsteigenden hydrothermalen Fluids mit einem sedimentären Fluidaquifer zurückzuführen sind. Während der Hauptphase wird durch den Influx von Fluiden mit relativ hoher Kupferaktivität silberhaltiges Fahlerz destabilisiert und das darin enthaltene Silber in Silbersulfosalze eingebaut, wobei das Fluid in Folge an Silber verarmt und sich silberarmes Fahlerz bildet. Anschließend erfährt die Mineralisation lokal mehrfach Umverteilungsprozesse, wobei Silber zum Teil angereichert aber auch verarmt wird. Die generelle Silberzonierung bleibt jedoch davon unbeeinflusst. Möglicherweise zeigen auch weitere Gänge im Nord- und Mittleren Schwarzwald ähnliche Zonierungen hinsichtlich silberhaltiger Phasen in größeren Teufen, wobei es zukünftig gilt, dies zu prüfen. Eine der prägnantesten lokalen Umverteilungsprozesse ist die Auflösung von Sulfiden durch bis zu 250°C heiße Fluide. Neuste Datierungen zeigen, dass solch heiße Fluide auf das Tertiär zu datieren sind und somit eine wesentlich jüngeres Event, als die Bildung der Silbermineralisation darstellt.

Weiter konnte gezeigt werden, dass Silber bei der Verwitterung von silberhaltigem Bleiglanz nur in geringem Ausmaß (max 13%) in die gebildeten Bleisekundärphasen eingebaut wird, sondern als Silberionen freigesetzt und mobilisiert wird. Ob eigenständige Silberphasen präzipitiert werden, hängt davon ab, ob Redoxprozesse stattfinden oder aber die lokale Fluidchemie zur Übersättigung und so zur Ausfällung führt. Berechnete Stabilitätsdiagramme zeigen, dass Chlorargyrit präzipitiert wird, wenn entweder die Verwitterungsfluide chloridreich sind oder aber der verwitterte Bleiglanz silberreich ist bzw. weitere Silberphasen verwittern. Natürliche Wasseranalysen in Kombination mit der Mineralchemie zeigen, dass die thermodynamischen Modelle für den Schwarzwald erfolgreich angewendet werden können. Ob dies auch für andere Lagerstättenreviere gilt, bleibt zu prüfen.

Weiter zeigte sich, dass bei der Verwitterung von Bi-haltigem Fahlerz die Mobilität von Schwermetallen zum einen vom Redoxzustand der Verwitterungsfluide, zum anderen von der lokalen Chemie der Fahlerze gesteuert wird. Ist beispielsweise das Fahlerz bismutreich, so wird bei dessen Verwitterung verhindert, dass Antimon mobilisiert wird, da sich schwerlösliche Sb-Bi-Fe-Phasen bilden. Außerdem wird Arsen nur dann mobilisiert, wenn bei der Verwitterung das Redoxpotential der Fluide gering ist. Unterschiedliche Redoxpotentiale machen sich nicht nur in der Mobilität der Elemente bemerkbar, sondern sie führen auch zur Bildung unterschiedlicher Texturen. Bei geringen Redoxpotentialen bilden sich fingerartige

Texturen, die dadurch charakterisiert sind, dass aus einer gelartigen Phase durch Dehydratisierung Mineralphasen kristallisieren. Bei hohen Redoxpotentialen hingegen bilden sich bei der Verdrängung von Fahlerz Verwitterungsfronten aus, wobei schlechtkristalline Phasen gebildet werden. Diese Texturen sind nicht nur für Fahlerz typisch, sondern wurden an weiteren Sulfiden beobachtet. Mittels Experimenten könnten in Zukunft weitere Erkenntnisse über Verdrängungsprozesse bei unterschiedlichen Redoxpotentialen gewonnen werden.

Unterschiedliche Redoxpotentiale bewirken auch die Bildung von Galenit Pseudomorphosen nach Galenit. Der mehrmalige Wechsel supergener, oxidierender Lösungen und reduziernder Thermalfluide konnte anhand von Wasseranalysen und Stabilitätsdiagrammen nachgewiesen werden. Pyromorphit wird durch sulfid-, calcium- und fluorreiche Fluide verdrängt, wobei ein Teil des Phosphats, dass bei der Verdrängung freigesetzt wird, als Fluorapatit repräzipitiert wird. Der Vergleich mit anderen europäischen Vorkommen zeigt, dass Blei jeweils nicht mobilisiert wird. Bislang konnte nicht geklärt werden, ob auch bei den anderen Lagerstätten Thermalfluide für die Bildung verantwortlich sind.

In einer weiteren Studie wurde die Bildung basischer Bleiminerale untersucht. Es konnte gezeigt werden, dass basische Bleiminerale bei geringen CO_2-Partialdrücken und hohen pH-Werten stabilisiert werden und die Löslichkeit von Blei kontrollieren können. Fluidpfadmodelle zeigen, dass basische Bleiminerale sich bei der Verwitterung von Bleioxiden im Kontakt zu Zement und bei erhöhten Verwitterungstemperaturen stabilisieren. Um das Fluidpfadmodell zukünftig für basische Blei-Kupfer Minerale erweitern zu können, müssten thermodynamische Daten beispielsweise für Elyit oder Chenit erhoben werden.

6 Referenzen

ABDUL-SAMAD, F.A., THOMAS, J.H., WILLIAMS, P.A., BIDEAUX, R.A., AND SYMES, R.F. (1982a) Mode of Formation of some rare copper (II) and lead (II) minerals from aqueous solution with particular reference to deposits at Tiger, Arizona. Transition Metal Chemistry, **7**, 32-37.

ABDUL-SAMAD, F.A., THOMAS, J.H., WILLIAMS, P.A., AND SYMES, R.F. (1982B) Chemistry of formation of lanarkite. Pb2OSO4. Mineralogical Magazine, **46**, 499-501.

AGRICOLA, G. (1556) De re metallica libri XII. Deutscher Verlag der Wissenschaften, Berlin, 931 S.

ALTHERR, R., HOLL, A., HEGNER, E., LANGER, C., KREUZER, H. (2000) High-potassium, calc-alkaline I-type plutonism in the European Variscides: northern Vosges (France) and Northern Schwarzwald (Germany). Lithos, **50**(1), 51-73.

APOPEI, A.I., DAMIAN, G., BUZGAR, N., BUZATU, A. (2016) Mineralogy and geochemistry of Pb–Sb/As-sulfosalts from Coranda-Hondol ore deposit (Romania)—Conditions of telluride deposition. Ore Geology Reviews, **72**, 857-873.

ARROYO, Y.R.R., SIEBE, C. (2007) Weathering of sulphide minerals and trace element speciation in tailings of various ages in the Guanajuato mining district, Mexico. Catena, **71**(3), 497-506.

BAJDA, T. (2010) Solubility of mimetite Pb5 (AsO4) 3Cl at 5–55°C. Environmental Chemistry, **7**(3), 268-278.

BAKER, B.J., BANFIELD, J.F. (2003) Microbial communities in acid mine drainage. FEMS microbiology ecology, **44**(2), 139-152.

BARNES, H.L. (1997) Geochemistry of Hydrothermal Ore Deposits. John Wiley & Sons, Inc., New York, 992 S.

BASTA, N.T., MCGOWEN, S.L. (2004) Evaluation of chemical immobilization treatments for reducing heavy metal transport in a smelter-contaminated soil. Environmental pollution, **127**(1), 73-82.

BAUMGÄRTL, U., BUROW, J. (2002) Grube Clara. Der Aufschluss, **54**, 274-403.

BEHR, H.J., GERLER, J. (1987) Inclusions of sedimentary brines in post-Variscan mineralizations in the Federal Republic of Germany—a study by neutron activation analysis. Chemical Geology, **61**, 65-77.

BEHR, H.J., HORN, E.E., FRENTZEL-BEYME, K., REUTEL, C. (1987) Fluid inclusion characteristics of the Variscan and post-Variscan mineralizing fluids in the Federal Republic of Germany. Chemical Geology, **61**, 273-285.

BETHKE, C.M., YEAKEL, S. (2015) GWB Essentials Guide: Aqueous Solutions. LLC Champaign, Illinois, 149 S.

BLASS, G., GRAF, H.W. (2001) Billingsleyit – die Grube Clara, weltweit der zweite Fundpunkt. Der Aufschluss, **14**, 4-6.

BLIEDTNER, M., MARTIN, M. (1986) Erz- und Minerallagerstätten des Mittleren Schwarzwaldes. LGRB, Freiburg. 782 S.

BLUM, J.R. (1843) Pseudomorphosen des Mineralienreichs. Schweizbart'sche Verlagsbuchhandlung, Stuttgart, 379 S.

BONS, P.D., FUSSWINKEL, T., GOMEZ-RIVAS, E., MARKL, G., WAGNER, T., WALTER, B. (2014) Fluid mixing from below in unconformity-related hydrothermal ore deposits. Geology, **42**(12),1035-1038

BORČINOVÁ-RADKOVÁ, A., JAMIESON, H., LALINSKÁ-VOLEKOVÁ, B., MAJZLAN, J., ŠTEVKO, M., CHOVAN, M. (2017) Mineralogical controls on antimony and arsenic mobility during tetrahedrite-tennantite weathering at historic mine sites Špania Dolina-Piesky and Ľubietová-Svätodušná, Slovakia. American Mineralogist, **102**(5), 1091-1100.

BOWELL, R.J. (2014) Hydrogeochemistry of the Tsumeb deposit: implications for arsenate mineral stability. Reviews in Mineralogy and Geochemistry, **79**(1), 589-627.

BOWELL, J.R., CLIFFORD, J.H. (2014) Leadhillite Tsumeb, Namibia. Rocks and Minerals, **89**, 354-362.

BUCHER, K., STOBER, I. (2010) Fluids in the upper continental crust. Geofluids, **10**, 241– 253.

BUCHER, K., ZHU, Y., STOBER, I. (2009) Groundwater in fractured crystalline rocks, the Clara mine, Black Forest (Germany). International Journal of Earth Sciences, **98**(7), 1727-1739.

BURISCH, M., MARKS, M.A., NOWAK, M., MARKL, G. (2016A) The effect of temperature and cataclastic deformation on the composition of upper crustal fluids—An experimental approach. Chemical Geology, **433**, 24-35.

BURISCH, M., GERDES, A., WALTER, B.F., NEUMANN, U., FETTEL, M., MARKL, G. (2017) Methane and the origin of five-element veins: mineralogy, age, fluid inclusion chemistry and ore forming processes in the Odenwald, SW Germany. Ore Geology Reviews, **81**, 42-61.

BURISCH, M., WALTER, B.F., GERDES, A., LANZ, M., MARKL, G. (2018) Late-stage anhydrite-gypsum-siderite-dolomite-calcite assemblages record the transition from a deep to a shallow hydrothermal system in the Schwarzwald mining district, SW Germany. Geochimica et Cosmochimica Acta, **223**, 259-278.

BURISCH, M., WALTER, B. F., WÄLLE, M., MARKL, G. (2016) Tracing fluid migration pathways in the root zone below unconformity-related hydrothermal veins: Insights from trace element systematics of individual fluid inclusions. Chemical Geology, **429**, 44-50.

BURMANN, F., KEIM, M.F., OELMANN, Y., TEIBER, H., MARKS, M.A., MARKL, G. (2013) The source of phosphate in the oxidation zone of ore deposits: Evidence from oxygen isotope compositions of pyromorphite. Geochimica et Cosmochimica Acta, **123**, 427-439.

CALLENDER, E. (2014) Heavy Metals in the Environment – Historical Trends in Treatise on Geochemistry, Elsevier 9144 S.

CIOMARTAN, D.A., CLARK, R.J.H., MCDONALD, L.J., ODLYHA, M. (1996) Studies on the thermal decomposition of basic lead (II) carbonate by Fourier-transform Raman spectroscopy, X-ray diffraction and thermal analysis. Journal of the Chemical Society, **18**, 3639-3645.

CRANE, M.J., SHARPE, J.L., WILLIAMS, P.A. (2001) Formation of chrysocolla and secondary copper phosphates in the highly weathered supergene zones of some Australian deposits. Records-Australian Museum, **53**(1), 49-56.

CRADDOCK, P.T. (1992) A short history of fire setting. Endeavour, **16**, 145-150.

DIETRICH, J.E., ORLIAC, M., PERMINGEAT, F. (1969) L'agardite, une nouvelle espèce minérale, et le problème du chlorotile. Bulletin de la Société francaise de minéralogie, **92**, 420-434.

DILL, H.G., MELCHER, F., KAUFHOLD, S., TECHMER, A., WEBER, B., BÄUMLER, W. (2010) Post-Miocene and Bronze-age supergene Cu–Pb arsenate–humate–oxalate–carbonate mineralization at Mega Livadi, Serifos, Greece. The Canadian Mineralogist, **48**(1), 163-181.

DRAHOTA, P., FILIPPI, M. (2009) Secondary arsenic minerals in the environment: a review. Environment international, **35**(8), 1243-1255.

DUDKA, S., ADRIANO, D.C. (1997) Environmental impacts of metal ore mining and processing: a review. Journal of environmental quality, **26**(3), 590-602.

DULTZ, S., BOY, J., DUPONT, C., HALISCH, M., BEHRENS, H., WELSCH, A. M., DEUBENER, J. (2014) Alteration of a submarine basaltic glass under environmental conditions conducive for microorganisms: growth patterns of the microbial community and mechanism of palagonite formation. Geomicrobiology Journal, **31**(9), 813-834.

EGLI, M., BERGER, A., KÜNDIG, R., KREBS, R., DE CASTRO PORTES, R., BERGER, R., WIDMER, R. (2017) The long-term interaction of mine tailings with soils and the wider environment: Examples from Mont Chemin, Switzerland. Journal of Geochemical Exploration, **182**, 53-69.

EPP, T. (2016) Mineralogical and geochemical investigation of hydrothermal veins in the Glottertal, SW Germany, Masterarbeit, Universität Tübingen.

ESSINGTON, M.E., FOSS, J.E., ROH, Y. (2004) The soil mineralogy of lead at Horace's villa. Soil Science Society of America Journal, **68**(3), 979-993.

ETTLER, V., ČERVINKA, R., JOHAN, Z. (2009A) Mineralogy of medieval slags from lead and silver smelting (Bohutín, Příbram district, Czech Republic): Towards estimation of hystorical smelting conditions. Archometry, **51**, 987-1007.

ETTLER, V., JOHAN, Z., KŘÍBEK, B., ŠEBEK, O., MIHALJEVIČ, M. (2009B) Mineralogy and environmental stability of slags from the Tsumeb smelter, Namibia. Applied Geochemistry, **24**, 1-15.

FÖRSTNER, U., WITTMANN, G.T. (2012) Metal pollution in the aquatic environment. Springer, Berlin, 488 S.

FRANKE, W. (1989) Variscan plate tectonics in Central Europe—current ideas and open questions. Tectonophysics, **169**(4), 221-228.

FUSSWINKEL, T., WAGNER, T., WÄLLE, M., WENZEL, T., HEINRICH, C., MARKL, G., (2013) Fluid mixing forms basement-hosted Pb-Zn deposits: Insight from metal and halogen geochemistry of individual fluid inclusions. Geology, **41**, 679-682.

GEORGE, L.L., COOK, N.J., CIOBANU, C.L. (2017) Minor and trace elements in natural tetrahedrite-tennantite: Effects on element partitioning among base metal sulphides. Minerals, **7**(2), 1-25.

GERGENS, N.N. (1856) Über einige Pseudomorphosen aus der Bleigrube von Kautenbach bei Berncastel an der Mosel. – Neues Jahrbuch für Mineralogie, Geognosie, Geologie und Petrefaktenkunde, 135–139.

GEYER, O.F., AND GWINNER, M.P. (2011) Geologie von Baden -Württemberg. – 5., völlig neu bearbeitete Auflage, Schweizerbart`sche Verlagsbuchhandlung, Stuttgart, 627 S.

GILG, H.A., HOCHLEITNER, R., KELLER, P., AND STRUCK, U. (2003) A fluid inclusion and stable isotope study of secondary oxidation minerals from the Tsumeb Cu-Pb-Zn deposit, Namibia: Proceedings ECROFI XI, Budapest, Hungary, June 5-7 (2003) Acta Mineralogica-Petrographica, Abstract Series, 78–79.

GÖB, S., GÜHRING, J.E., BAU, M., MARKL, G. (2013A) Remobilization of U and REE and the formation of secondary minerals in oxidized U deposits. American Mineralogist, **98**(4), 530-548.

GÖB, S., LOGES, A., NOLDE, N., BAU, M., JACOB, D.E., MARKL, G. (2013B) Major and trace element compositions (including REE) of mineral, thermal, mine and surface waters in SW Germany and implications for water–rock interaction. Applied Geochemistry, **33**, 127-152.

GÖB, S., WENZEL, T., BAU, M., JACOB, D.E., LOGES, A., MARKL, G. (2011) The redistribution of rare-earth elements in secondary minerals of hydrothermal veins, Schwarzwald, southwestern Germany. The Canadian Mineralogist, **49**(5), 1305-1333.

GOLDSTEIN, R.H., REYNOLDS, T.J. (1994) Systematics of Fluid Inclusions in Diagenetic Minerals. SEPM Short Course 31 Society for Sedimentary Geology, Tulsa, 199 S.

GUSTEANI, A., PEZZOTTA, F., VIGNOLA, P. (2006) Characterization and genetic inferences of arsenates, sulfates and vanadates of Fe, Cu, Pb, Zn from Mount Cervandone (Western Alps, Italy). Periodico di Mineralogica, **75**, 414-150.

HARSCH, J. (2015) Geochemische Untersuchungen an Fahlerzen und ihren Alterationsphasen. Bachelorarbeit, Universität Tübingen.

HARTLEY, A.J., RICE, C.M. (2005) Controls on supergene enrichment of porphyry copper deposits in the Central Andes: a review and discussion. Mineralium Deposita, **40**(5), 515-525.

HARVEY, M.C., SCHREIBER, M.E., RIMSTIDT, J.D., GRIFFITH, M.M. (2006) Scorodite dissolution kinetics: implications for arsenic release. Environmental Science & Technology, **40**(21), 6709-6714.

HAßLER, K., TAUBALD, H., MARKL, G. (2014) Carbon and oxygen isotope composition of Pb-, Cu-and Bi-carbonates of the Schwarzwald mining district: Carbon sources, first data on bismutite and the discovery of an oxidation zone formed by ascending thermal water. Geochimica et Cosmochimica Acta, **133**, 1-16.

HAUTMANN, S., LIPPOLT, H.J. (2000) 40Ar/39Ar dating of central European K–Mn oxides—a chronological framework of supergene alteration processes during the Neogene. Chemical Geology, **170**(1-4), 37-80.

HEINRICH, C.A., CANDELA, P.A. (2014) Fluids and Ore Formation in the Earth's Crust in Treatise on Geochemistry, Elsevier 9144 S.

HEYDE, R.VD. (2002) Paragenetische und aufbereitungstechnische Untersuchungen silberhaltiger Erze der Baryt-Flussspatgrube „Clara", Wolfach, Deutschland. Hallesches Jahrbuch für Geowissenschaften, **15**, 65-121.

HILMY, M.E., OSMAN, A. (1989) Remobilization of gold from a chalcopyrite-pyrite mineralization Hamash gold mine, Southeastern Desert, Egypt. Mineralium Deposita, **24**(4), 244-249.

HOUWERS, M. E. (2015) Numerical modelling study on the quantification of in-situ leaching (ISL) of copper in porphyry rock. Masterarbeit, Universität Utrecht.

HUCK, K. (1984) Beziehungen zwischen Tektonik und Paragenese unter Berücksichtigung Geochemischer Kriterien in der Fluß- und Schwerspatlagerstätte „Clara" bei Oberwolfach/Schwarzwald. Dissertation, Universiät Heidelberg.

HUDSON-EDWARDS, K.A., JAMIESON, H.E., LOTTERMOSER, B.G. (2011) Mine wastes: past, present, future. Elements, **7**(6), 375-380.

INGWERSEN, G. (1990) Die sekundären Mineralbildungen der Pb-Zn-Cu-Lagerstätte Tsumeb, Namibia (Physikalisch-chemische Modelle). Dissertation, Universität Stuttgart, 233 S.

JAHN, S. (2016) The Kautenbach Mine Bernkastel-Kues, Rhineland- Platinate Germany. Mineral Record, **2**,191– 211.

JAMIESON, H.E. (2011) Geochemistry and mineralogy of solid mine waste: essential knowledge for predicting environmental impact. Elements, **7**(6), 381-386.

JANSSEN, A., PUTNIS, A., GEISLER, T., PUTNIS, C.V. (2010) The experimental replacement of ilmenite by rutile in HCl solutions. Mineralogical Magazine, **74**, 633-644.

KALT, A., ALTHERR, R., HANEL, M. (2000) The Variscan Basement of the Schwarzwald. European Journal of Mineralogy, **12**, 1–43.

KAMENOV, G.D., MELCHIORRE, E.B., RICKER, F.N., DEWITT, E. (2013) Insights from Pb isotopes for native gold formation during hypogene and supergene processes at Rich Hill, Arizona. Economic Geology, **108**, 1577-1589.

KARUP-MØLLER, S. (1975) On the occurrence of the native lead, litharge, hydrocerussite and plattnerite within the Ilímaussaq alkaline intrusion in South Greenland. Neues Jahrbuch für Mineralogie, **37**, 230-241.

KEIM, M.F., MARKL, G. (2015) Weathering of galena: Mineralogical processes, hydrogeochemical fluid path modeling, and estimation of the growth rate of pyromorphite. American Mineralogist, **100**(7), 1584-1594.

KOLITSCH, U. (2000) Eine durch Betoneinwirkung entstandene Paragenese von Blei-Verbindungen aus der Grube Clara im mittleren Schwarzwald. Der Erzgräber, **14**, 48-53.

KOZUB, G.A. (2014) Distribution of Ag in Cu-sulfides in Kupferschiefer deposits, SW Poland. Geophysical Research Abstracts 16, EGU2014-8944.

KREISSL, S., GERDES, A., WALTER, B.F., NEUMANN, U., WENZEL, T., MARKL, G. (IN PRESS) Reconstruction of a >200 Ma multi-stage "five element" Bi-Co-Ni-Fe-As-S system in the Penninic Alps, Switzerland. Ore Geology Reviews.

KRONZ, A. (2005) Erzbergbau, Buntmetallmineralisationen und Silber-Metallurgie im Bereich der mittleren Mosel. Zeitschrift zur Geschichte des Berg- und Hüttenwesens. Fischbacher Hefte, **11**, 2–27.

KRUPP, R.E. (1989) Paragenesis and conditions of formation of the Moschellandsberg mercury deposit, SW Germany. Mineralium Deposita, **24**(2), 69-76.

LARA, R.H., BRIONES, R., MONROY, M.G., MULLET, M., HUMBERT, B., DOSSOT, M., CRUZ, R. (2011) Galena weathering under simulated calcareous soil conditions. Science of the total Environment, **409**(19), 3971-3979.

LEACH, D.L., LANDIS G.P., HOFSTRA A.H. (1988) Metamorphic origin of the Coeur d'Alene base- and precious-metal veins in the Belt basin, Idaho and Montana. Geology, **16**, 122-125.LEE, D. (2007) Formation of leadhillite and calcium lead silicate hydrate (C-Pb-S-H) in the solidification/stabilization of lead contaminants. Chemosphere, **66**, 1727-1733.

LEYBOURNE, M.I., PETER, J.M., LAYTON-MATTHEWS, D., VOLESKY, J., BOYLE, D.R. (2006) Mobility and fractionation of rare earth elements during supergene weathering and gossan formation and chemical modification of massive sulfide gossan. Geochimica et Cosmochimica Acta, **70**(5), 1097-1112.

LI, Y., ZHU, Y., ZHAO, S., LIU, X. (2015) The weathering and transformation process of lead in China's shooting ranges. Environmental Science: Processes & Impacts, **17**, 1620-1633.

LICHTNER, P.C., BIINO, G.G. (1992) A first principles approach to supergene enrichment of a porphyry copper protore: I. Cu-Fe-S subsystem. Geochimica et Cosmochimica Acta, **56**(11), 3987-4013.

LIN, Z. (1996) Secondary mineral phases of metallic lead in soils of shooting ranges from Örebro County, Sweden. Environmental Geology, **27**, 370-375.

LIST, K.A. (1969) Die Mineralisation auf den tieferen Sohlen der „Grube Clara". Diplomarbeit, Universität Freiburg.

LIVINGSTONE, A. (1993) Origin of the leadhillite polymorphs. Journal of the Russell Society, **5**, 11-14.

LOGES, A., WAGNER, T., BARTH, M., BAU, M., GÖB, S., MARKL, G. (2012A) Negative Ce anomalies in Mn oxides: the role of Ce4+ mobility during water–mineral interaction. Geochimica et Cosmochimica Acta, **86**, 296-317.

LOGES, A., WAGNER, T., KIRNBAUER, T., GÖB, S., BAU, M., BERNER, Z., MARKL, G. (2012B) Source and origin of active and fossil thermal spring systems, northern Upper Rhine Graben, Germany. Applied geochemistry, **27**(6), 1153-1169.

LU, X., WANG, H. (2012) Microbial oxidation of sulfide tailings and the environmental consequences. Elements, **8**(2), 119-124.

MAGALHÃES, M.C.F., JESUS, J.D.P., WILLIAMS, P.A. (1985) The chemistry of uranium dispersion in groundwaters at the Pinhal do Souto mine, Portugal. Inorganica chimica acta, **109**(2), 71-78.

MAGALHÃES, M.C.F., WILLIAMS, P.A. (1988) The chemistry of formation of some secondary arsenate minerals of Cu (II), Zn (II) and Pb (II). Mineralogical Magazine, **52**, 679-690.

MARKL, G. (2014C) Pyromrophit, Mimetesit und Vanadinit. Extra Lapis, **46**, 30–35

MARKL, G. (2015) Schwarzwald, Lagerstätten und Mineralien aus vier Jahrhunderten; Band 1 Nordschwarzwald & Grube Clara. Bode, Lauenstein, 627 S.

MARKL, G. (2016) Schwarzwald, Lagerstätten und Mineralien aus vier Jahrhunderten; Band 2 Mittlerer Schwarzwald Teil 1. Bode, Lauenstein, 648 S.

MARKL, G. (2017A) Schwarzwald, Lagerstätten und Mineralien aus vier Jahrhunderten; Band 3 Mittlerer Schwarzwald Teil 2. Bode, Lauenstein, 640 S.

MARKL, G. (2017B) Schwarzwald, Lagerstätten und Mineralien aus vier Jahrhunderten; Band 4 Südlicher Schwarzwald. Bode, Lauenstein, 880 S.

MARKL, G., MARKS, M.A., DERREY, I., GÜHRING, J.E. (2014A) Weathering of cobalt arsenides: Natural assemblages and calculated stability relations among secondary Ca-Mg-Co arsenates and carbonates. American Mineralogist, **99**(1), 44-56.

MARKL, G., MARKS, M.A., HOLZÄPFEL, J., WENZEL, T. (2014B) Major, minor, and trace element composition of pyromorphite-group minerals as recorder of supergene weathering processes from the Schwarzwald mining district, SW Germany. American Mineralogist, **99**(5-6), 1133-1146.

MARUSHCHENKO, L.I., BAKSHEEV, I.A., NAGORNAYA, E.V., CHITALIN, A.F., NIKOLAEV, Y.N., VLASOV, E. A. (IN PRESS) Compositional evolution of the tetrahedrite solid solution in porphyry-epithermal system: A case study of the Baimka Cu-Mo-Au trend, Chukchi Peninsula, Russia. Ore Geology Reviews.

MAUS, H.J., GUNDLACH, H., PODUFAL, P. (1979) Über den Sellait (MgF2) der Grube Clara, Oberwolfach, Mittler Schwarzwald. Neues Jahrbuch für Mineralogie - Abhandlungen **136**, 10–25

MELCHER, F., OBERTHÜR, T., RAMMLMAIR, D. (2006) Geochemical and mineralogical distribution of germanium in the Khusib Springs Cu–Zn–Pb–Ag sulfide deposit, Otavi Mountain Land, Namibia. Ore Geology Reviews, **28**(1), 32-56.

METZ, R., RICHTER, M., SCHÜRRENBERG, H. (1957) Die Blei-Zink Erzgänge des Schwarzwaldes. Geologisches Jahrbuch, Beihefte, **29**, 1-277.

MIKHLIN, Y.L., ROMANCHENKO, A.S., SHAGAEV, A.A. (2006) Scanning probe microscopy studies of PbS surfaces oxidized in air and etched in aqueous acid solutions. Applied surface science, **252**(16), 5645-5658.

MONCUR, M.C., JAMBOR, J.L., PTACEK, C.J., BLOWES, D.W. (2009) Mine drainage from the weathering of sulfide minerals and magnetite. Applied Geochemistry, **24**(12), 2362-2373.

MUELLER, A.G., MUHLING, J.R. (2013) Silver-rich telluride mineralization at Mount Charlotte and Au-Ag zonation in the giant Golden Mile deposit, Kalgoorlie, Western Australia. Mineralium Deposita, **48**, 295-311.

MURPHY, J.B., QUESADA, C., GUTIÉRREZ-ALONSO, G., JOHNSTON, S.T., WEIL, A. (2016) Reconciling competing models for the tectono-stratigraphic zonation of the Variscan orogen in Western Europe. Tectonophysics, **681**, 209-219.

NICKEL, E.H., WILLIAMS, P.A., DOWNES, P.J., BUCHERT, D.E., VAUGHAN, D. (2007) Secondary minerals in a tennantite boxwork from the Bali Lo prospect, Ashburton Downs, Western Australia. Australian Journal of Mineralogy, **13**, 31-39.

NÖGGERATH, J. (1846) Pseudomorphosen von Bleiglanz nach Pyromorphit gebildet, von Berncastel an der Mosel. – Neues Jahrbuch für Mineralogie, Geognosie, Geologie und Petrefaktenkunde, 163–170.

NORDSTROM, D.K. (2011) Mine waters: acidic to circum neutral. Elements, **7**(6), 393-398.

ONCKEN, O., WINTERFELD, C.V., DITTMAR, U. (1999) Accretion of a rifted passive margin: the Late Paleozoic Rhenohercynian fold and thrust belt (Middle European Variscides). Tectonics, **18**, 75 – 91.

PARK, C.F., MACDIARMID, R.A. (1975) Ore Deposits. W.H. Freeman and Company, San Francisco, 985 S.

PARKHURST, D.L., APPELO, C.A.J. (1999) User's guide to PHREEQC (Version 2): A computer program for speciation, batch-reaction, one-dimensional transport, and inverse geochemical calculations, USGS, 310 S.

PAULIŠ, P., NOVÁK, F., KOTATKO, L., JONÁSCARON, F., DVOŘÁK, Z., ŠEVCÚ, J. (2008) Nové vyskyty nerostů na Sn-W ložisku Cínovec. Bulletin Mineralogicko-Petrologickeho Oddeleni Narodniho Muzea v Praze, **16**, 113-117.

PÉREZ, I., CASAS, I., MARTÍN, M., BRUNO, J. (2000) The thermodynamics and kinetics of uranophane dissolution in bicarbonate test solutions. Geochimica et Cosmochimica Acta, **64**(4), 603-608.

PETRUNIC, B.M., AL T., WEAVER, L., HALL, D. (2009) Identification and characterization of secondary minerals formed in tungsten mine tailings using transmission electron microscopy. Applied Geochemistry, **24**, 2222-2233.

PFAFF, K., ROMER, R.L., MARKL, G. (2009) U-Pb ages of ferberite, chalcedony, agate, “U-mica” and pitchblende: constraints on the mineralization history of the Schwarzwald ore district. European Journal of Mineralogy, **21**, 817–36.

PFAFF, K., KOENIG, A., WENZEL, T., RIDLEY, I., HILDEBRANDT, L.H., LEACH, D.L., MARKL, G. (2011) Trace and minor element variations and sulfur isotopes in crystalline and colloform ZnS: Incorporation mechanisms and implications for their genesis. Chemical Geology, **286**(3-4), 118-134.

PFAFF, K., HILDEBRANDT, L.H., LEACH, D.L., JACOB, D.E., MARKL, G. (2010) Formation of the Wiesloch Mississippi Valley-type Zn-Pb-Ag deposit in the extensional setting of the Upper Rhinegraben, SW Germany. Mineralium Deposita, **45**(7), 647-666.

PLOTINSKAYA, O.Y., GRABEZHEV, A.I., SELTMANN, R. (2015) Fahlores compositional zoning in a porphyry-epithermal system: Biksizak occurrence, South Urals, Russia as an example. Geology of Ore Deposits, **57**, 42-63.

PLUMLEE, G.S., MORMAN, S.A. (2011) Mine wastes and human health. Elements, **7**(6), 399-404.

PUTNIS, A. (2014) Why mineral interfaces matter. Science, **343**(6178), 1441-1442

QIAN, G., BRUGGER, J., TESTEMALE, D., SKINNER, W., PRING, A. (2013) Formation of As (II)-pyrite during experimental replacement of magnetite under hydrothermal conditions. Geochimica et Cosmochimica Acta, **100**, 1-10.

REED, M.H., PALANDRI, J. (2006) Sulfide mineral precipitation from hydrothermal fluids. Reviews in Mineralogy and Geochemistry, **61**(1), 609-631.

REHREN, T. (1985) Untersuchungen zur Mineralogie und Aufbereitbarkeit verschiedener Erzproben der Grube Clara. Diplomarbeit, Universität Clausthal.

REICH, M., VASCONCELOS, P.M. (2015) Geological and economic significance of supergene metal deposits. Elements, **11**(5), 305-310.

REICHERT, J., BORG, G. (2008) Numerical simulation and a geochemical model of supergene carbonate-hosted non-sulphide zinc deposits. Ore Geology Reviews, **33**(2), 134-151.

RENOCK, D., BECKER, U. (2011) A first principles study of coupled substitution in galena. Ore Geology Reviews, **42**(1), 71-83.

REPSTOCK, A., VOUDOURIS, P., KOLITSCH, U. (2015) New occurrences of watanabeite, colusite, "arsenosulvanite" and "Cu-excess" tetrahedrite-tennantite at the Pefka high-sulfidation epithermmal deposit, northeastern Greece. Neues Jahrbuch für Mineralogie - Abhandlungen, **192**, 135-149.

ROMERO, A., GONZÁLEZ, I., GALÁN, E. (2006) Estimation of potential pollution of waste mining dumps at Pena del Hierro (Pyrite Belt, SW Spain) as a base for future mitigation actions. Applied Geochemistry, **21**(7), 1093-1108.

ROPER, A.J., WILLIAMS, P.A., FILELLA, M. (2012) Secondary antimony minerals: phases that control the dispersion of antimony in the supergene zone. Chemie der Erde-Geochemistry, **72**, 9-14.

RUBY, M.V., DAVIS, A., NICHOLSON, A. (1994) In situ formation of lead phosphates in soils as a method to immobilize lead. Environmental Science & Technology, **28**(4), 646-654.

RUPF, I., NITSCH, E. (2008) Das Geologische Landesmodell von Baden-Württemberg: Datengrundlagen, technische Umsetzung und erste geologische Ergebnisse. LGRB Information, 21.

SACK, R.O., FREDERICKS, R., HARDY, L.S., EBEL, D.S. (2005) Origin of high-Ag fahlores from the galena Mine, Wallace, Idaho, USA. American Mineralogist, **90**(5-6), 1000-1007.

SAJADI, S.A. (2011) A comparative investigation of lead sulfate and lead oxide sulfate study of morphology and thermal decomposition. American Journal of Analytical Chemistry, **2**, 206-211.

SATO, M. (1992) Persistency-field Eh-pH diagrams for sulfides and their application to supergene oxidation and enrichment of sulfide ore bodies. Geochimica et Cosmochimica Acta, **56**(8), 3133-3156.

SCHARRER, M., KREISSL, S., MARKL, G. (in prep) The mineralogical variability of five-element veins.

SCHARRER, M., VAUDRIN, R. (2016) Regional spatial variation of the Cu-Bi mineralization around Wittichen, SW Germany: a structural, mineralogical and geochemical study, Masterarbeit, Universität Tübingen.

SCHMELTZER, H. (1983) Eine Polybasitvererzung von der Grube Clara. Lapis, **8**, 37-40

SCHWINN, G., WAGNER, T., BAATARTSOGT, B., MARKL, G. (2006) Quantification of mixing processes in ore-forming hydrothermal systems by combination of s-isotope and fluid inclusion analyses. Geochimica et Cosmochimica Acta, **70**, 965-982.

SEWARD, T.M., BARNES, H.L. (1997) Metal transport by hydrothermal ore fluids. Geochemistryof hydrothermal ore deposits, **3**, 435-486.

SEWARD, T.M., WILLIAMS-JONES, A.E., MIGDISOV A. (2014) The chemistry of metal transport and deposition by ore forming hydrothermal fluids. In Treatise on Geochemistry, Elsevier 9144 S.

SHARP, T.G., BUSECK, P.R. (1993) The distribution of Ag and Sb in galena: inclusions versus solid solution. American Mineralogist, **78**(1-2), 85-95.

SHEPHERD, T.J., RANKIN, A.H., ALDERTON, D.H. (1985) A practical guide to fluid inclusion studies. Blackie, New York, 239 S.

SILLITOE, R.H. (2005) Supergene oxidized and enriched porphyry copper and related deposits. Econonomic Geology, **100**, 723-768.

STAUDE, S., BONS, P.D., MARKL, G. (2009) Hydrothermal vein formation by extension-driven dewatering of the middle crust: An example from SW Germany. Earth and Planetary Science Letters, **286**, 387-395.

STAUDE, S., DORN, A., PFAFF, K., MARKL, G. (2010a) Assemblages of Ag–Bi sulfosalts and conditions of their formation: the type locality of schapbachite (Ag0. 4Pb0. 2Bi0. 4S) and neighboring mines in the Schwarzwald ore district, southern Germany. The Canadian Mineralogist, **48**, 441-466.

STAUDE, S., MORDHORST, T., NAU, S., PFAFF, K., BRÜGMANN, G., JACOB, D.E., MARKL, G. (2012) hydrothermal carbonates of the Schwarzwald ore district, southwestern Germany: carbon source and conditions of formation using δ18O, δ13C, 87Sr/86Sr, and fluidinclusions. The Canadian Mineralogist, **50**, 1401-1434.

STAUDE, S., MORDHORST, T., NEUMANN, R., PREBECK, W., MARKL, G. (2010b) Compositional variation of the tennantite–tetrahedrite solid solution series in the Schwarzwald ore district (SW Germany): The role of mineralization processes and fluid source. Mineralogical Magazine, **74**(2), 309-339.

STAUDE, S., WERNER, W., MORDHORST, T., WEMMER, K., JACOB, D.E., MARKL, G. (2012) Multi-stage Ag–Bi–Co–Ni–U and Cu–Bi vein mineralization at Wittichen, Schwarzwald, SW Germany: geological setting, ore mineralogy, and fluid evolution. Mineralium Deposita, **47**(3), 251-276.

STAVINGA, D.B. (2014) Trace element geochemistry and metal mobility of oxide mineralization at the Prairie Creek zinc-lead-silver deposit, NWT, Masterarbeit, Universität Queens.

THORNBER, M.R. (1992) The chemical mobility and transport of elements in the weathering environment. In Handbook of exploration geochemistry (Vol. 4, pp. 79-96). Elsevier Science BV.

TIBBS, S.L., BRIGGS, D.E. PRÖSSL, K.F. (2003) Pyritisation of plant microfossils from the Devonian Hunsrück Slate of Germany. Paläontologische Zeitschrift, **77**, 241–246.

TREIMAN, A.H. (1999) Bad Water: Origin of Phoenicochroite-Lanarkite Solid Solution, Pb2O (CrO4SO4), in Martian Meteorite EETA79001. Lunar and Planetary Science Conference, **30**, 1124.

TYSZKA, R., KIERCZAK, J., PIETRANIK, A., ETTLER, V., MIHALJEVIČ, M. (2014) Extensive weathering of zinc smelting slag in a heap in Upper Silesia (Poland): potential environmental risks posed by mechanical disturbance of slag deposits. Applied Geochemistry, **40**, 70-81.

VAUGHAN, D.J., CRAIG J.R. (1997) Sulfide ore mineral stabilities, morphologies, and intergrowth textures. In Geochemistry of Hydrothermal Ore Deposits, John Wiley & Sons, New York, 367-434.

VAVELIDIS, M., MELFOS., V. (2004) Bi–Ag-bearing tetrahedrite-tennantite in the Kapsalina copper mineralisation, Thasos Island, Northern Greece. Neues Jahrbuch für Mineralogie –Abhandlungen, **180**(2), 149-169.

VERHAERT, M., BERNARD, A., DEKONINCK, A., LAFFORGUE, L., SADDIQI, O., YANS, J. (2017) Mineralogical and geochemical characterization of supergene Cu–Pb–Zn–V ores in the Oriental High Atlas, Morocco. Mineralium Deposita, **52**(7), 1049-1068.

WALENTA, K. (1984) Sulfidische Erzmineralien aus der Grube Clara im mittleren Schwarzwald und ihre Paragenesen. Der Aufschluss, **35**, 235-246

WALENTA, K. (1992) Die Mineralien des Schwarzwaldes. Weise Verlag, München, 336 S.

WALTER, B.F., BURISCH, M., FUSSWINKEL, T., MARKS, M.A.W., STEELE-MACINNIS, M., WÄLLE, M., APUKHTINA, O.B., MARKL, G. (2018) Multi-reservoir fluid mixing processes in rift-related hydrothermal veins, Schwarzwald, SW-Germany. Geoexploration, **186**, 158-186.

WALTER, B.F., BURISCH, M., MARKL, G. (2016) Long-term chemical evolution and modification of continental basement brines–a field study from the Schwarzwald, SW Germany. Geofluids, **16**, 604-623.

WALTER, B.F., BURISCH, M., MARKS, M.A., MARKL, G. (2017a) Major element compositions of fluid inclusions from hydrothermal vein-type deposits record eroded sedimentary units in the Schwarzwald district, SW Germany. Mineralium Deposita, **51**, 1-14.

WALTER, B.F., IMMENHAUSER, A., GESKE, A., MARKL, G. (2015) Exploration of hydrothermal carbonate magnesium isotope signatures as tracers for continental fluid aquifers, Schwarzwald mining district, SW Germany. Chemical Geology, **400**, 87-105.

WALTER, B.F., STEELE-MACINNIS, M., MARKL, G. (2017b) Sulfate brines in fluid inclusions of hydrothermal veins: Compositional determinations in the system H2O-Na-Ca-Cl-SO4. Geochimica et Cosmochimica Acta, **209**,184-203.

WERNER, A.G., HOFFMANN, C.A. (1789) Mineralsystem des Herrn Inspektor Werners mit dessen Erlaubnis herausgegeben von C. A. Hoffmann. Bergmännisches Journal **2**, 369 – 398.

WEBSTER, J.G., MANN, A.W. (1984) The influence of climate, geomorphology and primary geology on the supergene migration of gold and silver. Journal of Geochemical Exploration, **22**(1-3), 21-42.

WILLIAMS-JONES, A.E., HEINRICH, C.A. (2005) 100th Anniversary special paper: vapor transport of metals and the formation of magmatic-hydrothermal ore deposits. Economic Geology, **100**(7), 1287-1312.

WITTERN, A. (1988) Eine typische Mineralparagenese durch Feuersetzen. Der Aufschluss, **39**, 317-318.

WITTERN, A. (1994) Sekundärmineralien durch Feuersetzen in Oberschulenberg. Bönkhausen, Bleialf und Badenweiler. Der Aufschluss, **45**, 36-42.

WOHLGEMUTH-UEBERWASSER, C.C., VILJOEN, F., PETERSEN, S., VORSTER, C. (2015) Distribution and solubility limits of trace elements in hydrothermal black smoker sulfides: An in-situ LA-ICP-MS study. Geochimica et Cosmochimica Acta, **159**, 16-41.

WU, I., PETERSEN, U. (1977) Geochemistry of tetrahedrite and mineral zoning at Casapalca, Peru. Economic Geology, **72**(6), 993-1016.

YAMAGUCHI, J., SAWADA, Y., SAKURAI, O., UEMATSU, K., MIZUTANI, N., KATO, M. (1980) Thermal decomposition of cerussite (PbCO3) in carbon dioxide atmosphere (0–50 ATM). Thermochimica Acta, **35**, 307-313.

YESARES, L., SÁEZ, R., NIETO, J.M., DE ALMODÓVAR, G.R., COOPER, S. (2014) Supergene enrichment of precious metals by natural amalgamation in the Las Cruces weathering profile (Iberian Pyrite Belt, SW Spain). Ore Geology Reviews, **58**, 14-26.

YOSHIMURA, M., SUJARIDWORAKUN, P., KOH, F., FUJIWARA, T., PONGKAO, D., AHNIYAZ, A. (2004) Hydrothermal conversion of calcite crystals to hydroxyapatite. Materials Science and Engineering: C, **24**(4), 521-525.

ZHANG, P., RYAN, J.A. (1999) Formation of chloropyromorphite from galena (PbS) in the presence of hydroxyapatite. Environmental Science & Technology, **33**(4), 618-624.

ZIRNGAST, M. (1978) Zur Geologie und Geochemie der Schwerspatlagerstätte “Clara” bei Wolfach (Mittlerer Schwarzwald). Dissertation, Universität Braunschweig.

7 Anhang 1-5

Im Folgenden sind die Publikationen von Studie 1-5 zu finden. Die Berechtigungen zur Vervielfältigung der Einzelstudien sind auf den letzten Seiten der Dissertation zu finden.

Anhang 1:

Keim, M. F., Walther, B., Neumann, U., Kreissl, S., Markl, G. (in Press) Polyphase enrichment and redistribution processes in silver-rich associations of the hydrothermal fluorite-barite-Ag-Cu Clara deposit, SW Germany. Mineralium Deposita.

Akzeptiert zur Veröffentlichung: Ja
DOI: 10.1007/s00126-018-0799-z
Anzahl der Autoren: 5
Position in der Autorenliste: 1

Eigenanteile:

Idee	40%
Datenbeschaffung	80%
Auswertung und Interpretation	50%
Ausarbeitung der Publikation	60%

Walther B.:

Idee	0%
Datenbeschaffung	20%
Auswertung und Interpretation	10%
Ausarbeitung der Publikation	5%

Neumann U.:

Idee	0%
Datenbeschaffung	0%
Auswertung und Interpretation	10%
Ausarbeitung der Publikation	5%

Kreissl S.:

Idee	0%
Datenbeschaffung	0%
Auswertung und Interpretation	10%
Ausarbeitung der Publikation	0%

Markl G.:

Idee	60%
Datenbeschaffung	0%
Auswertung und Interpretation	20%
Ausarbeitung der Publikation	30%

Mineralium Deposita
https://doi.org/10.1007/s00126-018-0799-z

ARTICLE

Polyphase enrichment and redistribution processes in silver-rich mineral associations of the hydrothermal fluorite-barite-(Ag-Cu) Clara deposit, SW Germany

Maximilian F. Keim[1] · Benjamin F. Walter[1] · Udo Neumann[1] · Stefan Kreissl[1] · Richard Bayerl[2] · Gregor Markl[1]

Received: 13 September 2017 / Accepted: 8 March 2018

Abstract

The silver-copper sulfide mineralization associated with the fluorite-barite vein system at the Clara deposit in SW Germany shows large scale vertical zoning. Low to moderate silver contents prevail in the upper 350 m, whereas high silver contents occur in the subsequent 450 m of the currently known vein system. This change in Ag tenor is related to conspicuous mineralogical changes with depth. A detailed petrographic and fluid inclusion study identifies evidence for five subsequent hydrothermal and one alteration stage—all contributing to mineralogical diversity. The vertical Ag zoning, however, is attributed only to the first of these stages. During this first stage, increasing oxidation of ascending hydrothermal fluids (90–160 °C, 24.2–26.7 wt% NaCl+$CaCl_2$) led to the formation of high-Ag tetrahedrite-tennantite in the lower parts and basically Ag-free enargite in the upper parts of the vein system. The subsequent hydrothermal stage led to significant mineralogical changes, but inherited the pre-existing Ag zonation. In this second hydrothermal stage, which was related to fluids similar in composition to those of the first stage (70–125 °C, 23.1–26.5 wt% NaCl+$CaCl_2$), dissolution of high Ag-tetrahedrite-tennantite resulted in the formation of complex Ag-sulfosalts together with moderately Ag-bearing tetrahedrite-tennantite and chalcopyrite. The first two stages were formed by fluid mixing of a sedimentary and a hot basement fluid. The influx of fluids with high Ag, Bi and Pb activity during stage 3 and 5 resulted in the local replacement of earlier Ag-sulfosalts by galena and Ag-(Bi)-sulfosalts. The fourth stage is marked by partial dissolution of sulfides and sulfosalts by a late, hot, undiluted basement fluid (250 °C, 18.7–20.9 wt% NaCl+$CaCl_2$) precipitating fluorite, barite and quartz. Finally, supergene alteration lead to the dissolution of silver-bearing phases and the precipitation of acanthite and native silver. The study illustrates, how metal tenor and mineralogy are decoupled in vertically extensive, polyphase hydrothermal vein systems. This may be pertinent to similarly zoned polymetallic vein systems.

Keywords Fahlore · Tennantite-tetrahedrite · Polybasite-pearceite · Hydrothermal · Silver · Schwarzwald ore district

Introduction

The Schwarzwald ore district in SW Germany hosts numerous polymetallic hydrothermal veins consisting primarily of quartz, fluorite, barite, and minor calcite together with minor Ag, Pb, Zn, Sb, As, Cu, Co, and U mineralization (Bliedtner and Martin 1986; Staude et al. 2009). Various types of mineralization formed intermittently since the Permian with a maximum activity during the Jurassic-Cretaceous and Tertiary (Pfaff et al. 2009; Markl 2015). The vein deposits have been mined discontinuously during the last 5000 years (Goldenberg and Steuer 2004), but the Clara Mine currently represents the last active mine in the area (Staude et al. 2010a, b, and references therein; Markl 2015). The Clara vein system formed mainly during the Jurassic-Cretaceous by

Editorial handling: J. Gutzmer

Electronic supplementary material The online version of this article (https://doi.org/10.1007/s00126-018-0799-z) contains supplementary material, which is available to authorized users.

✉ Maximilian F. Keim
maximilian–felix.keim@uni–tuebingen.de

[1] Mathematisch-Naturwissenschaftliche Fakultät, Fachbereich Geowissenschaften, Universität Tübingen, Wilhelmstraße 56, D-72074 Tübingen, Germany

[2] Stuttgart, Germany

Published online: 29 March 2018

fluid mixing triggered by extensional processes during the opening of the Central Atlantic (Pfaff et al. 2009; Staude et al. 2009; Walter et al. 2016, 2017a). It is among the top five worldwide localities with respect to mineral diversity and type locality of 13 minerals (Markl 2015, and references therein). To a large extent, this is due to an extensive supergene overprint of an already unusually variable hydrothermal mineral assemblage (Bernard and Hyrsl 2006; Markl 2015). Several authors dealt with the Clara vein system focusing on the geology and structural relations (List 1969; Zirngast 1978; Maus et al. 1979; Huck 1984), mineralogy of hydrothermal and supergene minerals (e.g., Schmeltzer 1983; Kaiser 1984; Walenta 1984; Rehren 1985; Kolitsch et al. 1995; Baumgärtl and Burow 2002; Van der Heyde 2002; Staude et al. 2010a, b; Markl 2015), and the petrological-geochemical conditions of ore formation (Huck 1984, Pfaff et al. 2012; Walter et al. 2017a). The hydrothermal vein system, on which the Clara Mine operates today, has discontinuously been mined for copper, iron and silver since the seventeenth century (Bliedtner and Martin 1986; Werner and Dennert 2004). Since 1850, the vein system has been exploited for barite, from 1898 until today without any interruption. Since 1978, the newly discovered parallel striking fluorite-dominated vein has been mined for fluorite and since 1997, a Ag-Cu-concentrate is produced from sulfide-rich parts (called "silverspar" = Silberspat in German) of the barite vein. This silverspar becomes more prominent with depth (Baumgärtl and Burow 2002; Markl 2015). In 2015, about 150,000 t of raw ore were processed to 50,000 t of fluorite and 45,000 t of barite concentrate. Additionally, 170 t of an Ag-Cu-sulfide concentrate were produced in the same year, containing 4 t of silver and 50 t of copper (Elsner and Schmitz 2017).

The Clara vein system is remarkable for numerous reasons: it is one of few hydrothermal barite-fluorite vein systems with an exposed vertical extent of more than 800 m and it is marked by incredible mineralogical diversity (> 400 species known so far; Markl, 2015). These remarkable facts render detailed studies of this vein system scientifically relevant, as they contribute to the understanding of the origin and subsequent overprint of a complex, polyphase hydrothermal system. Here, we present a detailed description of the ore textures and paragenetic sequence of the silver-rich association hosted by the Clara barite vein, discuss the observed mineralogical variation with depth as well as redistribution processes using microscopy, electron microprobe, and fluid inclusion analyses.

Geology, mineralogy, and vein formation of the Clara deposit

Geological framework of the Schwarzwald ore district

The Schwarzwald is a mountain range of about 50 × 150 km size located in SW Germany, geologically consisting of exhumed Variscan basement rocks (mostly metasedimentary gneisses and granites) and Lower Permian to Upper Jurassic sedimentary cover rocks (Kalt et al. 2000). During Carboniferous collision processes, the paragneiss units (locally containing orthogneisses and amphibolites) were deformed and metamorphosed to upper amphibolite-facies grade (Geyer and Gwinner 2011). Between 335 Ma and 315 Ma, these gneiss units were intruded by post-collisional S-type granites (Altherr et al. 2000; Hann et al. 2003). Regional basins were filled by red bed arkoses and conglomerates during the Lower Permian. Due to subsidence from early Triassic to Jurassic, quarzitic sandstones, shales, and limestones were deposited unconformably on the basement rocks. During the Paleogene, rifting of the Upper Rhine Graben was initiated and the graben shoulders were exhumed due to uplift. The erosion of the sedimentary cover over the last 20–30 Ma resulted in the partial exposure of the basement (Geyer and Gwinner 2011, and references therein). Erosion was strongest in the southern parts; in the Central and Northern Schwarzwald, the basement-cover unconformity is still preserved. In the southern Schwarzwald, the basement gneisses have been eroded to a depth of about 1.5–2 km below the former unconformity (Nitsch and Rupf 2008). The Clara vein system is part of the Central Schwarzwald and extends from the basement gneisses into the Permian and Triassic red bed cover rocks.

Hydrothermal vein formation in the Schwarzwald

Various types of hydrothermal veins formed over the last 300 Ma in the Schwarzwald and are hosted by the Variscan basement rocks and their Permo-Triassic sedimentary cover (Pfaff et al. 2009; Staude et al. 2009; Walter et al. 2016). The over 1000 veins consist dominantly of barite, fluorite, quartz, and minor carbonates besides native metals, metal oxides, sulfides, and arsenides (Metz et al. 1957; Bliedtner and Martin 1986). Most of the hydrothermal activity occurred around 200–100 Ma during late pull-apart tectonics related to the break-up of the North Atlantic and during opening of the Rhine Graben rift system between 40 and 20 Ma (Staude et al. 2009; Burisch et al. 2018). Based on structural, mineralogical, and microthermometric studies, the hydrothermal veins have been subdivided into five formation stages comprising (i) Late Carboniferous quartz-tourmaline veins with W-Sb ores, (ii) Permian quartz veins with Sb-(Au)-(Ag) ores, (iii) Triassic-Jurassic quartz veins with Fe-ores, (iv) Jurassic-

Cretaceous fluorite-barite-quartz-carbonate veins with Pb-Zn-Cu, Fe-Mn or Ag-Bi-Co-Ni-U ores and (v) Post-Cretaceous quartz-barite-fluorite or carbonate veins with Pb-Zn-Cu-Ag and Cu-Ni-Bi-Ag ores (Walter et al. 2016). Based on fluid inclusion data, Bons et al. (2014), Fusswinkel et al. (2013) and Walter et al. (2016, 2017a, and references therein) provide strong evidence for binary fluid mixing as the dominant mechanism of hydrothermal mineral formation. Based on fluid chemistry and isotope systematics, mixing occurred between a highly saline, metal-rich basement brine and an almost equally saline metal-poor brine presumably sourced from Middle Triassic limestone (Muschelkalk) (Staude et al. 2010a, b, 2011; Fusswinkel et al. 2013; Bons et al. 2014; Walter et al. 2015, 2016, 2017a). This binary fluid mixing led to precipitation of large amounts of fluorite, barite, and quartz during the Jurassic-Cretaceous (Burisch et al. 2016b). Late-stage quartz is thought to have formed by either fluid mixing or cooling (Burisch et al. 2017b). Further information on classification, genesis and conditions of formation of the Schwarzwald hydrothermal veins can be found in Behr and Gerler (1987), Behr et al. (1987), Staude et al. (2009, 2010a, 2011, 2012a, b), Pfaff et al. (2009, 2010), Markl (2015), Walter et al. (2015, 2016, 2017a, 2017b, 2018), Burisch et al. (2016a, 2016b, 2018).

Local geology of the Clara Mine

The complex vein system of the Clara Mine is located north of the city of Wolfach in the Central Schwarzwald (Fig. 1). The veins are hosted by paragneiss and metatexite units predominantly composed of quartz, plagioclase, biotite, orthoclase, and minor hornblende (age of metamorphism about 330 Ma (Kalt et al. 1994)). The minerals of the host rock gneisses show strong sericitization and/or chloritization accompanied by a strong silicification and precipitation of hematite (Okujeni 1980; Huck 1984; Kloos 1990). The sedimentary cover consists of Permian arkoses and Triassic sandstones that unconformably rest on the basement gneisses. The Clara vein system has been subdivided into five mineralization stages including numerous substages (List 1969; Zirngast 1978; Maus et al. 1979; Huck 1984; For details see ESM and Table 1).

The *first stage (1)* is represented by intensive silicification and brecciation of the host gneiss and is followed by the *second stage (2)* (fluorite main stage) consisting of fluorite-quartz-sellaite (up to 12 m thickness; Werner and Dennert (2004)) together with minor pyrite, chalcopyrite, ferberite, and minerals of the tennantite-tetrahedrite solid-solution series (hereafter referred to as fahlore; chemical formulae and abbreviations for the most important minerals are listed in Table 2).

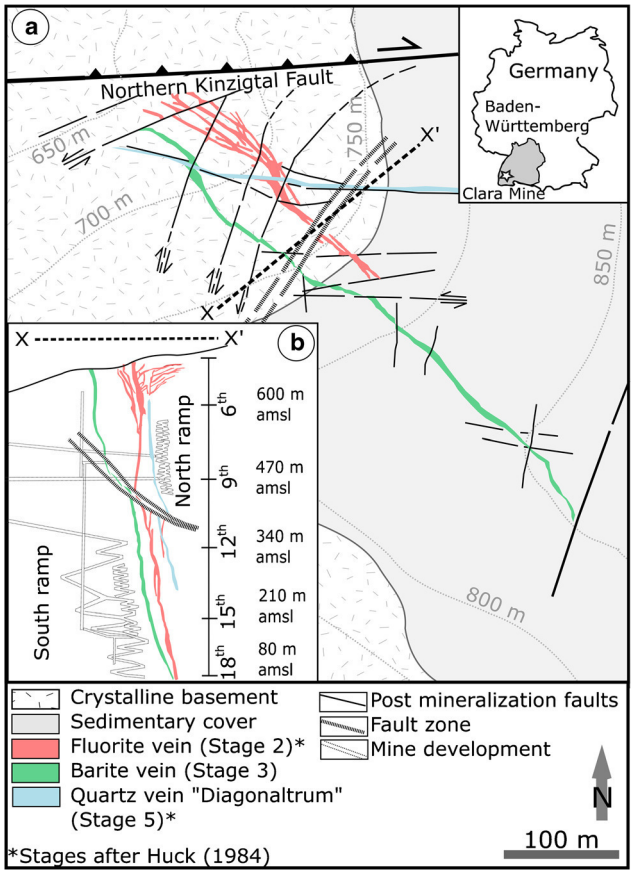

Fig. 1 **a** Geological map of the Clara vein system including main hydrothermal veins and major tectonics. **b** Cross-section of the Clara Mine with the projected mine development modified after Huck (1984) and Bucher et al. (2009)

The *third stage (3)* (barite main stage) crosscuts and follows the older fluorite vein particularly in the SE parts but mostly runs parallel to it and discordantly crosscuts the sedimentary cover (Huck 1984). The barite main stage is subdivided into 4 different substages (*3.1–3.4*; List 1969; Zirngast 1978; Huck 1984). The *first and second substages (3.1, 3.2)* consist of barite and fluorite together with small amounts of botryoidal pyrite-marcasite aggregates and minor chalcopyrite (Huck 1984). The *third substage (3.3)* is characterized by alternating layers of medium-grained white barite, gray fluorite, and quartz together with interbedded sulfides. The thickness of the sulfide layers varies from a few mm to some dm. Towards greater depth, the proportion of sulfides increases. The sulfide minerals predominantly occur in the southern part of the vein and consist of chalcopyrite and fahlore mostly intergrown with fluorite (List 1969). This substage is commonly

Table 1 Compilation of the mineralization stages of the Clara veins after Huck (1984) including main stages, sub stages, important sulfides, and age constraints

Main stages	Sub stages	Sulfide/oxide minerals	Age constraints
1. Silicification	1.1–1.3 Quartz	Hematite, pyrite, marcasite	
2. Fluorite main stage (Fluorite vein Fig. 1)	2.1–2.3 Fluorite + quartz + sellaite	Pyrite, chalcopyrite, fahlore, (ferberite)	130 ± 20 (fluorite/barite)[1]; 143 ± 2 (host rock sericite)[1]; 173 ± 2 (ferberite)[2];
3. Barite main stage (Barite vein Fig. 1)	3.1 Barite + fluorite + (quartz)	Pyrite, marcasite, chalcopyrite	144 ± 5 (host-rock illite)[1]
	3.2 Barite + (fluorite)	Pyrite, marcasite	
	3.3 Barite + fluorite + quartz	Minerals of the "silverspar"	
	3.4 Barite + (fluorite)	–	
4. Barite interstage	4.1; 4.2 Barite + fluorite + siderite	Chalcopyrite, marcasite	
5. Quartz main stage (Quartz vein; "Diagonaltrum" Fig. 1)	5.1–5.4 Quartz + barite + fluorite	Pyrite, galena, chalcopyrite	

[1] Mertz (1987); [2] Pfaff et al. (2009)

referred to as "silverspar," which is processed at Clara Mine to produce Ag and Cu concentrates. It is also this substage that the present contribution is mainly concerned with. The "silverspar" can be subdivided into two mineralogically different groups: the upper level group (*UG*) is characterized by a relatively simple mineralogy (fahlore + chalcopyrite and rare enargite) and is present between the 4th and the 10th level (690–450 m above mean sea level (amsl); Huck 1984; List 1969; Zirngast 1978). The lower level group (*LG*) was found only below the 10th level down to the present mining level (2017: 20th level, 10 m below mean sea level) and shows a more complex mineralogy including Ag-sulfosalts besides fahlore and chalcopyrite (Schmeltzer 1983; Huck 1984; Walenta 1984; Rehren 1985; Kolitsch et al. 1995; Van der Heyde 2002). Besides the normal Ag-Cu sulfide mineralization, the "silverspar" shows spatially confined mineralogical variations by the additional occurrence of large amounts of arsenopyrite and/or galena. Although it is likely that the

Table 2 Typical minerals of the "silverspar" with stoichiometric formulae and abbreviations (Abbr) used in Figs. 3, 4, and 8

Mineral	Formula	Abbr	Mineral	Formula	Abbr
Barite	$BaSO_4$	Brt	Famatinite	Cu_3SbS_4	Fam
Calcite	$CaCO_3$		Galena	PbS	Gn
Fluorite	CaF_2	Fl	Geocronite	$Pb_{14}(Sb,As)_6S_{23}$	
Quartz	SiO_2	Qtz	Hematite	Fe_2O_3	
Sellaite	MgF_2		Jordanite	$Pb_{14}(As,Sb)_6S_{23}$	
Siderite	$FeCO_3$		Luzonite	Cu_3AsS_4	Luz
Acanthite	AgS	Act	Marcasite	FeS_2	Mrc
Arsenopyrite	FeAsS	Apy	Matildite	$AgBiS_2$	
Berryite	$Cu_3Ag_2Pb_3Bi_7S_{16}$		Mckinstryite	$Ag_5Cu_3S_4$	
Bornite	Cu_5FeS_4	Brn	Native Silver	Ag	Ag
Chalcopyrite	$CuFeS_2$	Cp	Polybasite	$(Ag,Cu)_{16}(As)_2S_{11}$	Plb
Cobaltite	CoAsS		Pearceite	$(Ag,Cu)_{16}(Sb)_2S_{11}$	Prc
Covellite	CuS	Cv	Proustite	Ag_3AsS_3	Prs
Diaphorite	$Pb_2Ag_3Sb_3S_8$		Pyrargyrite	Ag_3SbS_3	Pya
Emplektite	$CuBiS_2$		Pyrite	FeS_2	Py
Enargite	Cu_3AsS_4	Eng	Stephanite	Ag_5SbS_4	
Fahlore	$(Cu,Ag)_{10}(Fe,Zn)_2(As,Sb)_4S_{13}$	Fh	Stibnite	Sb_2S_3	

"silverspar" also occurred above the 4th level, it is not preserve due to intensive weathering.

During the *fourth substage (3.4)* coarse-grained barite crystals grew together with fluorite and subordinate fahlore and chalcopyrite. Whether these sulfide grains represent remobilization products from substage 3 or can be attributed to a distinct mineralization stage remains unclear (List 1969; Huck 1984). The *fourth stage (4)* is called "barite interstage" and is characterized by different generations of barite, fluorite, siderite, and chalcopyrite plus marcasite.

The *fifth stage (5)* is dominated by quartz and is called "quartz main stage"; it crosscuts the older fluorite and barite veins. This stage developed in close relation to the ENE-WSW striking, major regional shear zone, the Northern Kinzigtal fault (NKF) (Huck 1984; Fig. 1). The formation of stage five is subdivided into 4 different substages (Huck 1984). The most important is the *fourth substage (5.4)*, which contains galena and chalcopyrite often crosscutting the earlier fluorite and barite veins leading to a prominent silicification of the gangue minerals, especially of barite. This substage reaches up to 5 m thickness in the northern part forming a separate vein, referred to as "Diagonaltrum."

Age dating of the "fluorite main stage" reveals ages of 130 ± 20 Ma (fluorite, barite; Rb-Sr method), 143 ± 2 Ma (host rock sericite; Rb-Sr method), and 173 ± 2 Ma (ferberite; U-Pb method), for the "barite main stage" of 144 ± 5 Ma (host rock illite; Rb-Sr method) (Pfaff et al. 2012, and references therein). This shows that the main mineralization of the Clara vein system belongs to the Jurassic-Cretaceous vein group, which according to Behr and Gerler (1987), Staude et al. (2009) and Walter et al. (2016) formed by fluid mixing.

Methods

For this study, a sample suite of 52 thin sections was investigated by light and electron microscopy, besides macroscopic observations on dozens of hand specimens. Fluid inclusion sections (4 samples) were prepared from the counterpart of the thin sections. Samples come from the mineral collection of the University of Tübingen and were sampled over the years on different mining levels. Also, samples collected from the mine dumps over the last 30 years were included. It was only roughly possible to assign the latter ones to a certain mining level.

Electron microprobe analysis (EMPA)

For qualitative and quantitative determination of the major and minor element compositions of sulfides and native elements, a JEOL 8900 electron microprobe was used at the Department of Geosciences, University of Tübingen, Germany, and a Cameca SX100 electron microprobe at the University of Stuttgart, Germany. Both microprobes running in wavelength-dispersive (WD) mode used a focused beam with 20 nA current and a 20 kV acceleration voltage. Due to the rapid decomposition of polybasite-pearceite, pyrargyrite-proustite, and billingsleyite under the electron beam, a beam diameter of 10 μm and a beam current of 5 nA were used. Matrix corrections were performed according to the JEOL ZAF method (Armstrong 1991). The elements for the quantitative program were selected after qualitative analyses in energy dispersive mode (EDS). Details of the WD-configuration used, including standards, counting times of the peak/background, analyzed fluorescence lines, and the average detection limits and the whole dataset are presented in the ESM.

Fluid inclusion microthermometry

Microthermometric analyses were performed in fluorite and quartz ($n = 132$) from one UG (MK-38; 6th level; 600 m amsl) and three LG samples (MK-7, MK-16, MK-34; below the 10th level; 450 m amsl) to determine the chronological sequence of fluid inclusion (FI) assemblages using a Linkam stage (model THMS 600) at the University of Tübingen. Observations were made in double polished thick sections (100 to 200 μm). The FI were classified as primary, pseudo-secondary, secondary, isolated inclusions, and clusters of inclusions (see ESM) with no geometrical relation to former crystal surfaces or fractures according to the FI-assemblages approach of Goldstein and Reynolds (1994). Each FI was analyzed triply to determine the final melting temperature of ice ($T_{m\text{-}ice}$) and hydrohalite ($T_{m\text{-}hh}$) and the homogenization temperature (T_h). The presented data include only FI for which all three analyses differ less than 0.1 °C for $T_{m\text{-}ice}$ and $T_{m\text{-}hh}$ and less than 1 °C for Th. Synthetic H_2O, H_2O-NaCl and H_2O-CO_2 standards were used for calibration. The salinity in the ternary NaCl-$CaCl_2$-H_2O system was determined according to Steele-MacInnes et al. (2011). The volume proportion for each FI was estimated based on filling degree tables and reported in the volume proportion notation (Shepherd et al. 1985; Bakker and Diamond 2006). FI showing evidence of post-entrapment modifications were excluded from analysis and data interpretation. A pressure correction considering the method of Bodnar and Vityk (1994) was applied, assuming hydrostatic conditions with a depth of the water column inferred

from the paleo-depth of 1.0–1.5 km as estimated by Geyer and Gwinner (2011). Uncertainties of this approach are discussed in Walter et al. (2015, 2016, 2017a, 2017b). Since hydrostatic conditions can be assumed and overburden is negligible for the Clara vein system, the pressure correction has only minor effects on the homogenization temperature (5–10 °C). Therefore, homogenization temperatures were presented as uncorrected values. Microthermometry of FI in barite is difficult, since they are easily destroyed during freezing or heating (decrepitation, leakage, necking-down). Consequently, microthermometric data obtained from FI in barite were only used for estimating salinities. All FI data can be found in the ESM.

Cathodoluminescence microscopy

Cathodoluminescence (CL) microscopy studies were performed to obtain additional qualitative information on the fluid petrography of FI-assemblages and on the paragenetic sequence of the gangue minerals. A hot cathode CL microscope (type HC1-LM) at the University of Tübingen was used with an acceleration voltage of typically ~ 14 kV and a beam current density of ~ 9 μA/mm^2 on the sample surface.

Geochemical modeling

For calculating predominance diagrams, The Geochemist's Workbench version 10.0 (Bethke and Yeakel 2015) was used. Calculations are based on the Thermoddem database (Blanc et al. 2012). Data for enargite were implemented to the Thermoddem database from the SOLTHERM database (Palandri and Reed 2017), data for tetrahedrite, freibergite, Ag-polybasite, Ag-Cu-polybasite were from Sack (2000) and Sack (2017). Combining the thermodynamic data from different sources is a potential source of error. However, Keim et al. (2017) showed that such errors are relatively small and have no influence on the general interpretation of the predominance diagrams in this work.

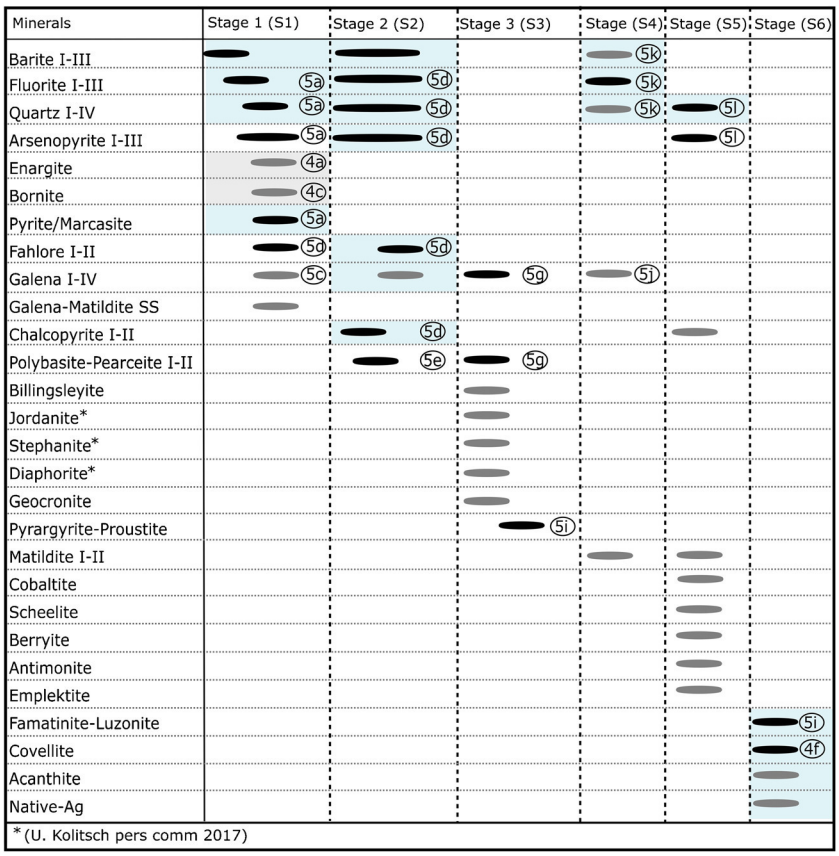

Fig. 2 Paragenetic sequence of the "silverspar" mineralization. Minerals occurring in both groups are shaded in blue, minerals occurring exclusively in the LG are not shaded, and minerals exclusively present in the UG are shaded in gray. Black bars represent minerals that occur frequently, gray bars represent minerals that are rare during a paragenetic stage. The circled lettered numeration refers to thin section photographs (Figs. 4 and 5)

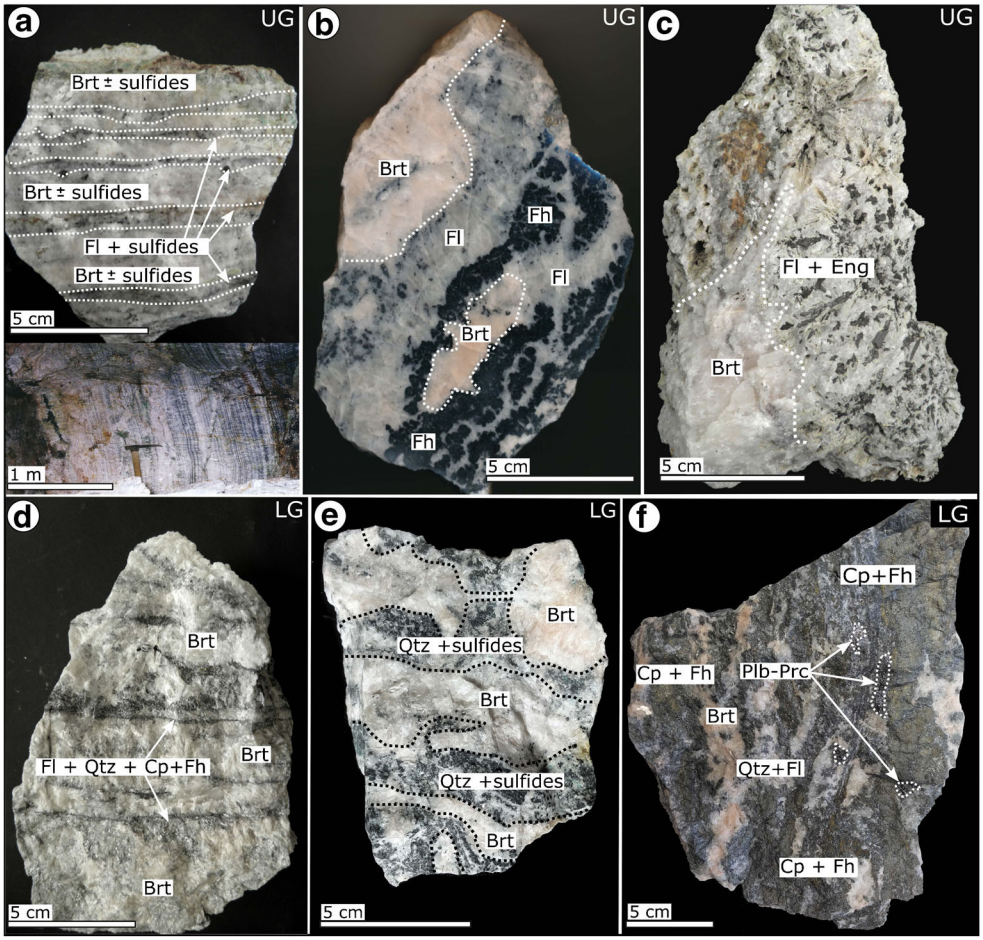

Fig. 3 Photographs of hand specimens showing typical textures of the "silverspar." **a** Top: Barite dominated sample with bands of fluorite with sulfides; bottom: Banded barite-fluorite ore exposed in the Clara Mine (photograph from Werner and Dennert 2004). **b** Sulfide bands in fluorite together with barite. **c** Nodular aggregate of enargite plus fluorite in barite. **d** Sulfide bands in a barite-dominated sample. **e** Quartz and sulfides randomly distributed in barite. **f** Massive sulfides together with barite, quartz, and fluorite

Results

Paragenetic/petrographic description of the "silverspar" in the barite vein

The mineralogical and petrographic description of the mineral textures in this study focuses on the "silverspar" (sub stage 3.3) of the "barite main stage" (stage 3). Samples of this study come from the 4th to 18th level of the Clara Mine. In the following, the paragenetic sequences of the UG and LG of the "silverspar" are presented separately. In the UG and LG, the "silverspar" can be subdivided into six different paragenetic stages (S1-S6; Fig. 2), although S3 and S5 are missing in the UG.

The upper level group (UG)

Macroscopically, the UG "silverspar" shows a smaller amount of sulfides compared to the LG and is characterized by meter-thick sequences of alternating, cm- to dm-thick bands of barite, fluorite, and quartz, which are accentuated by horizontally aligned, small, unconnected sulfide pods predominantly within fluorite II zones (Fig. 3a). Sulfides are also present as more massive aggregates of several cm to dm thickness, again predominantly in the fluorite-dominated parts of the vein (Fig. 3b), albeit much less common than in the LG.

The first paragenetic stage *S1* is characterized by the occurrence of columnar enargite together with nodular fluorite I enclosed in barite I plus quartz I (Figs. 3c and 4a). Enargite is overgrown by radial marcasite (Fig. 4b) crystals and associated with small amounts of bornite (Fig. 4c).

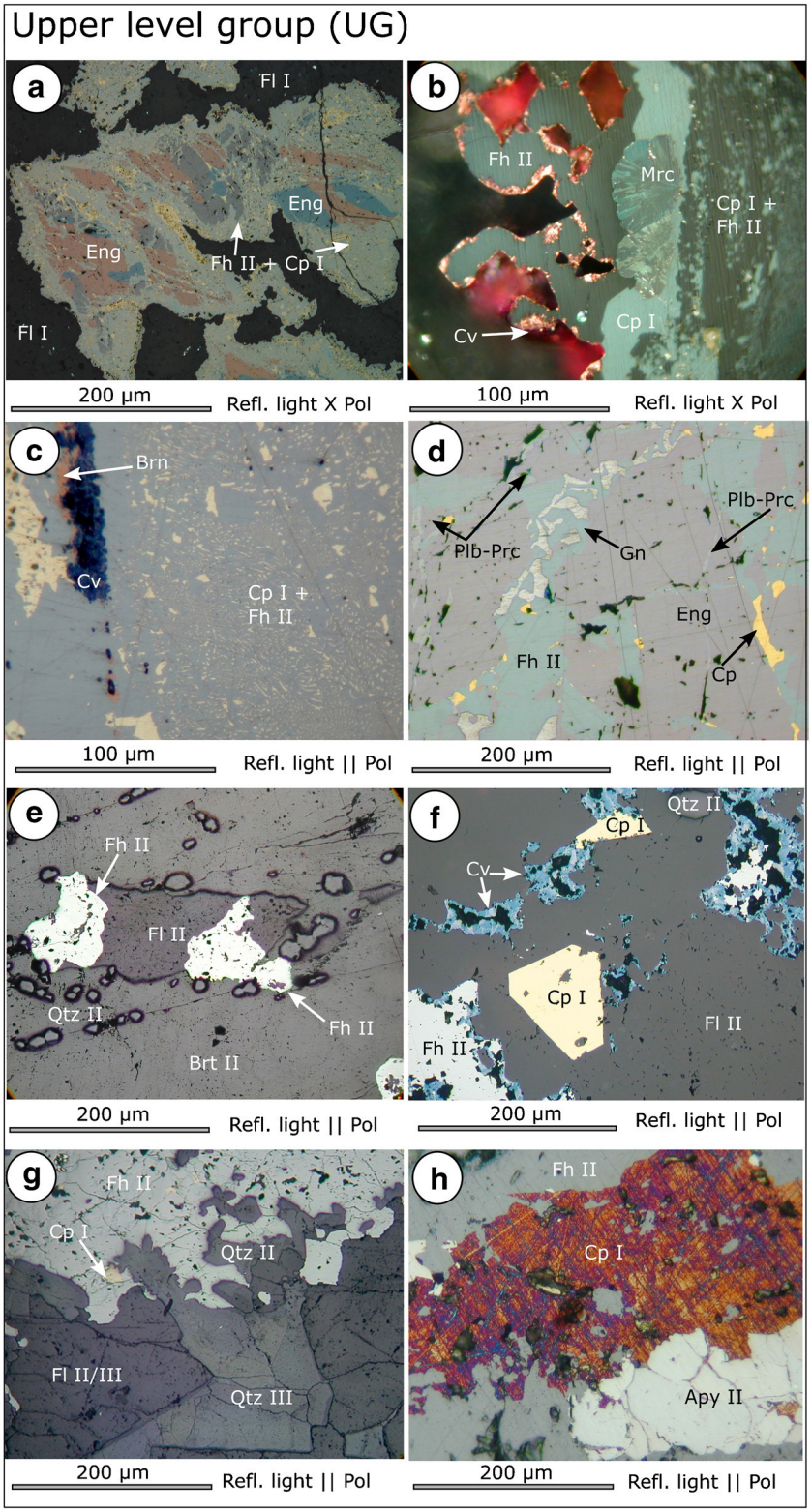

Fig. 4 Photomicrographs of the "silverspar" of the Clara Mine illustrating important ore textures. **a** Enargite replaced by fahlore plus chalcopyrite (MK-35). **b** Radial marcasite crystals overgrown by fahlore and chalcopyrite (MK-35). **c** Bornite and covellite together with minor fahlore enclosing fine-grained chalcopyrite (MK-35). **d** Galena and polybasite-pearceite together with enargite and fahlore (MK-35). **e** Fahlore enclosed in interstitial fluorite (MK-39). **f** Euhedral chalcopyrite and alterated fahlore (MK-37). **g** Large fahlore aggregate together with different generations of quartz and fluorite (MK-3). **h** Fahlore and chalcopyrite together with arsenopyrite (MK-3). For mineral abbreviation, see Table 2; Refl = reflected

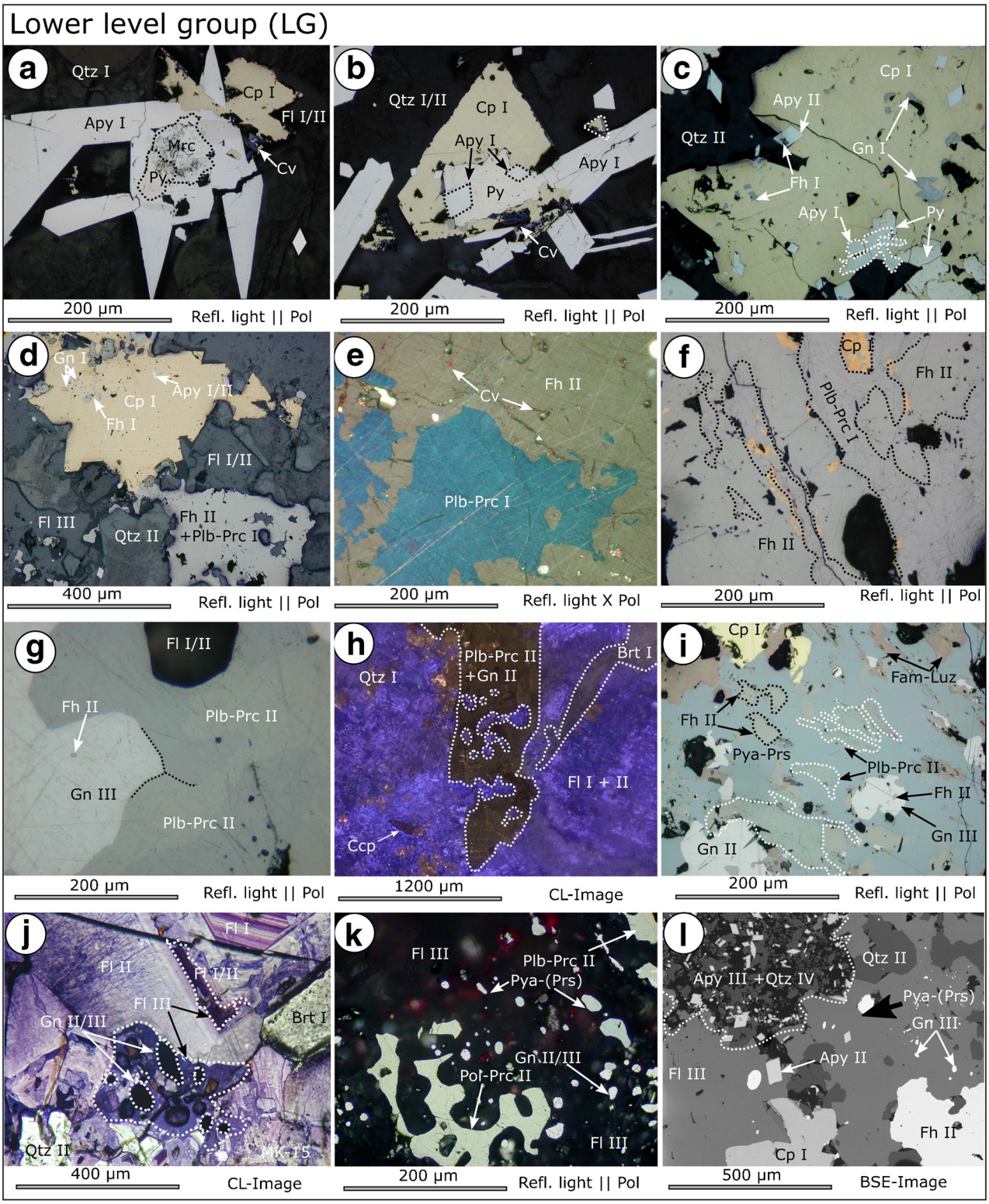

Fig. 5 Photomicrographs of the "silverspar" of the Clara Mine illustrating important textures. **a** Pyrite/marcasite enclosed by arsenopyrite (MK-43). **b** Pyrite and arsenopyrite enclosed by euhedral chalcopyrite (MK-43). **c** Fahlore, arsenopyrite, pyrite and galena enclosed by chalcopyrite (MK-17.1). **d** Chalcopyrite together with cogenetic fahlore (MK-12). **e** Polybasite-pearceite overgrown/replaced by fahlore (MK-12). **f** Polybasite-pearceite replaced by fahlore together with chalcopyrite (MK-36). **g** Polybasite pearceite together with galena (MK-48). **h** CL-image of polybasite-pearceite plus galena replacing fluorite (MK-1). **i** Polybasite-pearceite and fahlore replaced by pyrargyrite-(proustite) (MK-4). **j** CL-image of fluorite replacing galena (MK-1). **k** Fluorite replacing galena, polybasite-pearceite, and pyrargyrite-(proustite) (MK-2R). **l** Late quartz together with euhedral arsenopyrite (MK-15). For mineral abbreviation, see Table 2; Refl = reflected

During the second paragenetic stage *S2* enargite crystals are partly or entirely replaced by fahlore II and chalcopyrite I (Fig. 4a, d). Fahlore II and chalcopyrite I are accompanied by rare polybasite-pearceite I, galena II and covellite (Fig. 4d). This occurrence of polybasite-pearceite is the only example of a distinct primary Ag-phase in the UG samples. Their occurrence appears to be confined to the transition between UG and LG. Fahlore II and chalcopyrite I show no clear age relation and grow either on barite II crystals (Fig. 4e) or are enclosed by interstitial fluorite II (Fig. 4f). As accessory mineral, arsenopyrite II occurs enclosed in fahlore II (Fig. 4h). The following ore stages S3 and S5 are missing in the UG, but quartz II, fluorite II, and fahlore II show partial dissolution by later fluorite III and quartz III during *S4* (Fig. 4g). In paragenetic stage *S6*, fahlore II and chalcopyrite I are replaced by covellite (Fig. 4f) and/or famatinite-luzonite which are rarely intergrown with small μm-sized acanthite and native silver grains.

The lower level group (LG)

Macroscopically, the LG samples show alternating bands of barite, fluorite, and quartz. The sulfides form connected bands, mostly in the fluorite- and quartz-dominated zones (Fig. 3d). In some samples, however, a clear banding is not present and nest-like sulfide aggregates occur, usually in quartz-rich parts of the barite vein (Fig. 3e). Massively developed sulfide "pods" up to several dm in size or thickness are typical of the LG and contribute the largest portion to the overall sulfide content (Fig. 3f).

In *S1*, an early pyrite/marcasite phase is accompanied by arsenopyrite I (Fig. 5a, b), fahlore I, galena I (Fig. 5c), and exolved matildite-galena aggregates. These sulfides are typically replaced by later chalcopyrite I of *S2*.

Chalcopyrite I of *S2* forms either euhedral crystals (Fig. 5b), or is intergrown with fahlore II. Fahlore II frequently overgrows polybasite-pearceite I (Figs. 5e, f and 3g). Galena II is relatively rare and cogenetic with chalcopyrite I. Euhedral grains of arsenopyrite II are variably abundant and crystallized during the entire stage (Fig. 5c).

In some samples, S1 and S2 are overprinted by the younger mineralization of stage three (*S3*). Here, aggregates of polybasite-pearceite II ± galena III (Fig. 5g) replace fluorite I/II (Fig. 5h), fahlore II and polybasite-pearceite II (Fig. 4i). Additionally, polybasite-pearceite II enclose minerals of S1 + S2 (Fig. 5i). In this association, also billingsleyite, diaphorite, stephanite, jordanite, and geocronite occur in trace amounts (Kolitsch, pers comm 2017). Polybasite-pearceite II and chalcopyrite I are commonly replaced by later pyrargyrite-proustite solid solution (Fig. 5i). This paragenetic stage represents a galena-rich variety of the "silverspar" that occurs locally (Markl 2015).

During *S4*, fluorite III, barite III, and quartz III partially replace the earlier S1-S3 sulfides. This replacement process can be observed mostly in fluorite III, which encloses small roundish and amoeboid-like grains of the earlier sulfides (Fig. 5j, k). Fluorite III is accompanied by needle-like matildite I and galena IV.

The subsequent paragenetic sequence *S5* is characterized by fine-grained quartz IV together with variable amounts of predominantly arsenopyrite III (Fig. 5l). Arsenopyrite III occurs either enclosed in quartz IV or as prismatic rhombs in vugs and on the surface of late-stage chalcopyrite II. Matildite II, cobaltite, berryite, stibnite, and scheelite also occur, either growing in vugs or enclosed by chalcopyrite II. This paragenetic stage is responsible for the (arsenopyrite + quartz)-rich variety of the "silverspar." During *S6,* the sulfides undergo alteration to famatinite-luzonite, covellite and—especially in the vicinity of the silver sulfosalts—larger amounts native silver and acanthite occur.

Compositional variation of sulfides

The following minerals were analyzed by electron microprobe: Fahlore ($n = 434$), polybasite-pearceite ($n = 130$), pyrargyrite-proustite ($n = 37$), billingsleyite ($n = 7$), pyrite ($n = 30$), marcasite ($n = 5$), chalcopyrite ($n = 81$), galena ($n = 79$), matildite ($n = 17$), arsenopyrite ($n = 74$), famatinite-luzonite ($n = 83$), enargite ($n = 11$), covellite ($n = 14$), native Ag ($n = 15$), acanthite ($n = 5$). Representative analyses with calculated formulae for each mineral can be found in the ESM.

Tennantite-tetrahedrite solid-solution series ($(Cu,Ag)_{10}(Zn,Fe)_2(As,Sb,Bi)_4S_{13}$)

Fahlore I and II can be distinguished by their molar XAg (defined as: Ag/(Cu + Ag)) (Fig. 6a). For fahlore I, XAg ranges between 0.19 and 0.37 (average of 0.28) and for fahlore II between < 0.01 and 0.18 (average of 0.05). About 20 (of 80) individual analyses of fahlore I show freibergitic compositions (> 20 wt% Ag; Riley 1974).

The molar XAs (defined as: As/(As+Sb + Bi)) of both fahlore generations is highly variable and ranges for fahlore

Fig. 6 Compositional variation of the sulfide minerals of the "silverspar." **a** Molar As/(As+Sb) versus molar Ag/(Ag + Cu) showing the chemical variation of fahlore I and fahlore II. Gray stars show distinct samples for both groups. **b** Molar As/(As+Sb) versus molar Ag/(Ag + Cu) showing chemical variation of fahlore in the UG and the LG. **c** Molar As/(As+Sb) versus Zn/(Zn + Fe) showing the chemical variation of fahlore from the UG and the LG. **d** Molar As/(As+Sb) versus molar Ag/(Ag + Cu) showing the chemical variation of polybasite–pearceite I and II. **e** Molar As versus Sb showing the chemical variation of famatinite and luzonite/enargite. Stars mark end-member compositions, gray points stand for enargite, blue points for pyrargyrite-proustite analyses

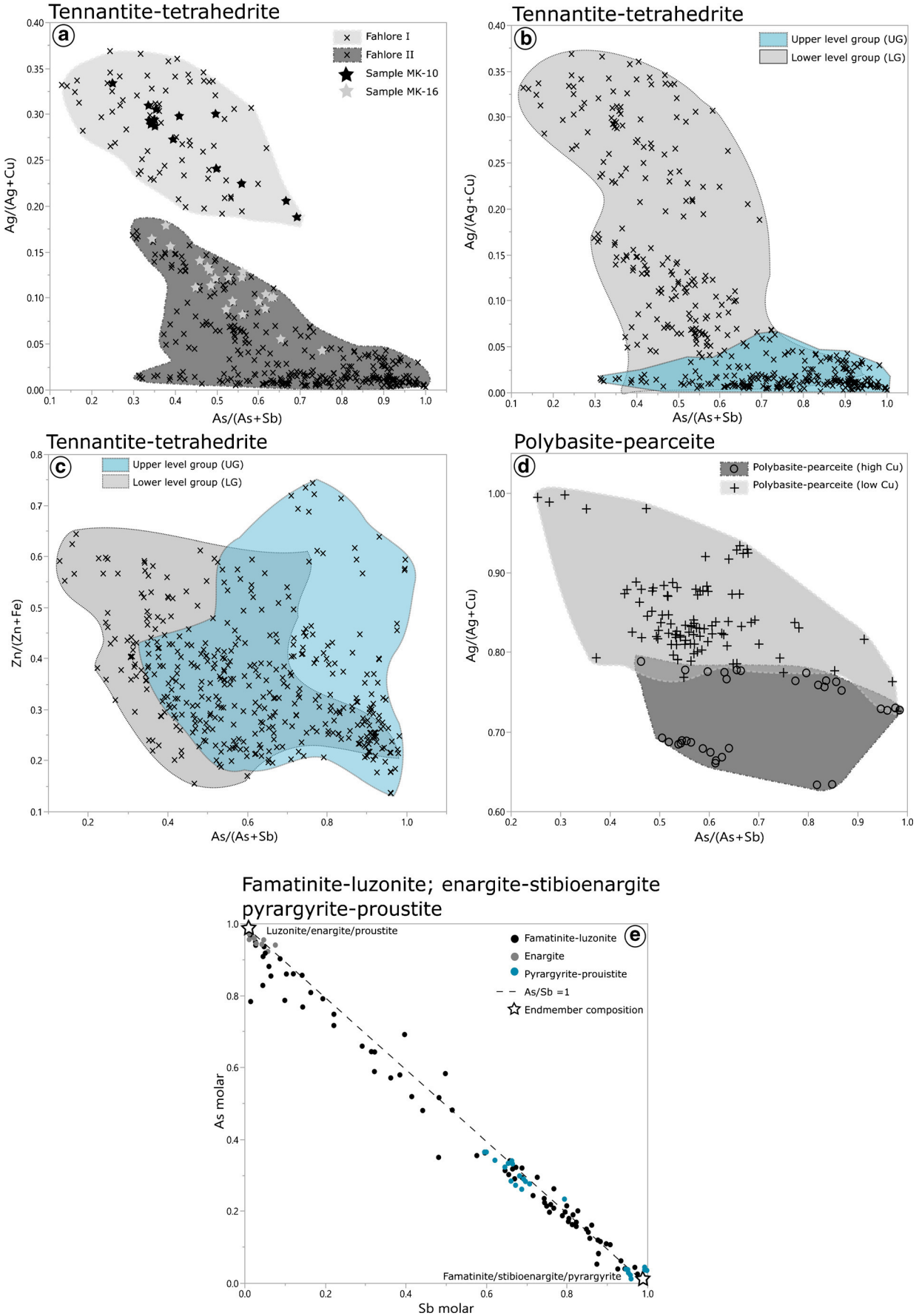
Tennantite-tetrahedrite
a
Fahlore I
Fahlore II
Sample MK-10
Sample MK-16
Ag/(Ag+Cu)
As/(As+Sb)
Tennantite-tetrahedrite
b
Upper level group (UG)
Lower level group (LG)
Ag/(Ag+Cu)
As/(As+Sb)
Tennantite-tetrahedrite
c
Upper level group (UG)
Lower level group (LG)
Zn/(Zn+Fe)
As/(As+Sb)
Polybasite-pearceite
d
Polybasite-pearceite (high Cu)
Polybasite-pearceite (low Cu)
Ag/(Ag+Cu)
As/(As+Sb)
Famatinite-luzonite; enargite-stibioenargite
pyrargyrite-proustite
e
Luzonite/enargite/proustite
Famatinite-luzonite
Enargite
Pyrargyrite-prouistite
As/Sb =1
Endmember composition
Famatinite/stibioenargite/pyrargyrite
As molar
Sb molar

I between 0.13 and 0.69 and for fahlore II between 0.28 and 0.99. The Bi contents are generally low with maximum contents of 4.3 wt%. Fahlore I has a higher average Bi content (0.13 wt%) than fahlore II (0.02 wt%). Within individual samples, increasing XAg is correlated with decreasing XAs (see stars in Fig. 6a). This has been observed by several authors (e.g., Hackbarth and Petersen 1984; Kemkin and Kemkina 2013) and was explained by the little tolerance of both atoms in the fahlore structure (Johnson et al. 1986, and references therein). A separation of the fahlore generations by molar XZn (defined as: Zn/(Zn + Fe)) ratios is not possible, since they widely overlap. XZn for fahlore I ranges between 0.04 and 0.68 (average of 0.41) and for fahlore II between < 0.01 and 0.77 (average of 0.40). Mercury contents reach up to 0.3 wt% and Se contents up to 0.2 wt%. All other elements are below 0.1 wt%.

XAg of fahlore from the UG ranges between 0.01 and 0.37 (average of 0.13) and for LG between < 0.01 and 0.06 (average of 0.01) (Fig. 6b). The molar XAs for fahlore in the UG and LG overlaps over a large range, but LG fahlore reaches lower XAs than the UG samples. The Bi content in both groups averages at 0.02 wt%. A separation of the UG and LG by XZn is not possible (Fig. 6c).

Polybasite-pearceite solid solution series ($(Ag,Cu)_{16}(As,Sb)_2S_{11}$)

For the minerals of the *polybasite-pearceite* solid solution series, the term pearceite is used for molar XAs > 0.5 and polybasite for XAs < 0.5 (Bindi et al. 2007a). If Cu contents are > 4.0 atoms per formula unit (apfu), a structural change can be observed and the minerals are then named cupropolybasite and cupropearceite (Bindi et al. 2007b).

Polybasite-pearceite I and II can be clearly distinguished based on their molar XAg ratio (Fig. 6d). XAg for polybasite-pearceite I ranges between 0.63 and 0.87 (average of 0.72), for polybasite-pearceite II between 0.73 and 1.00 (average of 0.85). XAs ratios vary for polybasite-pearceite I between 0.46 and 0.89 (average of 0.70), for polybasite-pearceite II between 0.25 and 0.98 (average of 0.58). Most of our analyses (< 80%) belong to pearceite and cupropearceite with XAs between 0.5 and 0.98 and XAg between 0.63 and 0.98 corresponding to maximum copper contents of 19.0 wt% (Fig. 6d). Cupropolybasites were not observed. In examples of the *polybasite-pearceite* solid solution series from both LG and UG minor and trace element contents are consistently low with maximum Se contents of 0.2 wt%, Zn contents of 1.4 wt% and Bi contents of 0.5 wt%.

Pyrargyrite-proustite solid-solution series ($Ag_3(Sb,As)S_3$) and billingsleyite ($Ag_7(As,Sb)S_6$)

Minerals of the *pyrargyrite-proustite* series show variable XAs ranging from 0.01 to 0.37 with an average of 0.17 and are, therefore, Sb-dominated. Maximum Cu and Bi contents are 0.1 wt% and 1.5 wt%, respectively. All other trace elements are < 0.1 wt%. The chemical formula for *billingsleyite* (normalized to 14 apfu) is $(Ag_{7.14}Cu_{0.11})_{\sum 7.25}(As_{0.74}Sb_{0.10}Bi_{0.01})_{\sum 0.84}S_{5.90}$ (average of 7 analyses). Maximum Cu contents are 1.0 wt%, maximum Sb and Bi contents each 1.2 wt%. All other minor elements are < 0.1 wt% and/or below the element-specific detection limit.

Pyrite (FeS_2)/marcasite (FeS_2), chalcopyrite ($CuFeS_2$), galena (PbS), matildite ($AgBiS_2$), and arsenopyrite (FeAsS)

Galena contains variable amounts of Ag, Cu, Fe, Hg, Sb, and Bi. Silver contents reach up to 2.1 wt%, Cu contents up to 1.8 wt%, Bi contents up to 4.3 wt%, Fe contents up to 2.7 wt%, Sb contents up to 0.9 wt%, and Hg contents up to 0.2 wt%. All other minor element contents are < 0.1 wt%. The different galena generations are chemically indistinguishable. *Arsenopyrite* shows variable molar As/S ratios ranging from 0.62 to 0.92. Co contents are generally low with maximum contents of 0.4 wt%. Se occurs in all analyzed grains between 0.1 and 0.2 wt%. The concentrations of other minor elements is generally below 0.1 wt% and/or below the element specific detection limit. *Chalcopyrite* contains Ag as major impurity with average contents of 0.2 wt% and a maximum of 2.7 wt%. As and Sb contents reach 0.9 and 1.0 wt%, respectively. *Pyrite* commonly shows As contents up to 7.4 wt%, Ni and Co contents up to 2.0 wt%, and

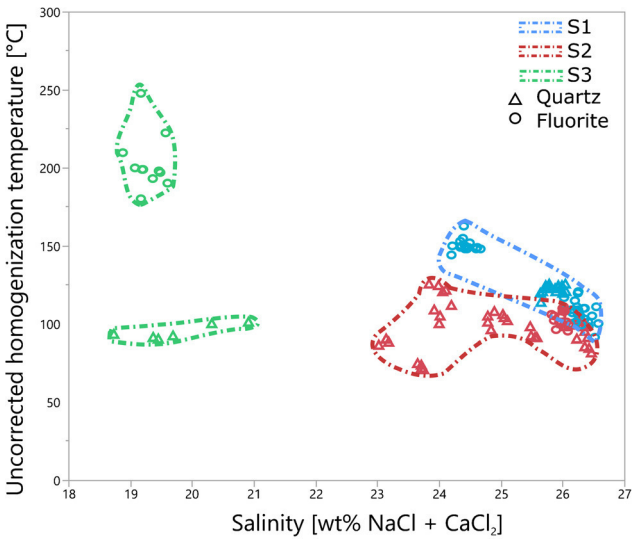

Fig. 7 Uncorrected homogenization temperatures versus salinity (NaCl+$CaCl_2$) for FI of different quartz (triangles) and fluorite (circles) generations (S1, S2, S3) of the "silverspar"

Cu contents up to 4.0 wt%. *Matildite* contains Pb, Cu, and Fe as major impurities with average contents of 3.2, 1.3, and 0.8 wt%, respectively.

Famatinite-luzonite ($Cu_3(As,Sb)S_4$) solid-solution series, enargite (Cu_3AsS_4), covellite (CuS) and native silver (Ag)

As can be seen in Fig. 6e, *famatinite-luzonite* shows an extensive exchange of As and Sb, with molar XAs (As/As+Sb) varying between 0.02 and 0.98. Most important minor elements are Ag with average contents of 3.1 wt% and Fe with average contents of 0.51 wt%. *Enargite* is clearly As-dominated with maximum Sb contents of 1.74 wt% (Fig. 6e). Silver contents are up to 0.9 wt%, all other elements are below 0.1 wt%. *Native silver* contains on average 0.3 wt% and a maximum of 0.7 wt% Cu. All other element concentrations remain < 0.1 wt%. The most important trace element in *covellite* is silver with average contents of 2.1 wt%.

Fluid inclusion characteristics of the "silverspar"-related gangue minerals

Fluid inclusions (FI) in fluorite ($n = 71$) and quartz ($n = 61$) cogenetic to sulphide mineral assemblages in the

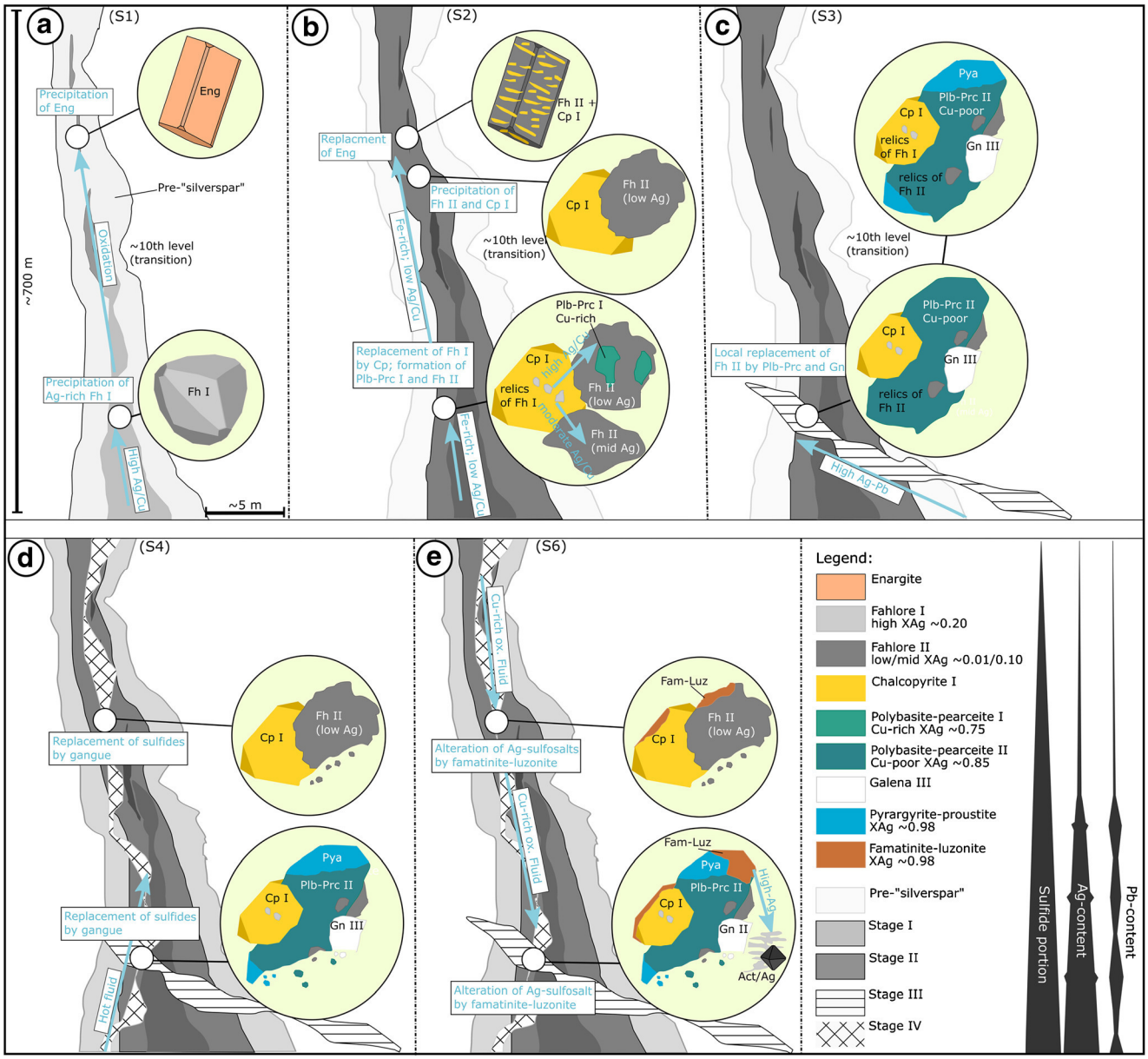

Fig. 8 Schematic illustration of the vein formation of the "silverspar" showing the different paragenetic stages S1 **(a)**; S2 **(b)**; S3 **(c)**; S4 **(d)**; S6 **(e)** over a depth profile of 700 m (note that S4 is not pictured). Labeled, blue arrows mark fluids involved in the formation of the different stages. Black bars beside the legend show the schematic sulfide portion, Ag-contents, and Pb-contents of the "silverspar" over depth. For further explanation of the paragenetic stages, see text

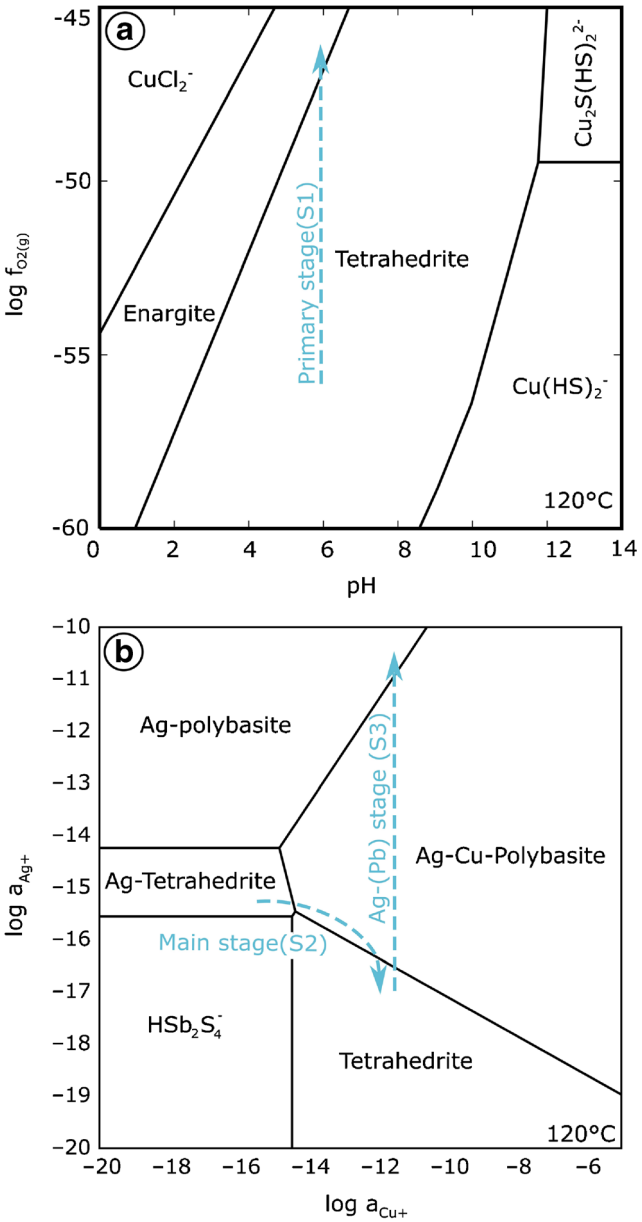

Fig. 9 **a** log $f_{O2(g)}$-pH dependent predominance diagram of enargite (Cu_3AsS_4) and tetrahedrite ($Cu_{12}Fe_2Sb_4S_{13}$) and aqueous species. Blue arrow shows qualitative fluid evolution during paragenetic stage S1. As input parameters, following values were used: $T = 120$ °C; $P = 300$ bar (Note: pressure only used for calculation of water stability); log $a_{Cu2+} = 10^{-5}$; log $f_{S2} = 10^{-17}$; log $a_{Fe2+} = 10^{-4}$; log $a_{Sb(OH)3} = 10^{-4}$; log $a_{H2AsO4-} = 10^{-6}$; log $a_{Cl-} = 10^{-1}$. **b** log $f_{(O2)}$-pH dependent predominance diagram of Ag-polybasite ($Ag_{16}Sb_2S_{11}$), Ag-tetrahedrite ($Ag_{12}Fe_2Sb_4S_{13}$), Ag-Cu-polybasite ($Ag_8Cu_8Sb_2S_{11}$), tetrahedrite ($Cu_{12}Fe_2Sb_4S_{13}$), and aqueous species. Blue arrow shows qualitative fluid evolution during paragenetic stage S2 and S3. As input parameters, following values were used: pH = 6; log $f_{O2(g)} = -55$; $T = 120$ °C; $P = 300$ bar (Note: pressure only used for calculation of water stability); log $f_{S2} = 10^{-17}$; log $a_{Fe2+} = 10^{-4}$; log $a_{Sb(OH)3} = 10^{-4}$; log $a_{H2AsO4-} = 10^{-6}$; log $a_{Cl-} = 10^{-1}$

"silverspar" were studied. FI-assemblages contain primary (p), pseudosecondary (ps) and isolated (iso) inclusions (For exemplary FI petrography see Fig. 1 in ESM). Primary FI are situated on growth zones of the host minerals and typically show angular shapes and are of small size (< 20 μm in diameter). Pseudosecondary inclusions were recognized on sealed cracks strictly bordered by the grain boundaries of a host mineral generation; they typically have rounded shapes and are larger in size (up to 70 μm in diameter) than the primary FI. Numerous secondary mono-phase aqueous inclusions were recognized in all gangue minerals. These were not investigated as part of this study.

Both primary and pseudosecondary FI show high-salinity aqueous fluids (Fig. 7), which freeze between − 70 and − 100 °C. First melting can be detected above − 50 °C implying a ternary NaCl-$CaCl_2$-H_2O system with a eutectic temperature of − 52.0 °C. Ice and hydrohalite are last-dissolving phases (for data plotted in the ternary NaCl-$CaCl_2$-H_2O diagram see Fig. 2 in ESM). The final melting temperature of ice is in the range of − 15.9 °C to − 33.0 °C, of hydrohalite between − 14.7 and − 41.0 °C, which records a salinity of 18.7 to 26.7 wt% (NaCl+$CaCl_2$). Uncorrected homogenization temperatures vary from 70 to 250 °C. Calculated Ca/(Ca + Na) molar ratios of the fluids vary between 0.21 and 0.82. Within single FIAs (independent of their fluid petrographic position), salinity and T_h are almost constant, but they vary significantly between different trails within one sample. The degree of fill is constant at 0.95. As Fig. 7 shows, fluorite III and quartz III have lower salinities (18.7–20.9 wt% NaCl+$CaCl_2$) compared to FI in fluorite I/II and quartz I/II of the earlier stages (23.1–26.7 wt% NaCl+$CaCl_2$). Furthermore, the uncorrected homogenization temperatures of fluorite III are much higher (190–250 °C) than those of the earlier fluorite I/II and quartz I/II (70–160 °C) and also of quartz III (90–100 °C).

Discussion

Depth zonation of the "silverspar" and polyphase redistribution of silver within the vein

Fahlore I is the first silver-bearing sulfide in the LG of the Clara vein system. In the UG, it is very rare or missing and enargite occurs instead (Fig. 8a). The presence of As^{5+} in enargite compared to As^{3+} in fahlore indicates that an oxidation process during fluid ascent could be responsible for this mineralogical zoning. The calculated predominance fields (Fig. 9) support this assumption as they show that oxidation (e.g., at neutral pH) stabilizes enargite instead of tetrahedrite (see also Eq. 1 in Table 3). Since enargite does not incorporate silver in relevant amounts, the oxidation is believed to be the reason for the large scale silver zoning during the initial stage. A gradual silver

Table 3 Equations 1–4 used in the text

Equation 1

$Cu_7Ag_3(Fe,Zn)As_4S_{13} + 3H_2S + 5Cu^+ + 2H^+ + 2O_2 = 4Cu_3AsS_4 + Fe^{2+} + Zn^{2+} + 3Ag^+ + 4H_2O$

fahlore I + fluid phase 1 = enargite + fluid phase 2

Equation 2

$23Cu_7Ag_3(Fe, Zn)(As_1Sb_3)S_{13} + 148Cu^+ + 43As(OH)_3 + 37Fe^{2+} + 7Zn^{2+} + 184H_2S + 7.5O_2 = 30Cu_9Ag_1(Fe, Zn)(As_2Sb_2)S_{13} + 3Ag_{13}Cu_3As_2S_{11} + 30CuFeS_2 + 9Sb(OH)_3 + 117H_2O + 236H^+$

fahlore I + fluid phase 1 = fahlore II + polybasite-pearceite I + chalcopyrite I + fluid phase 2

Equation 3

$4Cu_3AsS_4 + H_2S + 3H_2O + 3Fe^{2+} + Zn^{2+} = 2CuFeS_2 + Cu_{10}(Fe_1Zn_1)As_4S_{13} + 1.5O_2 + 8H^+$

enargite + fluid phase 1 = chalcopyrite I + fahlore II + fluid phase 2

Equation 4

$Ag_{16}As_2S_{11} + 6Cu^+ + O_2 + 10H^+ = 2Cu_3AsS_4 + 16Ag^+ + 2H_2O + 3H_2S$

pearceite + fluid phase 1 = luzonite + fluid phase 2

depletion in an ascending fluid system seems to be unlikely, since there is no systematic decrease in silver contents of fahlore I.

The oxidation is probably due to the increasing portion of a more oxidized (meteoric) fluid from a sedimentary fluid aquifer during fluid mixing in the vicinity of the basement/cover unconformity, which is situated at about 800 m amsl. The shift in mineral stability seems to be more or less abrupt, since enargite and fahlore I do not occur in the same samples. However, higher sulfur fugacities also favor the presence of enargite instead of fahlore (Einaudi et al. 2003). Sulfur may be derived from the sediment-hosted fluid aquifer (Walter et al. 2017a, 2018, and references therein), again supporting the occurrence of enargite at shallower depth of the Clara vein system.

Sulfides of S2 are ubiquitous in both the UG and LG samples. In terms of quantity, they represent the main sulfide mineralization of the "silverspar." Interestingly, the proportion of massive to low-volume banded sulfides clearly increases with depth, which would fit with the idea of an ascending fluid system precipitating sulfides and therefore depleting the system in metal(oids) on ascent. Alternatively, changes in the mixing process responsible for mineral precipitation (e.g., due to involvement of different aquifers or different proportions of the respective end members) may be invoked to explain this zonation in the amount of sulfides. In addition to the different amounts present in the "silverspar", fahlore II shows a chemical division between the UG and the LG with regards to its silver content (Fig. 6b). This is most likely caused by the pre-enrichment of silver in the LG by fahlore I (Fig. 8b), which is replaced by chalcopyrite I, polybasite-pearceite I, and fahlore II with moderate Ag-contents (see Eq. 2 in Table 3; comprising the stoichiometry of the analyzed sulfides). In the UG, where fahlore I is missing, a silver-poor association of chalcopyrite I and silver-poor fahlore II occurs.

The equation shows that the fluid leading to the replacement of fahlore I in the LG had to introduce Cu, Zn, Fe, As, and S, under the assumption that silver behaves conservatively. High Cu activity during the replacement process is also reflected by the high Cu contents in polybasite-pearceite I (Fig. 6d). We suggest a similar fluid with high Zn, Fe, and S-activity for the replacement of enargite by chalcopyrite I and silver-poor fahlore II in the UG (Eq. 3 in Table 3; Fig. 8b)

In the LG, Cu-rich polybasite-pearceite I is typically overgrown by fahlore II with low to moderate Ag-contents. This texture is interpreted to reflect the evolution of a fluid with high Ag activity (by the dissolution of fahlore I) to a fluid with lower Ag activity due to the precipitation of polybasite-pearceite I. This interpretation is supported by the calculated predominance fields (Fig. 9b) as they show that during increasing Cu activity (see arrow) Ag-rich fahlore is not stable anymore and Cu-rich polybasite will form instead. Due to polybasite precipitation, the system will develop towards lower Ag-activity ending up with Ag-poor fahlore. Note that in some LG samples, polybasite-pearceite I is missing and fahlore II shows relatively high Ag contents. This observation probably records too high Cu activity to stabilize polybasite-pearceite.

During S3, the local replacement of Cu-rich polybasite I and fahlore II by Cu-poor polybasite II and Ag-rich galena III (rarely accompanied by jordanite, stephanite, diaphorite, and geocronite) records the presence of a fluid with high Ag and Pb activity (Fig. 8c). The subordinate appearance of galena during S1 and S2 makes a redistribution of earlier (Pb)-sulfides unlikely and renders an influx of a new metal-bearing fluid more probable. The subsequent replacement of polybasite-pearceite II and I by pyrargyrite-proustite (which have the lowest Cu contents of all observed phases) again supports a significant increase of the fluid Ag activity during this stage. The calculated predominance diagram of Fig. 9b

shows that due to increasing Ag-activity (see arrow) Cu-rich polybasite and fahlore are not stable anymore and Ag-rich polybasite will form instead. The replacement of primary fahlore by polybasite-pearceite and pyrargyrite-proustite was also observed e.g., by Petrova and Ilieev (2007) in a Ag-Pb deposit in Bulgaria.

During S4, the earlier formed sulfides are partially dissolved and replaced by gangue minerals and no new sulfides form; silver is locally depleted during this process (Fig. 8d; see discussion below). Note that during paragenetic stage S5, the minerals of S1-S4 show no modification in terms of Ag- redistribution. Lastly, during S6, the Ag-sulfosalts underwent alteration to famatinite-luzonite (Fig. 8e). Equation 4 (Table 3) shows that this process requires the influx of relatively oxidized, Cu-rich fluids, which are probably related to the increasing influence of oxidized near-surface, possibly meteoric fluids.

Such fluids percolating in the uppermost parts of the vein system may be enriched in copper due to reaction with chalcopyrite or fahlore. Since famatinite-luzonite incorporates only minor amounts of silver, the released Ag re-precipitates as distinct silver minerals (native silver, acanthite) in the vicinity (see also Keim et al. 2016).

The source of silver for the Schwarzwald deposits are probably biotite and plagioclases since they carry up to 0.3 ppm and 0.5 ppm Ag respectively (Kortenbruck 2014). If these minerals become altered by fluids in the root zone of the hydrothermal vein systems, this Ag is probably mobilized.

Dissolution of sulfides

In paragenetic stage S4, fluids precipitate fluorite III and quartz III and dissolve existing sulfides of stages S2 and S3 (see Figs. 5k and 8d). Primary and pseudosecondary FI in these fluorite III and quartz III crystals show salinities of 18.7–20.9 wt% NaCl+$CaCl_2$ and uncorrected homogenization temperatures of 180–250 °C, which are significantly different from the fluids responsible for the formation of the sulfides of S1 and S2 (~ 23.1–26.7 wt% NaCl+$CaCl_2$ and 70–160 °C see above).

Walter et al. (2016, 2017a, and references therein) suggested the formation of the Jurassic-Cretaceous vein system in the Schwarzwald by mixing of relatively hot basement fluids (300–350 °C; Schwinn et al. 2006) with salinities around 21 wt% NaCl+$CaCl_2$ with a cooler sedimentary cover-related fluid aquifer with salinities up to 28 wt% NaCl+$CaCl_2$. This mixing process results in a typical temperature range of 60–180 °C (depending on the mixing ratio) and salinities between 23 and 26 wt% NaCl+$CaCl_2$. This corresponds well to FI-analyses from the literature for the Clara fluorite vein on quartz and fluorite (Staude et al. 2010a; Pfaff et al. 2012) and in the gangue minerals related to the main sulfide precipitation in paragenetic stage S1 and S2 reveal homogenization temperatures between 70 °C and 160 °C and salinities between 23.1 and 26.7 wt% NaCl+$CaCl_2$.

In contrast, the FI in fluorite III and quartz III (Fig. 7) show the lowest salinities (18.7–20.9 wt% NaCl+$CaCl_2$ wt%) and the highest temperatures (up to 250 °C) reported for any Jurassic-Cretaceous vein in the Schwarzwald so far (50–180 °C, 20–28 wt% NaCl+$CaCl_2$ (Walter et al. 2016)). A tentative explanation would involve a higher than usual proportion or even a pure basement brine with moderate salinity, which would not be in equilibrium with the sulfides (as shown by their dissolution).

The temperature decrease from reservoir temperatures (300–350 °C, Schwinn et al. 2006) to fluorite III (around 210 °C) to quartz III (around 90 °C) would reflect ascent and cooling of such a basement brine, which would explain the amount of observed quartz (e.g., Burisch et al. 2017b). Only small amounts of galena and matildite precipitated during this stage, indicating that most metals remained in the hot fluid. These metals may have been re-precipitated in parts of the vein system that were not sampled during this study.

Influence of the quartz main stage on the "silverspar"

During the paragenetic stages S3 and S5, a Pb-Ag-Bi-As-rich mineral assemblage overprints the "silverspar" locally; this assemblage is quartz-rich and crosscuts the mineralization stages of S1 and S2. The abundance of quartz suggests that this overprint could be related to the quartz main stage ("Diagonaltrum"; Fig. 1), the formation of which is associated to the NKF (Huck 1984). Other NKF-related deposits show similar mineral assemblages of Pb-Ag-Bi-(As) sulfosalts (Staude et al. 2010a) comprised of benjaminite, berryite, galena, gustavite, and matildite together with other Ag-Bi-Pb-Cu minerals. Several of these minerals (galena, matildite, emplektite, and berryite) have also been observed in S3 and S5 of the "silverspar". Huck (1984) and Van der Heyde (2002) described chalcopyrite, fahlore, pyrite, and polybasite-pearceite as typical sulfides associated with the quartz main stage. Based on these mineralogical similarities of the quartz main stage with S3 and S5, the "silverspar" appears to have been locally overprinted by fluids from the quartz main stage. The local influence of these fluids lead to the spatially limited enrichment of Ag-Pb (S3) and As-(Bi) (S5), compared to the primary and the main stage (S1, S2). The enrichment especially of Bi in NKF-related mineral assemblages remains poorly understood (see also Staude et al. 2010a).

Formation of the banded barite-fluorite-sulfide texture

A striking feature of the "silverspar" is the alternating sequence of early euhedral-subhedral barite with little or no sulfides and interstitial fluorite with much larger amounts of sulfides (Fig. 3a). Barite forms during the mixing of a hot, Ba-bearing, sulfur-poor basement fluid with the sulfate-bearing

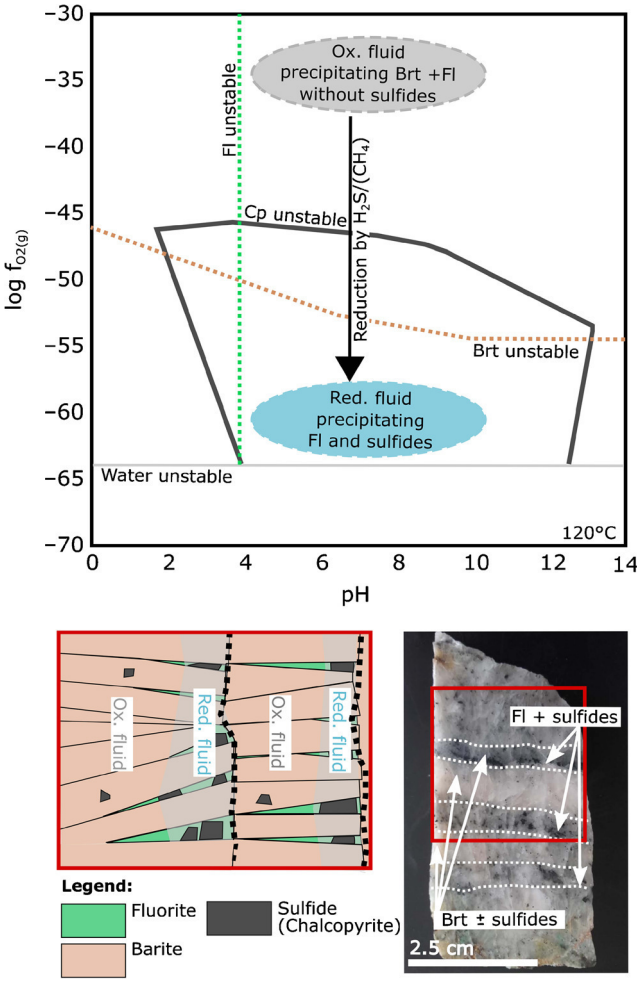

Fig. 10 **a** pH-$f_{O2(g)}$ dependent predominance diagram of fluorite, barite, and chalcopyrite. Solid dark-gray line marks the limits of chalcopyrite stability, green dashed line of fluorite stability, and brown dashed line of barite stability. Black arrow symbolizes repeated reduction of an oxidized system by the influx of a reducing agent. Gray area marks oxidized, blue area a reduced fluid system. Input parameters are based on Burisch et al. (2017a) ($T = 120$ °C; $P = 300$ bar (Note: pressure only used for calculation of water stability); log $a_{H4SiO4} = -3$; log $a_{Cu2+} = -5$; log $a_{Cl-} = -1$; log $a_{SO42-} = -3$; log $a_{Ca2+} = -2$; log $a_{Ba2+} = -2$; log $a_{Fe2+} = -5$). All elements were speciated over pH and f_{O2}. **b** Illustration of the alternating sequence including the pulsed reduction. Ox. = oxidation; Red. = reduction. **c** Photograph of the banded "silverspar"

sediment-related fluid aquifer (dissolution of evaporites like gypsum; Walter et al. 2018). This mixing process also leads to the precipitation of fluorite. In contrast to calcium, which is present in both fluids (carbonate dissolution, plagioclase alteration), fluorine is present in the basement fluid aquifer only (Bucher and Stober 2010; Burisch et al. 2016a; Walter et al. 2018). For the precipitation of the sulfides, an additional reducing agent like methane and/or H_2S is needed (Markl et al. 2016; Burisch et al. 2017a; Walter et al. 2018).

The calculated predominance field diagram (Fig. 10) reveals that a relatively oxidized fluid system first precipitates barite and fluorite without sulfides. If chalcopyrite is chosen as a representative sulfide, the diagrams indicate that chalcopyrite stability is reached at an exemplary pH of 7 around a log f_{O2} of −45. At these conditions, barite + fluorite + chalcopyrite can precipitate. If reduction continues, barite is not stable anymore (at pH = 7 at log f_{O2} of −52) and fluorite plus chalcopyrite precipitate instead. Thus, the rare association of barite with sulfides and the common association of fluorite with sulfides can be explained by a fast reduction process during the influx of a reducing fluid (see e.g., Markl et al. 2016). For the multiple changes from barite to fluorite plus sulfides (in some parts of the "silverspar" more than 100 times, c. f. Fig. 3a), we suggest the following scenario: An ascending basement fluid first forms barite and fluorite without sulfides by fluid mixing with a sediment-related fluid. Due to the influx of a reducing fluid, barite becomes unstable and the association of fluorite + sulfides precipitates instead. A likely source of such a reduced fluid is the interaction of a fluid in with the (in parts) pyrite- and graphite-bearing host rocks. Calculations from Pfaff et al. (2012) support this assumption, since calculated oxygen fugacities for a fluid in equilibrium with the Clara Mine host rock gneisses are low (log $f_{O2} \leq -75.9$). Methane as redox agent seems unlikely since no carbonates precipitated during the formation of the "silverspar", which would be the case, if methane would be oxidized to CO_2/HCO_3^- in a Ca-rich fluid system (see e.g., Burisch et al. 2017a). The recurrent banding of the "silverspar" may, therefore, be caused by the pulsed influx of a reducing fluid in a relatively oxidized system precipitating fluorite and barite.

Conclusions

The Cu-Ag mineralization hosted by the Clara vein system in the Central Schwarzwald, South Germany, shows a pronounced mineralogical and chemical zoning. During the first paragenetic stage (S1), an ascending fluid system with relatively high Ag/Cu ratios lead to a Ag-rich mineralization in the lower parts (below 450 m amsl) comprising fahlore I with up to freibergitic composition. This fluid became increasingly oxidized towards shallower depth of the vein and enargite became stable instead of fahlore. The typical, meter-thick alternating sequences of sulfide-free barite and sulfide-bearing fluorite reflect a recurrent influx of a reducing agent in a fluid system precipitating barite and fluorite.

The vertical zonation imprinted by the first hydrothermal stage was overprinted by a second hydrothermal stage (S2) that involved fluids with high Cu and Fe activity, leading to precipitation of chalcopyrite I, fahlore II with intermediate Ag contents and Ag sulfosalts in the lower parts of the vein, and fahlore with low Ag contents and no discrete Ag sulfosalts in the upper parts. Fluid inclusion temperatures reveal that the primary silver

mineralization (S1) and the following main sulfide stage (S2) formed at temperatures between 70 and 160 °C and from fluids with high salinities, as they are typical of the Jurassic-Cretaceous veins in the Schwarzwald. The local overprint by Ag-Pb and/or As-Bi fluids (S3, S5) is likely to be connected to Ag-Bi-Pb mineralization related to the large-scale North Kinzigtal fault system (NKF). A further hydrothermal stage (S4) is related to the influx of a hot (190–250 °C) undiluted basement fluid; this is expressed by paragenetically late fluorite + quartz mineralization and partial dissolution and replacement of pre-existing sulfides. Lastly, the Ag-sulfosalts underwent alteration by a Cu-rich, more oxidized fluid (S6), which released Ag and re-precipitated it as native metal or acanthite in the vicinity. This may be related to the exhumation of the vein system during the Paleogene (see also Burisch et al. 2018).

Despite profound mineralogical changes, large-scale silver zonation of the first stage (S1) appears to have been preserved through successive hydrothermal overprints of the vein system at the Clara Mine (S2-S6). Based on these findings, a similar enrichment of silver towards deeper parts of other hydrothermal veins of the Central and Northern Schwarzwald may be expected, where similar vein systems of similar age and architecture have been less deeply eroded and mined. More generally speaking, the study illustrates, how metal tenor and mineralogy may remain decoupled in vertically extensive, polyphase hydrothermal vein systems. This may be pertinent to similarly zoned hydrothermal vein systems elsewhere.

Acknowledgments We are grateful to T. Wenzel and T. Theye for their friendly assistance during EMP analysis, S. Staude, U. Kolitsch, and K. Huck for their helpful input during discussions and interpretation of the results, and S. Schafflick for the professional sample preparation. This work is a contribution of the r^4 project "ResErVar—Ressourcenpotential hydrothermaler Lagerstätten der Varisziden" funded by the German Ministry of Education and Research (BMBF; Project reference number 033R129E).

References

Altherr R, Holl A, Hegner E, Langer C, Kreuzer H (2000) High-potassium, calc-alkaline I-type plutonism in the European Variscides: northern Vosges (France) and northern Schwarzwald (Germany). Lithos 50:51–73. https://doi.org/10.1016/S0024-4937(99)00052-3

Armstrong JT (1991) Quantitative elemental analysis of individual micro particles with electron beam instruments; Electron probe quantitation. Springer, New York

Bakker RJ, Diamond LW (2006) Estimation of volume fractions of liquid and vapor phases in fluid inclusions, and definition of inclusion shapes. Am Mineral 91:635–657. https://doi.org/10.2138/am.2006.1845

Baumgärtl U, Burow J (2002) Grube Clara. Der Aufschluss 54:274–403

Behr HJ, Gerler J (1987) Inclusions of sedimentary brines in post-Variscan mineralizations in the Federal Republic of Germany—a study by neutron activation analysis. Chem Geol 61:65–77. https://doi.org/10.1016/0009-2541(87)90028-3

Behr HJ, Horn EE, Frentzel-Beyme K, Reutel C (1987) Fluid inclusion characteristics of the Variscan and post-Variscan mineralizing fluids in the Federal Republic of Germany. Chem Geol 61:273–285. https://doi.org/10.1016/0009-2541(87)90046-5

Bernard JH, Hyrsl J (2006) Minerals and their localities. Granit Publishing House, Praha

Bethke CM, Yeakel S (2015) GWB Essentials Guide: Aqueous Solutions. LLC Champaign, Illinois

Bindi L, Evain M, Spry PG, Menchetti S (2007a) The pearceite-polybasite group of minerals: crystal chemistry and new nomenclature rules. Am Mineral 92:918–925. https://doi.org/10.2138/am.2007.2440

Bindi L, Evain M, Spry PG, Tait KT, Menchetti S (2007b) Structural role of copper in the minerals of the pearceite-polybasite group: the case of the new minerals cupropearceite and cupropolybasite. Mineral Mag 71:641–650. https://doi.org/10.1180/minmag.2007.071.6.641

Blanc P, Lassin A, Piantone P, Azaroual M, Jacquemet N, Fabbri A, Gaucher EC (2012) Thermoddem: a geochemical database focused on low temperature water/rock interactions and waste materials. Appl Geochem 27:2107–2116. https://doi.org/10.1016/j.apgeochem.2012.06.002

Bliedtner M, Martin M (1986) Erz- und Minerallagerstätten des Mittleren Schwarzwaldes. LGRB, Freiburg

Bodnar RJ, Vityk MO (1994) Interpretation of microthermometric data for H2O-NaCl fluid inclusions. In: DeVivo B, Frezzotti ML (eds) Fluid inclusions in minerals: methods and applications. Short course IMA. Virginia Polytechnic Institute, Siena, pp 117–130

Bons PD, Fusswinkel T, Gomez-Rivas E, Markl G, Wagner T, Walter B (2014) Fluid mixing from below in unconformity-related hydrothermal ore deposits. Geology 42:1035–1038. https://doi.org/10.1130/G35708.1

Bucher K, Stober I (2010) Fluids in the upper continental crust. Geofluids 10:241–253. https://doi.org/10.1111/j.1468-8123.2010.00279.x

Bucher K, Zhu Y, Stober I (2009) Groundwater in fractured crystalline rocks, the Clara Mine, Black Forest (Germany). Int J Earth Sci 98:1727–1739. https://doi.org/10.1007/s00531-008-0328-x

Burisch M, Marks MA, Nowak M, Markl G (2016a) The effect of temperature and cataclastic deformation on the composition of upper crustal fluids—an experimental approach. Chem Geol 433:24–35. https://doi.org/10.1016/j.chemgeo.2016.03.031

Burisch M, Walter BF, Wälle M, Markl G (2016b) Tracing fluid migration pathways in the root zone below unconformity-related hydrothermal veins: insights from trace element systematics of individual fluid inclusions. Chem Geol 429:44–50. https://doi.org/10.1016/j.chemgeo.2016.03.004

Burisch M, Gerdes A, Walter BF, Neumann U, Fettel M, Markl G (2017a) Methane and the origin of five-element veins: mineralogy, age, fluid inclusion chemistry and ore forming processes in the Odenwald, SW Germany. Ore Geol Rev 81:42–61. https://doi.org/10.1016/j.oregeorev.2016.10.033

Burisch M, Walter BF, Markl G (2017b) Silification of hydrothermal gangue minerals in Pb-Zn-Cu-fluorite-quartz-barite veins. Can Mineral 55:501–514. https://doi.org/10.3749/canmin.1700005

Burisch M, Walter BF, Gerdes A, Lanz M, Markl G (2018) Late-stage anhydrite-gypsum-siderite-dolomite-calcite assemblages record the transition from a deep to a shallow hydrothermal system in the Schwarzwald mining district, SW Germany. Geochim Cosmochim Acta 223:259–278. https://doi.org/10.1016/j.gca.2017.12.002

Einaudi MT, Hedenquist JW, Inan EE (2003) Sulfidation state of fluids in active and extinct hydrothermal systems: transitions from porphyry to epithermal environments. Spec Publ-Soc Econ Geol 10:285–314

Elsner H, Schmitz M (2017) Rohstoffgewinnung in Deutschland. GMIT 68:7–20

Fusswinkel T, Wagner T, Wälle M, Wenzel T, Heinrich CA, Markl G (2013) Fluid mixing forms basement-hosted Pb-Zn deposits: insight from metal and halogen geochemistry of individual fluid inclusions. Geology 41:679–682. https://doi.org/10.1130/G34092.1

Geyer OF, Gwinner MP (2011) Geologie von Baden-Württemberg. Schweizerbart'sche Verlagsbuchhandlung, Stuttgart

Goldenberg G, Steuer H (2004) Mittelalterlicher Silberbergbau im Südschwarzwald. In: Silber Kupfer Kobalt - Bergbau im Schwarzwald. Markstein Verlag, Filderstadt

Goldstein RH, Reynolds TJ (1994) Systematics of fluid inclusionsin diagenetic minerals. SEPM Short Course Notes 31:1–199

Hackbarth CJ, Petersen U (1984) A fractional crystallization model for the deposition of argentian tetrahedrite. Econ Geol 79:448–460. https://doi.org/10.2113/gsecongeo.79.3.448

Hann HP, Chen F, Zedler H, Frisch W, Loeschke J (2003) The rand granite in the southern Schwarzwald and its geodynamic significance in the Variscan belt of SW Germany. Int J Earth Sci 92:821–842

Heyde R (2002) Paragenetische und aufbereitungstechnische Untersuchungen silberhaltiger Erze der Baryt-Flussspatgrube "Clara", Wolfach, Deutschland. Hallesches Jahrbuch für Geowissenschaften 15:65–121

Huck K (1984) Beziehungen zwischen Tektonik und Paragenese unter Berücksichtigung geochemischer Kriterien in der Fluß- und Schwerspatlagerstätte "Clara" bei Oberwolfach/Schwarzwald. Dissertation, University of Heidelberg

Johnson NE, Craig JR, Rimstidt JD (1986) Compositional trends in tetrahedrite. Can Mineral 24:385–397

Kaiser H (1984) Die Grube Clara zu Wolfach im Schwarzwald, ein Handbuch für Sammler und Liebhaber schöner Mineralien. Karl Schillinger, Freiburg

Kalt A, Grauert B, Baumann A (1994) Rb-Sr and U-Pb isotopestudies on migmatites from the Schwarzwald (Germany): constraints on isotopic resetting during Variscan high-temperature metamorphism. J Metamorph Geol 12:667–680. https://doi.org/10.1111/j.1525-1314.1994.tb00050.x

Kalt A, Altherr R, Hanel M (2000) The Variscan basement of the Schwarzwald. Eur J Mineral 12:1–43. https://doi.org/10.1127/0935-1221/2009/0021-1944

Keim MF, Vaudrin R, Markl G (2016) Redistribution of silver during supergene oxidation of argentiferous galena: a case study from the Schwarzwald, SW Germany. Neues JB Miner Abh 193:295–309

Keim MF, Gassmann B, Markl G (2017) Formation of basic lead phases during fire-setting and other natural and man-made processes. Am Mineral 102:1482–1500. https://doi.org/10.2138/am-2017-5931

Kemkin IV, Kemkina RA (2013) Microheterogeneity of the Koupol deposit fahlores as a reflection of changing of physicochemical parameters of the ore-forming solution. J Earth Sci 24:179–187

Kloos M (1990) Petrographie der Metamorphite und Ganggesteine aus dem Niveau der 13. Sohle der Grube Clara/Mittlerer Schwarzwald. Diploma Thesis, University of Heidelberg

Kolitsch U, Gröbner J, Bayerl R (1995) Die Mineralien der Silber-Antimon-Vererzungen der Grube Clara im Zeitraum 1993 bis 1995. Erzgräber 9:61–81

Kortenbruck P (2014) Spurenelementgehalte in Mineralen aus Graniten und Gneisen und deren Änderung bei der Alteration. Bachelor Thesis, University of Tuebingen

List KA (1969) Die Mineralisation auf den tieferen Sohlen der "Grube Clara". Diploma Thesis, University of Freiburg

Markl G (2015) Schwarzwald, Lagerstätten und Mineralien aus vier Jahrhunderten; Band 1 Nordschwarzwald & Grube Clara. Bode, Lauenstein

Markl G, Burisch M, Neumann U (2016) Natural fracking and the genesis of five-element veins. Mineral Deposita 51:703–712. https://doi.org/10.1007/s00126-016-0662-z

Maus HJ, Gundlach H, Podufal P (1979) Über den Sellait (MgF2) der Grube Clara, Oberwolfach, Mittler Schwarzwald. Neues Jb Mineral Abh 136:10–25

Mertz DF (1987) Isotopengeochemische und mineralogische Untersuchungen an postvariszischen hydrothermalen Silikaten. Dissertation, University of Heidelberg

Metz R, Richter M, Schürrenberg H (1957) Die Blei-Zink Erzgänge des Schwarzwaldes. Geol Jb Beihefte 29:1–277

Nitsch E, Rupf I (2008) Palaogeographie und Tektonik in Baden-Wuerttemberg seit dem Perm: Erste Ergebnisse aus dem Digitalen Geologischen Landesmodell des LGRB. Geotectonic Res 95:122–124

Okujeni CD (1980) Geochemische Untersuchungen an den Gesteinen der Fluorit/Barytgrube Wolfach im Schwarzwald

Palandri J, Reed M (2017) SOLTHERM.XPT, a database of equilibrium constants for minerals, gases, and aqueous species. URL: http://pages.uoregon.edu/palandri/. Accessed 06.09.2017

Petrova M, Ilieev T (2007) Compositional variations in the tetrahedrite-tennantite fahlores and polybasite-pearceite series from the Chiprovtsi Ag-Pb deposit, northwestern Bulgaria. Au-Ag tellurideselenide deposits, Field Workshop Espoo. Finland 26:39–43

Pfaff K, Romer RL, Markl G (2009) U-Pb ages of ferberite, chalcedony, agate, "U-mica" and pitchblende: constraints on the mineralization history of the Schwarzwald ore district. Eur J Mineral 21:817–836. https://doi.org/10.1127/0935-1221/2009/0021-1944

Pfaff K, Hildebrandt LH, Leach DL, Jacob DE, Markl G (2010) Formation of the Wiesloch Mississippi Valley-type Zn-Pb-ag deposit in the extensional setting of the upper Rhinegraben, SW Germany. Mineral Deposita 45:647–666. https://doi.org/10.1007/s00126-010-0296-5

Pfaff K, Staude S, Markl G (2012) On the origin of sellaite (MgF2)-rich deposits in Mg-poor environments. Am Mineral 97:1987–1997. https://doi.org/10.2138/am.2012.4113

Rehren T (1985) Untersuchungen zur Mineralogie und Aufbereitbarkeit verschiedener Erzproben der Grube Clara. University of Clausthal, Diploma Thesis

Riley JF (1974) The tetrahedrite-freibergite series, with reference to the Mount Isa Pb-Zn-ag orebody. Mineral Deposita 9:117–124

Sack RO (2000) Internally consistent database for sulfides and sulfosalts in the system Ag2S–Cu2S–ZnS–Sb2S3–As2S3. Geochim Cosmochim Acta 64:3803–3812. https://doi.org/10.1016/j.gca.2004.08.017

Sack RO (2017) Fahlore thermochemistry: gaps inside the (Cu,Ag)10(Fe,Zn)2(As,Sb)4S13 Cube. Petrology 25:498–515. https://doi.org/10.1134/S0869591117050071

Schmeltzer H (1983) Eine Polybasitvererzung von der Grube Clara. Lapis 8:37–40

Schwinn G, Wagner T, Baatartsogt B, Markl G (2006) Quantification of mixing processes in ore-forming hydrothermal systems by combination of s-isotope and fluid inclusion analyses. Geochim Cosmochim Acta 70:965–982. https://doi.org/10.1016/j.gca.2005.10.022

Shepherd TJ, Rankin AH, Alderton DHM (1985) A practical guide to fluid inclusion studies. Blackie Academic & Professional, Glasgow

Staude S, Bons PD, Markl G (2009) Hydrothermal vein formation by extension-driven dewatering of the middle crust: an example from

SW Germany. Earth Planet Sci Lett 286:387–395. https://doi.org/10.1016/j.epsl.2009.07.012

Staude S, Dorn A, Pfaff K, Markl G (2010a) Assemblages of Ag–Bi sulfosalts and conditions of their formation: the type locality of schapbachite (Ag0. 4Pb0. 2Bi0. 4S) and neighboring mines in the Schwarzwald ore district, southern Germany. Can Mineral 48:441–466. https://doi.org/10.3749/canmin.48.3.441

Staude S, Mordhorst T, Neumann R, Prebeck W, Markl G (2010b) Compositional variation of the tennantite–tetrahedrite solidsolution series in the Schwarzwald ore district (SW Germany): the role of mineralization processes and fluid source. Mineral Mag 74:309–339. https://doi.org/10.1180/minmag.2010.074.2.309

Staude S, Göb S, Pfaff K, Ströbele F, Premo WR, Markl G (2011) Deciphering fluid sources of hydrothermal systems: a combined Sr-and S-isotope study on barite (Schwarzwald, SW Germany). ChemGeol 286:1–20. https://doi.org/10.1016/j.chemgeo.2011.04.009

Staude S, Mordhorst T, Nau S, Pfaff K, Brügmann G, Jacob DE, Markl G (2012a) Hydrothermal carbonates of the Schwarzwald ore district, southwestern Germany: carbon source and conditions of formation using δ18O, δ13C, 87Sr/86Sr, and fluid inclusions. Can Mineral 50:1401–1434. https://doi.org/10.3749/canmin.50.5.1401

Staude S, Werner W, Mordhorst T, Wemmer K, Jacob DE, Markl G (2012b) Multi-stage Ag–Bi–Co–Ni–U and Cu–Bi vein mineralization at Wittichen, Schwarzwald, SW Germany: geological setting, ore mineralogy, and fluid evolution. Mineral Deposita 47:251–276. https://doi.org/10.1007/s00126-011-0365-4

Steele-MacInnes M, Bodnar RJ, Naden J (2011) Numerical model to determine the composition of H2O-NaCl-CaCl2 fluid inclusions based on microthermometric and microanalytical data. Geochim Cosmochim Acta 75:21–40. https://doi.org/10.1016/j.gca.2010.10.002

Walenta K (1984) Sulfidische Erzmineralien aus der Grube Clara im mittleren Schwarzwald und ihre Paragenesen. Aufschluss 35:235–246

Walter BF, Immenhauser A, Geske A, Markl G (2015) Exploration of hydrothermal carbonate magnesium isotope signatures as tracers for continental fluid aquifers, Schwarzwald mining district, SW Germany. Chem Geol 400:87–105. https://doi.org/10.1016/j.chemgeo.2015.02.009

Walter BF, Burisch M, Markl G (2016) Long-term chemical evolution and modification of continental basement brines–a field study from the Schwarzwald, SW Germany. Geofluids 16:604–623. https://doi.org/10.1111/gfl.12167

Walter BF, Burisch M, Marks MA, Markl G (2017a) Major element compositions of fluid inclusions from hydrothermal vein-type deposits record eroded sedimentary units in the Schwarzwald district, SW Germany. Mineral Deposita 51:1–14. https://doi.org/10.1007/s00126-017-0719-7

Walter BF, Steele-MacInnis M, Markl G (2017b) Sulfate brines in fluid inclusions of hydrothermal veins: compositional determinations in the system H_2O-Na-Ca-Cl-SO_4. Geochim Cosmochim Acta 209:184–203. https://doi.org/10.1016/j.gca.2017.04.027

Walter BF, Burisch M, Fusswinkel T, Marks MAW, Steele-MacInnis M, Wälle M, Apukhtina OB, Markl G (2018) Multi-reservoir fluid mixing processes in rift-related hydrothermal veins, Schwarzwald, SW-Germany. Gexplo 186:158–186. https://doi.org/10.1016/j.gexplo.2017.12.004

Werner W, Dennert V (2004) Lagerstätten und Bergbau im Schwarzwald. LGRB, Freiburg

Zirngast M (1978) Zur Geologie und Geochemie der Schwerspatlagerstätte "Clara" bei Wolfach (Mittlerer Schwarzwald). Dissertation, University of Braunschweig

Anhang 2:

Keim, M.F., Vaudrin, R., Markl, G. (2016) Redistribution of silver during supergene oxidation of argentiferous galena: A case study from the Schwarzwald, SW Germany. Neues Jahrbuch für Mineralogie - Abhandlungen: Journal of Mineralogy and Geochemistry, **193**(3), 295-309.

Akzeptiert zur Veröffentlichung: Ja
DOI: 10.1127/njma/2016/0002
Anzahl der Autoren: 3
Position in der Autorenliste: 1

Eigenanteile:

Idee	30%
Datenbeschaffung	0%
Auswertung und Interpretation	50%
Ausarbeitung der Publikation	70%

Vaudrin R.:

Idee	10%
Datenbeschaffung	100%
Auswertung und Interpretation	30%
Ausarbeitung der Publikation	0%

Markl G.:

Idee	60%
Datenbeschaffung	0%
Auswertung und Interpretation	20%
Ausarbeitung der Publikation	30%

https://doi.org/10.1127/njma/2016/0002

Redistribution of silver during supergene oxidation of argentiferous galena: A case study from the Schwarzwald, SW Germany

Maximilian F. Keim[*1], Rafael Vaudrin[1], Gregor Markl[1]

[1]Mathematisch-Naturwissenschaftliche Fakultät, Fachbereich Geowissenschaften, Universität Tübingen, Wilhelmstraße 56, D-72074 Tübingen, Germany.

*corresponding author: maximilian-felix.keim@uni-tuebingen.de

Abstract

Argentiferous galena is unstable under surface conditions and secondary lead minerals form during its decomposition. This contribution investigates to which extent silver released from weathered hydrothermal galena is retained in the the supergene lead phases cerussite, anglesite, pyromorphite, and mimetite which are texturally related to the weathering process. Therefore, trace element analyses of galena and supergene lead phases from various supergene ore deposits of the Schwarzwald, SW-Germany, were performed by laser ablation-inductively coupled plasma-mass spectroscopy (LA-ICP-MS).

The analyzed galena contains between 32 and 18,000 ppm silver. The secondary lead minerals contain 124 ppm silver as a maximum (pyromorphite) and in every case they have less than 13% of the corresponding galena from the same hand specimen. Cerussite and anglesite are virtually silver-free. This leads to the conclusion that silver set free during weathering of argentiferous galena is likely to be removed as soluble ions/complexes or reprecipitated as distinct silver phases.

Thermodynamic modelling based on a closed system approach and modern-day conditions suggests that silver released by the weathering of argentiferous galena or other silver-bearing sulfides is likely to be reprecipitated as native silver due to redox processes or depletion of oxygen.

The formation of chlorargyrite is only possible in environments with elevated silver and chloride concentrations. Enrichment of silver during weathering is possible if galena has high silver contents or if other silver minerals serve as additional silver source. Enrichment of chloride is possible in geogenic microenvironments or due to anthropogenic input. The field observations agree with the thermodynamic calculations, since secondary native silver and acanthite are widespread and chlorargyrite is very rare to absent within the oxidized parts of the Schwarzwald ore deposits.

Keywords: silver; supergene; weathering; galena; stability relations; chlorargyrite; native silver; acanthite

Introduction

Galena [PbS] holds a special position in the economically interesting sources of silver as it occurs frequently and incorporates up to 9.8 wt.% silver, mainly by the coupled substitution $Ag^{+} + (Bi, Sb)^{3+} \leftrightarrow 2Pb^{2+}$ (Foord *et al.* 1988, Renock & Becker 2011). In addition, silver is

present in galena as sub-micron-scale inclusions of silver-bearing phases (George *et al*. 2015 and references therein). Argentiferous galena is the primary source of silver because of its abundance (e.g. Foord & Shawe 1989, Pohl, 2011) and easy smelting process (Butterman & Hilliard 2005, Brooks 2013).

Lead behaves immobile during weathering and normally forms stable secondary lead phases like cerussite [$PbCO_3$], anglesite [$PbSO_4$], pyromorphite [$Pb_5(PO_4)_3Cl$], and mimetite [$Pb_5(AsO_4)_3Cl$] (e.g. Morris *et al.* 1952, Guilbert & Park 1984, Keim & Markl 2015). Whether the silver contained in galena is removed as soluble ions/complexes, reprecipitated as distinct silver phases, accumulated in secondary lead phases or a combination of these possibilities, is hitherto unknown.

Despite the common occurrence of galena and secondary lead minerals, data on the silver contents of the secondary lead phases are rare to absent. Markl *et al.* (2014b) investigated minor and trace element contents of pyromorphite-mimetite solid solutions observing average silver contents of about 30 ppm with a maximum of 500 ppm. Mimetite shows significantly lower silver contents than pyromorphite. With regards to cerussite, Ramsy (1981) observes up to 30 ppm, Stavinga (2014) up to 2000 ppm silver. None of these studies systematically investigated silver contents of galena along with secondary lead minerals occurring in close spatial relation.

During weathering of silver-bearing sulfides like argentiferous galena, native silver [Ag] and acanthite [Ag_2S] are the typical mineral phases formed in oxidation zones of temperate climates (Guilbert & Park 1984) due to redox processes (e.g. Mann 1984). Chlorargyrite [AgCl] is the dominant secondary silver phase under arid and tropical climate (e.g. Boyle 1997). Minerals/phases like chlorargyrite are either formed naturally (e.g. Gołębiowska *et al.* 2010, Alfieris *et al.* 2013) or due to anthropogenic influence (Dill *et al.* 2013, Dill 2015).

Stability diagrams of the Ag-(Au)-Cl-S-CO_2-H_2O system show the stability relations of the most important secondary silver phases and complexes (e.g. Sangameshwar & Barnes, 1983 Krupp & Weiser 1992, Sato 1992, Saunders 1993, Levard *et al*. 2012). Chlorargyrite is stable under oxidizing conditions over the whole relevant pH-range. Native silver is stable under reduced and acanthite under even more reduced conditions.

This contribution presents a systematic study of silver contents in argentiferous galena and spatially associated secondary lead minerals from the same hand specimens which derive from various locations in the Schwarzwald. Furthermore, the redistribution of silver under present-day conditions is discussed using stability diagrams based on Schwarzwald mine water chemistry data from Göb *et al*. (2011), (2013a), (2013b) and Markl *et al*. (2014a). Since silver is a valuable metal it is important to understand redistribution processes within the supergene

parts of ore deposits. The thermodynamic considerations presented here improve our understanding of the sources and sinks of this noble metal during supergene processes.

Samples and geological background

The samples of this study come from the Schwarzwald in Southern Germany, a low mountain range of about 50 by 100 km size and part of the European Variscan basement (Fig. 1) (Geyer & Gwinner 2011). The basement is composed of crystalline rocks like gneisses, granites and migmatites (Kalt *et al*. 2000) and is discordantly overlain by Permian, Triassic and Jurassic sediments.

The basement and the Triassic/Jurassic sedimentary cover rocks host more than 1000 hydrothermal veins (Metz *et al*. 1957) mainly composed of fluorite, barite, quartz, and carbonates as gangue (Bliedtner & Martin 1986). Galena is the most widespread ore mineral in these veins (Metz *et al*. 1957) and occurs unevenly distributed all over the Schwarzwald (Markl *et al*. 2014b). The earliest evidence for mining these veins on silver-bearing galena dates back to the 2nd/3rd century in late Roman times (Metz *et al.* 1957, Kirchheimer 1976). Since the Miocene (Hautmann & Lippolt 2000), the hydrothermal veins have been weathered in their upper parts and various secondary supergene minerals formed (e.g. Walenta 1991, Göb *et al.* 2011, Göb *et al.* 2013a, Markl 2014a, b, Keim & Markl 2015).

For studying silver contents of galena and secondary lead phases, 34 samples containing galena and supergene lead phases from 15 locations in the Central and Southern Schwarzwald were chosen. They include different mineral assemblages and host rock lithologies (Table 1; Fig. 1). The choice was based on the following criteria:

- close spatial correlation or even reaction textures of galena and the supergene minerals;
- variable silver content of galena based on preliminary measurements;
- secondary minerals were microscopically free of any sulfide micro-inclusions;

For the LA-ICP-MS measurements, mineral separates as well as thin sections were investigated. The samples typically show the replacement of galena by fine-grained anglesite, cerussite and/or pyromorphite and mimetite (Fig. 2a; *cf*., Keim & Markl 2015). The replacement of galena by cerussite and anglesite starts *in situ* at its margins, along cleavages or fissures. Cerussite is more abundant than anglesite. In addition, euhedral crystals of anglesite and cerussite form in vugs, either caused by dissolution of galena or in cavities present in the ore body and host rocks (Fig. 2b, c). These crystals are typically clear and free of galena remnants,

while the *in situ* formation of cerussite and anglesite often causes remnants of galena to be enclosed (Fig. 2d) which leads to a light grey to black color of the crystals. Euhedral pyromorphite and mimetite grow rarely directly on galena and almost never contain sulfide relics. Typically, they are found on cerussite and anglesite or even further away in fractures, on host rock or gangue minerals (Fig. 2a, e, f).

Methods

LA-ICP-MS

Trace elements of secondary lead phases and galena were analyzed by LA-ICP-MS at the GeoZentrum Nordbayern, Universität Erlangen-Nürnberg, Germany. An Agilent 7500i ICP-MS coupled with a UP193FX New Wave Research Laser with an output wavelength of 193 nm was used. Two measurement programs were accomplished. For galena and anglesite the ideal stoichiometric sulfur content of galena and anglesite were taken as internal standards, while for cerussite, pyromorphite, and mimetite their ideal stoichiometric lead content was taken as internal standard. In both cases, Ar and He were used as carrier gas, ablation was carried out with a pulse rate of 15 Hz and measurement times were set to 45 s (background 20 s). For galena and anglesite a 25 µm spot size, energy density of 2.6 J/cm², and laser energy of 0.53 GW/cm² were chosen. For cerussite, pyromorphite, and mimetite, a 35 µm spot size, an energy density of 3.2 J/cm² and a laser energy of 0.64 GW/cm² were chosen, respectively.

The software GLITTER 3.0 (Macquarie University) was used for data reduction. External standards for galena and anglesite were PO724 for Au and Mass-1 for all other trace elements. For cerussite, pyromorphite, and mimetite, Mass-1was used for Te and Hg and NIST SRM 612 for all other trace elements (see Table 2 for mean 1 σ errors and detection limits for each mineral).

Hydrogeochemical modelling

To evaluate the stability relations of primary and secondary lead and silver phases, stability diagrams were computed using The Geochemist's Workbench in the version 10.0 (Bethke & Yeakel, 2015). Activity calculations were conducted using PHREEQC in the version 2.18.3 (Parkhurst & Appelo 1999). All calculations are based on the thermodynamic wateq4f.dat database (Ball & Nordstrom 1991). The equilibrium constants used are listed in Table 3.

Results

165 The silver contents of galena and associated secondary lead minerals for each individual locality
166 are plotted in Fig. 3. Galena shows the highest amounts and the highest variation of silver
167 contents, varying between 31 ppm in samples from the Schauinsland and 18,000 ppm in
168 samples from the Clara mine. The overall average is about 1,050 ppm. The highest silver
169 content at the Clara mine is most probably due to mineral inclusions (see below).

170 Cerussite has very low silver contents, commonly below the detection limit (for mineral-
171 specific detection limits see Table 2). The maximum value is 1.7 ppm at the Michael mine, the
172 average silver content is 0.08 ppm. A maximum of about 3% and an average of about 0.3% of
173 the galena's silver is incorporated into cerussite. All 21 anglesite analyses have silver contents
174 below the detection limit.

175 Pyromorphite has the highest silver contents of all analyzed secondary minerals. All analyses
176 show silver contents well above the detection limit, averaging at about 18.5 ppm. The highest
177 amount was found in the sample from the Klöpfe locality (124 ppm). A maximum of about 13%
178 and an average of 3.5% of the silver content of the preexisting galena is incorporated into
179 pyromorphite. Mimetite also contains relatively much silver, all analyses lying above the
180 detection limit, but significantly less than pyromorphite. The maximum silver content is 19.5
181 ppm at the Karlstollen locality and the average is about 5.2 ppm. The average content of all
182 analyzed trace elements (Cr, Co, Ni, Cu, As, Se, Ag, Sb, Te, Ba, Au, Hg, Tl, Bi) for each sample
183 can be found in Table 4.

184

185 **Discussion**

186 *Silver accumulation in galena and secondary phases*

187 The covariation of Ag + Cu + Tl and Bi + Sb for each galena sample is shown in Fig. 4. Some
188 analyses plot on the 1:1 line implying an isomorphic exchange of $Ag^{+} + Cu^{+} + Tl^{+} + (Bi, Sb)^{3+}$
189 $\leftrightarrow 2Pb^{2+}$ (George *et al.* 2015). Many other points, however, do not show a 1:1 correlation,
190 which indicates the involvement of vacancies within the galena lattice ($2(Bi, Sb)^{3+} + \square = 3Pb^{2+}$)
191 or the incorporation of mineral inclusions with a high (As + Sb)/Ag ratio (George *et al.* 2015).
192 Such inclusions are only found in galena from the Clara mine. Here, few µm-large inclusions
193 of an Ag-Sb-S phase not further determined were identified using secondary electron
194 microscopy (SEM). The high silver contents of up to 18,000 ppm at this locality can be related
195 to these silver-bearing inclusions. All other grains of galena do not show any silver-bearing

196 inclusions on the µm-scale. Sub-micron inclusions, however, cannot be fully excluded.
197 Furthermore, LA-ICP-MS measurements show no significant signal changes, neither in Ag nor
198 in Sb + Bi, which is an indication of mineral inclusions playing only a subordinate role (e.g.
199 Pettke 2006).

200 Our results show that silver contents in the analyzed secondary lead minerals are considerably
201 lower than in the hydrothermal galena from which they were derived. Cerussite is almost silver-
202 free and can be texturally subdivided into two generations: early *in situ* replacement of galena
203 and euhedral crystals growing in cavities of partly/completely dissolved galena or in the host
204 rock (Szczerba & Sawlowicz 2009, Keim & Markl 2015). If free of galena remnants, both
205 generations show low silver contents, often below the detection limit. As an example, Fig. 5a
206 shows clear cerussite crystals *in situ* replacing galena with silver contents below the detection
207 limit. In contrast, Fig. 5b shows that silver contents are much higher if galena and/or other
208 sulfide relics are present as small crystallites; if free of galena remnants, cerussite is almost Ag-
209 free. This explains the high silver contents up to 2,000 ppm observed by Stavinga (2014), since
210 these crystals show a dark grey color. In contrast, clear cerussite crystals investigated by
211 Stavinga (2014) show much lower silver concentrations between 0.2 and 170 ppm. The
212 contamination of cerussite by galena also explains why secondary lead minerals have been
213 mined historically as silver ores in some cases. Such contaminated measurement spots were not
214 included in the present study.

215 Anglesite invariably shows silver contents below the detection limit. Pyromorphite and
216 mimetite show the highest silver contents of all secondary minerals. They are visually free of
217 ore remnants, although Tuduri *et al.* (2011) report that scarce inclusions of acanthite enclosed
218 in mimetite can occur. Consequently, it may be possible that Ag_2S or other silver-bearing
219 phases, which were not visible under the SEM, are responsible for the higher silver contents in
220 pyromorphite and mimetite compared to cerussite and anglesite. On the other hand: why should
221 such inclusions be confined to pyromorphite and mimetite only? In summary, our data suggest
222 that pyromorphite group minerals indeed can accommodate more silver than cerussite and
223 anglesite. Why mimetite shows significantly lower silver contents than pyromorphite is
224 unknown. Interestingly, the data of Markl *et al.* (2014b) show, that silver contents increase with
225 higher phosphorous content, while arsenic endmembers are almost free of silver.

226 The limited structural incorporation of silver into the secondary lead minerals is probably due
227 to crystal chemical effects. Since no studies investigated the structural incorporation of silver
228 in cerussite, anglesite, pyromorphite, or mimetite, this question remains open for the moment.

Occurrence of native silver, acanthite and chlorargyrite in the Schwarzwald

Since silver incorporation into secondary lead minerals is limited, the released silver is most likely removed as aqueous complexes/ions and/or is reprecipitated as distinct silver phases like native silver, acanthite or chlorargyrite in the vicinity of weathered galena or further away.

Our analyzed samples do not show separate silver-phases, but these are present on other specimens from the same sample localities (see Fig. 6) and are reported also from the literature. In the following, some examples are given.

At the Schauinsland, kidney-shaped aggregates of silver occur in the oxidized portion of the mineralization, together with clear white cerussite (Fig. 6a). Very young acanthite on the silver has formed during sample storage and is therefore doubtlessly not geogenic. Wire-shaped, platy and skeletal branches of native silver on corroded galena and cerussite were also reported by Schlomann & Steen (1988) from this locality. At the Friedrich Christian locality, native silver (Fig. 6b) occurs together with linarite [$PbCu(SO_4)(OH)_2$] and cerussite in direct vicinity to corroded galena (Fig. 6c). This observation was also made by Schlomann & Steen (1991). Additionally, they report acanthite as acicular crystals in moss-like aggregates overgrowing anglesite formed on corroded galena. Native silver has also been found at the Herrensegen locality associated with cerussite, goethite [FeOOH], malachite [$Cu_2(CO_3)(OH)_2$] and bismutite [$Bi_2(CO_3)O_2$] (Fig. 6d). Crusts of native silver on cerussite accompanied by mimetite and a prismatic black aggregate of acanthite were reported from the Michael locality by Walenta (1989).

To our best knowledge chlorargyrite is only rarely found in the Schwarzwald, and if it is found, it only occurs in association with other silver-bearing phases like silver-bearing fahlore (i.e. argentotennantite [$(Ag,Cu)_{10}(Zn,Fe)_2(As,Sb)_4S_{13}$]), native silver or pyrargyrite [Ag_3SbS_3] at Wittichen, the Wenzel- and the Clara mines (Walenta 1992) and at the Hornbühl (Walenta & Schmeltzer 1990). In summary, native silver and acanthite are much more widespread than chlorargyrite in the oxidation zones of hydrothermal ore deposits in the Schwarzwald, and the only secondary silver minerals present in contact to weathered galena.

Redistribution of silver under present conditions; Thermodynamic considerations

In the following, calculated stability diagrams are used to clarify the rarity of chlorargyrite in the Schwarzwald and the redistribution of silver in the oxidation zones. Note, that interactions with biomass, clays, Fe-oxi/-hydroxides and kinetic effects are not taken in account here.

Stability diagrams were calculated based on input parameters from Keim & Markl (2015) representing a typical, average Schwarzwald mine water (Smw) chemistry under present-day conditions (P = 1 bar; T = 10°C; S = 1.35×10^{-4} M; $\log a_{CO2}$ = -3.55; $\log a_{O2}$ = -0.68) from Göb *et al*. (2011, 2013a, 2013b) and Markl *et al*. (2014a). Silver contents of Smw are often below the detection limit and in no case supersaturated with respect to any silver-bearing phase. In order to simulate the silver activity of a weathering fluid in direct vicinity to argentiferous galena, Smw was in calculations equilibrated with argentiferous galena. For the activity calculations, congruent dissolution of galena with 100 ppm, 1,000 ppm and 5,000 ppm silver was assumed. The emerging silver activities, calculated with PHREEQC, were used to calculate the stability diagrams. The whole approach is based on the assumption of a closed system, which locally occur in parts of the supergene zones (Perelman 1967). The stability relations of acanthite, native silver, chlorargyrite and silver ions/complexes for silver-contents of 5,000 ppm, 1,000 ppm and 100 ppm considering variable chloride activity and oxygen fugacities are shown in Fig. 7a-d. In general, silver ions and chloride complexes and/or chlorargyrite are stable under oxidized, native silver and acanthite under more reduced conditions (Fig. 7a-d).

Chlorargyrite is the stable silver phase under oxidized conditions. In general, the chlorargyrite stability decreases with decreasing silver content in galena (Fig. 7a-d) and disappears at contents <1,000 ppm (Fig. 7d) or if the temperature is slightly increased at silver contents of galena of e.g. 1,000 ppm (Fig. 7c). Such a temperature increase of mine water up to nearly 20°C is realized for example in some parts of the Clara mine (Bucher *et al.* 2009). If the silver and/or chloride activities are low, silver is present as Ag^+-ions, or as silver chloride complexes like $AgCl^0$, $AgCl_2^-$, and $AgCl_4^{3-}$ instead of the solid phase chlorargyrite (Webster & Mann 1984, Mann 1984, Saunders 1993, Jin *et al*. 2010). If pH is changed towards more basic conditions, the stability of native silver is enlarged towards lower a_{O2} (Fig 7b). Complexation with sulfur as $Ag(HS)^-_2$ in our case only plays a very minor role under strongly reduced conditions.

The grey box in Fig. 7a-d shows the whole chloride activity range, the grey bar the average value of a_{Cl^-} realized in Smw (Göb *et al*. 2011, 2013a, 2013b, Markl *et al*. 2014a). Taking the average chloride activity of Smw, silver is present as silver ions independent of the silver content of galena. Regarding the whole range of Smw chloride activities, chlorargyrite stability is potentially reached under oxidizing or slightly reduced conditions if silver contents in galena

292 are sufficiently high. The field observations above, however, indicate that this is may be only
293 the case at very few localities like the Clara mine.

294 To clarify the observation that chlorargyrite only forms at some places, which are enriched in
295 silver, Smw analyses of localities, where water data and silver contents of galena are available,
296 are compared (Clara mine, Kammentobel, Wilhelminenstollen, Schauinsland, Karlstollen). The
297 water analyses are plotted in a $\log a_{Ag+}$ versus $\log a_{Cl-}$ stability diagram (Fig. 7e) at a fixed pH of
298 7, a temperature of 10°C and oxidizing conditions according to water in equilibrium with
299 atmospheric oxygen. Chlorargyrite is thermodynamically stable at high silver and chloride
300 activities, whereas silver ions and complexes are stable at low silver and chloride activities,
301 respectively. The stability fields shown are temperature-dependent, since chlorargyrite stability
302 decreases at higher temperatures (see Fig. 7c, e). The possible pathways of silver released
303 during galena weathering are summarized in Fig. 8. Comparing the localities plotted in Fig. 7e,
304 chlorargyrite stability is only reached at the Clara mine, which agrees with the field
305 observations (see above). This is explained by the high silver content of galena up to 18,000
306 ppm (average of 5,500 ppm). Since chlorargyrite occurs together with other silver bearing
307 phases like argentotennantite or polybasite group minerals $[(Ag,Cu)_{16}(Sb,As)_2S_{11}]$ it is very
308 likely, that such silver-bearing minerals additionally lead to a silver enrichment and therefore
309 help the fluids to reach the stability of chlorargyrite in microenvironments. The same
310 explanation also applies to the chlorargyrite-bearing Wittichen and Hornbühl localities, where
311 chlorargyrite is associated with native silver (Wittichen) and pyrargyrite (Hornbühl). These
312 localities, however, can't be plotted in Fig. 7e, since they do not bear galena. Another possible
313 way to stabilize chlorargyrite thermodynamically would be the influx of high-chlorine waters
314 if galena contains sufficient amounts of silver. To our knowledge, however, there are no
315 locations known to date, where such a process can be demonstrated to have led to chlorargyrite
316 formation. Generally, High chlorine contents are possibly reached by the dissolution of salt, in
317 evaporitic sediments, near to the coast or due to the anthropogenic input of road salt. Input of
318 chlorine by the sea is for example the explanation of the chlorargyrite occurrence at the Milos
319 deposit in Greece, where chlorargyrite forms in contact to seawater replacing silver sulfides and
320 native silver (Alfieris *et al.* 2013) or at the Shizukari mine in Japan where native silver and
321 pyrargyrite occur together with chlorargyrite (Ishihara & Matsueda 1997). This locality is only
322 about 1 km away from the sea, in humid climate. The driving factor for chlorargyrite
323 stabilization at these localities, however, is most probably not the high chlorine contents, but
324 the high silver activities due to dissolution of primary silver phases.

325 At the other localities plotted in Fig 7e (Kammentobel, Wilhelminenstollen, Schauinsland,
326 Karlstollen), the silver released is present as Ag^+-ions. Silver at these localities is either
327 transported away since there are no secondary silver phases found (Kammentobel, Karlstollen)
328 or is reprecipitated as distinct silver phases like native silver and acanthite (Schauinsland,
329 Wilhelminenstollen).

330 The occurrence of secondary native silver and acanthite in the oxidation zones of hydrothermal
331 veins in the Schwarzwald (cf. Fig. 6) clearly indicates reprecipitation of the released Ag^+ ions
332 and complexes as distinct phases. The possible modes of redistribution discussed here are also
333 summarized in Fig. 8. To which extent the weathering of other silver-bearing sulfides supports
334 the formation of native silver remains debatable. Different precipitation mechanisms for native
335 silver are possible, such as the reduction of Ag^+ by Fe^{2+} (e.g. Park & MacDiarmid 1975, Mann
336 1984) in contact to pyrite [FeS_2], siderite [$FeCO_3$] or other Fe^{2+}-bearing phases. Also,
337 microenvironments depleted in oxygen are likely to precipitate Ag^+-ions as native silver (Fig.
338 7 a-d). Such oxygen depletion, even in oxidation zones, is possible due to prior sulfide oxidation
339 or biological processes in environments isolated or inhibited from oxygen supply like soils (e.g.
340 Tan 2011). In strongly reduced environments also the precipitation of acanthite is likely. If
341 silver, however, is complexed by chloride, a reduction by iron cannot take place (Mann 1984)
342 and the silver complexes are likely to migrate away or precipitate due to the dilution with low-
343 Cl ground or surface waters, changing the stability of silver chloride complexes. The
344 precipitation of acanthite on the surface of sulfide minerals is described by e.g. Scaini *et al.*
345 (1997) and Bell & Kramer (1999) and is explained by a cation exchange reaction like

346 $$2PbS + 10Ag^+ + 4H_2O \rightarrow 2Pb^{2+} + Ag_2S + 8Ag_{(s)} + SO_4^{2-} + 8H^+$$

347 Unlike other metal sulfides, crystalline acanthite forms very rapidly at room temperature and
348 typically grows on the surface of native silver and is therefore of artificial origin in some cases
349 (cf. Fig. 6a).

350 In arid climates and close to seawater, chlorargyrite is the thermodynamically stable silver
351 phase due to the increased chloride activities (e.g. Saunders 1993). If the Br/Cl and/or the I/Cl
352 ratios are sufficiently high, aqueous silver bromide-iodine complexes and Br-I-bearing solid
353 phases become increasingly important (Boyle 1997, Gammons & Yu 1997). Silver halide
354 minerals like bromargyrite [AgBr] and iodargyrite [AgI] can precipitate from such solutions
355 (Gołębiowska *et al.* 2010, Andreu *et al.* 2015). In the Schwarzwald, bromine and iodine
356 concentrations in mine waters are very low and chloride is by far the dominant halogen in the

357 weathering solutions. However, in the Clara mine, both bromargyrite and iodargyrite, and at
358 the Fortuna mine near Wolfach, bromargyrite have been observed in close contact to weathered
359 pyrargyrite or polybasite-pearceite solid solutions (Walenta 1992).

360

361 **Conclusions**

362 During the weathering of argentiferous galena, silver is only sparsely incorporated into
363 secondary lead minerals. Cerussite and anglesite are almost silver-free, whereas pyromorphite
364 and mimetite can accommodate minor portions (a maximum of 13% of the galena's content) of
365 silver.

366 The major part of the silver set free during dissolution of argentiferous galena, is - depending
367 on the fluid chemistry - either reprecipitated as distinct phases or transported away. The stability
368 calculations show, that under modern-day conditions the released silver is present as soluble
369 silver ions in the Schwarzwald. Since field observations show that secondary silver phases like
370 native silver and acanthite occur beside weathered galena, it is likely that the silver ions were
371 reprecipitated due to redox reactions.

372 Although the silver halide chlorargyrite is the stable silver phase under oxidizing conditions, it
373 is found only at few localities. The stability diagrams combined with water analyses and
374 measured silver contents of galena show that the rarity or lack of chlorargyrite is explained by
375 relatively low silver contents of galena in combination with the relatively low chloride
376 concentrations in the oxidizing water. Only at localities where silver contents of galena are high
377 or weathering of additional silver-bearing phases like fahlore or pyrargyrite occurs (e.g. the
378 Clara mine), chlorargyrite is thermodynamically stable and has been observed in the field. Also
379 an increase of the chloride activity e.g. close to the coast, due to aerosols or below evaporitic
380 sediments, as well as the anthropogenic input of road salt probably would support the
381 precipitation of chlorargyrite, even if silver contents of galena are relatively low.

382

383 **Acknowledgments**

384 We thank H. Brätz from the GeoZentrum Nordbayern for her help during LA-ICP-MS
385 measurements, S. Schafflick for the careful sample preparation and M. Burisch and S. Kreissl
386 for numerous discussions. We are also grateful to editor T. Neumann for his friendly and

387 professional handling of this paper. This work is a contribution of the r^4 project "ResErVar—
388 Ressourcenpotential hydrothermaler Lagerstätten der Varisziden" funded by the German
389 Ministry of Education and Research (BMBF).
390

391

392 **References**

393 ALFIERIS, D., VOUDOURIS, P., & SPRY, P. G., 2013: Shallow submarine epithermal Pb–Zn–Cu–
394 Au–Ag–Te mineralization on western Milos Island, Aegean Volcanic Arc, Greece:
395 Mineralogical, geological and geochemical constraints. –Ore Geol. Rev. **53:** 159-180.

396 ANDREU, E., TORRÓ, L., PROENZA, J. A. DOMENECH, C., GARCÍA-CASCO, A., DE BENAVENT, C.
397 V., & LEWIS, J. F., 2015: Weathering profile of the Cerro de Maimón VMS deposit
398 (Dominican Republic): textures, mineralogy, gossan evolution and mobility of gold and
399 silver. –Ore Geol. Rev. **65:** 165-179.

400 BALL, J. W., & NORDSTROM, D. K., 1991: User's manual for WATEQ4F, with revised
401 thermodynamic data base and test cases for calculating speciation of major, trace, and
402 redox elements in natural waters. U.S. Geological Survey Open-File Report, 91-183.

403 BELL, R. A., & KRAMER, J. R., 1999: Structural chemistry and geochemistry of silver and sulfur
404 compounds: Critical review. –Environ. Toxicol. Chem. **18:** 9-22.

405 BETHKE, C. M., & YEAKEL, S., 2015: GWB Essentials Guide. Aqueous Solutions, LLC
406 Champaign, Illinois, USA, 149 pp.

407 BLIEDTNER, M., & MARTIN, M., 1986: Erz- und Minerallagerstätten des Mittleren
408 Schwarzwaldes, LGRB, Freiburg, Germany 782 pp. (in German)

409 BOYLE, D. R., (1997): Iodargyrite as an indicator of arid climatic conditions and its association
410 with gold-bearing glacial tills of the Chibougamau-Chapais Area Ouebec. –Can. Mineral.
411 **35:** 23-34.

412 BROOKS, W. E., 2013: Silver (Ag): Metal prices in the United States through 2010, USGS,
413 p.167.

414 BUCHER, K., ZHU, Y., & STOBER, I., 2009: Groundwater in fractured crystalline rocks, the Clara
415 mine, Black Forest (Germany). –Int. J. Earth Sci. ***98***, 1727-1739.

416 BUTTERMAN, W. C. & HILLIARD, H. E., 2005: Mineral commodity profiles. USGS open-file
417 Report, 2004-1251.

418 DILL, H. G., 2015: Supergene Alteration of Ore Deposits: From Nature to Humans. –Elements.
419 **11:** 311-316.

DILL, H. G., WEBER, B., & BOTZ, R., 2013: Metalliferous duricrusts. –N. Jb. Miner. Abh. **190:** 123-195.

FOORD, E. E., DANIEL, R., & CONKLIN, N. M., 1988: Coexisting galena PbS_{ss} and sulfosalts: evidence for multiple episodes of mineralization in the Round Mountain and Manharan gold district, Nevada. –Can. Mineral. **26:** 355-376.

FOORD, E. E., & SHAWE, D. R., 1989: The Pb-Bi-Ag-Cu-(Hg) chemistry of galena and some associated sulfosalts: A review and some new data from Colorado, California and Pennsylvania. –Can. Mineral. **27:** 363-382.

GAMMONS, C. H., & YU, Y., 1997: The stability of aqueous silver bromide and iodide complexes at 25–300 C: experiments, theory and geologic applications. –Chem. Geol. **137:** 155-173.

GEORGE, L., COOK, N. J., CRISTIANA, L., & WADE, B. P., 2015: Trace and minor elements in galena: A reconnaissance LA-ICP-MS study. –Amer. Miner. **100:** 548-569.

GEYER, O. F., & GWINNER, M. P., 2011: Geologie von Baden Württemberg. Schweizerbart'sche Verlagsbuchhandlung, Stuttgart, Germany, 627 pp. (in German)

GÖB, S., GÜHRING, J. E., BAU, M., & MARKL, G., 2013a: Remobilization of U and REE and the formation of secondary minerals in oxidized U deposits. –Amer. Miner. **98:** 530-548.

GÖB, S., LOGES, A., NOLDE, N., BAU, M., JACOB, D. E., & MARKL, G., 2013b: Major and trace element compositions (including REE) of mineral, thermal, mine and surface waters in SW Germany and implications for water–rock interaction. –Appl. Geochem. **33:** 127-152.

GÖB, S., WENZEL, T., BAU, M., JACOB, D. E., LOGES, A., & MARKL, G., 2011: The redistribution of rare-earth elements in secondary minerals of hydrothermal veins, Schwarzwald, southwestern Germany. –Can. Mineral. **49:** 1305-1333.

GOŁĘBIOWSKA, B., PIECZKA, A., RZEPA, G., MATYSZKIEWICZ, J., & KRAJEWSKI, M., 2010: Iodargyrite from Zalas (Cracow area, Poland) as an indicator of Oligocene–Miocene aridity in Central Europe. –Palaeogeogr. Palaeoclimatol. Palaeoecol. **296:** 130-137.

GUILBERT, J. M., PARK, C. F., 1984: The Geology of Ore Deposits. W.H. Freeman and Company, New York, USA, 985 pp.

447 HAUTMANN, S., & LIPPOLT, H. J., 2000: 40Ar/39Ar dating of central European K-Mn oxides-a
448 chronological framework of supergene alteration processes during the Neogene. –Chem.
449 Geol. **170:** 37-80.

450 ISHIHARA S., & MATSUEDA, H., (1997): Genesis of Two Contrasting Metallogenic Provinces in
451 the Back-Arc Basins of Hokkaido, Japan; In Proceedings of the 30th International
452 Geological Congress volume 9. Zeist, Netherlands, 515 pp.

453 JIN, X., LI, M., WANG, J., MARAMBIO-JONES, C., PENG, F., HUANG, X., & HOEK, E. M., 2010:
454 High-throughput screening of silver nanoparticle stability and bacterial inactivation in
455 aquatic media: influence of specific ions. –Environ. Sci. Technol. **44:** 7321-7328.

456 KALT, A., ALTHERR, R., & HANEL, M., 2000: The Variscan basement of the Schwarzwald.
457 Supplement to Eur. J. Mineral. **12:** 1-43.

458 KEIM, M. F., & MARKL, G., 2015: Weathering of galena: Mineralogical processes,
459 hydrogeochemical fluid path modeling, and estimation of the growth rate of pyromorphite.
460 –Amer. Miner. **100:** 1584-1594.

461 KIRCHHEIMER, F., 1976: Bericht über Spuren römerzeitlichen Bergbaus in Baden-Württemberg.
462 –Aufschluss, **27:** 361–371. (in German)

463 KRUPP, R. E., & WEISER, T., 1992: On the stability of gold-silver alloys in the weathering
464 environment. –Miner. Depos. **27:** 268-275.

465 LEVARD, C., HOTZE, E. M., LOWRY, G. V., & BROWN JR, G. E., 2012: Environmental
466 transformations of silver nanoparticles: impact on stability and toxicity. –Environ. Sci.
467 Technol. **46:** 6900-6914.

468 MANN, A. W., 1984: Mobility of Gold and Silver in lateritic weathering profiles: Some
469 observations from Western Australia. –Econ. Geol. **79:** 38-49.

470 MARKL, G., MARKS, M. A., & DERREY, I., 2014a: Weathering of cobalt arsenides: Natural
471 assemblages and calculated stability relations among secondary Ca-Mg-Co arsenates and
472 carbonates. –Amer. Miner. **99:** 44-56.

473 MARKL, G., MARKS, M. A., HOLZÄPFEL, J., & WENZEL, T., 2014b: Major, minor, and trace
474 element composition of pyromorphite-group minerals as recorder of supergene weathering

475 processes from the Schwarzwald mining district, SW Germany. –Amer. Miner. **99:** 1133-
476 1146.

477 METZ, R., RICHTER, M., & SCHÜRENBERG, H., 1957: Die Blei-Zink-Erzgänge des
478 Schwarzwaldes, –Beihefte zum Geol. Jb. **29:** 1-277. (in German)

479 MORRIS, H. T., & LOVERING, T. S., 1952: Supergene and hydrothermal dispersion of heavy
480 metals in wall rocks near ore bodies, Tintic District, Utah. –Econ. Geol. **47:** 685-716.

481 PARK, C. F., & MACDIARMID, R. A., 1975: Ore Deposits. W. H. Freeman and Company, San
482 Francisco, USA, 985 pp.

483 PARKHURST, D. L., & APPELO, C. A. J., 1999: User's guide to PHREEQC (ver. 2)-A computer
484 program for speciation, batch-reaction, one-dimensional transport, and inverse
485 geochemical calculations. U.S. Geological Survey Water-Resources Investigations Report,
486 99-4259.

487 PERELMAN. A. I., 1967: Geochemistry of Epigenesis, Springer, New York, USA, 265 pp.

488 PETTKE, T., 2006: In situ laser-ablation-ICP-MS chemical analysis of melt inclusions and
489 prospects for constraining subduction zone magmatism. Mineralogical Association of
490 Canada, Short Course, **36:** 51-80.

491 POHL, W.L., 2011: Economic Geology: Principles and Practice. John Wiley & Sons Ltd,
492 Sussex, United Kingdom, 663 pp.

493 RAMSY, M., 1981: Trace-element content of galenas and associated minerals in some Miocene
494 lead-zinc deposits near Red Sea coast, –Egypt. Geol. Rundsch. **70:** 874-881.

495 RENOCK, D., & BECKER, U., 2011: A first principles study of coupled substitution in galena. –
496 Ore Geol. Rev. **42:** 71-83.

497 SANGAMESHWAR, S. R., & BARNES, H. L., 1983: Supergene processes in zinc-lead-silver sulfide
498 ores in carbonates. –Econ. Geol. **78:** 1379-1397.

499 SATO, M., 1992: Persistency-field Eh-pH diagrams for sulfides and their application to
500 supergene oxidation and enrichment of sulfide ore bodies. –Geochim. Cosmochim. Acta
501 **56:** 3133-3156.

SAUNDERS. J. A., 1993: Supergene oxidation of bonanza Au-Ag veins at the Sleeper Deposit, Nevada,USA: Implications for hydrogeochemical exploration in the Great Basin. –J. Geochem. Explor. **47:** 359-375.

SCAINI, M. J., BANCROFT, G. M., & KNIPE, S. W., 1997: An XPS, AES, and SEM study of the interactions of gold and silver chloride species with PbS and FeS2: Comparison to natural samples. –Geochim. Cosmochim. Acta **61:** 1223-1231.

SCHLOMANN, C., & STEEN, H., 1988: Über Sekundärmineralien vom Schauinsland. –Aufschluss **42:** 213-223. (in German)

SCHLOMANN, C. & STEEN, H., 1991: Mineralien aus dem Revier Bad Ripoldsau-Schapbach im mittleren Schwarzwald. –Aufschluss **24:** 213-223. (in German)

STAVINGA, D. B., 2014: Trace element geochemistry and metal mobility of oxide mineralization at the Prairie Creek zinc-lead-silver deposit, NWT, Master thesis, Queens University, Ontario, Canada, 295 pp.

SZCZERBA, M., & SAWLOWICZ, Z., 2009: Remarks on the origin of cerussite in the Upper Silesian Zn-Pb deposits. –Pol. Mineral.**40:** 54-64.

TAN, K. H., 2011: Principles of Soil Chemistry, CRC Press, Boca Raton, USA, 390 pp.

TUDURI, J., POURRET, O., CHAUVET, A., BARBANSON, L., GAOUZI, A., & ENNACIRI, A., 2011: Rare earth elements as proxies of supergene alteration processes from the giant Imiter silver deposit (Morocco). In 11th meeting SGA, 2011, Vol. 2, 982 pp.

WALENTA, K., 1989: Neufunde aus dem Schwarzwald, 3. Folge. –Lapis **14:** 30-37. (in German)

WALENTA, K., 1991: Neufunde aus dem Schwarzwald, 4.Folge. –Lapis **15:** 27-31. (in German)

WALENTA. K., 1992: Die Mineralien des Schwarzwaldes und ihre Fundstellen, Christian Weise Verlag, München, Germany, 336 pp. (in German)

WALENTA, K., SCHMELTZER, H., 1990: Die Sekundärmineralien der hydrothermalen Gänge am Hornbühl bei Waldkirch. –Erzgräber **4:** 222-224. (in German)

WEBSTER, J. G., & MANN, A. W., 1984: The influence of climate, geomorphology and primary geology on the supergene migration of gold and silver. –J. Geochem. Explor. **22:** 21-42.

529

530

531

532

533

534

535

536

537

538

539

540

541

542 **Table 1.** Studied samples of galena and associated secondary lead minerals along the localities (Fig. 1), analyzed minerals, mineralization type of the
543 vein, supergene lead paragenesis, secondary silver mineralization, host rocks, and altitude of the respective hydrothermal veins.

No. in Fig.1	locality	area	sample number	analyzed minerals	main mineralization of the vein	supergene lead mineralization	secondary silver mineralization	host rock	altitude [m.a.s.l.]
1	Michael mine	Lahr	R1-R3	Gn, Cer	Brt – Fh – Gn – Sph – native arsenic	Ang + Cer + Mim + additional Pb-minerals	Act, Ag	gneiss/granite	350
2	Clara	Wolfach	R4, R5	Gn, Cer, Pyr	Brt – Fl – Qtz – Gn – Fh – Ccp	Ang + Cer + Pyr + Mim + additional Pb-minerals	Act, Ag, Cea, Ia, Ba	gneiss	500
3	Friedrich-Christian	Schapbach	R6	Gn, Cer	Fl – Qtz – Gn - Ccp	Ang + Cer + Pyr + Mim + additional Pb-minerals	Act, Ag	gneiss	500
4	Herrensegen	Schapbach	R7-R10	Gn, Cer, Ang, Pyr	Fl – Qtz – Gn – Ccp	Ang + Cer + Pyr + Lan + Lin	no Ag-minerals	gneiss	550
5	Silberbrünnle	Gengenbach,	R11-R12	Gn, Cer, Pyr	Qtz – Ccp – Gn - Fh	Ang + Cer + Pyr + Mim + additional Pb-minerals	Act, Ag,	gneiss	500
6	Kammentobel	Feldberg	R13- R15	Gn, Cer, Pyr	Sd/(Gt) – Gn	Ang + Cer + Pyr	no Ag-minerals	migmatite	1300
7	Katzensteig	St. Willhelm	R16	Gn, Cer, Pyr	Qtz – Gn – (Fh)	Cer + Pyr + Mim + additional Pb-minerals	no Ag-minerals	gneiss	900
8	Aitern-Süd	Schönau	R17	Gn, Cer	Fl – Brt – Qtz – Gn – Sph - Ccp	Ang + Cer + Pyr + Mim + additional Pb-minerals	no Ag-minerals	Schist	700
9	Anton	Wieden	R18	Gn, Cer	Fl – Brt – Qtz – Gn – Sph - Ccp	Cer + Pyr + Mim + additional Pb-minerals	Ag	gneiss/Granite	950
10	no exact location	Schauinsland	R20	Gn, Pyr	Qtz – Gn – Sph	Ang + Cer + Pyr + Mim + additional Pb-minerals	Act, Ag	migmatite	-
11	Klöpfe	Münstertal	R21	Gn, Pyr	Qtz – Brt – Gn	Ang + Cer + Pyr + Mim + additional Pb-minerals	Act, Ag	migmatite	450
12	Urberg	St. Blasien	R22-R24	Gn, Cer, Pyr	Qtz - Fl - Brt – Gn	Ang + Cer + Pyr + Mim + additional Pb-minerals	Act, Ag	gneiss/granite	950
13	Hausbaden	Badenweiler	R25-R29	Gn, Cer, Ang, Pyr, Mim	Qtz – Brt - Gn	Ang + Cer + Pyr + Mim + additional Pb-minerals	Ag	granite	650
14	Karlstollen	Badenweiler	R30, R31	Gn, Ang, Pyr, Mim	Qtz – Brt – Gn	Cer + Pyr + Mim + Wlf + Hin	No Ag-minerals	rhyolite/schist	500

15	Willhelminenstollen	Badenweiler	R32-R34	Gn, Cer, Pyr	Qtz – Brt – Gn	Cer + Ang + Pyr	Ag	granite	500

abbreviations: Act = acanthite; Ag = native silver; Ang = anglesite; Ba = bromargyrite; Brt = Barite; Ccp = chalcopyrite; Cea = chlorargyrite; Fh = fahlore; Fl = fluorite; Gn = galena; Gt = goethite; Hin = hinsdalit; Ia = iodargyrite; Lan = lanarkite; Lin = linarite; Mim = mimetite; Pyr = pyromorphite; Qtz = quartz; Sd = siderite; Sph = sphalerite; Wlf = wulfenite

548 **Table 2.** Average 1 σ errors and detection limits for the LA-ICP-MS measurements for each
549 analyzed mineral.

element	analyzed minerals									
	galena		cerussite		anglesite		pyromorphite		mimetite	
	n = 98		n = 81		n = 21		n = 66		n = 9	
	mean 1σ	dl [ppm]	mean 1σ	dl [ppm]	mean 1σ	dl [ppm]	mean 1σ	dl [ppm]	mean 1σ	dl [ppm]
Cr	bdl	0.22	0.25	0.41	bdl	0.26	7.89	0.53	0.96	0.45
Co	0.03	0.01	0.01	0.02	bdl	0.01	0.01	0.02	bdl	0.02
Ni	0.07	0.04	0.04	0.10	bdl	0.06	0.07	0.13	bdl	0.10
Cu	14.4	0.04	0.78	0.09	0.08	0.05	8.2	0.12	1.02	0.09
As	0.06	0.04	0.33	0.56	0.03	0.15	623	0.61	5826	0.89
Se	0.31	0.23	0.37	0.60	0.40	0.33	0.45	0.79	0.34	0.57
Ag	73.2	0.01	7.43	0.01	0.09	0.01	0.99	0.02	0.26	0.01
Sb	147	0.01	6.26	0.02	0.01	0.01	3.3	0.03	3.4	0.02
Te	0.02	0.03	bdl	0.16	0.01	0.06	0.06	0.15	bdl	0.11
Ba	480	0.14	2.58	0.03	970	0.13	13.6	0.03	0.67	0.03
Au	0.01	0.01	0.03	0.01	bdl	0.01	0.04	0.01	0.02	0.01
Hg	0.18	0.05	0.21	0.12	bdl	0.07	0.76	0.15	0.07	0.14
Tl	0.28	0.004	0.01	0.02	bdl	0.01	0.03	0.02	0.12	0.02
Bi	26.4	0.002	3.32	0.01	0.01	0.001	0.73	0.01	0.38	0.01

abbreviations: dl = detection limit; bdl = all analysis below detection limit

550

551

552 **Table 3.** Equilibrium constants for minerals and complexes used for the thermodynamic
553 calculations.

mineral/complex	equilibrium constant [logk]*
chlorargyrite	-9.8
native silver	-13.5
acanthite	-36.1
$AgCl^0$	3.3
$AgCl_2^-$	5.3
$AgCl_4^{3-}$	5.5
Ag_2CO_3	-11.1
$Ag(HS)_2^-$	18.5

* wateq4.dat database (Ball & Nordstrom 1991)

554

555

556 **Table 4.** Average contents of all measured elements (LA-ICP-MS) for the minerals galena, cerussite, anglesite, pyromorphite, and mimetite.

557

	average contents of each sample [ppm]													
Samples	**Cr**	**Co**	**Ni**	**Cu**	**As**	**Se**	**Ag**	**Sb**	**Te**	**Ba**	**Au**	**Hg**	**Tl**	**Bi**
							galena [n=98]							
R1	bdl	bdl	bdl	6.5	1.4	bdl	84	774	bdl	bdl	0.01	bdl	0.8	0.0
R2	bdl	bdl	bdl	bdl	0.3	bdl	56	560	bdl	bdl	bdl	bdl	0.6	0.1
R3	bdl	bdl	bdl	0.1	0.7	bdl	55	295	bdl	bdl	bdl	0.2	0.6	0.0
R4	bdl	bdl	bdl	5.7	0.4	bdl	1339	1703	bdl	6.1	bdl	bdl	0.6	130
R5	bdl	bdl	bdl	9.2	0.2	13.7	9735	657	bdl	bdl	0.02	0.1	4.2	20156
R6	bdl	bdl	bdl	0.5	0.2	0.4	680	782	bdl	0.3	0.01	0.3	0.2	492
R7	bdl	bdl	bdl	2.4	0.2	bdl	594	1027	0.0	0.3	0.13	0.1	0.5	50.9
R8	bdl	bdl	0.6	3229	0.1	bdl	596	8107	bdl	0.3	bdl	bdl	4.0	0.1
R9	bdl	bdl	0.3	12.2	0.1	bdl	593	1938	bdl	bdl	bdl	bdl	0.8	0.2
R10	bdl	bdl	bdl	131	0.6	bdl	423	1066	bdl	bdl	bdl	0.3	0.6	1.3
R11	bdl	bdl	bdl	26.8	0.4	bdl	520	309	bdl	bdl	0.0	0.2	0.4	597
R12	bdl	bdl	bdl	40.3	0.4	0.6	831	1346	0.2	35.7	0.1	5.2	0.6	138
R13	bdl	0.3	0.4	3.4	5.5	bdl	2837	3915	bdl	122	0.1	0.2	4.3	0.1
R14	bdl	bdl	bdl	bdl	0.2	0.3	396	919	bdl	bdl	0.1	bdl	0.1	0.4
R15	bdl	bdl	bdl	3.3	0.8	0.4	678	1592	bdl	0.4	bdl	bdl	1.0	0.0
R16	bdl	bdl	0.4	30.7	1.9	bdl	1996	7324	0.0	0.5	bdl	bdl	15.5	0.0
R17	bdl	bdl	0.2	12.7	1.4	bdl	4506	9655	bdl	bdl	0.0	bdl	77.2	0.0
R18	bdl	bdl	bdl	13.9	0.4	7.1	46	1838	bdl	bdl	bdl	bdl	3.4	0.1
R19	bdl	bdl	bdl	35.6	0.5	0.5	787	3562	0.0	6926	0.0	2.6	2.3	5.3
R20	bdl	bdl	bdl	2.6	2.3	2.8	292	361	bdl	bdl	0.0	0.7	0.2	2.4
R21	bdl	bdl	bdl	14.8	0.5	bdl	930	3534	bdl	bdl	0.0	bdl	3.2	90.5
R22	bdl	bdl	bdl	13.3	0.1	bdl	378	2206	0.0	bdl	bdl	0.1	6.2	45.8
R23	bdl	bdl	bdl	0.6	0.5	bdl	614	1273	bdl	bdl	0.4	0.2	0.5	0.0
R24	bdl	bdl	bdl	279	0.3	bdl	900	1150	0.0	0.3	0.5	16.4	0.5	0.0
R25	bdl	bdl	bdl	15.0	0.4	bdl	304	375	0.1	bdl	0.0	bdl	0.1	0.2
R26	bdl	bdl	bdl	0.2	0.1	2.0	915	1749	bdl	bdl	0.3	0.1	0.8	18.3
R27	bdl	bdl	bdl	25.9	0.4	bdl	554	1098	bdl	bdl	0.3	0.1	0.4	0.0
R28	bdl	bdl	bdl	bdl	0.4	1.4	496	840	bdl	bdl	0.7	bdl	0.2	3.5
R29	bdl	bdl	bdl	1.7	0.2	bdl	1149	2076	bdl	bdl	0.1	bdl	0.7	0.7
R30	bdl	bdl	bdl	0.1	0.3	bdl	461	797	0.1	bdl	0.0	0.2	0.3	1.1
R31	bdl	bdl	bdl	bdl	0.1	bdl	336	392	bdl	bdl	bdl	bdl	0.1	0.5
R32	bdl	bdl	bdl	bdl	0.2	0.7	438	614	bdl	bdl	0.0	0.2	0.1	3.9
							cerussite [n=81]							
R1	bdl	bdl	bdl	0.5	bdl	bdl	0.1	0.2	bdl	2.4	bdl	bdl	bdl	0.0
R2	bdl	bdl	bdl	bdl	1.1	bdl	0.0	bdl	bdl	1.2	bdl	bdl	bdl	0.0
R3	bdl	bdl	bdl	bdl	0.6	bdl	0.4	0.0	bdl	bdl	0.0	0.9	bdl	0.0
R4	bdl	bdl	bdl	bdl	0.6	bdl	0.1	0.0	bdl	bdl	0.0	0.9	bdl	4.3
R5	1.6	0.2	bdl	26.9	0.8	bdl	0.2	1017	bdl	41.6	0.0	2.2	0.0	435
R6	bdl	bdl	bdl	0.1	bdl	bdl	0.0	0.1	bdl	12.6	bdl	0.2	bdl	12.4
R8	bdl	bdl	bdl	bdl	bdl	2.9	0.0	0.1	bdl	0.2	bdl	bdl	bdl	0.0

R11	bdl	bdl	bdl	0.7	1.2	bdl	0.0	0.1	bdl	0.7	bdl	bdl	bdl	9.7
R13	bdl	bdl	bdl	bdl	1.2	1.1	0.4	0.0	bdl	5.8	bdl	0.1	bdl	0.0
R18	bdl	bdl	bdl	bdl	1.8	bdl	0	bdl	bdl	20.2	bdl	bdl	bdl	0.0
R18	bdl	bdl	bdl	bdl	1.8	bdl	0.2	bdl	bdl	20.2	bdl	bdl	bdl	0.0
R22	bdl	bdl	bdl	bdl	1.1	bdl	0.0	bdl	bdl	4.3	bdl	0.3	bdl	14.9
R25	bdl	bdl	bdl	2.0	1.6	bdl	0.0	0.1	bdl	348	0.8	1.0	bdl	0.0
R28	bdl	bdl	bdl	bdl	1.1	bdl	0.1	0.1	bdl	0.2	bdl	bdl	bdl	0.5
R32	4.1	bdl	bdl	bdl	bdl	bdl	0.0	bdl	bdl	bdl	bdl	bdl	bdl	0.2
R33	bdl	bdl	bdl	bdl	bdl	bdl	0.0	0.1	bdl	0.1	bdl	bdl	bdl	0.5
R34	bdl	bdl	bdl	bdl	bdl	bdl	0.0	0.0	bdl	0.2	0.1	bdl	bdl	2.9
							anglesite [n=21]							
R8	bdl	bdl	bdl	bdl	bdl	0.1	bdl	0.0	0.045	789	bdl	bdl	bdl	bdl
R9	bdl	bdl	bdl	bdl	1.0	bdl	bdl	1.5	0.086	1.1	bdl	bdl	bdl	bdl
R10	bdl	bdl	bdl	bdl	bdl	0.8	bdl	bdl	bdl	2886	bdl	bdl	0.14	bdl
R26	bdl	bdl	bdl	bdl	bdl	0.1	bdl	0.0	bdl	1270	bdl	bdl	bdl	bdl
R29	bdl	bdl	bdl	bdl	bdl	0.2	bdl	0.0	bdl	15052	bdl	bdl	bdl	bdl
R30	bdl	bdl	bdl	bdl	bdl	0.2	bdl	0.0	bdl	1697	bdl	bdl	bdl	bdl
							pyromorphite [n=66]							
R5	60.8	bdl	bdl	181	2330	1.8	19	0.6	bdl	138	bdl	bdl	bdl	50.4
R7	63.5	bdl	bdl	876	4585	5.1	23	383	bdl	145	bdl	0.391	bdl	151
R12	58.1	bdl	bdl	934	7078	5.1	7	78.1	bdl	54.2	bdl	0.391	bdl	62.8
R14	204	0.1	0.4	145	634	1.1	56	101	bdl	2189	0.2	0.465	0.2	0.4
R15	82.7	bdl	bdl	8.2	626	1.4	8	0.7	bdl	1.0	bdl	bdl	bdl	0.0
R20	51	bdl	bdl	10.1	197	1.7	2	0.7	bdl	16.6	bdl	0.246	bdl	0.0
R21	36.8	bdl	bdl	3.7	400	1.8	52	2.9	0.222	49.3	0.0	bdl	bdl	1.9
R23	380	0.1	0.3	14.5	3635	1.4	45	24.3	bdl	39.6	0.0	bdl	bdl	3.5
R24	1171	bdl	bdl	31.7	17940	1.1	7	4.9	bdl	82.0	bdl	bdl	bdl	10.6
R27	388	0.1	0.2	29.8	2479	2.1	15	9.9	bdl	38.5	0.0	bdl	bdl	1.3
R28	94.2	0.1	0.2	49.4	69817	2.1	8	125	bdl	32.8	0.1	bdl	bdl	19.6
R32	127	bdl	bdl	10.2	1369	0.9	3	11.3	bdl	532	bdl	bdl	0.2	13.3
R34	48.0	bdl	bdl	17.4	19250	0.9	20	63.6	bdl	291	bdl	bdl	0.2	12.2
R33	44.5	bdl	bdl	17.2	18658	1.0	8	13.2	bdl	114	bdl	bdl	0.2	8.5
							mimetite [n=9]							
R28	20.6	bdl	bdl	54.3	86652	bdl	6	154	bdl	31.4	0.1	0.3	1.8	24.2
R31	8.99	bdl	bdl	3.6	117382	1.6	5	1.6	bdl	2.4	bdl	0.2	bdl	0.4

abbreviation: bdl = below detection limit (for detection limits see Table 2)

Figure captions

Figure 1. Simplified geologic map of the Schwarzwald in SW-Germany, including sample locations, (for details see Table 1) major geologic units, main tectonics, and secondary silver minerals/phases (modified after Kalt *et al.* 2000). Abbreviations: Act = acanthite; Ag = native silver; Ba = bromargyrite; Cha = chlorargyrite; Ia = bromargyrite;

Figure 2. (a) Photograph of galena which is converted *in situ* to cerussite/anglesite. Green pyromorphite and brown mimetite grow at the rim; width of photograph (WoP) = 4.5 cm. **(b)** Photograph of euhedral, clear cerussite crystals associated with slightly weathered galena; WoP = 2.3 cm. **(c)** Photograph of euhedral anglesite crystals associated to slightly weathered galena; WoP = 1.5 cm **(d)** Reflected light image of cerussite crystals with numerous galena remnants; WoP = 430 µm. **(e)** Photograph of acicular pyromorphite crystals growing on barite beside galena; WoP = 2.5 cm **(f)** Photograph of mimetite crusts growing on slightly weathered galena WoP = 3.3 cm. Abbreviations: Ang = anglesite; Cer = cerussite; Fl = fluorite; Gn = galena; Mim = mimetite; Pyr = pyromorphite; Qtz = quartz.

Figure 3. Boxplots showing silver contents of galena and associated secondary lead minerals for each locality (1-15 corresponding to Fig. 1 & Table 1). The boxes show the silver-variation of each sample, the line in the box represents the mean value. The percentage stands for the silver portion of the secondary mineral compared to the associated primary galena.

Figure 4. Plot showing the molar inter-element correlation of (Ag + Cu + Tl) versus (Sb + Bi). Dashed grey line shows the ideal 1:1 correlation.

Figure 5. (a) and **(b)** left side: Combined reflected and transmitted light image of galena and cerussite together with the LA-ICP-MS measuring spots for the Aitern and the Katzensteig locality. Right side: silver contents in ppm for galena (black circles), cerussite dispersed by galena remnants (black/grey circles), and cerussite without ore remnants (grey circles). Abbreviations: Ang = anglesite; Cer = cerussite; Gn = galena.

Figure 6. (a) Clear cerussite crystals beside native silver which is overgrown by acanthite WoP = 3 mm and 4 mm. **(b)** native silver together with linarite growing on corroded galena; WoP = 2 mm.

(c) Native silver beside cerussite and corroded galena; WoP = 2 mm. **(d)** native silver together with bismutite and malachite; WoP = 2 mm. Abbreviations: Act = acanthite; Ag = native silver; Bis = bismutite; Fl = fluorite; Gn = galena; Lin = linarite; Mal = malachite; Qtz = quartz.

Figure 7. (a)-(d) log a_{O2}-loga_{Cl^-} diagram showing the stability relation of the aqueous silver ions/complexes as well as native silver, acanthite and chlorargyrite for different silver-contents of galena, variable pH **(b)** and temperature **(c)**. **(e)** loga_{Ag+} - loga_{Cl^-} diagram showing the stability relation of aqueous silver ions/complexes and chlorargyrite. Different localities showing specific silver and chloride activities are included as numbers (for detailed explanation see Text). Abbreviations: Gn = galena.

Figure 8. Schematic sketch showing the most important pathways for silver mobilization and precipitation during weathering of argentiferous galena (see text for explanation).

Keim et al. Figure 1

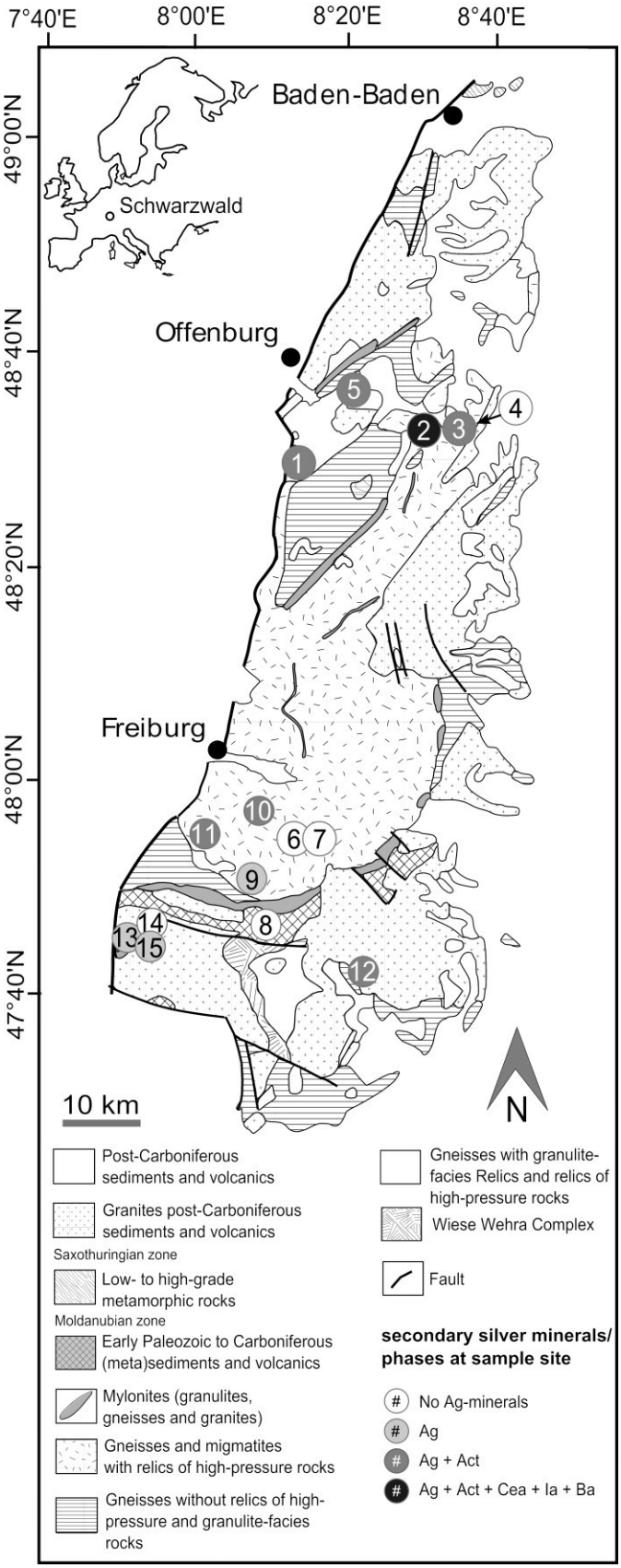

Keim et al. Figure 2

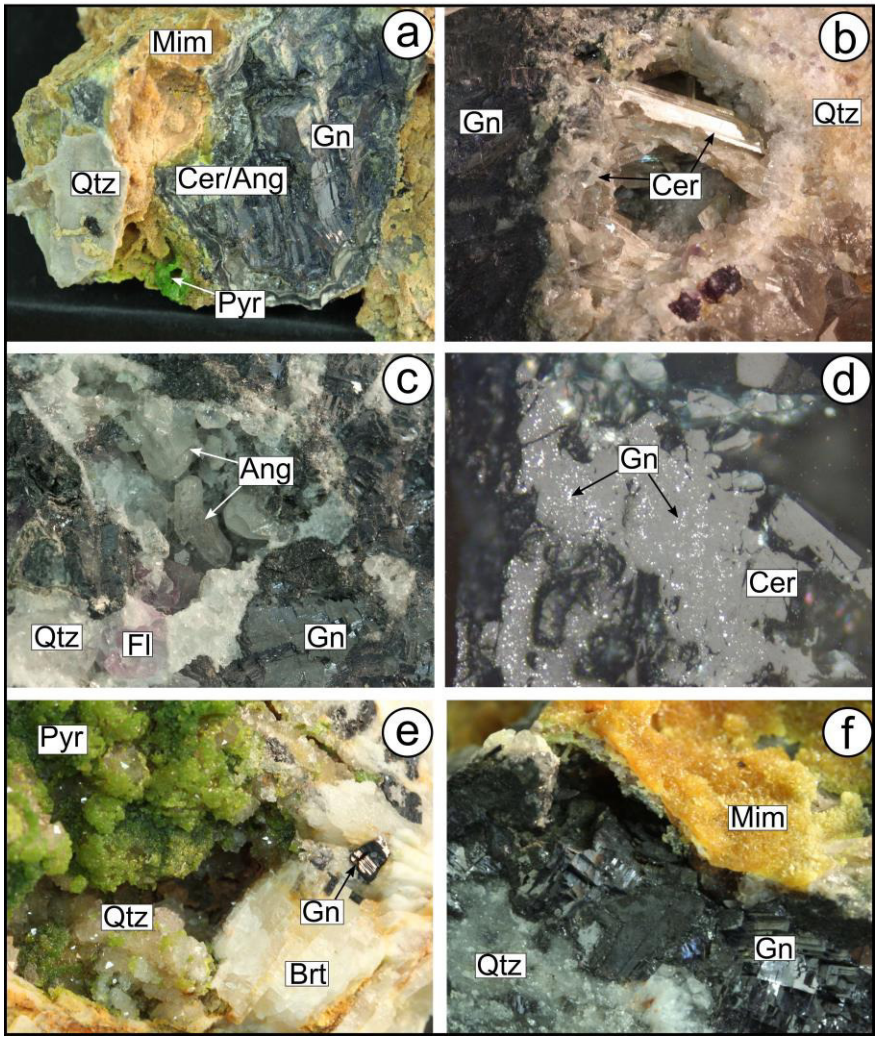

Keim et al. Figure 3

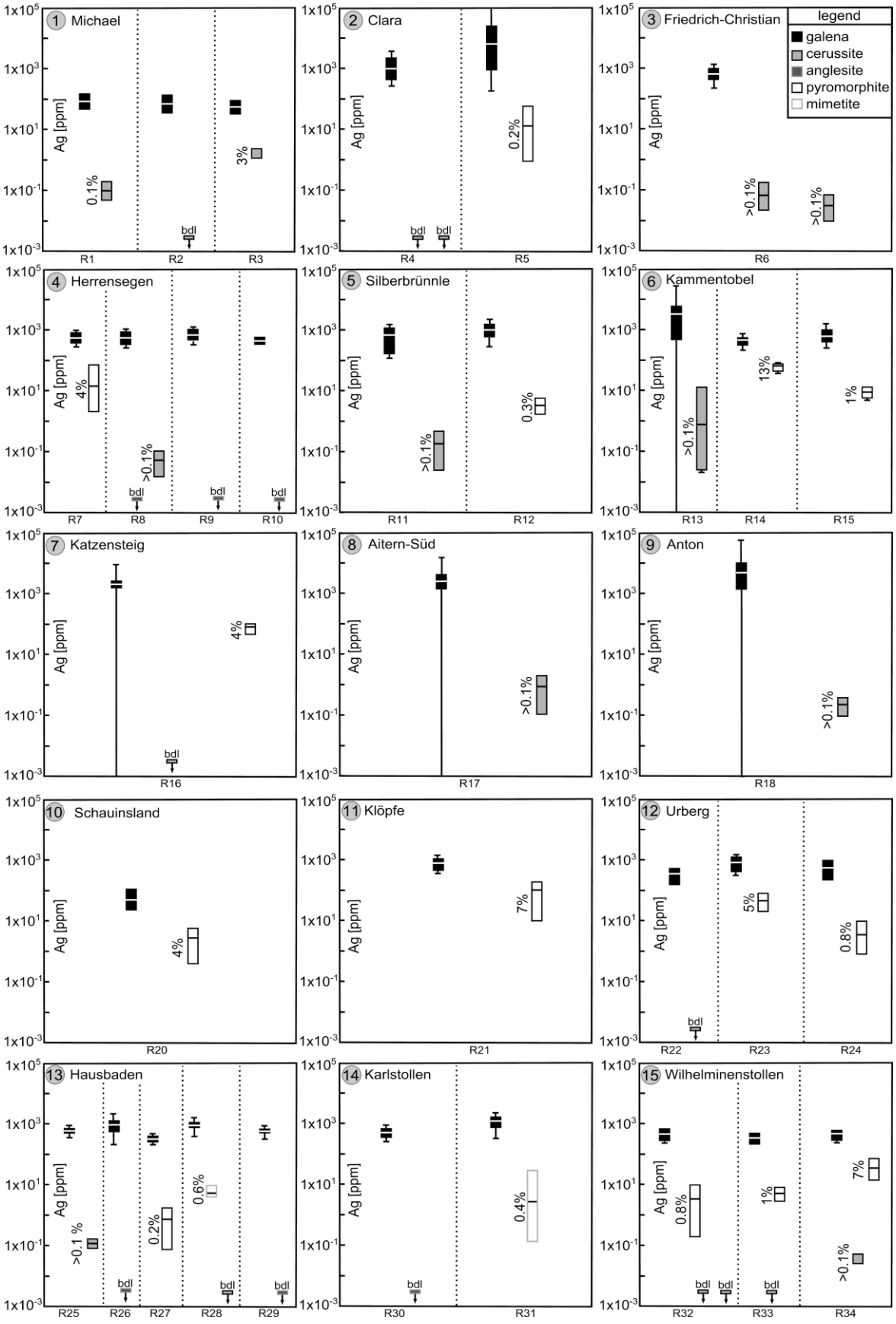

Keim et al. Figure 4

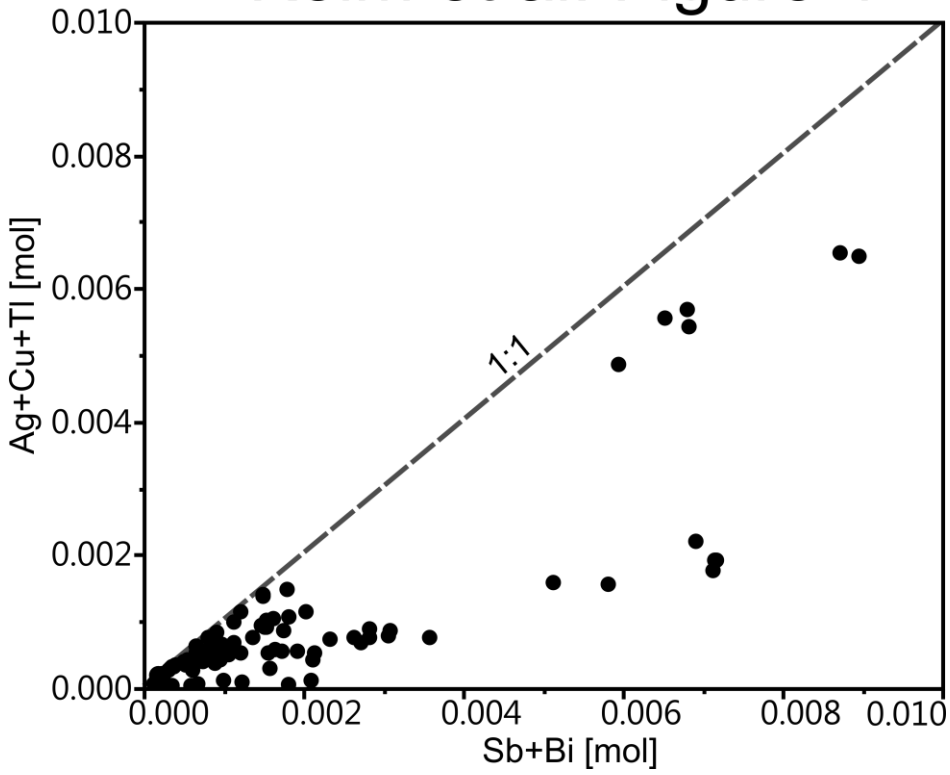

Keim et al. Figure 5

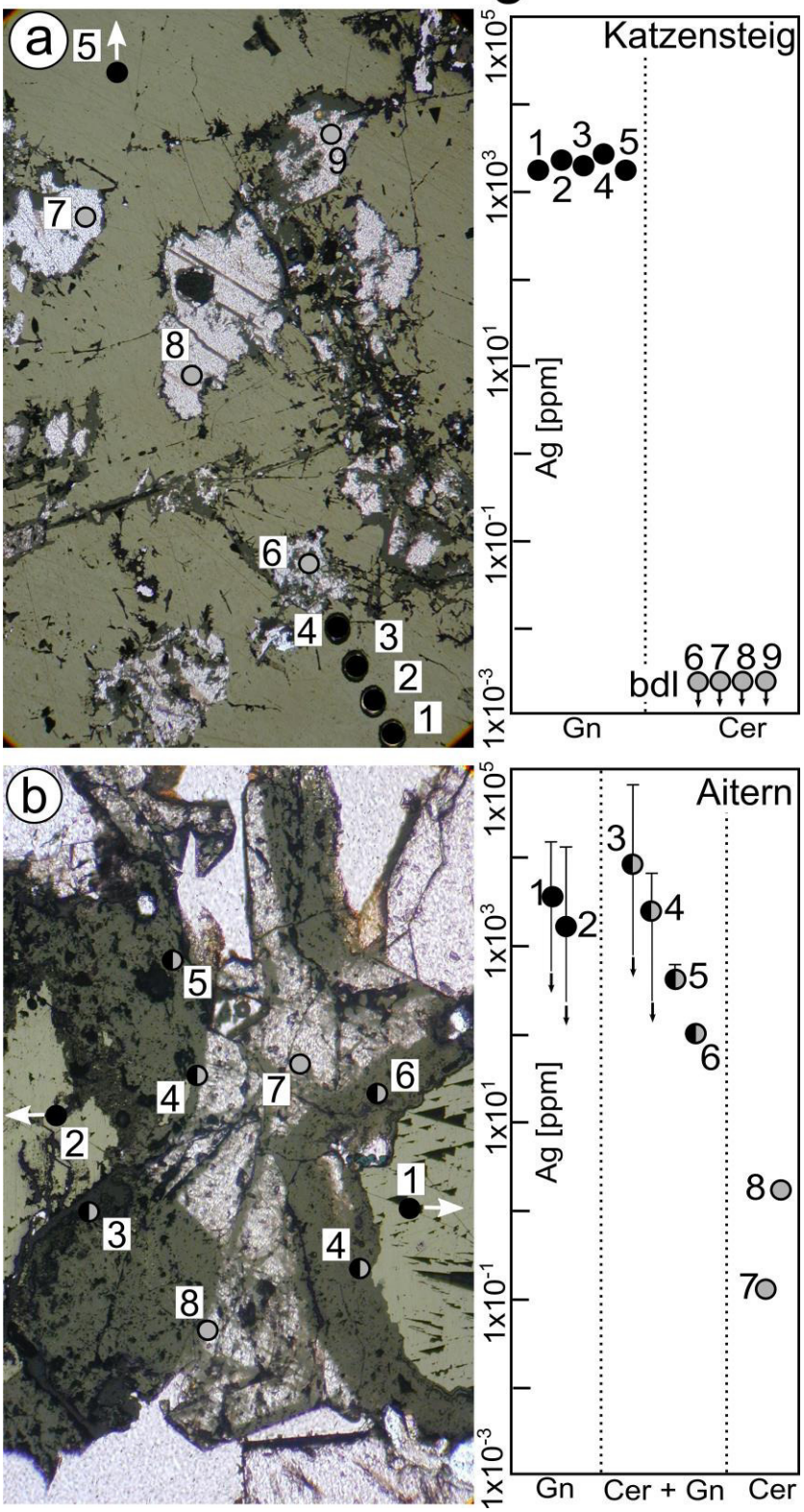

Keim et al. Figure 6

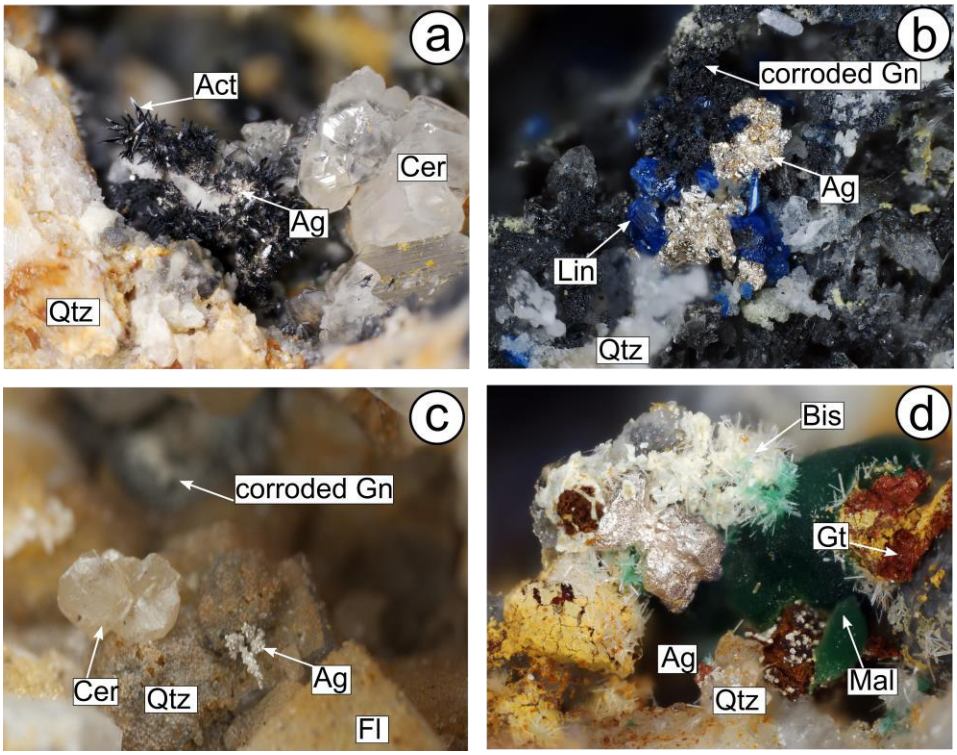

Keim et al. Figure 7

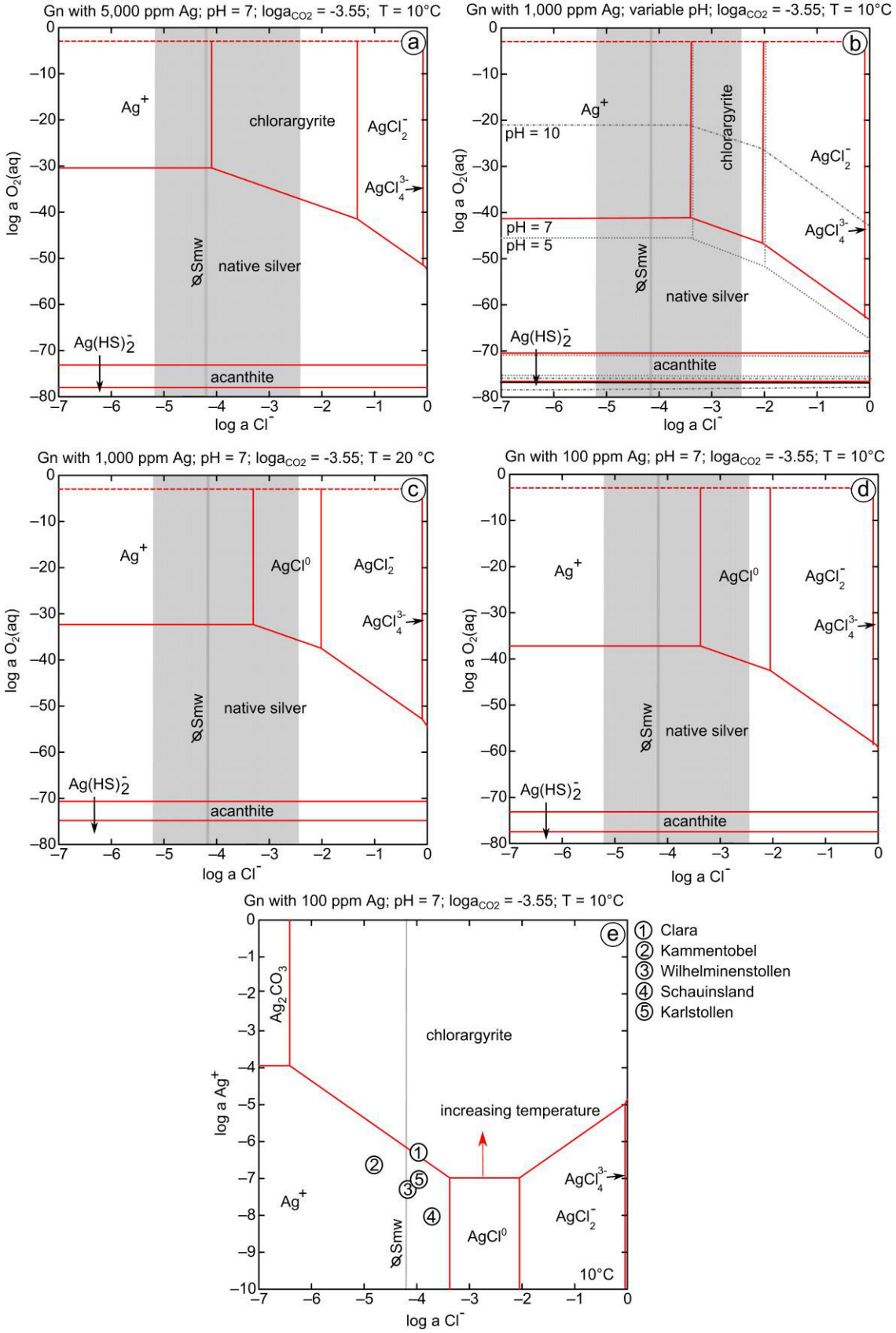

Keim et al. Figure 8

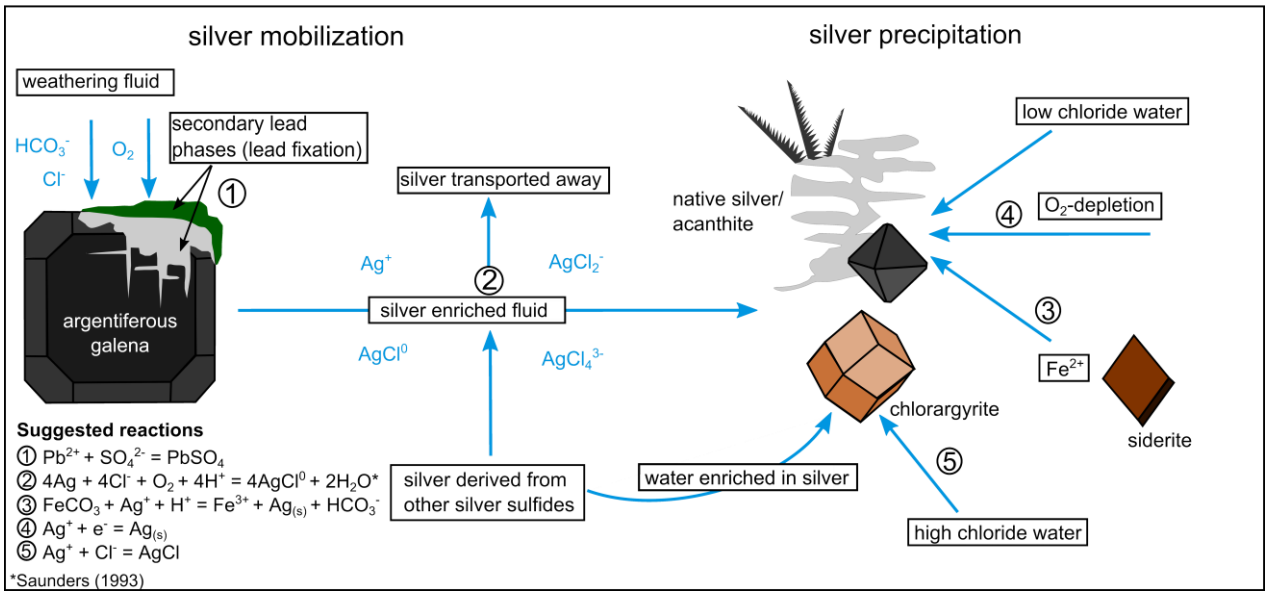

Anhang 3:

Keim, M.F., Staude, S., Marquardt, K., Opitz, J., Bachmann, K., Markl, G. (eingereicht) Weathering of Bi-rich Tennantite.

Akzeptiert zur Veröffentlichung: Nein
Anzahl der Autoren: 6
Position in der Autorenliste: 1

Eigenanteile:

Idee	30%
Datenbeschaffung	30%
Auswertung und Interpretation	30%
Ausarbeitung der Publikation	30%

Staude S.:

Idee	30%
Datenbeschaffung	30%
Auswertung und Interpretation	30%
Ausarbeitung der Publikation	30%

Marquardt K.:

Idee	0%
Datenbeschaffung	15%
Auswertung und Interpretation	10%
Ausarbeitung der Publikation	5%

Opitz J.:

Idee	0%
Datenbeschaffung	15%
Auswertung und Interpretation	5%
Ausarbeitung der Publikation	5%

Bachmann K.:

Idee	0%
Datenbeschaffung	10%
Auswertung und Interpretation	5%
Ausarbeitung der Publikation	5%

Markl G.:

Idee	40%
Datenbeschaffung	0%
Auswertung und Interpretation	20%
Ausarbeitung der Publikation	25%

Da diese Publikation noch nicht „accepted“ ist und der Verlag noch nicht feststeht, wird aufgrund möglicher Copyright Schwierigkeiten darauf verzichtet die Publikation hier zu drucken.

Anhang 4:

Keim, M. F., Markl, G. (2017) Formation of galena pseudomorphs after pyromorphite. Neues Jahrbuch für Mineralogie-Abhandlungen: Journal of Mineralogy and Geochemistry, **194**(3), 209-226.

Akzeptiert zur Veröffentlichung: Ja
DOI: 10.1127/njma/2017/0058
Anzahl der Autoren: 2
Position in der Autorenliste: 1

Eigenanteile:

Idee	40%
Datenbeschaffung	80%
Auswertung und Interpretation	70%
Ausarbeitung der Publikation	70%

Markl G.:

Idee	60%
Datenbeschaffung	20%
Auswertung und Interpretation	30%
Ausarbeitung der Publikation	30%

https://doi.org/10.1127/njma/2017/0058

Formation of galena pseudomorphs after pyromorphite

Maximilian F. Keim*[1], Gregor Markl[1]

[1] Mathematisch-Naturwissenschaftliche Fakultät, Fachbereich Geowissenschaften, Universität Tübingen, Wilhelmstraße 56, D-72074 Tübingen, Germany

* Corresponding author: maximilian-felix.keim@uni-tuebingen.de

Abstract

Galena pseudomorphs after pyromorphite, also called “Blaubleierz” (BBE, blue lead ore in German), is one of the most famous and exceptional European classics among museum mineral specimens. Despite the high interest it has in the museum and mineral collecting community, a detailed textural analysis and the quantitative understanding of the processes leading to its formation by modern mineralogical and hydrogeochemical techniques have not been undertaken yet. In this study, we focus on these remarkable pseudomorphs combining historical mineral samples with water analyses from the Kautenbach Mine near Bernkastel, Germany (the most famous locality of these specimens) and combine them with hydrogeochemical modelling to present a specific formation model for the Kautenbach locality. For textural comparison, mineral samples from the three other known BBE occurrences (Zschopau, Ore Mountains, Germany; Huelgoat, Brittany, France; Wheal Hope, Cornwall, UK) were investigated. Textures from the Kautenbach samples show that galena replacing pyromorphite occurs in symplectic/spongy intergrowth with fluorapatite. On some samples this texture is again overgrown by later pyromorphite. Calculated stability diagrams show that galena and fluorapatite can only coprecipitate in a small pH-f_{O2} range from a (Ca + F)-bearing fluid. The analyzed thermal waters from the Kautenbach mine fulfill these requirements and the formation of BBE is reproduced by a thermodynamic fluid path model using the water analyses.

The spongy appearance of galena at the Kautenbach Mine is also observed at the BBE samples from Wheal Hope and Zschopau. This common textural feature speaks for a 1:1 conversion of pyromorphite to galena/(fluorapatite) caused by the different mineral densities. In contrast to Kautenbach, the spongy appearance at Zschopau and Wheal Hope is not caused by symplectic intergrowth with fluorapatite, but by the appearance of empty cavities. At Huelgoat, galena does not occur spongy, but compact. To form this texture without cavities, additional lead is needed because the amount of lead within prior pyromorphite is not sufficient to form massive galena. Since lead and sulfide cannot be transported by the same fluid due to the low solubility of galena, this feature could possibly be explained by a small-scale fluid mixing of an oxidized supergene lead-bearing fluid with a reduced sulfide-bearing fluid.

In all cases, the formation of BBE impressively shows the drastic change of fluid regimes in these near-surface system. An oxidational milieu forming pyromorphite can change to a reduced sulfide-

bearing one precipitating galena and vice versa. This study, motivates to look at sulfide minerals related to oxidation zones with a different view, especially in the vicinity of thermal fluids.

Keywords: galena, pyromorphite, pseudomorphs, Blaubleierz, fluorapatite, blue lead ore

Introduction

Galena [PbS] pseudomorphs after pyromorphite [$Pb_5(PO_4)_3Cl$] are a sought-after mineral specialty for museums and mineral collectors worldwide. A collection catalogue from 1772, where specimens from the Dreifaltigkeits Mine near Zschopau in Saxony, Germany, are listed, represents the earliest written document on such specimens (Born 1772). These samples were not recognized as pseudomorphs but as a discrete mineral and were named "Blaubleierz" by Werner and Hoffmann (1789). This denotation is still in use today and in German literally means blue lead ore. The expression "blue" derives from fine-grained covellite [CuS] on the surface of some BBE samples giving them a shiny blue coating. Blum (1843) was the first to discover that BBE does not represent a discrete mineral but a pseudomorph of galena after pyromorphite. In contrast, Breithaupt (1863) regarded the BBE as a dimorph of galena and named it plumbeine, plumbeus or sexangulite.

BBE is known from only five relevant localities worldwide, namely Dreifaltigkeits (type locality) and Himmelfürst Mines, Saxony, Germany; Kautenbach Mine, Rhineland-Palatinate, Germany; Huelgoet, Bretange, France, and Wheal Hope, Cornwall, United Kingdom (Blum 1843; Gait and Back 1992). By far the most famous and best described locality certainly is the Kautenbach Mine. According to our knowledge, the only locality for galena pseudomorphs after mimetite [$Pb_5(AsO_4)_3Cl$] is the Tsumeb Mine, Namibia (Markl 2014). At Huelgoat, compact galena crystals filled paramorphoses of plumbogummite after pyromorphite. This texture implies a small scale fluid mixing of a lead-bearing oxidized and a reduced hydrogen sulfide-bearing fluid (probably as a consequence of a reaction with hydrothermal or diagenetic pyrite) in the oxidation zone.

During supergene weathering of lead-bearing ore deposits, secondary lead minerals like cerussite [$PbCO_3$], anglesite [$PbSO_4$], and pyromorphite group minerals (PyGM) form, depending on the fluid chemistry (Keim and Markl 2015 and references therein). The PyGM have the general formulae of Pb_5X_3Cl ($X = PO_4$, AsO_4, VO_4). Lead can be substituted by calcium up to a ratio of 3:2 and then the mineral is called hedyphane or phosphohedyphane (Kampf et al. 2006).

In rare cases (see above), pyromorphite can be replaced by galena. The process of pseudomorphing pyromorphite by galena always works from the outside to the inside (Blum 1843; Gergens 1856). Pyromorphite is either entirely or partly replaced by galena (e.g., Jahn 2016 and references therein). Already Nöggerath (1846) noted for the Kautenbach locality that the replacement of the typical oxidation zone mineral pyromorphite by a sulfide (galena) implies a reduced event after the

oxidized supergene weathering. He related this unusual change to the occurrence of bisulfide-rich thermal waters welling up at the Kautenbach Mine.

Although many authors described BBE (especially from the Kautenbach Mine) and postulated its formation in connection to the thermal springs, no study has described the textures of BBE and its conditions of formation by modern mineralogical techniques. Therefore, we focus on water and mineral samples from the Kautenbach locality using electron and ore microscopy, water analyses, and thermodynamic calculations to quantify the BBE appearance. Additionally, mineral samples from Zschopau, Wheal Hope, and Huelgoat were used for comparison.

Geologic setting of the Kautenbach Mine

The Kautenbach Mine lies in the mining area of Bernkastel and is located about 25 km NE of the city of Trier in the Rhenish Massive in Rhineland-Palatinate, Germany. The Kautenbach base metal veins are of post-Variscan age and are hosted by Devonian low-grade metamorphic slates, silt stones, and quartzites partially enriched in diagenetic pyrite [FeS_2] (e.g., Tibbs 2003). The metamorphic schists are overlain by pre-Devonian gneissic basement rocks (Dittmar 1994; Oncken et al. 1999). The veins of the Kautenbach Mine are represented by two parallel NW-SE striking quartz veins dipping to the south (Kronz 2005). The first vein is predominantly mineralized by galena, sphalerite [ZnS], and subordinately chalcopyrite [$CuFeS_2$], pyrrhotite [$Fe_{1-x}S$], fahlore [$(Cu,Ag)_{10}(Fe,Zn)_2(As,Sb)_4S_{13}$], and nickeline [NiAs]. The second vein is mainly mineralized by chalcopyrite at which galena occurs only subordinately (Jahn 2016).

The BBE originates from a galena-dominated vein showing intensive oxidation especially near the crossing point of the so called Wilhelm and Clara Mine (Fig.1). Here, compact and well crystallized pyromorphite together with cerussite appear in an up to 60 cm wide chasm to a depth of 60 m (Nöggerath 1846). Pyromorphite grows directly on the host rock (Gergens, 1856) and was at this place mined historically as a lead and silver ore. For further information on the mining history of the Kautenbach Mine, see the up to date compilation of Jahn (2016).

During mining activities, several thermal springs were encountered at different locations in the mine. The earliest report of a thermal spring welling up in the Wilhelm Mine was by Schreiber in 1795, but he did not describe the exact position. In 1820, another thermal spring was encountered during building of the Deep Kautenbach Mine drainage tunnel, located at the crossing point to the Fuseler Mine, which follows a pottery clay chasm (Jahn 2016 and references therein; c.f. Fig. 1). This thermal spring is called the Old Spring and is situated around 300 m away from the New

Spring, which was encountered in 1882 during pyrite exploration in the Eleonoren Mine, close to the Fuseler Mine (Jahn 2016). Water of this latter thermal spring wells up in two separate sources and is in use by the nearby thermal bath, the Wildstein Therme in Traben-Trarbach. In addition, a thermal spring is described in the BBE-bearing chasm near the Clara Mine (Nöggerath 1846). Directly accessible today are only the New Springs. The Old Spring is indirectly accessible as flowing water at the entrance of the Deep Kautenbach Mine about 250 m away from the actual spring. The spring from the BBE chasm is not accessible any more.

Sample description

BBE from the Kautenbach Mine

Blum (1843) was the first to describe the textures of BBE from the Kautenbach Mine in detail. On the basis of this work and own observations, Nöggerath (1846) differentiated between four different types of BBE:

- Relics of pyromorphite are preserved as small cores
- Very thin crusts of galena around pyromorphite crystals
- Complete transformation of pyromorphite crystals to galena
- Cavernous pseudomorphs, where pyromorphite is partly or completely dissolved and filled by small galena crystals

BBE at Kautenbach Mine occurs either as compact aggregates or as euhedral six-sided prismatic crystals up to 4 cm (Fig. 2a, 2b). Small crystallites are often completely replaced by galena. In contrast, larger ones show often only a partial replacement by galena (Gergens 1856; Fig. 2c). The thickness of the galena crusts varies between <1 mm and a few mm, often within the same sample (Markl 2014). A dull gloss on the surface of fractures was described by Blum (1843) and was interpreted to be the result of a fine-grained mixture of galena and pyromorphite. Pyromorphite shows a dirty-yellow to greenish or brownish color and is in some samples not firmly intergrown with the galena crusts (Nöggerath 1846; Hintze 1933). Galena and pyromorphite may form rhythmic layering, sometimes together with cerussite (Gergens, 1856). Some samples are partly covered by a thin layer of covellite, from which the BBE gets its eponymous blue coating (c.f. Fig. 2a). Additionally, Some BBE samples are overgrown by a later generation of goethite [FeOOH] (Fig. 2c) and/or greenish pyromorphite (Fig. 2d). Botryoidal aggregates of pyrite and marcasite [FeS_2] were also observed on the surface of some samples (Blum 1843; Gergens, 1856; Hintze

160 1933; Fig. 2b). The BBE samples do not show primary galena, however, cubic galena crystals were
161 described to occur in the Kautenbach Mine at other places. These galena crystals are partially
162 overgrown by pyromorphite representing the usual supergene oxidation.
163 Our own investigations on thin sections of three different historical BBE samples show that
164 pyromorphite is present as relic cores in all samples. Therefore, they can be identified with the first
165 and second type described by Nöggerath (1846). The thickness of the crusts varies between <1mm
166 and 4.5 mm. Pyromorphite is pale-yellow, shows a slight zoning in the BSE images and encloses
167 discrete Ca-rich pyromorphite crystals (Fig. 2e). The outer shell in all samples consists of galena,
168 in a symplectic/spongy intergrowth with fluorapatite [$Ca_5(PO_4)_3F$] (Fig. 2e, f). The replacement by
169 fluorapatite/galena also occurs along cracks lancing into the pyromorphite crystal. The spongy
170 appearance of galena/fluorapatite typically mimics the former pyromorphite crystal morphology
171 (Fig. 2f). Fluorapatite also forms euhedral crystals with rhythmic zoning growing on the outer part
172 of the galena/apatite shell (Fig. 2g). Additionally, fine-grained fluorapatite aggregates preferably
173 replace the discrete Ca-rich pyromorphite crystallites enclosed in pyromorphite (Fig. 2e). Pyrite
174 can be found as a few µm thick crusts, typically at the outermost part of the BBE (Fig. 2h). In one
175 sample, a layer of botryoidal goethite retraces the former crystal morphology of pyromorphite and
176 is infiltrated of later galena along cracks (Fig. 2h). Hence, goethite represents a normal supergene
177 weathering product prior to the formation of later galena. Pyromorphite often shows such layered
178 intergrowth with goethite at other localities.
179
180 **BBE from Zschopau, Wheal Hope and Huelgoat**
181 Information on the textures of BBE from the other localities are to our knowledge rare to absent.
182 Macroscopically, BBE from the localities show clear differences. In contrast to the stocky crystals
183 from the Kautenbach Mine (c.f. Fig. 2a), samples from the Huelgoat and Wheal Hope mines are
184 thinner and more prismatic (Fig. 2i, j, k). In contrast to the samples from the Huelgoat, BBE from
185 Wheal Hope does not show relic pyromorphite cores (Markl 2014). Hintze (1933) describes the
186 occurrence of light brown pyromorphite relics and cavernous BBE crystals from Huelgoat.
187 Our own observations on thin sections from these localities show the same spongy appearance of
188 galena for Zschopau and Wheal Hope (Fig. 2l, m) like for the Kautenbach samples. However, the
189 small cavities are not filled with fluorapatite. At the Zschopau locality, a large core of primary
190 pyromorphite is present and galena is partly replaced by later cerussite and anglesite from the
191 margin (Fig. 2m). In contrast to Zschopau, galena from Wheal Hope shows no replacement by later

cerussite or anglesite. At Wheal Hope, no pyromorphite core is present, but small relics of pyromorphite occur in the galena shell (Fig. 2l).

BBE textures from Huelgoat differ from the other three localities and show no spongy appearance of galena. Here, BBE looks either compact with almost no cavities or shows areas with larger cavities up to 100 µm in diameter. Sometimes, these cavities are filled by later euhedral pyromorphite, but no relic pyromorphite is present. Pyrite often forms the base of the BBE crystals at Huelgoat (Fig 2k). Galena is bordered by small euhedral plumbogummite crystals [$PbAl_3(PO_4)_2(OH)_5 \cdot H_2O$] (note that Huelgoat is the type locality of plumbogummite) forming mostly straight grain boundaries, but also grows along cracks to the inner, galena-filled part (Fig. 2n, o). Sometimes, the plumbogummite rim is overgrown by later euhedral galena crystals (Fig. 2o).

Water samples from Kautenbach

For this study, six water samples from Kautenbach were taken. The exact sample localities are recorded in the mine map of Figure 1. From the New Springs in the Eleonoren Mine, water samples were taken from the right (K-1) and from the left spring (K-2). Water was sampled about 400 m apart from the thermal spring from the two water pipes recharging the nearby thermal bath. Furthermore, two water samples were taken from the so called Old Spring at the Deep Kautenbach Mine. The sample K-3 represents flowing water, the sample K-4 stagnating water. Both samples were taken near the mine entrance about 250 m away from the actual spring. In addition, one dripping water sample from the Eleonoren Mine (K-5) and river water from the Kautenbach (K-6) were collected.

Analytical methods

Water analyses

Water samples were filled in 1 L polyethylene bottles, which had been cleaned three times by 2 M HNO_3 and ultra-pure (Milli-Q) water before. Temperature, pH, redox potential, specific conductivity, and alkalinity were determined in the field using a PCE-PHD1 data logger and digital burette from Brand. Triple measurements of major anions (F^-, Cl^-, Br^-, I^-, NO_3^-, PO_4^{3-}, SO_4^{2-}) and cations (Li^+, Na^+, K^+, Mg^{2+}, Ca^{2+}, Ba^{2+}) were performed by a Dionex ICS-1000 ion chromatography at the Department of Geoscience, Tübingen, Germany. The system is equipped

with an IonPac CS 12-A column for cations. For the analysis, the samples were measured undiluted and diluted 1:10 using ultrapure water. During the injection of the samples RC-20/25 and PVDF-20/25, syringe filters were used. Based on routine standard measurements, errors for major anions and cations are generally <10% and detection limits generally <15 µg/L. Duplicated analyses of the (trace) metals Mn, Fe, Co, Ni, Cu, Zn, As, Rb, Sr, Ba, and Pb were conducted using total reflection X-ray fluorescence (TXRF) (see Klockenkämper 1996; Wobrauschek 2007). For the measurements, 190 µL of sample solution were mixed and homogenized with 10 µL of 5 mg/L Se standard solution. Afterwards, two aliquots of 10 µL each were put onto purged quartz-disks, dried at 80 °C and were analyzed with a S2 PICOFOX benchtop TXRF system from Bruker AXS Microanalysis equipped with a Mo X-ray tube, running at 50 kV and 600 µA for 10 min each. Effective detection limits for the analyzed metals lay around 1 µg/L. Based on the frequent analysis of various multi-element standard solutions (Merck, Darmstadt, Germany) and reference material NIST1643c (trace elements in water) the relative standard deviation from the target values for most elements is well below 10%; only for Ba and Fe, larger deviations of up to about 15% were detected.

Geochemical modeling

For calculating stability diagrams, The Geochemist's Workbench in the version 10.0 (Bethke and Yeakel 2015) was used. Fluid modelling was conducted using Phreeqc in the version 2.18.3 (Parkhurst and Appelo 1999). All calculations are based on the thermodynamic wateq4f.dat database (Ball and Nordstrom 1991). For the Phreeqc input code of the Fluid Path model see Appendix B.

Electron microprobe (EMP) and scanning electron microscopy (SEM)

For quantification of the major and minor element composition of pyromorphite, a JEOL 8900 electron microprobe in wavelength-dispersive (WD) mode was used at the Department of Geoscience, Tübingen, Germany. The acceleration voltage was set to 20 kV and the probe current to 15 nA. The beam diameter was 5 µm. The CaK_{α}- overlap by $PbL_{\gamma}1$ was corrected using a factor of 0.00769. For the elements Pb, P, As, and Cl, external pyromorphite and mimetite standards were used following Markl et al. (2014). Matrix corrections were performed according to the JEOL φρz method (Armstrong 1991). Due to the systematic underestimation of phosphorus in samples with

significant calcium concentrations (>130 ppm), the phosphorous contents were corrected by using the apatite standard (Holzäpfel 2010; Eq. 1).

$$P_{corrected} = (\Delta Ca_{standard}) \cdot (Ca_{measured}/Ca_{apatite} \cdot \#P + P_{measured} \quad (1)$$

Here, ΔCa represents the difference between measured Ca and the actual Ca content of the apatite standard. This value is multiplied by the quotient of the measured and actual Ca content of the apatite standard. The phosphorus number #P is defined as #P = P/(As + P + V). $P_{measured}$ represents the measured P content of the sample. The apatite standard was used since its Ca and P contents are well known. Details of the WDS configuration used, standards, counting times of the peak/background, and the average detection limits are summarized in Table A1 in the supplemental material. Visual images and qualitative EDS spectra were obtained using a TM3030+ Tabletop Microscope from Hitachi.

Results

EMP

The EMP measurements of the BBE samples from the Kautenbach locality show that pyromorphite has up to ~10% mimetite component (maximum 2.3 wt.% As; c.f. Fig. 3). Vanadium contents in most samples are below the detection limit of 130 ppm and show maximum contents of 600 ppm. The pyromorphite analyses show either calcium contents below the detection limit (or slightly above) or they contain between ~7.5 and ~10 wt.%. The average structural formula of these Ca-rich regions is $Pb_{3.3}Ca_{1.7}(PO_4)_{2.9}Cl_{1.1}$, which is close to the phosphohedyphane composition. All pyromorphite analyses are chlorine-dominated with no analysis showing F contents above the detection limit of 370 ppm. The growth zonation of the pyromorphite crystals visible in BSE images is caused by small differences in the As and P content - brighter zones show higher As contents.

Besides pyromorphite and phosphohedyphane, also fluorapatite was analyzed, which is in symplectic intergrowth with galena. The fluorapatite shows lead contents of up to ~7 wt.%, is fluorine-dominated, and shows only traces of chlorine and arsenic (average formulae: $Ca_{5.0}Pb_{0.2}(PO_4)_{2.8}F_{1.0}$). For representative measurements see Table 1.

Geochemical characterization of the water analyses

The analyzed water samples show pH values between 2.95 and 8.40. Water samples from the Deep Kautenbach Mine (K-3, K-4) and dripping water from the Eleonoren Mine (K-5) show low pH values ranging from 2.95 to 3.41. Water samples from the New Springs (K-1; K-2) and from the Kautenbach river (K-6) show pH-values between 7.68 and 8.35. Temperatures from the thermal springs range from 16.0°C (stagnating water) to 27.8°C. Electrical conductivity is relatively low, ranging between 229 and 824 µS/cm. The oxygen fugacity calculated from the redox potential of the waters is generally low ranging from log f_{O2} -56.9 to -36.0. The water samples from the thermal springs are Na^+-HCO_3^--SO_4^{2-}-dominated and have fluorine contents up to 460 ppb (K-1). For the thermal springs, the metal(oid) concentrations are generally low and variable, at which the concentrations from the Old Spring (K-3; K-4) are higher. Dripping water from the Eleonoren Mine (K-5) shows also high metal(oid) concentrations compared to the New Springs (K-1; K-2). Iron concentrations of the river water and the New Springs are low, ranging between 3 and 8 ppb, but concentrations from the Deep Kautenbach Mine and the dripping water are much higher between ~1100 and ~2400 ppb Fe. Copper concentrations range from 3 ppb in the river water up to 4600 ppb in water sample of the Deep Kautenbach Mine. For the whole dataset of water analyses see Table 2.

Calculated stability diagrams

Figure 4a shows the stability relation of galena and the supergene lead minerals pyromorphite, cerussite, and anglesite at variable pH and log f_{O2}. Galena is stable over the whole pH range. At low pH, the stability field reaches up to log f_{O2} of -64 and at high pH up to -72. Above, anglesite is stable at low pH (0 to 1.5), pyromorphite at acid to basic pH (1.5 to 12.9) and cerussite at high pH (12.9 to 14). Note that the small stability ranges of cerussite and anglesite are explained by the use of relatively high $H_2PO_4^-$ activities. Figure 4b additionally shows the stability fields of fluorapatite and hydroxyapatite [$Ca_5(PO_4)_3OH$] by using Ca^{2+} and F^- activities from the New Spring water analysis (K-1). Fluorapatite is stable at neutral to slightly basic pH (6.6 to 9.2) and hydroxyapatite at basic pH. At neutral to acidc pH and at highly basic pH, aqueous Ca^{2+} ions and $CaPO_4^-$ complexes, respectively, are predominant. Figure 4c shows the stability relations of pyromorphite, plumbogummite, and hinsdalite [$PbAl_3(SO_4)(PO_4)(OH)_6$] at variable pH and variable log a_{Al3+}. Pyromorphite is stable over the whole a_{Al3+}-range at acid to neutral pH, but its stability field narrows down at high a_{Al3+}. Plumbogummite shows a relatively small stability field

315 in terms of pH, slightly enlarging towards higher a_{Al3+}. Hinsdalite shows the largest stability field
316 reaching from neutral to basic pH over the whole a_{Al3+} range.

317

318 **Discussion**

319 In the following, the hydrological situation and the geochemical character of the fluids from
320 Kautenbach is discussed in order to evaluate which fluid can be responsible for the formation of
321 BBE at the Kautenbach Mine. Based on these findings, the stepwise formation of the BBE is
322 quantified using stability diagrams and fluid modelling. In addition, the textures from the three
323 other known BBE occurrences are compared with the Kautenbach samples.

324

325 **Hydrological situation at the Kautenbach Mine: The BBE formation fluid**

326 The stability diagrams in Figure 4a, b show that the symplectic intergrowth of fluorapatite and
327 galena is thermodynamically only reasonable in the pH range of 6.6 to 9.2 and log f_{O2} range of ~-
328 68 to -88. Water analyses from the New Springs (K-1; K-2), the Old Spring (K-3; K-4) and the
329 dripping water (K-5) do not plot in this field, because the oxygen fugacity of all water analyses are
330 too high (Fig. 4a, b). Additionally, the pH of the waters does not fit to the fluorapatite stability
331 field, except for the analysis of the New Springs. This means, that none of the sampled water
332 analyses could be responsible for the formation of BBE without any modification. However, all
333 waters have already reacted with the atmosphere before the determination by the oxygen probe and
334 hence, their measured oxygen fugacity cannot be regarded as pristine. Reaction with oxygen occurs
335 when the strongly reduced waters come into contact with the atmospheric oxygen in the mines or
336 during discharge in the pipes. Reaction with oxygen can be impressively seen at the Deep
337 Kautenbach Mine and at the sampling point of the dripping water (K-3; K-4; K-5) by the
338 precipitation of large amounts of iron hydroxides. In contrast, no iron hydroxides precipitate at the
339 New Springs (K-1; K-2), indicating a lower Fe concentration, which is confirmed by the water
340 analysis (Table 2).
341 If lower oxygen activities are supposed, one can easily reach the galena stability field for all water
342 samples. The only water analyses additionally plotting in the fluorapatite stability field are the
343 thermal waters from the New Springs (K-1; K-2), rendering them good candidates for the formation
344 of the BBE at the Kautenbach mine and for our fluid path model in the following chapter (Figure
345 4 b).

Why is the geochemical character of the New Springs and the Old Spring so different? All described thermal springs in the Kautenbach Mine are not far apart and thus it is reasonable that they are connected to a larger fluid system. This assumption is important for the later fluid path model, because the thermal spring welling up in the BBE chasm is not available today and we have to assume that the water from the New Springs (plotting in the fluorapatite/galena stability field) is also representative of the thermal spring in the BBE chasm.

As mentioned above, the geochemical character of the main cations and anions, metal(oid) concentrations, and the pH value of the New and the Old spring are chemically quite different (Table 2). If one fluid source for all thermal springs in the Kautenbach Mine is assumed, this discrepancy can be either explained by mixing with an additional fluid or if the water has reacted with different host rock lithologies. In fact, the host rock slates show inhomogeneities being partially enriched in diagenetic pyrite (e.g., Tibbs 2003) and also interstratified by ore-bearing quartz veins (Jahn, 2016). Reaction of the same source fluid with different amounts of pyrite and/or other sulfides could easily explain the variable metal(oid) concentrations and pH, but not the discrepancies of the main cations and anions. In consequence, the reaction with varying host rocks is regarded unlikely.

Since the water analysis from the Old Spring could only be sampled about 250 m away from the actual discharge (Fig. 1), reaction with dripping percolate water during its flow through the mine is very likely. In the case of the New Springs (K-1; K-2), reaction with dripping fluids after the discharge can be excluded because of the direct discharge into a pipe system. If the analyzed dripping water (K-5) from the Eleonoren Mine is mixed 1:1 with the thermal water from the New Springs (average of K-1 and K-2), one gets a very good agreement with the measured concentrations in water from the Deep Kautenbacher Mine (K-3), especially for the main cations and anions (Fig. 5). This is a strong indicator that the water sampled in the Deep Kautenbach Mine represents a mixture of a thermal water (having the same fluid source as the New Springs (K-1; K-2) in the Eleonoren Mine) with percolating water (K-5). In summary, it is reasonable to assume that also the thermal spring welling up in the BBE chasm is connected to the same thermal fluid system as the New and the Old Spring, since it occurs in a close distance (300 m).

Hydrologically, at least two different fluid sources are active at the Kautenbach Mine. The first fluid source is connected to meteoric waters (fluid source A), which have reacted with the host rock schist/pyrite and are now present as dripping water (K-5), having low pH and high metal content. The river water from the Kautenbach is also representative of a meteoric oxidation zone

fluid, although it does not record any intensive reaction with host rock schists. Such a fluid could be representative for the upper parts of the oxidation zone, where fluids have only reacted to a small degree with the host rock. The second fluid source (fluid source B) is connected to a thermal system having high pH values and temperatures. The high pH values around 8.3 and the Cl/Br ratios averaging at 106 from the New Springs are typical of gneiss/granite-related basement waters (Stober and Bucher 1999; Bucher & Stober 2010; Fusswinkel et al. 2013). Consequently, the thermal springs at the Kautenbach Mine are likely to originate from basement rocks at depth. Such rocks are known to occur below the metamorphic slates of the Kautenbach Mine at a depth of less than 3 km (Oncken et al. 1999). A large fault system (Boppard Thrust system) reaching down to this basement (shown by reflection seismic data) in the Kautenbach mining area is a reasonable transport path bringing up such reduced crustal fluids to the surface. The general simplified hydrological model for the Kautenbach mine including the different fluid sources A and B and the sampling localities is presented in Figure 6.

Formation of BBE textures at the Kautenbach Mine

The formation of BBE can be subdivided into three steps and is explained in the following. In addition, the formation steps together with the hydrological situation and the topology of the mine are illustrated in Figure 7.

I. Formation of pyromorphite by supergene weathering. In a first step, the hydrothermally formed galena comes in contact with oxidizing fluids in the supergene zone (fluid source A). The increase in oxygen activity leads to the formation of thermodynamically more stable secondary lead phases (Figure 4a). Which secondary mineral forms depends strongly on the fluid chemistry (Keim and Markl 2015). The large amount of pyromorphite compared to cerussite described by Nöggerath (1846) from the BBE chasm indicates a weathering fluid having sufficient amounts of chlorine and phosphorous (Eq. 2).

$$5PbS + Cl^- + 10O_2 + 3H_2PO_4^- = Pb_5(PO_4)_3Cl + 5SO_4^{2-} + 6H^+ \quad (2)$$

II. Formation of galena by a reduced fluid. In a second step, the supergene pyromorphite comes in contact with the thermal fluids (fluid source B). This drastic change from fluid system A to B can be explained for example by a changing stress regime facilitating the fluid flow from the basement.

In order to model the interaction of the thermal fluid with the supergene pyromorphite, the thermal fluid from the New Spring (K-1) was reacted with $2.5x10^{-5}$ M pyromorphite (input codes for Phreeqc calculations can be seen in Appendix B). Before the reaction with pyromorphite, the fluid was reduced to a $logf_{O2}$ of -70 in order to compensate for the artificial reaction with atmospheric oxygen in the mine (Figure 4d step 1.1). The interaction with the reduced, high pH, and (S + Ca + F)-bearing fluid leads to a coprecipitation of galena and fluorapatite (both saturation indices >0), explaining their symplectic intergrowth (c.f. Fig. 2f). The pH value will change to lower values according to the equation below (Eq. 3; Fig. 4d step 1.2). Note that Breithaupt (1863) believed that BBE was a dimorph of galena and recognized differences in density for galena and BBE. Most likely, this measured discrepancy was caused by the intergrowth of galena with fluorapatite.

$$Pb_5(PO_4)_3Cl + 5Ca^{2+} + 5HS^- + F^- = Ca_5(PO_4)_3F + 5PbS + Cl^- + 5H^+ \quad (3)$$

The reaction shows, that the crucial external factor for forming galena from pyromorphite is the existence of a reduced sulfur species (HS^-) in the fluid which is inseparably tied to the oxygen fugacity. As can be seen in Figure 8, approximately 35% of the total sulfur has to be present as HS^- to reach galena stability, which is realized at $logf_{O2}$ of ~-68. At the oxygen activities chosen for the calculations ($logf_{O2}$ = -70), the reduced species almost equal the oxidized sulfur species. At a pH of 8.8, the hydrogen sulfide activity is log a_{HS^-} = -4.5 compared to a sulfate activity of log a_{SO42^-} = -4.0. Pyrite crusts on the outermost part of the BBE (Fig. 2h) also support the presence of reduced sulfur during the replacement of pyromorphite.

III. Repeated supergene weathering. On the BBE surface, some samples show an overgrowth of later pyromorphite (c.f. Figure 2d). Additionally, Gergens (1856) described alternating crusts of galena and pyromorphite.

In order to get again in the pyromorphite stability field, fluid source A has to become dominant again (Figure 4d step 2). Formation of pyromorphite is possible either by the reaction with the Kautenbach river water, which is representative of an oxidizing fluid with high water/rock (W/R) ratio or with the dripping water, representative of a fluid having a low W/R ratio. The change of the dominant fluid systems could be either connected to tectonics closing or reducing the fluid pathways of the thermal spring or if the total amount of fluid A increases compared to fluid B. Such increased influx of oxidized waters is possibly connected to seasonal or climatic changes. Such a scenario could explain the multiple change of oxidized and reduced conditions forming the alternating layers of pyromorphite and galena described by Gergens (1856). Goethite can be also

441 found on the surface of some BBE samples (Fig. 2c) probably showing the supergene weathering,
442 of the pyrite crusts formed during the BBE formation.
443
444 **BBE from other localities: comparison with Kautenbach**
445 The spongy appearance of galena looks almost identical for Kautenbach, Zschopau and Wheal
446 Hope, implying the same replacement process of pyromorphite by galena. Based on mineral
447 densities from Lide (2005), the volume reduces by about 17.5% during the conversion of galena to
448 pyromorphite. Our own recalculations using image editing of different areas and samples show that
449 the small sponge-like cavities average to ~19% of the total area for these localities, which is in
450 good agreement with the calculated value. This means that pyromorphite is 1:1 transformed to
451 galena at Kautenbach, Zschopau, and Wheal Hope and the spongy textural appearance results from
452 the differences of densities between galena and pyromorphite. The lack of fluorapatite at Wheal
453 Hope and Zschopau can be explained either by a thermal fluid lacking fluorine and/or calcium or
454 by a fluid having a lower pH (c.f. Fig. 4b). The appearance of anglesite and cerussite at the
455 Zschopau locality represents a later supergene weathering process of galena comparable to the later
456 overgrowth of pyromorphite at the Kautenbach Mine.
457 At Huelgoat, the textures of galena replacing pyromorphite look quite different compared to the
458 other localities. Galena shows areas with large cavities (not comparable with the spongy
459 appearance of galena at the other localities) and areas showing almost no cavities. Image analysis
460 shows that at Huelgoat the cavities make up an average of only ~7% of the total area, which is a
461 large discrepancy to the theoretical value for a 1:1 conversion (17.5%). An additional discrepancy
462 at Huelgoat is the rim of plumbogummite, forming a sharp boundary to the massive galena. Since
463 the rim perfectly retraces the former crystal shape of pyromorphite, it is very likely that
464 plumbogummite has overgrown pyromorphite before the actual BBE formation. Such an
465 overgrowth/replacement of plumbogummite is also known from other places. Gait and Back (1992)
466 describe empty paramorphoses of plumbogummite after pyromorphite. In soils, plumbogummite
467 is believed to be the weathering end product because it is less soluble than pyromorphite (Nriagu
468 1974 and references therein; Strawn 2007). Considering the stability diagrams, plumbogummite
469 instead of pyromorphite forms in a relatively small pH range at neutral to slightly acid conditions,
470 depending on the aluminum activity (Fig. 4c). In summary, we suggest that BBE at Huelgoat
471 formed as follows: First, the supergene pyromorphite was overgrown and partly replaced by

plumbogummite (c.f. Fig. 2 n, o), then preferably dissolved leaving empty or almost empty paramorphoses (c.f. Gait and Back 1992) which were then filled and partly overgrown by galena. Due to the low solubility product of galena, it is not possible to transport lead and reduced sulfur (e.g. HS^-) in the same fluid. This supports the conclusion that two fluids had to mix on a small scale in the weathering zone of the Huelgoat deposit to form the galena: One fluid was a normal, more or less oxidized lead- and sulfate-bearing supergene fluid which mixed with a sulfide- bearing one. Such a reduced, sulfide-bearing fluid could be generated in the empty paramorphoses by reaction with pyrite which forms the base of many BBE at Huelgoat (c.f. Fig. 2k).

Conclusion

BBE from the Kautenbach Mine formed during the interplay of an oxidized and a reduced fluid during changing fluid conditions in a hydrothermal system in contact to the oxidation zone. First, the hydrothermal galena comes in contact to oxidizing meteoric fluids forming pyromorphite. This oxidized fluid milieu then changed to reduced conditions. This change could be evoked by a changing tectonic regime, facilitating the ascent of deeper, reducing thermal waters. These fluids replaced the supergene pyromorphite by a symplectic intergrowth of galena + fluorapatite.

New water analyses of the thermal springs welling up in the Kautenbach Mine show that they have high pH values, low f_{O2} and are sulfide-, calcium-, and fluorine-bearing. Stability diagrams and thermodynamic fluid path calculations confirm that the thermal waters are able to coprecipitate galena + fluorapatite during the replacement of pyromorphite, explaining this unusual texture. The high pH and low Cl/Br ratio around 100 of the thermal water implies an origin from underlying granitic/gneissic basement rocks. Later crusts of pyromorphite on the BBE indicate a repeated change of the fluid system to more oxidized conditions. The worldwide rarity of BBE shows that such dramatic changes are very unusual for most oxidation zones.

BBE from the other localities (Wheal Hope, Huelgoat, and Zschopau) show similar replacement textures, but no symplectic intergrowth with fluorapatite. This implies either the formation at other pH values or in contact to a (Ca + F)-poor fluid. The spongy appearance of galena at Kautenbach, Wheal Hope, and Zschopau implies a 1:1 conversion of pyromorphite to galena/(fluorapatite) explained by the different densities of the minerals. At Huelgoat, compact galena crystals filled paramorphoses of plumbogummite after pyromorphite. This texture implies a small scale fluid mixing of a lead-bearing oxidized and a reduced hydrogen sulfide-bearing fluid (probably as a consequence of a reaction with hydrothermal or diagenetic pyrite) in the oxidation zone.

Acknowledgments

We are grateful to T. Wenzel for his friendly assistance during EMPA analyzes. We thank the waterworks of Kröv-Bausendorf and J. Burch for their help during water sampling, G. Stoschek for the help during water analysis and S. Schafflick for the professional sample preparation. This work is a contribution of the r^4 project "ResErVar—Ressourcenpotential hydrothermaler Lagerstätten der Variszіden" funded by the German Ministry of Education and Research (BMBF).

References

ARMSTRONG, J. T., 1991: Quantitative elemental analysis of individual micro particles with electron beam instruments. Springer, New York, USA, 315pp.

BALL, J. W., & NORDSTROM, D. K., 1991: User's manual for WATEQ4F, with revised thermodynamic data base and test cases for calculating speciation of major, trace, and redox elements in natural waters. U.S. Geological Survey Open-File Report, 91-183.

BETHKE, C. M., & YEAKEL, S., 2015: GWB Essentials Guide. Aqueous Solutions. LLC Champaign, Illinois, USA, 149 pp.

BLUM, J. R., 1843: Pseudomorphosen des Mineralienreichs. Schweizbartsche Verlagsbuchandlung, Stuttgart, Germany, 379 pp. (in German)

BORN, I., 1772: Lithophylacium Bornium, Index Fossilium. Wolfgang Gerle, Prague, Czech Republic, 100pp.

BUCHER, K., & STOBER, I., 2010: Fluids in the upper continental crust. –Geofluids, 10, 241-253.

BREITHAUPT, A., 1863: Neue Plemorphien und Isomorphieen. –Berg und Hüttenmännische Zeitung, **22:** 25-27.

DITTMAR, U., 1994: Profilbilanzierung und Verformungsanalyse im südwestlichen Rheinischen Schiefergebirge – zur Konfiguration, Deformation und Entwicklungsgeschichte eines passiven Varistischen Kontinentalrandes. –Beringeria Würzburger geowissenschaftliche Mitteilungen, **17:** 1- 347. (in German)

FUSSWINKEL, T., WAGNER, T., WÄLLE, M., WENZEL, T., HEINRICH, C. A., & MARKL, G., 2013: Fluid mixing forms basement-hosted Pb-Zn deposits: Insight from metal and halogen geochemistry of individual fluid inclusions. –Geology, **41:** 679-682.

GAIT, R. I., & BACK, M. E. 1992: Featured Mineral at the 1992 Tucson Show: Pyromorphite a Review. –Rocks & Minerals, **67:** 22-36.

GERGENS, N.N., 1856: Über einige Pseudomorphosen aus der Bleigrube von Kautenbach bei Berncastel an der Mosel. –Neues Jahrbuch für Mineralogie, Geognosie, Geologie und Petrefakten Kunde, 135-139. (in German)

HINTZE, C., 1933: Handbuch der Minaralogie 1. Band. De Gruyter, Berlin/Leipzig, Germany 1454 pp. (in German)

HOLZÄPFEL, J. 2010: Haupt- und Spurenelementsystematik von Mineralen der Pyromorphitgruppe aus Lagerstätten des Schwarzwaldes. Diplomarbeit, Universität Tübingen, FB Geowissenschaften AB Mineralogie u. Geodynamik, 219 pp. (in German)

JAHN, S. 2016: The Kautenbach Mine Bernkastel-Kues, Rhineland-Platinate Germany. –Mineral Rec, **2:** 191-211.

KAMPF, A. R., STEELE, I. M., & JENKINS, R. A., 2006: Phosphohedyphane, $Ca_2Pb_3(PO_4)_3Cl$, the phosphate analog of hedyphane: Description and crystal structure. –Amer. Miner. **91:** 1909-1917.

KEIM, M. F., & MARKL, G. (2015) Weathering of galena: Mineralogical processes, hydrogeochemical fluid path modeling, and estimation of the growth rate of pyromorphite. –Amer. Miner. **100:** 1584-1594.

KLOCKENKÄMPER, R., 1996: Total-reflection X-Ray Fluorescence Analysis. John Wiley & Sons, New Jersey, USA, 245 pp.

KRONZ, A., 2005: Erzbergbau, Buntmetallmineralisationen und Silber-Metallurgie im Bereich der mittleren Mosel. –Zeitschrift zur Geschichte des Berg- und Hüttenwesens. Fischbacher Hefte, **11:** 2-27. (in German)

LIDE, D. R., 2005: CRC Handbook of Chemistry and Physics. CRC Press, Boca Raton, USA 2661pp.

MARKL, G., 2014: Pyromrophit, Mimetesit und Vanadinit. –Extra Lapis, **46:** 30-35. (in German)

MARKL, G., MARKS, M. A., HOLZÄPFEL, J., & WENZEL, T., 2014: Major, minor, and trace element composition of pyromorphite-group minerals as recorder of supergene weathering processes from the Schwarzwald mining district, SW Germany. –Amer. Miner. **99:** 1133-1146.

NÖGGERATH, J., 1846: Pseudomorphosen von Bleiglanz nach Pyromorphit gebildet, von Berncastel an der Mosel. –Neues Jahrbuch für Mineralogie, Geognosie, Geologie und Petrefakten Kunde, 163-170.

NRIAGU, J. O., 1974: Lead orthophosphates—IV Formation and stability in the environment. –Geochim. Cosmochim. Acta, **38:** 887-898.

ONCKEN, O., WINTERFELD, C.V., & DITTMAR, U., 1999: Accretion of a rifted passive margin: the Late Paleozoic Rhenohercynian fold and thrust belt (Middle European Variscides). –Tectonics, **18:** 75-91.

PARKHURST, D. L., & APPELO, C.A. 1999: User's guide to Phreeqc (ver. 2)-A computer program for speciation, batch-reaction, one-dimensional transport, and inverse geochemical calculations. U.S. Geological Survey Water-Resources Investigations Report, 99-4259.

SCHREIBER, J. G., 1795: Rapport sur les mines situés dans le grand baillage de Trarbach, faisant paritie du douche de Deux-Ponts, sur a rive drouite de la Moselle. –Journal des Mines, **2:** 43-74 (in French).

STOBER, I., & BUCHER, K., 1999: Origin of salinity of deep groundwater in crystalline rocks. –Terra Nova, **11:** 181-185.

STRAWN, D. G., HICKEY, P., KNUDSEN, A., & BAKER, L. 2007: Geochemistry of lead contaminated wetland soils amended with phosphorus. –Environ Geol, **52:** 109-122.

TIBBS, S. L., BRIGGS, D. E., & PRÖSSL, K. F. 2003: Pyritisation of plant microfossils from the Devonian Hunsrück Slate of Germany. –Paläontologische Zeitschrift, **77:** 241-246.

583 WERNER, A. G. & HOFFMANN C. A., 1789: Mineralsystem des Herrn Inspektor Werners mit dessen
584 Erlaubnis herausgegeben von C.A. Hoffmann. –Bergmännisches Journal, **2:** 369-398. (in
585 German)

586 WOBRAUSCHEK, P., 2007: Total reflection x-ray fluorescence analysis, a review. –X-Ray
587 Spectrometry, **36:** 289-300.

588

589 # Tables

590

591 **Table 1.** Representative EMP results for pyromorphite, apatite, and phosphohedyphane.

	samples [wt. %]										
elements/oxides	**60.4**	**60.9**	**60.13**	**61.2**	**61.1**	**62.3**	**62.9**	**60.2**	**62.13**	**61.16**	**61.17**
F	bdl	bdl	bdl	bdl	bdl	bdl	bdl	3.6	3.19	bdl	bdl
As_2O_5	1.1	1.8	2.3	0.84	0.45	0.66	1.2	bdl	bdl	bdl	0.09
P_2O_5*	15.2	15.0	14.5	15.3	15.6	15.4	15.0	38.6	38.6	20.32	19.94
Ag_2O	bdl	bdl	bdl	bdl	bdl	bdl	bdl	bdl	bdl	bdl	bdl
SiO_2	bdl	bdl	bdl	0.02	bdl	0.05	bdl	0.03	0.02	0.06	0.05
SO_3	bdl	bdl	0.01	bdl	0.02	0.04	bdl	0.48	0.01	bdl	0.01
ZnO	bdl	bdl	0.05	0.06	0.01	0.03	bdl	0.04	bdl	bdl	bdl
Cl	3.0	3.0	2.9	2.9	2.98	2.98	2.98	0.01	0.01	3.6	3.4
FeO	0.02	bdl	0.03	0.03	0.01	bdl	bdl	0.17	0.46	0.27	0.54
CaO	bdl	bdl	bdl	bdl	bdl	bdl	bdl	49.5	48.9	9.2	8.2
V_2O_3	bdl	bdl	bdl	bdl	bdl	bdl	bdl	0.03	0.05	bdl	0.01
BaO	bdl	0.01	0.03	bdl	bdl	bdl	bdl	0.06	0.06	bdl	0.03
PbO	80.1	80.4	80.2	80.9	80.9	81.0	80.5	7.4	6.1	64.5	66.6
UO_2	bdl	bdl	bdl	bdl	bdl	bdl	bdl	bdl	bdl	bdl	bdl
total	99.5	100.2	100.0	100.2	99.9	100.3	99.8	100.0	97.4	98.1	99.0
mineral	Pyr	Pyr	Pyr	Pyr	Pyr	Pyr	Pyr	Ap	Ap	Phed	Phed

abbrevations: bdl = below detection limit (For detection limits see Table A1); Pyr = pyromorphite; Ap = fluorapatite; Phed = phosphohedyphane;*P_2O_5 corrected by Eq (1)

592

593

594

595

596

597

598

599

600

601

602

603

604

605 **Table 2.** Water analysis from the Kautenbach locality

	samples					
	K-1	**K-2**	**K-3**	**K-4**	**K-5**	**K-6**
Temp. [°C]	27.1 °C	27.8	24.4	16.0	17.9	9.1
conductivity [mS/cm]	0.448	0.440	0.824	0.318	0.731	0.229
pH	8.3	8.4	3.0	3.0	3.4	7.7
O_2-content[mg/l]	3.6	4.6	6.7	8.0	3.3	10.8
redox [mV]	-121	-64	4	312	240	168
eH*	0.082	0.139	0.211	0.522	0.450	0.385
pe*	1	2	4	9	8	7
fO_2*	-44	-40	-57	-36	-39	-21
$HCO3^-$ content [mg/l]	258	253	nm.	nm.	73	378
F^- [µg/l]	460	207	198	155	258	60
Cl^- [mg/l]	7	7	6	3	5	21
Br^- [µg/l]	60	74	34	33	21	21
NO_3^- [µg/l]	85	29	150	11340	14	21340
SO_4^{2-} [mg/l]	27	26	124	55	154	17
PO_4^{3-} [µg/l]	bdl	bdl	bdl	bdl	bdl	bdl
Li^+ [µg/l]	67	69	59	8	58	1
Na^+ [mg/l]	88	86	57	4	24	14
K^+ [mg/l]	3	3	2	1	2	3
Mg^+ [mg/l]	1	1	5	4	8	6
Ca^{2+} [mg/l]	10	10	15	10	24	15
Sr^{2+} [µg/l]	3	4	6	0	8	2
Ba^{2+} [µg/l]	39	36	41	0	61	30
Mn [µg/l]	35	27	274	11	574	0
Fe [µg/l]	6	8	1094	65	2447	3
Co [µg/l]	<2	<2	127	<2	141	<2
Ni [µg/l]	<2	<2	217	12	275	2
Cu [µg/l]	14	15	4650	154	1990	3
Zn [µg/l]	19	15	636	35	628	6
Ge [µg/l]	<2	<2	<2	<2	<2	<2
As [µg/l]	2	<5	<5	<5	<5	<5
Rb [µg/l]	6	5	5	<1	5	<1
W [µg/l]	<2	<2	<2	<2	<2	<2
Pb [µg/l]	<5	<5	208	225	319	<5

abbreviation: bdl = below detection limit; nm = not measured; *calculated

606
607
608
609
610
611
612
613
614
615

Figure captions

Figure 1. Mine map of the Kautenbach Mine including sample locations and thermal springs. The cross section X-X' can be seen in Figure 6.

Figure 2. (a) BBE together with covellite. (b) Large BBE crystal together with bulbous pyrite/marcasite. (c) Thin galena crust on brownish pyromorphite coated by goethite. (d) Prismatic BBE overgrown by greenish pyromorphite. (e) BSE image of fine grained apatite preferably replacing Ca-rich pyromorphite. (f) BSE image of symplectic intergrowth of galena and apatite replacing pyromorphite. (g) BSE image of euhedral apatite growing on the surface of BBE. (h) Reflected light image of botryoidal goethite, overgrowing and retracing former pyromorphite morphology. Pyrite grows on the outer rim. (i) long prismatic BBE from Wheal Hope. (j, k) prismatic BBE from Huelgoat. (l) BSE image of spongy galena partially replaced by cerussite/anglesite. (m) BSE image of spongy galena partially replaced by cerussite/anglesite. (n, o) BSE images of plumbogummite forming the outer shell of BBE partly overgrown by small galena crystals. Abbreviations: ang = anglesite, cer = cerussite, gn = galena, goe = goethite, mar = marcasite, pgm = plumbogummite, py = pyrite.

Figure 3. EMPA analysis showing the chemistry of pyromorphite/mimetite, phosphohedyphane and fluorapatite from the Kautenbach samples. Stars represent endmember compositions.

Figure 4. (a) log f_{O2} vs. pH stability diagram for the minerals pyromorphite, cerussite and galena (input parameters: T = 25°C; P = 1 bar; log a_{Pb2+} = -3.0; log a_{SO42-} = -2.0; log a_{H2PO4-} = -4.0; log f_{CO2} = -3.40; log a_{Cl-} = -4.0). **(b)** The grey stability fields represent the stability relations of fluorapatite, hydroxyapatite and the aqueous species Ca^{2+} and $CaPO_4^-$ (input parameters: T = 25°C; P = 1 bar; log a_{Ca2+} = -3.79; log a_F = -4.8; log a_{H2PO4-} = -4.0). **(c)** log a_{Al3+} vs. pH stability diagram for the minerals pyromorphite, plumbogummite and hinsdalite (input parameters: T = 25°C; P = 1

bar; log a_{H2PO4-} = -4.0; log a_{SO42-} = -2.0; log a_{Pb2+} = -3 log a_{Cl-} = -4.0; log $f_{O2(aq)}$ = -30) **(d**) Stability diagram of the minerals galena, pyromorphite, cerussite, anglesite, fluorapatite, and hydroxyapatite with modeled fluid path (for further information see text)

Figure 5. Percentaged comparison of the main cations, anions, and metals for fluid K-5 (dripping water), K-1 & K-2 (New Springs) and the calculated fluid expressed as their deviation from fluid analysis K-3 (Deep Kautenbach Mine).

Figure 6. Cross section of the hydrological situation at the Kautenbach mine together with the sampling localities of the water analysis.

Figure 7. Block model for the thermal system of the Kautenbach Mine (left side) and the formation of the BBE textures (right side).

Figure 8. Percentaged distribution of HS^- and SO_4^{2-} at varying logf_{O2} for water analysis K-1. Grey dashed line shows stability transition of pyromorphite and galena.

652 **Figures**

Keim & Markl Figure 1

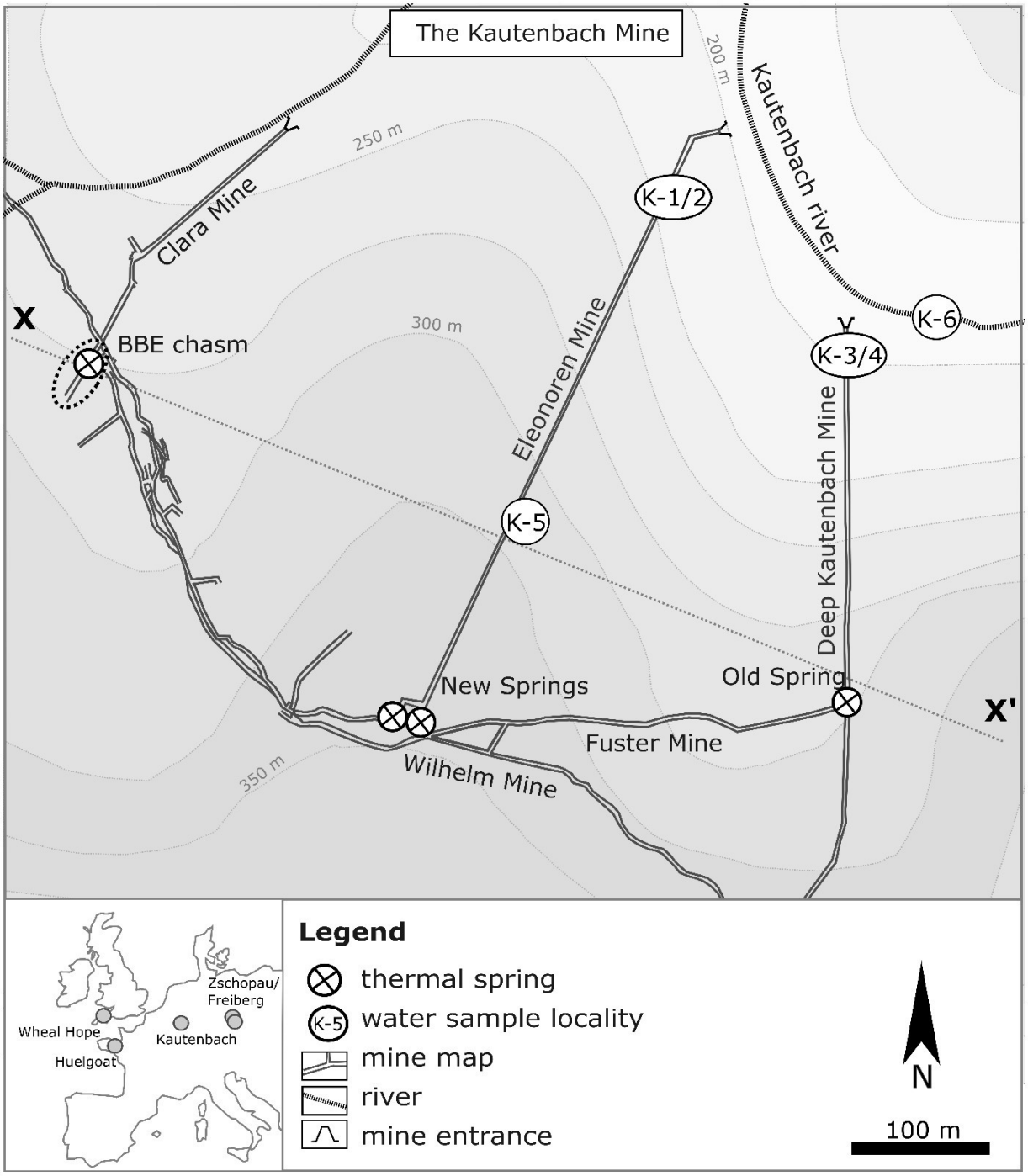

653

654

Keim & Markl Figure 2

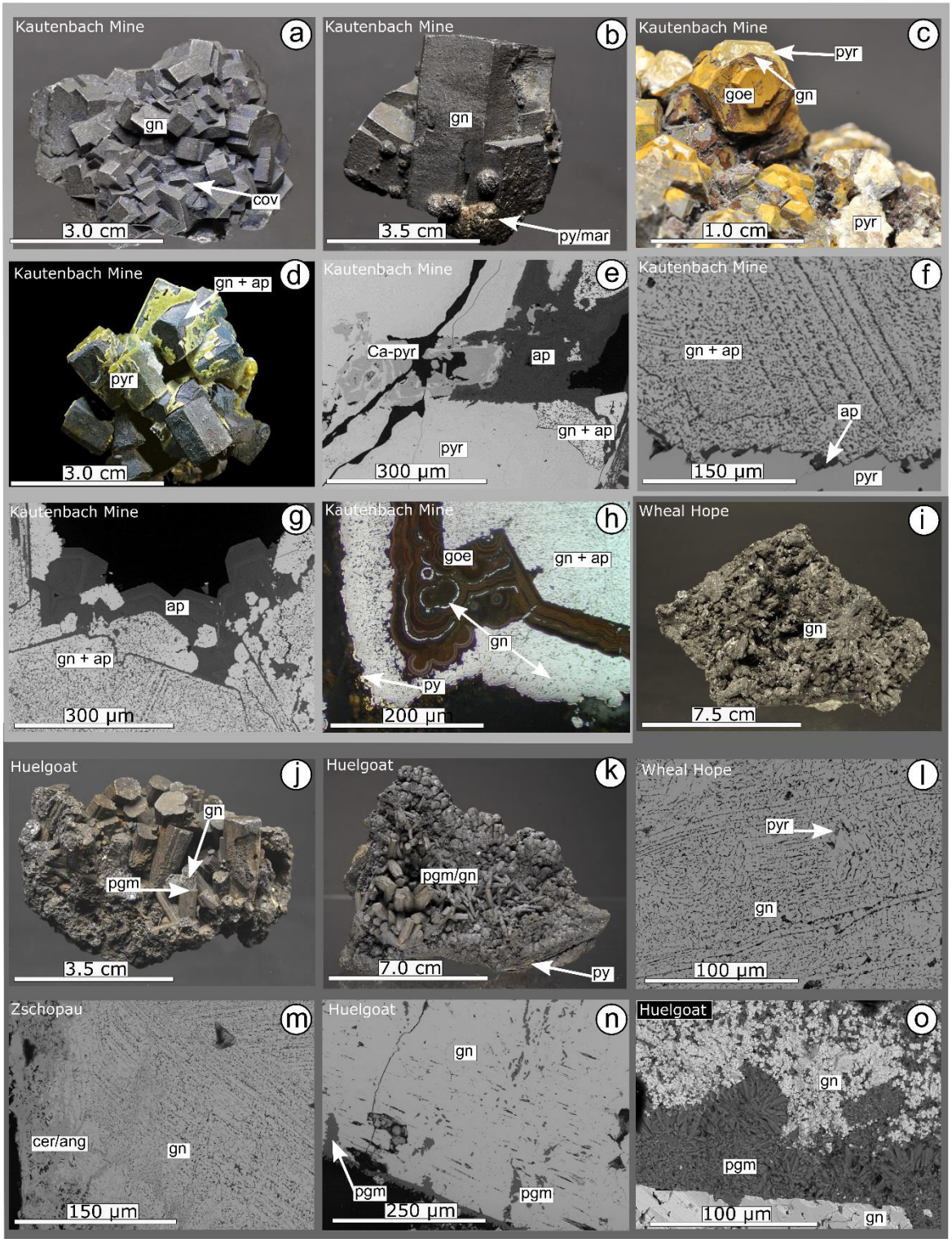

655

656

657

658

Keim & Markl Figure 3

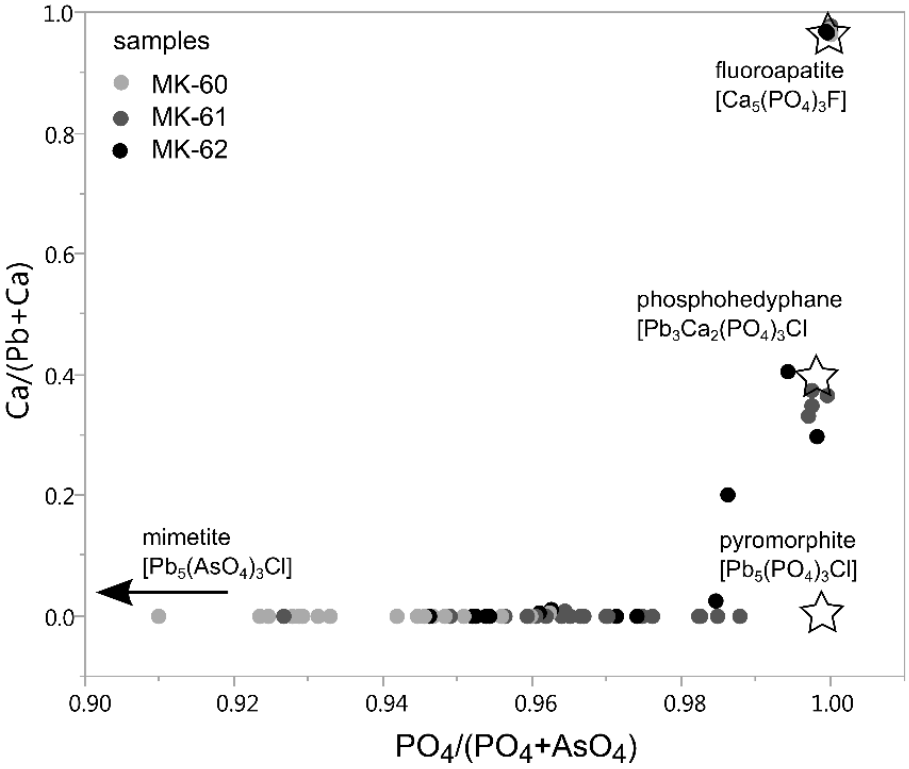

659

Keim & Markl Figure 4

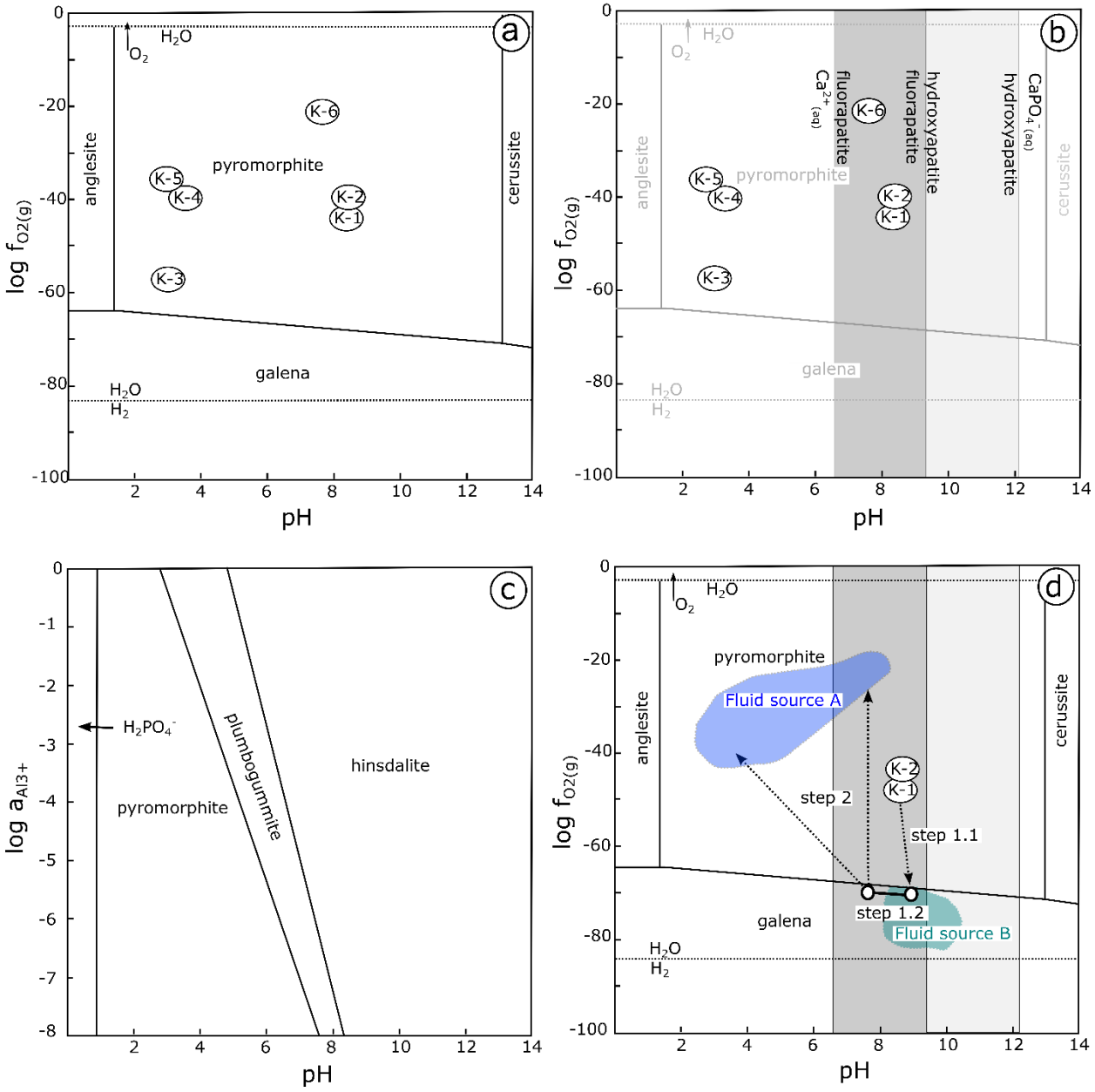

Keim & Markl Figure 5

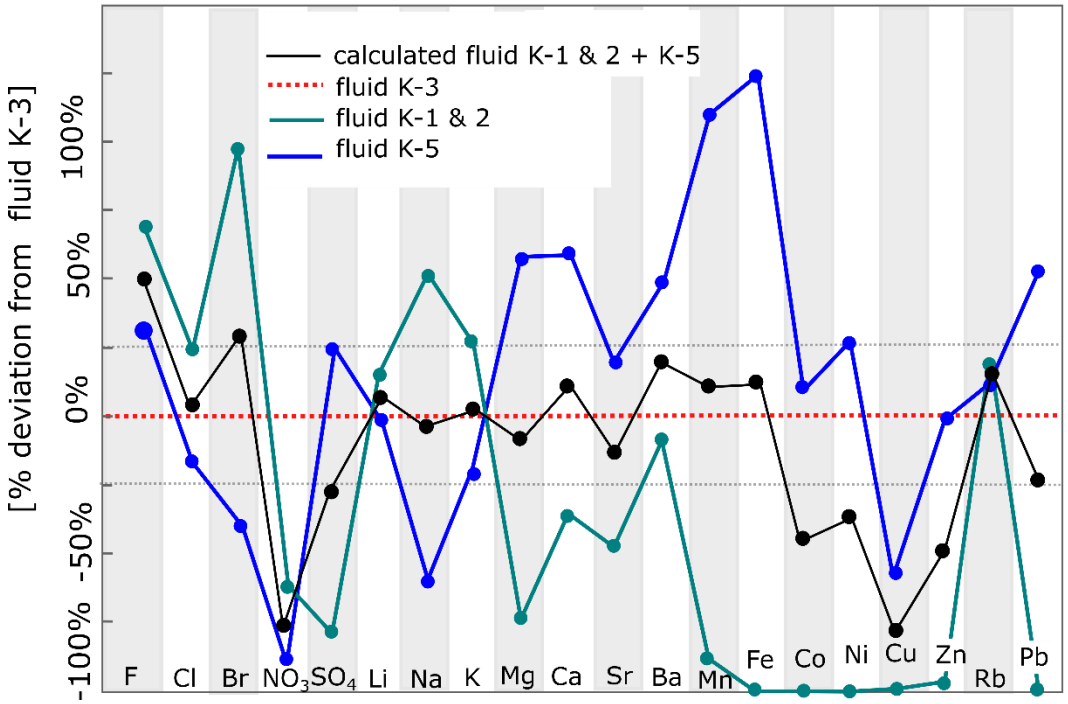

Keim & Markl Figure 6

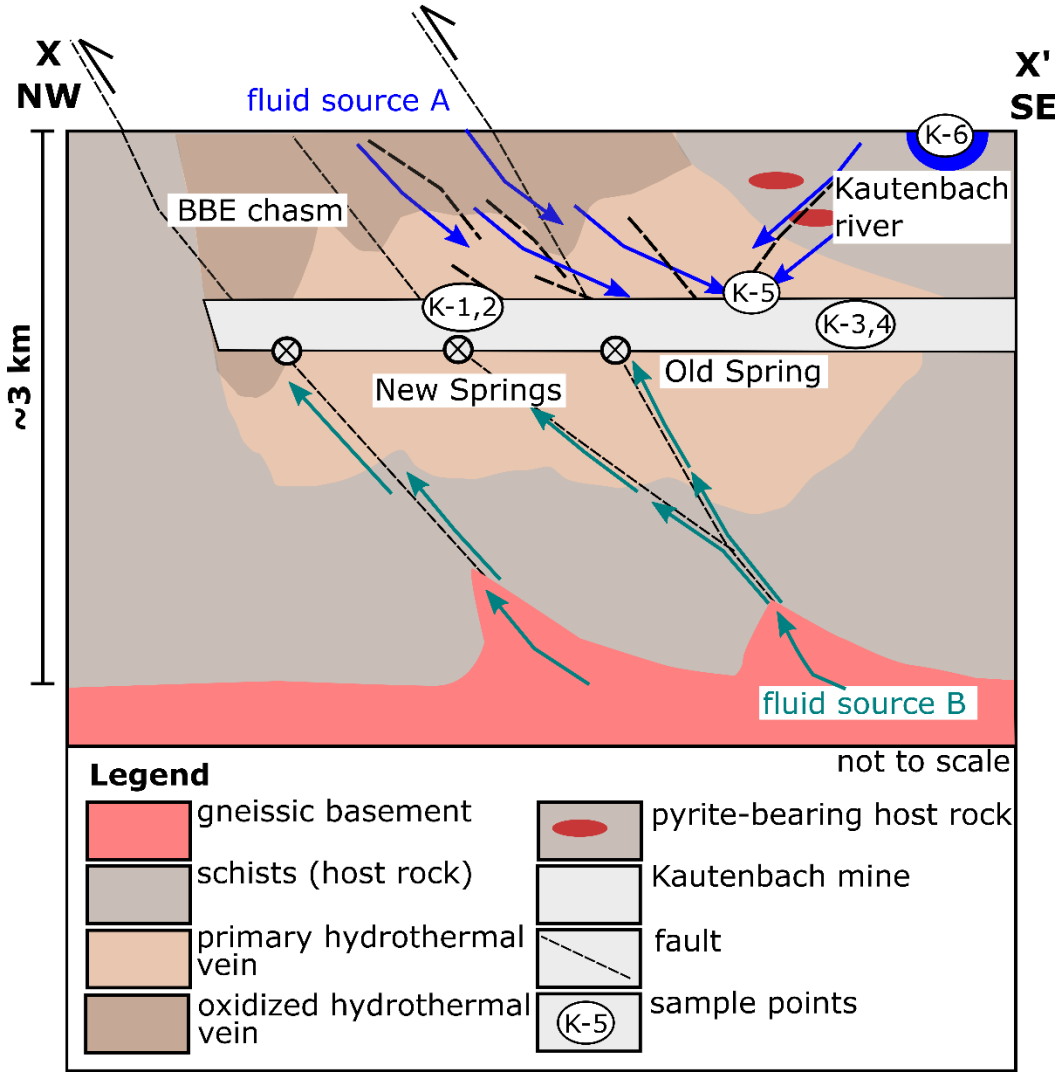

Keim & Markl Figure 7

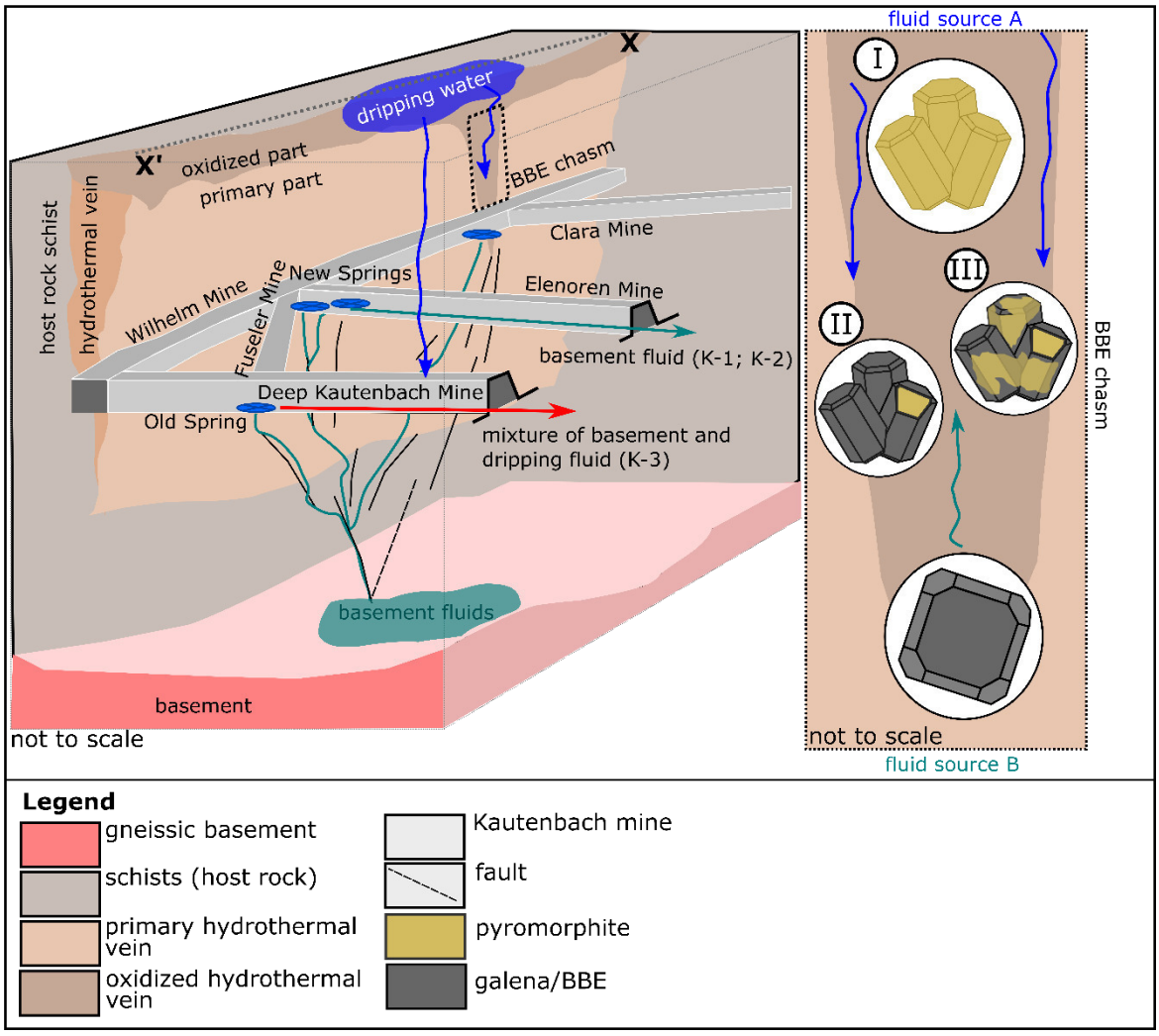

Keim & Markl Figure 8

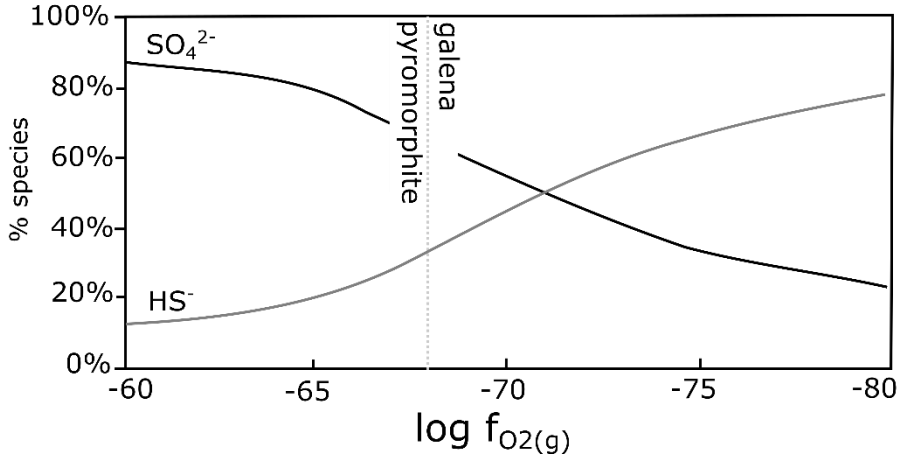

706
707
708
709
710

711 **Authors address**

712

713 Mathematisch-Naturwissenschaftliche Fakultät, Fachbereich Geowissenschaften, Universität

714 Tübingen, Wilhelmstraße 56, D-72074 Tübingen, Germany.

715

716 **Authors mail address**

717 **Maximilian Felix Keim:** maximilian-felix.keim@uni-tuebingen.de

718 **Gregor Markl:** markl@uni-tuebingen.de

Anhang 5:

Keim, M. F., Gassmann, B., Markl, G. (2017). Formation of basic lead phases in anthropogenic influenced and natural environments. American Mineralogist, **102**, 1482-1500.

Akzeptiert zur Veröffentlichung: Ja
DOI: 10.2138/am-2017-5931
Anzahl der Autoren: 3
Position in der Autorenliste: 1

Eigenanteile:

Idee	50%
Datenbeschaffung	80%
Auswertung und Interpretation	70%
Ausarbeitung der Publikation	70%

Gassmann B.:

Idee	0%
Datenbeschaffung	20%
Auswertung und Interpretation	0%
Ausarbeitung der Publikation	0%

Markl G.:

Idee	50%
Datenbeschaffung	0%
Auswertung und Interpretation	30%
Ausarbeitung der Publikation	30%

American Mineralogist, Volume 102, pages 1482–1500, 2017

Formation of basic lead phases during fire-setting and other natural and man-made processes

Maximilian F. Keim[1,*], Bernd Gassmann[2], and Gregor Markl[1]

[1]Mathematisch-Naturwissenschaftliche Fakultät, Fachbereich Geowissenschaften, Universität Tübingen, Wilhelmstrasse 56, D-72074 Tübingen, Germany
[2]Hansjakobstrasse 24, D-79206 Breisach, Germany

Abstract

Basic lead phases are relatively rare compounds occurring in various natural and anthropogenically influenced environments, most importantly those related to fire-setting (FS). The medieval FS mining method and subsequent alteration processes lead to a complex set of basic lead phases including caledonite, hydrocerussite, leadhillite, and lanarkite. Although basic lead phases have been known for over 100 years, their mode of formation and stability relations are only insufficiently known. In this study, the formation of this interesting phase assemblage is described in detail including textures, genesis, and conditions of formation. Samples include ones collected in a medieval mining district in SW-Germany and ones that underwent short-term (50 days) experiments mimicking FS and subsequent mine dump processes. The mode of occurrence and the stability relation of basic lead phases formed during FS is discussed using thermodynamic models that are adapted to also explain their occurrence in other anthropogenic and in natural environments.

Textures indicate a three step development of the FS assemblage starting with formation of cerussite during supergene weathering of primary galena prior to FS. This is followed by the decarbonization of the supergene cerussite during FS leading to the formation of lead oxides. Finally, the newly formed lead oxides were hydrated by rain and soil water in the mine dumps producing basic lead phases. Chemical composition of partially produced melt indicates that FS temperatures of up to 950 °C were reached in rare cases, whereas the lack of melt phase and predominance of litharge and lead oxycarbonates in most other samples implies that temperatures in most cases do not exceed 540 °C. Calculated stability diagrams reveal that most basic lead phases are stable at moderate to high pH and low P_{CO_2}. Thermodynamic models quantitatively explain their formation in the medieval mine dumps by the reaction of the lead oxides with a weathering fluid that increases pH and consumes CO_2 that favors the precipitation of basic lead phases. This also explains the occurrence of basic lead phases in other anthropogenic environments like slag dumps, lead contaminated soils or in contact to concrete, where the reaction of a fluid with portlandite produces high pH and low P_{CO_2}-environments. One possible explanation for the rare formation of basic lead minerals in natural oxidation zones in the absence of lead oxides is the alteration of primary galena under elevated temperatures, since the stability fields of the basic lead phases hydrocerussite and lanarkite are enlarged under elevated temperatures.

The short-term experiments show that the precipitation of basic lead phases is almost independent of the external fluid from which they precipitate. Hence, their stability is controlled by microenvironments formed at the mineral-water interface. Consequently, no closed systems in terms of CO_2 or external high pH-fluids are needed to stabilize basic lead phases in contact with lead oxides. Analyses of the experimental fluid phase show that the solubility of lead in environments, where lead oxides predominate, is mainly controlled by the basic lead phase hydrocerussite. The present study can be used to quantify the formation of basic lead phases at lead contaminated sites or in natural environments. The observations on the natural samples and the experiments show that in specific rock types, like the medieval FS ones, basic lead phases control the availability of the toxic element lead better than anglesite or cerussite over a wide pH-range. In addition, the described FS phase assemblage can help mining archeologists to understand the details of the FS method even without mining traces and provide constraints on temperatures reached during this process.

Keywords: Basic lead phases, fire-setting, stability relation, leadhillite, lanarkite, hydrocerussite, caledonite

Introduction

The worldwide used fire-setting (FS) process is one of the oldest technologies for mining resistive rocks (Craddock 1992; Willies and Weisgerber 2000). The process includes stacking of wood against the rock surface followed by igniting and burning it (Agricola 1556). By this treatment, the uppermost centimeters of the rock are heated up to partial melting (in rare cases) and cracks develop. In some cases, the hot rock was doused with water after the fire ceased. Depending on the rock type this causes further cracking (Haupt 1884; Craddock 1992). At these sites, a characteristic phase assemblage first described by Wittern (1988, 1994) developed. The assemblage involves the oxides minium, massicot, litharge, and tenorite and the basic lead phases

* E-mail: maximilian-felix.keim@uni-tuebingen.de

0003-004X/17/0007–1482$05.00/DOI: http://dx.doi.org/10.2138/am-2017-5931

hydrocerussite, caledonite, leadhillite, lanarkite, elyite, chenite, and others. Mineral names used in this paper are for phases having natural equivalents; all phases used in the text, including their formulas, are summarized alphabetically in Table 1. The assemblage was initially known from various locations in Germany (Markl 1991) and has now been found in other places in Europe as well (e.g., Kolitsch 1997). According to Kolitsch and Tillmanns (2003) also lead nitrates like $[Pb_2(OH)_3(NO_3)]$ belong to the FS assemblage. The detailed conditions under which the FS assemblage and related melts form have remained unclear.

Basic lead phases also form in other anthropogenically influenced environments like in smelting slags (e.g., Schnorrer-Köhler et al. 1982; Schnorrer-Köhler 1987, 1988; Ettler et al. 2009b), lead contaminated soils (e.g., Lin et al. 1995, 2015; Lin 1996; Essington et al. 2004; Ma et al. 2007) or if lead ores come in contact with concrete (Kolitsch 2000; Lee 2007). Additionally, basic lead minerals are formed in rare cases during natural supergene weathering of galena (e.g., Ingwersen 1990; Stalder et al. 1998; Young et al. 2005; Anserment 2012; Bowell and Clifford 2014).

Basic lead phases are known to be stable under neutral to alkaline pH-conditions only (Abdul-Samad et al. 1982a; Ingwersen 1990). Stability relations of leadhillite, hydrocerussite, and caledonite were evaluated by Abdul-Samad et al. (1982a) under low P_{CO_2} at 25 °C, at variable pH values and sulfur activities. These diagrams show a relatively small intermediate leadhillite field appearing between the anglesite and cerussite/hydrocerussite boundary (hydrocerussite being stable below a logP_{CO_2} of –3.7). The stability of lanarkite in the Pb-S-O system was calculated by Treiman (1999), which indicates that lanarkite is stable over a wide range of P_{O_2} and a_{SO_4} at slightly basic pH. These data are, however, at odds with the observation, how rare this mineral is in natural environments—less than 10 natural occurrences are known. Little is known about the stability relations of basic lead phases under increased temperatures and under variable (low) P_{CO_2} but Essington et al. (2004) mention the enlargement of the hydrocerussite stability field toward lower P_{CO_2} at slightly higher temperatures of 35 °C.

In this study, the stability relations and modes of formation of caledonite, hydrocerussite, lanarkite, and leadhillite were evaluated with the help of new stability diagrams and fluid path modeling to explain their occurrence during FS. These models were adapted also to unravel the basic lead phase occurrence at other anthropogenic and natural localities. Furthermore, the first detailed textural and chemical study and experiments on the formation of the FS assemblage are presented.

Geologic background

Samples of this study originate from the former mining area at the Altemannfels south of Badenweiler in the Southern Schwarzwald, SW Germany (see Fig. A1 of Appendix[1] A). The Altemannfels is a prominent, tens of meters high-quartz rock formed by hydrothermal waters on the Rhinegraben boundary fault that separates the Rhinegraben in the west from the Variscan basement in the east (Geyer and Gwinner 2011). This rock is mainly composed of different generations of quartz, barite, and fluorite as gangue, which are mineralized by galena, chalcopyrite, and minor sphalerite. Supergene weathering produced secondary lead and copper minerals like anglesite, cerussite, pyromorphite, mimetite, malachite, and azurite (Metz et al. 1957; Schlomann and Steen 1990). Mining at Badenweiler was proven to have started probably in Roman times (Kirchheimer 1976). Mineral samples for this study were taken from an old mine dump right in front of a medieval FS place. Charcoal found in the mine dump was age dated by the CEZ Archaeometry GmbH, Mannheim, Germany, to an age of about 750 ± 21 A.D. (Markl, unpublished data). Besides charcoal relics, the smooth rock face with few or no tool marks, the shape, ash layers, blackened surfaces, and dumps containing typically red-colored rock specimens are distinctive features for such former FS sites.

Methods

All phase and water analyses were conducted at the Department of Geosciences, University Tübingen, Germany.

Electron microprobe analysis (EMPA) and scanning electron microscopy (SEM)

For quantitative and qualitative determination of the major and minor element compositions of the FS-related melt a JEOL 8900 electron microprobe in wavelength-dispersive mode (WDS) was used. The analyses were conducted using a focused beam with 20 nA current and 20 kV acceleration voltage. Matrix corrections were performed according to JEOL φρz method (Armstrong 1991). The elements for the quantitative program were selected after qualitative analyses in energy-dispersive mode (EDS). Fluorine was not included in the program, since WDS-scans on the fluorine *K*α-line yielded no significant signal. For details of the WDS-configuration used, including standards, counting times of the peak/background, and the average detection limits see Table A1 in the Appendix[1] A. On the SEM, visual images and qualitative EDS spectra were obtained using a Hitachi TM3030 Tabletop Microscope.

[1]Deposit item AM-17-75931, Appendix files. Deposit items are free to all readers and found on the MSA web site, via the specific issue's Table of Contents (go to http://www.minsocam.org/MSA/AmMin/TOC/2017/Jul2017_data/Jul2017_data.html).

Table 1. Mineral names, abbreviations, and formulas used in the text

Mineral name	Formula		Mineral name	Formula	
Alamosite	$PbSiO_3$	–	[a]Leadhillite	$Pb_4(SO_4)(CO_3)_2(OH)_2$	ldh
Anglesite	$PbSO_4$	ang	Linarite	$PbCu(SO_4)(OH)_2$	lin
Calcite	$CaCO_3$	–	[a]Litharge	PbO (tetragonal)	lith
[a]Caledonite	$Pb_5Cu_2(CO_3)(SO_4)_3(OH)_6$	cld	Malachite	$Cu_2(CO_3)(OH)_2$	mal
[a]Cerussite	$PbCO_3$	cer	[a]Massicot	PbO (orthorombic)	mas
Chalcopyrite	$CuFeS_2$	ccp	Mimetite	$Pb_5(AsO_4)_3Cl$	–
[a]Chenite	$Pb_4Cu(SO_4)_2(OH)_6$	che	[a]Minium	$Pb^{4+}Pb_2^{2+}O_3$	min
[a]Elyite	$CuPb_4O_2SO_4(OH)_4{\cdot}H_2O$	elt	Portlandite	$Ca(OH)_2$	–
Galena	PbS	gn	Pyromorphite	$Pb_5(PO_4)_3Cl$	–
[a]Hydrocerussite	$Pb_3(CO_3)_2(OH)_2$	hcer	[a]Scotlandite	$PbSO_3$	scd
[a]Lanarkite	Pb_2OSO_4	lan	Shannonite	Pb_2OCO_3	shan
Larsenite	Zn_2SiO_4	–	[a]Tenorite	CuO	–

[a] Minerals of the FS assemblage after Wittern (1988, 1994).

Geochemical modeling

To evaluate the stability relations among the basic lead phases, stability diagrams were calculated using The Geochemist Workbench in the version 10.0 (Bethke and Yeakel 2015). Fluid evolution paths and saturation indices were calculated using PHREEQC in the version 2.18.3 (Parkhurst and Appelo 1999). All calculations are based on the Thermoddem database (Blanc et al. 2012).

Solubility constants ($\log K_{sp}$) for leadhillite, caledonite, and linarite were taken from Abdul-Samad et al. (1982a). Since Abdul-Samad et al. (1982a) did not provide adequate information about the thermodynamic data used for the determination of the $\log K_{sp}$, there is a potential source of error combining the solubility constants from Abdul-Samad et al. (1982a) with the Thermoddem database. Therefore, we decided to re-determine the solubility constants of caledonite, linarite, and leadhillite with PHREEQC, using the solution composition of the solubility experiments from Abdul-Samad et al. (1982a). To correct the electrical charge balance of the solutions, we chose NO_3^- as passive anion. The re-determined $\log K_{sp}$ for caledonite (–26.24) differs only slightly (1.35%) from the literature value (–26.60). Also for linarite, the calculated $\log K_{sp}$ (–3.64) only differs by 1.1% from the literature value (–3.60). These small differences have only small effects on the size of the calculated stability fields.

For leadhillite, however, PHREEQC failed to converge on the solution composition from Abdul-Samad et al. (1982a) and it was not possible to re-determine the $\log K_{sp}$ in the same manner as for caledonite and linarite. We therefore assume that for leadhillite the discrepancy between the value of Abdul-Samad et al. (1982a) and a re-determined value would be in the same range as for caledonite/linarite (maximum deviation of 1.35%). For plotting leadhillite in the stability diagrams, we decided to take the $\log K_{sp}$ value from the literature (–26,70, Abdul-Samad et al. 1982a) adding a precental error of ±1.35% to it. To show these uncertainties, the stability field of leadhillite is bounded by thick gray bars instead of thin black lines. The thickness of the gray bars represents the ±1.35% uncertainty. For the calculation of the fluid path and the saturation indices, consistently the solubility constant of –26.30 (–26.70 + 1.35%) for leadhillite was taken. The input codes for the calculated fluid paths are presented in Appendix[1] B, the used $\log K_{sp}$ and ΔH values are reported in Appendix A, Table A2.

Micro-Raman spectroscopy

Micro-Raman analyses of phase grains and thin sections were performed using a confocal Reinshaw InVia Reflex Raman spectrometer with a laser wavelength of 532 nm and 20–25 mW power. The used 50× objective results in a numerical aperture of 0.55 with an opening angle of 66.7°. The diameter of the laser spot is ~2 µm. Measurement time was set to 30 s with a three to five-rate accumulation. WiRE 3.0 software was used and the measured Raman shifts were compared with the RRUFF database (Downs 2006).

µXRD analysis

X-ray microdiffraction was used to characterize fine-grained phase aggregates or mixtures. Measurements were performed on a Bruker D8 Discover GADDS Θ/Θ microdiffractometer with a Co-Anode (wavelength λ = 1.79 Å) at 30 kV, 30 mA, and room temperature. Monocapillary optics of 500 µm with 300 µm pinhole and a two-dimensional VÅNTEC500 detector was used (see Berthold et al. 2009). The patterns were integrated individually for each sample with a step size of 0.05 °2Θ. The incident angle was fixed to 15° and measurement time was set to 120 s per frame.

Experimental setup to simulate the FS process

To simulate the FS and the subsequent processes on the mine dump, experiments were conducted. Weathered rock samples from Badenweiler and mineral separates were collected, which consisted of quartz, barite, chalcopyrite, and partially weathered galena. Supergene weathering products were mainly cerussite and smaller amounts of malachite, anglesite, pyromorphite, and covellite.

The mineral separates (galena, chalcopyrite, malachite, and anglesite) were crushed down to a grain size of 0.5–1.5 mm. It was not possible to crush cerussite in the same way because of its fibrous habit. Generally, cerussite grainsize varied between 15 and >1 mm.

For simulating the FS process, the Badenweiler sample material was heated for about 120 min to ~700–800 °C using a wood stove. The cerussite and malachite mineral separates were heated using small ceramic bowls and a Bunsen burner at ~650 °C for about 15 min to get complete transformation to lead (massicot-litharge) and copper (tenorite) oxides, respectively. To simulate the processes in the mine dump, we chose to use two different pH setups to figure out the impact of this external factor on the formation of basic lead phases and their capability to control the availability of lead in aqueous systems. The first setup (A) was prepared with Milli-Q water equilibrated with the atmosphere, resulting in an initial pH of 6.0. The second setup (B) was prepared from river water mixed with wood ash, resulting in an initial pH of 9.7. This was done by mixing 1.0 L river water with 1.8 g wood ash. Since rainwater was not available for setup (B), river water was chosen because its composition is closer to rainwater than Milli-Q water. Wood ash was chosen for the high-pH setup, since charcoal and wood ash were typically thrown on the mine dump after FS (Willies and Weisgerber 2000). This habit was certainly important for creating a high-pH environment.

Five different mineral sets for each pH-setup were chosen (see Table 2). All experiments dealing with mineral separates (A1–A4, B1–B4) were conducted with 13 g of mineral material and 60 mL of water (W/R ~4.5) and were stored in tumblers at room temperature (~20–25 °C) for 50 days. Also the Badenweiler sample material was stored in 60 mL of water (W/R of A5 = 1.4; W/R of B5 = 1.1). To prevent evaporation of the fluid, the tumblers were covered (not airtight). The coverage was removed for 15 min every day for equilibration with the atmospheric gases. Water samples were analyzed before the experiments and after 50 days at the end of the experiments by using a pipette removing the supernatant solution. The alkalinity of the solution was calculated, since the amount of water was too low for double titration.

Water analyses

Duplicate water analyses were performed before and after the experiments. Temperature, pH, and specific conductivity of the weathering solutions were determined using a PCE-PHD1 data logger. Major anions (F^-, Cl^-, Br^-, NO_3^-, PO_4^{3-}, SO_4^{2-}) and cations (Li^+, Na^+, K^+, Mg^{2+}, Ca^{2+}, Ba^{2+}) were determined by a Dionex ICS-1000 ion chromatography system equipped with an IonPac CS 12-A column for cations. All samples were diluted 1:1 with MilliQ-water to get adequate amounts of sample water. Disposable syringe filters (RC-20/25 and PVDF-20/25) were used during injection of the samples. Based on routine standard measurements, errors for major anions and cations are generally ~10% and detection limits generally <15 µg/L.

All samples were analyzed by total reflection X-ray fluorescence (TXRF) (see Klockenkämper 1996; Wobrauschek 2007) for the following (trace) metals: Mn, Fe, Co, Ni, Cu, Zn, As, Rb, Sr, Ba, and Pb. First, 190 µL of sample solution were mixed and homogenized with 10 µL of 5 ppm Ga solution as internal standard. Then, two aliquots (each 10 µL) were put onto polished quartz disks, dried at 80 °C and subsequently analyzed with a S2 PICOFOX benchtop TXRF system from Bruker AXS Microanalysis equipped with a Mo X-ray tube, operating at 50 kV and 600 µA for 10 min. Effective detection limits for the above named elements are around 1 µg/L. Based on the repetitive analysis of various multi-element standard solutions (Merck, Darmstadt, Germany) and reference material NIST1643c (trace elements in water), the relative standard deviation from the target values for most elements is below 10%; only for Ba and Fe, larger deviations of up to about 15% were detected. The pH values, TDS, conductivity, alkalinity, and concentration data of the studied water samples are given in Table 3, the original data in Table A3 in the Appendix[1] A.

Results

Sample description

The FS assemblage. Macroscopically, the FS samples are typically red colored (Fig. 1a) and friable to crumbly. Galena is

Table 2. Phase assemblages of the experimental setups

Setup	Phase assemblage	Initial weight (g)	Newly formed phases after 50 days
A1/B1	litharge/masssicot	13	hydrocerussite[A,B]
A2/B2	litharge/massicot + tenorite	6.5/6.5	hydrocerussite[A,B]; cerussite[A,B]
A3/B3	litharge/massicot + chalcopyrite + galena	4.5/4.5/4.5	hydrocerussite[A,B]; cerussite[A]
A4/B4	litharge/massicot + tenorite + anglesite	4.5/4.5/4.5	hydrocerussite[A,B]; cerussite[A,B]; elyite[A]; chenite[A]
A5/B5	Badenweiler sample material	43/55	hydrocerussite[A,B]; elyite[B]; chenite[B]

Note: Superscript A,B indicates in which experiment the newly formed phases occur.

TABLE 3. Analyzed waters of the experiments

	Setup A						Setup B					
Samples	A1	A2	A3	A4	A5	A6	B1	B2	B3	B4	B5	B6
pH	7.4	7.7	7.0	6.2	7.0	6.0	8.8	8.6	7.8	7.1	7.9	9.7
EC [ms]	0.05	0.04	0.05	0.1	0.5	0.001	0.8	1.1	1.1	1.4	1.3	1.1
$(HCO_3)^-$ [mg/L][a] [analyses in µg/L]	29	17	12	4.0	81		273	155	269	389	314	289
IC-data												
Li^+	1	1	2	1	85	n.d.	12	18	17	8	40	16
Na^+	1470	1110	2730	990	7980	n.d.	58300	58800	54300	26400	54040	42300
K^+	960	922	984	793	60700	n.d.	165000	167000	149976	75200	157000	129000
Mg^{2+}	550	628	473	416	3670	n.d.	536	23400	19800	47300	26700	30400
Ca^{2+}	7270	4880	3880	3410	40100	n.d.	3092	24700	23500	103000	52400	53300
Sr^{2+}	850	418	467	487	3130	n.d.	1464	1970	1870	22300	2720	2120
Ba^{2+}	66	87	18	28	83	n.d.	0.0	90	85	28358	97	107
F^-	458	72	259	198	3060	n.d.	1230	321	490	1250	2370	610
Cl^-	36.8	19	24	21	2590	n.d.	593.5	7382	4480	3588	19300	54000
Br^-	5.8	2.8	n.d.	n.d.	12.8	n.d.	n.d.	n.d.	n.d.	5.9	39	36
$(NO_3)^-$	26.9	n.d.	n.d.	6.3	422	n.d.	9099	9050	34810	30577	22700	26200
$(SO_4)^{2-}$	1217	5140	8290	12300	132000	21.9	110000	196808	189000	269110	244000	172100
$(PO_4)^{3-}$	n.d.	n.d.	741	n.d.	n.d.	n.d.	n.d.	n.d.	n.d.	n.d.	n.d.	1220
TXRF data												
Mn	<15	<15	<15	<15	148	<15	<15	<15	<15	<15	17	<15
Fe	<2	<2	<2	3.3	<2	2	<2	<2	<2	<2	<2	<2
Co	<3	<3	<3	<3	12	<3	<3	<3	<3	<3	4	<3
Ni	<3	<3	<3	<3	8	<3	<3	<3	<3	<3	<3	<3
Cu	<3	24	10	378	146	0.7	9	17	55	26	32	<3
Zn	9.8	33	50	137	356	9	<1	17	14	44	27	7.4
As	<5	<5	<5	<5	<5	<5	<5	<5	<5	<5	<5	<5
Rb	3	3	2	0.7	110	<2	178	149	129	124	170	113
Pb	123	269	931	3790	1490	<5	65.8	174	292	529	232	<5

Note: n.d. = not detected; [a] = calculated by charge balance.

in situ converted to cerussite and anglesite along its cleavage planes and grain boundaries. Based on textural observations, these phases are interpreted to have formed before the FS process as normal weathering products. The following phases are texturally later. Fine-grained hematite infiltrates the gangue minerals along cracks and grain boundaries and is responsible for their characteristic reddish color. While anglesite seems to be unaffected, cerussite is frequently replaced by lead oxycarbonates like shannonite and lead oxides like litharge, minium or massicot (Figs. 1b, 2a, and 2d). Often, the replacement leads to complete or incomplete pseudomorphs, typically lanced by cracks (Fig. 1c).

The pseudomorphic lead oxides are frequently overgrown and/or replaced by hydrous phases like leadhillite, lanarkite, hydrocerussite, caledonite, and lead oxide carbonate hydroxide (Figs. 2b and 2c). The phases occur as euhedral crystals (Fig. 1d) and fine-grained aggregates (Fig. 1e). In many cases, replacement is not complete and lead oxides remain as relics (Fig. 1f).

The most frequent newly formed phase is fine-grained hydrocerussite forming white crusts with typical luster on the surface of lead oxides and along cracks (Fig. 1e) or euhedral, hexagonal, colorless platy crystals (Fig. 1g). In some samples, hydrocerussite seems to be an early phase, overgrown by later generations of basic lead phases like caledonite and leadhillite. The monoclinic leadhillite has two polymorphs, the trigonal susannite and the orthorhombic macphersonite, with susannite as high-temperature modification being metastable at ambient conditions (Livingstone 1993). Our XRD results, however, lead to no distinct identification of one of these polymorphs.

Lanarkite is often associated with lead oxides, hydrocerussite, and caledonite forming white, asbestos-like needles (Fig. 1g). The most striking phase in this assemblage is elyite forming crusts, spherulites, or needles of a typical intense purple color (Figs. 1h and 1b). Elyite is a late phase frequently occurring along cracks and at the margin of lead oxide pseudomorphs and is sometimes accompanied by light blue chenite (Fig. 1j). Caledonite forms light blue crusts and bunches (Fig. 1d), leadhillite occurs as (pseudo)hexagonal colorless to pale yellow platy crystals (Figs. 1d and 2c) and as fine-grained pale-yellow aggregates (Fig. 1e) associated with lead oxides, anglesite, hydrocerussite, elyite, and caledonite. The rare sulfite scotlandite forms either small, acute brownish crystals growing in cerussite cavities or bulbous yellowish to brownish crystal aggregates (Figs. 1i and 2c). In most samples, it is almost impossible to determine the paragenetic sequence of the hydrous phases, as they are intergrown chaotically on a very small scale.

Former melt. Very rare specimens show slag-like surfaces or vesicular, glassy, colored crusts that can be macroscopically identified as former melt (Fig. 3a). In thin section, they are texturally composed of a deterred melt (µXRD patterns show no crystallinity) and a crystal phase. Typically, the former melt is characterized by round pores of different size representing former gas-filled bubbles (Fig. 3b). In reflected light, at least four different types of crystals can be distinguished based on reflectance and shape (Type I–IV). The crystals with high reflectance are fibrous (Type I, Fig. 3c), short needles (Type II, Fig. 3d) and blocky (Type III, Fig. 3d). The fourth crystal type forms rectangular, blocky crystals with much lower reflectance (Type IV, Fig. 3d). All of these crystals are intergrown with former melt commonly showing straight grain boundaries and concentric zonation textures.

The former melt phase (glass) can be subdivided texturally in four groups as well (Type i-iv). The first group is glass in direct intergrowth with the different crystal types (Type i; Figs. 3c and 3d), the second is homogeneous glass without crystals (Type ii;

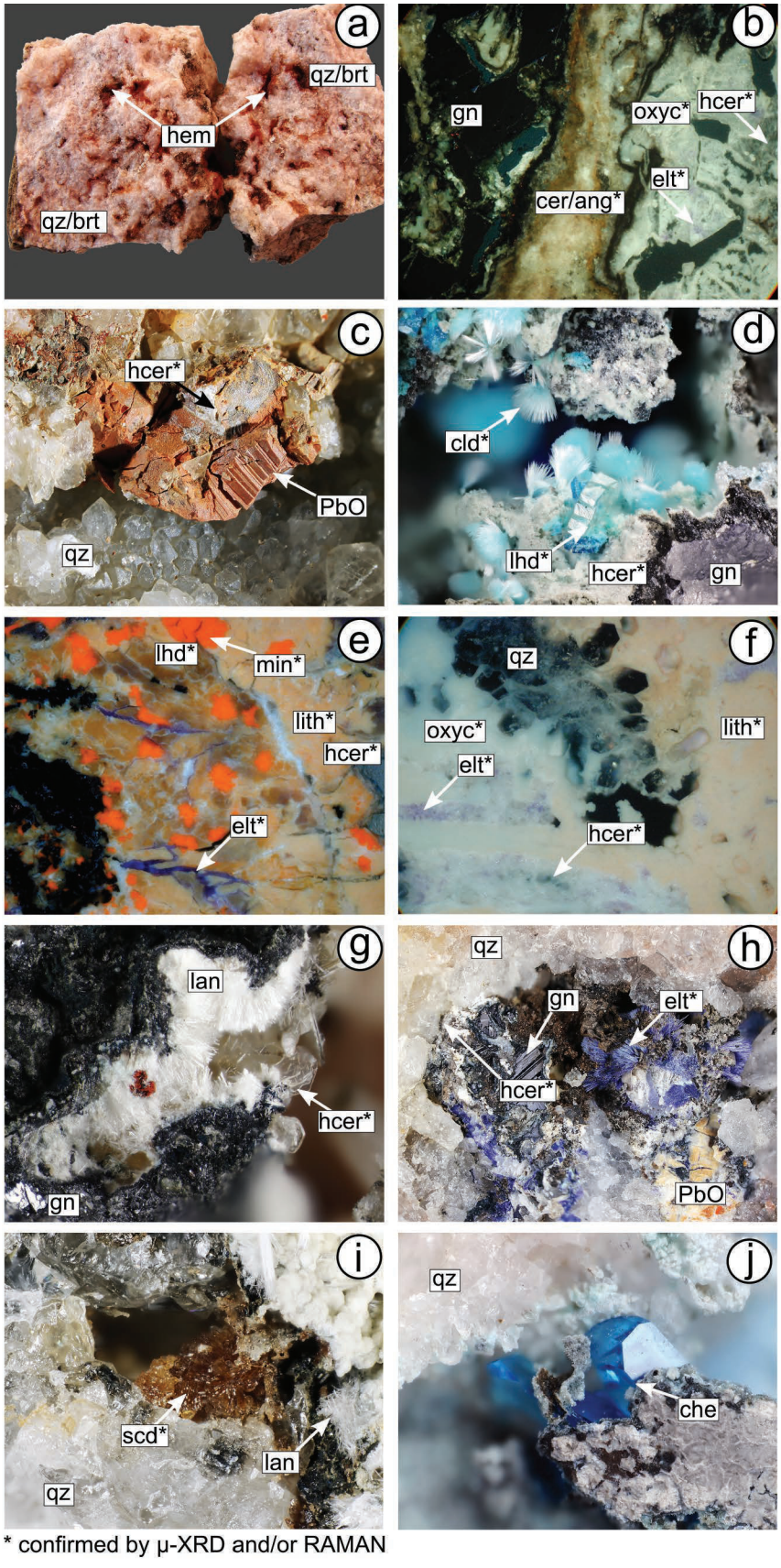

◀**FIGURE 1.** (**a**) Photograph of typical red-colored barite-quartz FS specimens; width of photograph (WoP) = 7 cm. (**b**) Reflected light image with crossed polarizers of galena weathered to cerussite and anglesite. At the rim, cerussite is converted to lead oxycarbonates, which are partly replaced by elyite and hydrocerussite WoP = 860 μm. (**c**) Photograph of lead oxides pseudomorphic after cerussite with typical shrinkage cracks, partly overgrown by hydrocerussite; WoP = 1 cm. (**d**) Photograph of euhedral leadhillite and caledonite crystals growing on hydrocerussite; WoP = 2 mm. (**e**) Reflected light image with crossed polarizers of litharge and minium infiltrated by elyite, hydrocerussite, and leadhillite along cracks; WoP is about 430 μm. (**f**) Reflected light image with crossed polarizers of lead oxy carbonates, partly replaced by litharge. Elyite and hydrocerussite occur along cracks; WoP = 860 μm. (**g**) Photograph of euhedral lanarkite and hydrocerussite; WoP = 1 mm. (**h**) Photograph of euhedral elyite and hydrocerussite growing on lead oxides; WoP = 7 mm. (**i**) Photograph of brownish, bulbous scotlandite crystals aggregates accompanied by lanarkite needles; WoP = 1 mm. (**j**) Photograph of a euhedral chenite crystal; WoP = 1.5 mm. Abbreviations: ang = anglesite, cer = cerussite, che = chenite, cld = caledonite, elt = elyite, fl = fluorite, gn = galenite, hcer = hydrocerussite, lan = lanarkite, lith = litharge, min = minium, oxyc = lead oxy carbonates, PbO = not further distinguished lead oxides, qtz = quartz, scd = scotlandite. (Color online.)

Fig. 3b), the third is lanced by numerous small bubbles (Type iii; Fig. 3e) and the fourth forms layered, zoned textures (Type iv; Fig. 3f). Frequently, the glass encloses or penetrates mineral grains like barite, fluorite, quartz, and/or sphalerite, which show dissolution textures like well-rounded grain boundaries. Small, spherical metal inclusions with high reflectance are frequently enclosed in the former melt (e.g., Figs. 3b and 3d).

Compositional variations of former melt and associated crystal phases

Former deterred melt and crystal phases formed during FS were investigated in four samples with a total of about 300 analyses (the whole data set is reported in the Appendix[1] A,

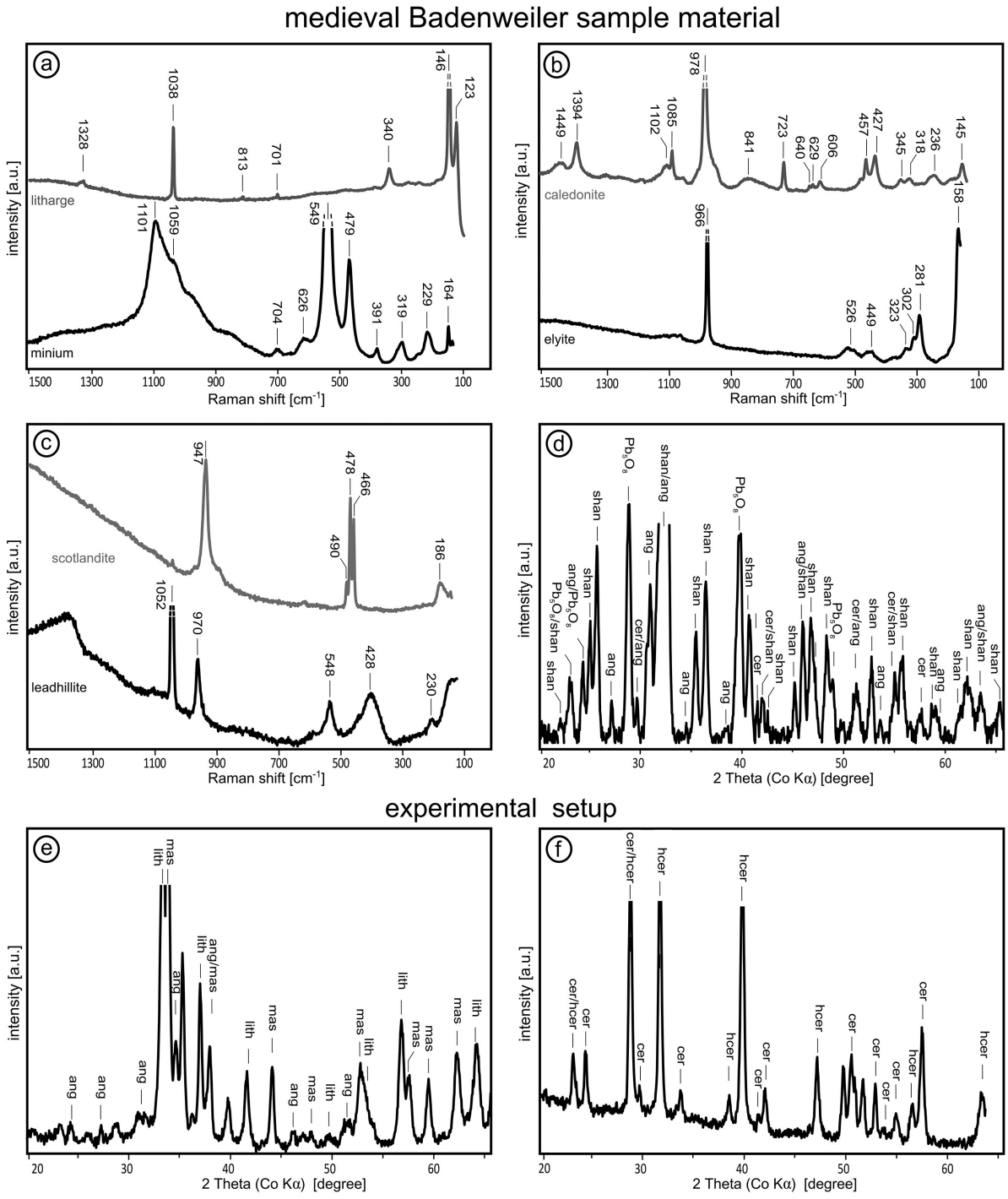

FIGURE 2. (**a**–**c**) representative Raman spectra of the phases litharge, minium, caledonite, elyite, scotlandite, and leadhillite. (**d**–**f**) μ-XRD patterns of mineral aggregates of the medieval fire-setting and the experimental setup. Abbreviations: ang = anglesite, cer = cerussite, hcer = hydrocerussite, lith = litharge, mas = massicot.

Table A4). EMP totals of most former melt and crystal phases are close to 100 wt% with an average of 98.8 wt%. Only melt type iv has significantly lower totals on the order of 82 wt%. Type IV crystals have lower totals between 94.4 and 98.8 wt% with an average of 96.8 wt% (see Table 4 for representative analyses). Low melt and crystal totals are interpreted to reflect H_2O incorporation, since EDS analyses did not indicate any missing element.

Figure 4a shows that the former melts and crystals show a large compositional variability, being predominantly com-

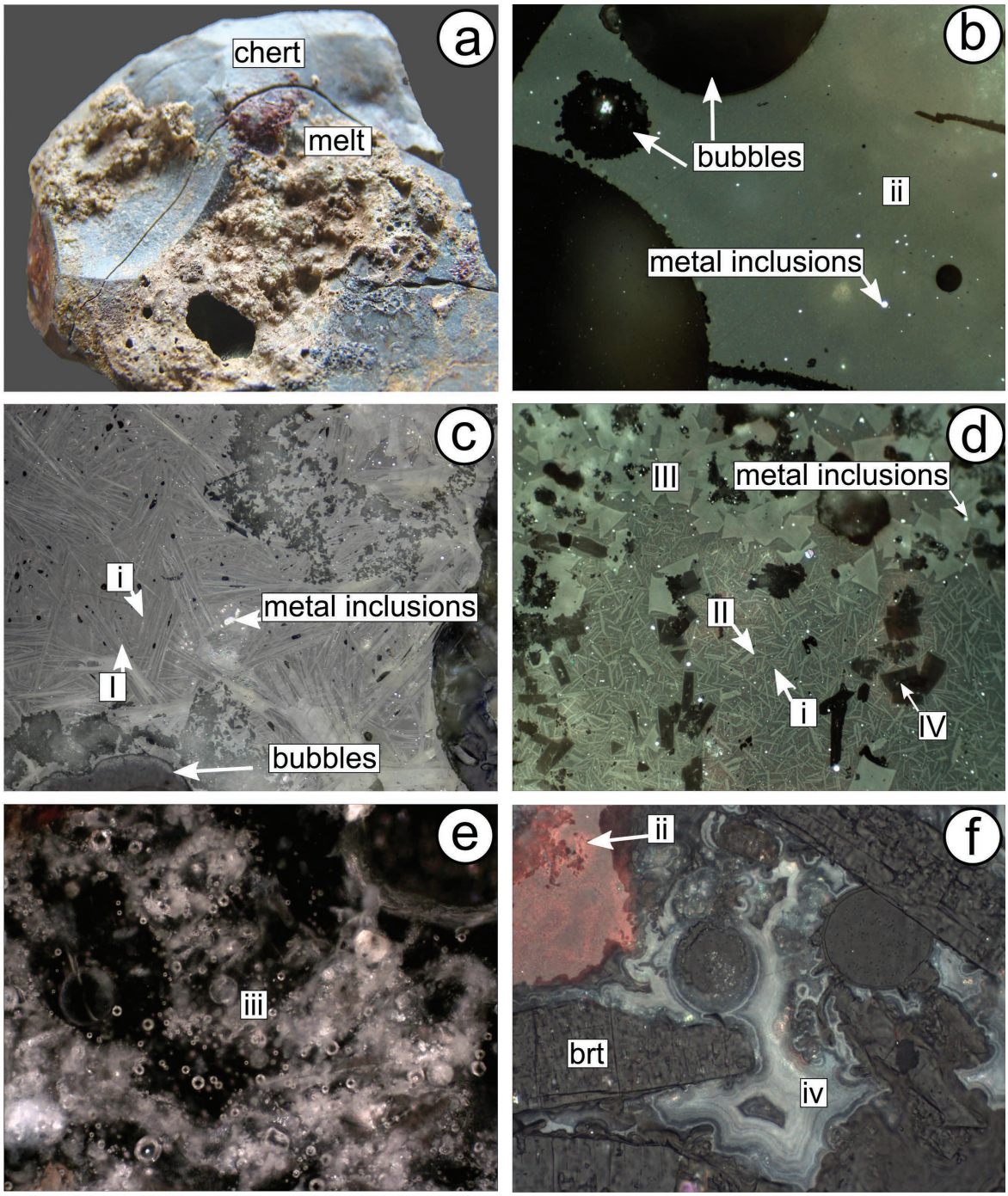

FIGURE 3. (**a**) Photograph of spongy, red-brown colored FS related former melt, lanced by bubbles on gray chert; (WoP) = 3.5 cm. (**b**) Reflected light image of melt type ii with large round bubbles and small, metal inclusions; WoP = 860 µm. (**c**) Reflected light image of crystal type I (light gray) associated to melt type i (dark gray); WoP = 860 µm. (**d**) Reflected light image of crystal type II, III, and IV associated to melt type i; WoP = 860 µm. (**e**) Reflected light image with crossed polarizers of melt type iii, lanced by numerous small bubbles; WoP = 430 µm. (**f**) Reflected light image of melt type iv, which is layered and surrounds barite crystals; WoP = 860 µm. Abbreviations: brt = barite, fl = fluorite, hem = hematite, and qtz = quartz.

posed of silicon, lead, zinc, and calcium. Highest Si contents for the former melt are up to 65 and 62 mol% for the crystals, and also the mean contents in the former melts are higher than in the crystal phases. Except for Zn, Ca, and P, all other elements have higher mean contents in the former melt than in the crystal phase.

In Figures 4b, 4c, and 4d, the mean molar ZnO and CaO

contents of different crystal types and melt types, which are directly intergrown with the crystals, are plotted against X_{SiO_2} [X_{SiO_2} defined as $SiO_2/(SiO_2+PbO)\cdot 100$] for the different samples (see Table 5 for structural formula). In sample MK-08, the former melt phase shows relatively low CaO and ZnO contents, with a maximum of 7.5 mol% ZnO and 6.1 mol% CaO (Fig. 4b) and ranges in X_{SiO_2} between 58.1 and 66.3 mol%. Dark blocky crystals of Type IV have quite variable X_{SiO_2} between 76.3 and 96.6 mol%, moderate ZnO contents up to 19.4 mol% and high CaO contents up 45.8 mol%. Short needles with of Type II have X_{SiO2} between 52.6 and 57.4 mol%, and low ZnO contents up to 2.2 mol% and high CaO contents up to 17.8 mol%. Blocky bright crystals of Type III form two distinct groups. The first group is nearly identical in composition to the bright needles of Type I, just having slightly higher CaO contents up to 25.6 mol%. The second group, however, has much higher ZnO contents up to 33.0 mol%.

Fibrous crystals of Type I and the former melt of sample MK_06 (Fig. 4c) only show minor amounts of CaO and ZnO below 1 mol%. The X_{SiO_2} of the former melt (46.2–62.0 mol%) is slightly higher than in the crystals (45.1–50.3 mol%).

The former melt phase of sample MK-22 again shows higher X_{SiO_2} than the fibrous crystals of Type I (Fig. 4d). Former melts and crystals show CaO and ZnO contents below 1 mol% but intermediate CaO contents up to 5.6 mol%.

The bulk compositions plotted in Figures 4b, 4c, and 4d were recalculated based on BSE image analysis using common graphic software and appropriate crystal and former melt compositions. The bulk compositions represent a mixture of the former melt and the crystal composition the position depends on the portion of former melt and crystal phase. Qualitative EDS analyses of the metal inclusions show that they are either composed of Ag or Pb only, or of Pb+Cu, Ag+S, Cu+S or Ag+Cu+S.

FS experiments

The experimental setup reproduces a wide spectrum of phases and textures of the medieval FS assemblage. During roasting, supergene cerussite of the Badenweiler sample material was replaced by a mixture of the lead oxides massicot and litharge (Fig. 2e), typically lanced by cracks (Fig. 5a). Also the typical red color, partial melting, and the crumbly appearance of the experimental samples matches the medieval ones. In the experimental setups dealing with mineral separates, phase growth was macroscopically visible in setup A1 after only 12h. In all other experimental setups mineral growth was visible within the first five days.

SEM shows that during all experiments hydrocerussite overgrows the lead oxides as fine-grained sheds (Figs. 5b and 5c), but in larger amounts in experimental setup A compared to setup B. The μXRD diagrams indicate that the newly grown phases in parts are not well crystalized. Subordinately, prismatic cerussite crystals can be found in experimental setup A2, A4, A3, B2, B4 (Figs. 5d and 2f), which were newly grown on the lead oxide surface beside hydrocerussite.

TABLE 4. Representative EMP results of the different former melts and the crystal phases

	Samples (crystal phase) (wt%)											
Oxides	MK-06-111	MK-06-114	MK-06-109	R-1.12	R-1.13	R-1.24	MK-08.46	R-1.39	R-1.7	R-1.1	R-1.47	R-1.18
Na_2O	0.04	0.07	bdl	0.01	0.02	0.02	bdl	0.03	0.03	bdl	0.02	bdl
SO_3	bdl	0.07	bdl	0.08	0.06	0.04	bdl	bdl	bdl	bdl	0.02	bdl
P_2O_5	0.04	0.08	0.06	0.34	0.29	0.32	0.16	0.17	0.43	0.07	0.03	0.09
Al_2O_3	0.57	1.3	0.03	1.2	1.1	1.06	0.03	1.5	0.05	0.06	0.06	0.36
PbO	78.0	77.6	81.0	66.5	67.0	65.4	57.6	68.5	67.4	5.5	3.2	32.5
Ag_2O	bdl	bdl	bdl	bdl	bdl	bdl	bdl	bdl	bdl	bdl	bdl	bdl
SiO_2	18.9	2bdl	18.7	21.6	21.8	23.3	20.1	22.4	20.7	50.3	51.0	31.5
K_2O	0.20	0.35	bdl	0.40	0.30	0.61	0.07	0.66	0.04	0.04	0.01	0.17
BaO	0.06	0.12	0.27	1.0	0.88	0.99	0.40	1.1	0.29	0.09	0.05	0.26
CaO	0.06	bdl	0.02	4.9	6.1	5.1	0.58	2.5	10.7	42.9	44.0	16.8
TiO_2	0.01	0.01	bdl	0.07	0.04	0.05	bdl	0.06	bdl	0.01	0.01	bdl
ZnO	0.01	0.01	0.03	0.82	0.80	1.43	20.9	1.4	0.24	0.32	0.32	16.9
CuO	Bdl	0.11	0.07	0.06	bdl	bdl	bdl	0.15	bdl	0.09	bdl	bdl
FeO	1.9	0.11	0.12	1.60	1.2	1.2	0.20	1.4	0.20	0.27	0.22	0.25
Total	99.7	99.8	100.3	98.5	99.5	99.6	100.0	99.8	100.0	99.7	98.8	98.9
Crystal type[a]	I	I	I	II	II	II	III	III	III	IV	IV	IV
	Samples (melt-phase) (wt%)											
Oxides	MK-06-103	MK-06-14	MK-08-40	MK-06-61	MK-06-54	MK-22-20	MK-06-50	MK-06.73	MK-06.79	MK-08.13	MK-08.27	MK-08.28
Na_2O	0.05	0.03	bdl	0.09	0.06	bdl	bdl	0.01	0.02	0.03	0.04	0.05
SO_3	0.33	0.25	0.33	2.8	0.18	0.15	bdl	bdl	bdl	0.01	bdl	bdl
P_2O_5	0.07	0.01	0.18	0.14	0.03	bdl	0.36	0.07	0.01	0.10	0.21	0.08
Al_2O_3	2.6	0.37	0.85	2.3	1.9	0.09	1.4	1.7	2.0	1.8	6.6	0.73
PbO	75.4	68.1	62.0	59.2	68.6	69.6	81.8	69.4	70.3	71.8	38.9	79.4
Ag_2O	bdl	bdl	bdl	bdl	bdl	bdl	bdl	bdl	bdl	bdl	0.02	bdl
SiO_2	21.8	29.0	29.1	25.1	28.8	29.1	17.4	30.0	28.4	12.5	28.2	5.6
K_2O	0.63	0.45	0.78	0.69	0.88	0.01	0.08	0.26	0.55	0.04	0.04	0.02
BaO	0.15	0.13	0.17	8.69	0.48	0.22	0.03	0.02	bdl	0.11	0.06	0.08
CaO	bdl	bdl	1.94	0.03	0.24	0.11	0.03	0.03	bdl	0.03	0.14	0.01
TiO_2	0.08	0.02	0.04	0.43	0.11	bdl	0.09	0.01	bdl	0.03	0.08	0.04
ZnO	0.05	0.06	3.06	0.04	bdl	0.01	bdl	bdl	0.01	0.33	0.41	0.14
CuO	bdl	0.97	1.03	0.08	0.02	bdl	bdl	bdl	bdl	0.31	0.59	0.11
FeO	0.06	0.04	0.83	0.23	0.10	0.04	0.30	0.14	0.08	0.77	1.63	0.74
Total	101.1	99.4	100.3	99.9	101.3	99.3	101.5	101.6	101.4	87.9	76.9	87.00
Melt type[a]	i	i	i	ii	ii	ii	iii	iii	iii	iv	iv	iv

[a] For definition of crystal and melt types, see sample description in the text; for structural formula see Table 5; bdl = below detection limit (For detection limits see Appendix[1] Table A1).

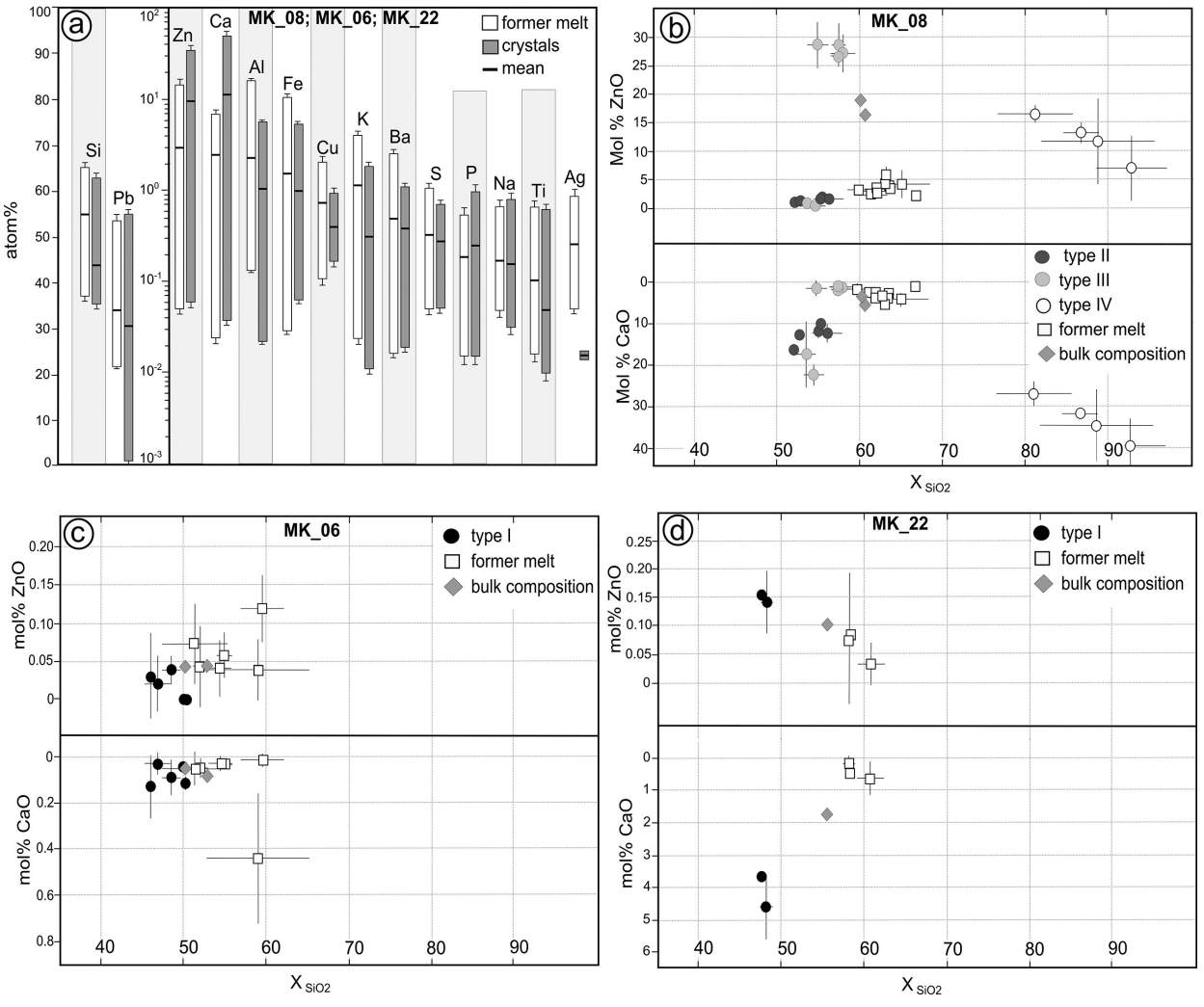

FIGURE 4. (**a**) Element contents in mol% of former melt phase (white bars) including types i and ii and corresponding crystal phase (gray bars). The mean values of all measurements are plotted as black bars. Note: the y-axis for Pb/Ca is linear, for all other elements logarithmic. (**b**–**d**) Mean molar ZnO and CaO contents vs. X_{SiO_2} of former melt and the different associated crystals types for each sample MK_08, MK_06, and MK_22.

Besides hydrocerussite and cerussite, light blue chenite and purple elyite grow as fiberous needles in experimental setup A4 and B5 (Figs. 5e and 5f; cf. Table 2). It was not possible to determine elyite and chenite by µXRD analyses, but Raman analyses lead to a unique identification.

The pH values of the experimental water in setup A are slightly higher than the initial pH of 6.0 (6.2–7.1). Experimental setup B leads to lower pH values than the initial pH of 9.5 (7.0–8.8). Setup A shows higher lead contents than setup B at least by the factor 1.5 (cf. Table 3). Lowest amount of lead was found in experimental setup A1 and B1, most in A4 and B4. Generally, lead contents of the experimental waters are relatively low and show an increase with lower pH values.

PHREEQC calculations show that the waters are undersaturated with regard to most basic lead phases (see Table 6). Only caledonite and linarite show supersaturation in most experiments including initial copper phases. Also hydrocerussite shows supersaturation in setup A2, A3, and A5, leadhillite in A3 and A5. Besides the basic lead minerals, cerussite shows supersaturation in setups A2, A3, A5, B2, B3, B4, and B5 and pyromorphite in setup A3.

TABLE 5. Summary of the structural formulas of the different crystal phases

Crystal type	Description	Structural formula (EMPA)	Natural equivalent
I	high reflectance, fibrous	$Pb_{1.01}Si_{0.95}O_3$	alamosite [$PbSiO_3$]
II	high reflectance, short needles	$Pb_{0.72}Ca_{0.25}Si_{0.92}O_3$	Ca-rich alamosite [$(Pb,Ca)SiO_3$]
III	high reflectance, blocky	Zn rich: $Pb_{0.84}Zn_{0.83}Si_{1.11}O_4$	larsenite [$PbZnSiO_4$]
		Ca rich: $Pb_{0.99}Ca_{0.62}Si_{1.14}O_4$	no natural equivalent
IV	low reflectance, blocky	$Ca_{1.60}Pb_{0.33}Zn_{0.6}Si_{2.14}O_7$	no natural equivalent

Stability relations of basic lead phases

To evaluate the stability relations of anglesite, cerussite, hydrocerussite, leadhillite, lanarkite, minium, and caledonite, stability diagrams with respect to variable pH, P_{CO_2}, Cu concentrations, and temperature were calculated using The Geochemist Workbench. For the basic lead phases elyite and chenite, unfortunately, no

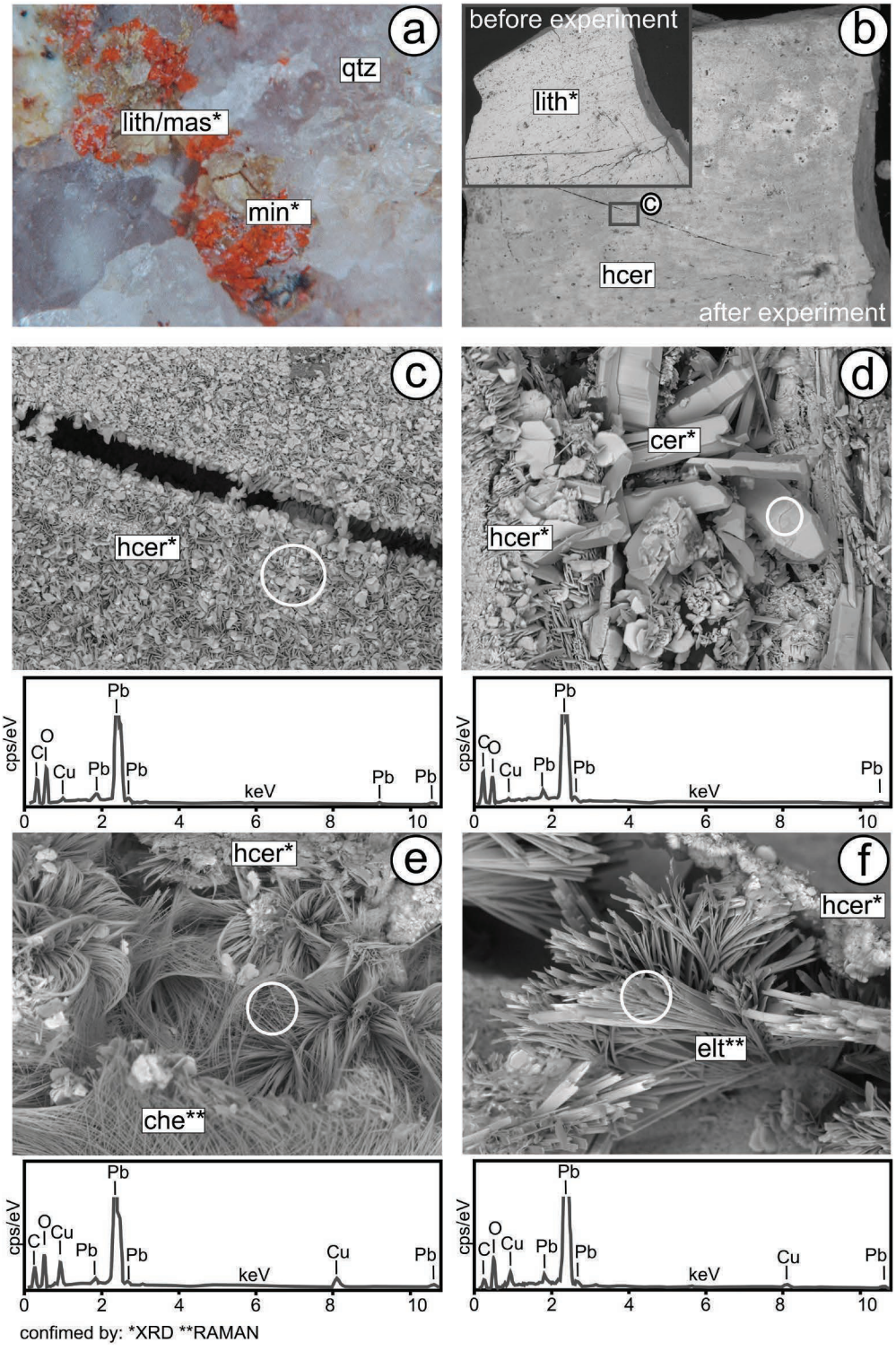

Figure 5. (**a**) Photograph of minium + litharge + massicot pseudomorphic after cerussite; WoP = 6 mm. (**b**) BSE-image of litharge (see upper left) overgrown by hydrocerussite; WoP = 3 mm. (**c**) Magnified excerpt of **b** showing hydrocerussite sheds grown on litharge; WoP = 250 µm. Lower part shows EDS spectra of the analyzed area marked as circle. (**d**) BSE image of blocky cerussite crystals together with hydrocerussite; WoP = 300 µm. Lower part shows EDS spectra. (**e** and **f**) Fibrous chenite and needle-like elyite crystals together with hydrocerussite. WoP = 350 and 150 µm. Lower part shows EDS spectra. Abbreviations: cer = cerussite, che = chenite, elt = elyite, hcer = hydrocerussite, lith = litharge, min = minium, mas = massicot, qtz = quartz.

TABLE 6. Saturation indices of the experimental waters calculated with PHREEQC (supersaturation is marked bold)

		Setup A					Setup B					
Mineral/phase	Formula	A1	A2	A3	A4	A5	B1	B2	B3	B4	B5	B6
Anglesite	$PbSO_4$	–3.8	–2.9	–1.0	–0.6	–1.0	–4.5	–3.7	–2.6	–1.8	–2.7	–
Barite	$BaSO_4$	–0.9	–0.1	–0.5	–0.2	**1.0**	–	**1.1**	**1.0**	**3.7**	**1.2**	**1.1**
Calcite	$CaCO_3$	–1.6	–1.7	–2.7	–4.0	–1.0	**0.1**	**0.7**	**0.1**	**0.1**	**0.3**	**1.8**
Caledonite	$Pb_5Cu_2(CO_3)(SO_4)_3(OH)_6$	–	**5.9**	**10**	**9.5**	**11**	–0.5	**2.9**	**6.7**	**5.6**	**0.6**	–
Cerussite	$PbCO_3$	–0.2	**0.2**	**1.0**	–0.1	**0.8**	–0.3	**0.1**	**0.4**	**0.4**	**0.3**	–
Hydrocerussite	$Pb_3(CO_3)_2(OH)_2$	–1.4	**0.3**	**2.2**	–1.1	**0.6**	–1.3	–0.4	–0.3	–1.0	–0.6	–
Lanarkite	Pb_2OSO_4	–6.7	–4.8	–2.6	–3.6	–3.7	–7.0	–6.1	–5.5	–5.5	–5.7	–
Leadhillite	$Pb_4(SO_4)(CO_3)_2(OH)_2$	–4.2	–1.7	**2.1**	–0.8	**0.6**	–4.9	–3.1	–2.0	–1.9	–2.4	–
Linarite	$PbCu(OH)_2(SO_4)$	–	**1.1**	**2.0**	**2.4**	**2.8**	–0.8	**0.3**	**1.6**	**1.2**	**1.1**	
Litharge	PbO (tetragonal)	–5.0	–4.0	–3.8	–5.1	–4.8	–5.0	–4.5	–5.0	–5.8	–5.1	–
Massicot	PbO (orthorombic)	–5.1	–4.2	–3.9	–5.2	–5.2	–5.2	–4.6	–5.1	–6.9	–5.2	–
Minium	$Pb^{4+}Pb_2^{2+}O_3$	–28	–25	–24	–30	–28	–23	–24	–27	–31	–27	–
Pyromorphite	$Pb_5(PO_4)_3Cl$	–	–	**26.7**	–	–	–	–	–	–	–	–

thermodynamic data are available, hence no quantitative statements of their stability can be given (a qualitative stability diagram of both phases can be found in Appendix[1] A, Fig. A2).

Figure 6a shows the stability relations of the above named phases with respect to variable pH, P_{CO_2} as well as fixed lead and sulfur concentrations. Charge balance was maintained by adding nitrate as conservative ion. As shown in Figure 6a for 25 °C, anglesite is the stable secondary lead phase at acidic to neutral pH values becoming more stable toward higher pH values at low P_{CO_2}. The cerussite/hydrocerussite stability field

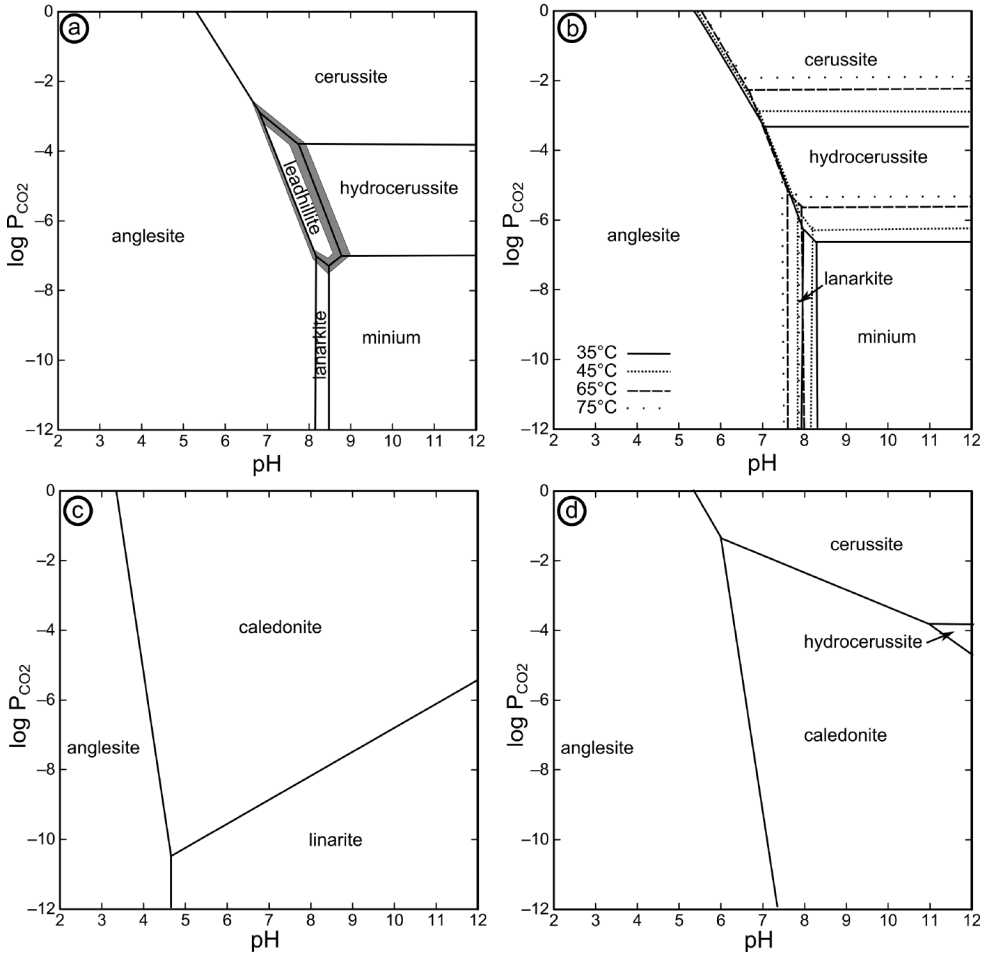

FIGURE 6. The logP_{CO_2}-pH diagram showing (**a**) stability relation for the lead phases hydrocerussite, lanarkite, minium, anglesite, and cerussite. (**b**) Stability fields of the lead phases for variable temperatures (35, 45, 65, and 75 °C), marked as dashed lines. (**c**) Stability relation for the basic lead phases hydrocerussite, anglesite, caledonite, and linarite including copper contents of Cu = 1.0×10^{-5} M. **(d)** Stability relation for the lead phases including copper contents of Cu = 1.0×10^{-15} M. Stability diagrams were calculated for P = 1 bar, $\log_{PO_2}$ = –0.68bar, T = 25 °C, S = 1×10^{-2} M, Pb = 1×10^{-2} M.

depends on P_{CO_2}, with cerussite being stable at higher P_{CO_2}. Leadhillite has a relatively small stability field around neutral pH-values and moderate to low P_{CO_2} and is framed by anglesite and cerussite/hydrocerussite, lanarkite, and minium. Lanarkite has a relatively small stability field under neutral to basic pH-values and low P_{CO_2}. Minium is stable at slightly basic to basic pH values and low P_{CO_2}.

Figure 6b shows the stability relations of anglesite, cerussite, leadhillite, lanarkite, and minium at variable temperatures. Due to the lack of enthalpies for leadhillite, no statement can be made on the size of the stability field at higher temperatures than 25 °C. Increasing temperatures expand the stability field of hydrocerussite to much higher P_{CO_2}. In addition, the stability field of lanarkite expands to slightly higher P_{CO_2} and lower pH.

Figures 6c and 6d show the stability relations of anglesite, cerussite, hydrocerussite, leadhillite, lanarkite, minium, caledonite, and linarite with respect to variable pH, P_{CO_2}, and Cu concentrations at fixed lead and sulfur concentrations and a fixed temperature of 25 °C. At high copper concentrations of 1×10^{-5} M (see Fig. 6c), anglesite is stable at low pH values over the whole P_{CO_2}-range. Linarite is stable at low P_{CO_2} and caledonite at high P_{CO_2} over a wide pH range. At low Cu concentrations of 1×10^{-15} M (see Fig. 6d), the stability field of anglesite enlarges to higher pH values and hydrocerussite becomes additionally stable at high pH.

Discussion

In the following section, the formation mechanisms of the FS assemblage are discussed and quantified using fluid path models. Additionally, the stability diagrams and fluid path models are used to explain the formation of basic lead minerals in other anthropogenic influenced and natural environments. The short-term experiments provide additional insights to the formation mechanisms and show how the basic lead minerals are capable to control the lead concentration in aqueous solutions. Furthermore, a temperature estimation of the FS process was done by using the mineralogy of lead oxides and the chemical composition of the melt phase.

Formation steps of the fire-setting assemblage

The observed textures of the FS assemblage and the identified phases imply a three step process (Step I–III), which is sketched and summarized in Figure 7. The steps are the different processes before, during, and after FS. This classification is in good agreement with observations made by Wittern (1994).

Step I: Supergene weathering. First, supergene weathering of primary galena lead to the formation of thermodynamically more stable secondary lead minerals like cerussite (Eq. 1) and anglesite (Eq. 2) (cerussite dominates in the investigated samples from Badenweiler).

$$PbS\,(galena) + H_2O + CO_2 + 2O_2 = PbCO_3\,(cerussite) + SO_4^{2-} + 2H^+ \quad (1)$$

$$PbS\,(galena) + 2O_2 = PbSO_4\,(anglesite) \quad (2)$$

Cerussite and anglesite replace galena along its rims and typical cleavage planes. Within cavities, euhedral or subhedral crystals up to centimeter-size develop. Whether cerussite and/or anglesite are stable depends, for example, on pH, P_{CO_2}, and temperature of the supergene weathering fluid (Keim and Markl 2015).

Step II: fire-setting. During the FS process, lead oxides and lead oxycarbonates like shannonite form (cf. Figs. 1b, 1c, 2a, and 2d) due to decarbonization reactions of cerussite induced by the strong heat impact of the fire. The temperature-dependent stepwise transformation process of cerussite to lead oxides under atmospheric pressures was described by Yamaguchi et al. (1980). The modified transformation reaction is presented in Equations 3a–3c. The temperature-dependent formation of lead oxides is discussed below.

$$2PbCO_3\,(cerussite) \rightarrow\sim_{300\,^\circ C}\rightarrow PbCO_3 \cdot PbO + CO_2 \quad (3a)$$

$$3PbCO_3 \cdot 3PbO \rightarrow\sim_{370\,^\circ C}\rightarrow 2PbCO_3 \cdot 4PbO + CO_2 \quad (3b)$$

$$PbCO_3 \cdot 2PbO \rightarrow\sim_{440\,^\circ C}\rightarrow 3PbO + CO_2 \quad (3c)$$

Conversion of malachite to tenorite during FS has been proposed by Graf (1991) and has been observed at some localities such as Neubulach, Schwarzwald, Germany (Markl 2015).

Anglesite, pyromorphite, or any other phosphates and arsenates (also copper arsenates like olivenite in Cu-dominated environments) remain unaffected during Fs (cf. Fig. 1b). The only exception is pseudomalachite, which reacts to a new, naturally unknown copper phosphate (Markl 2015). This is also observed during mine fires, where cerussite is converted to oxycarbonates and lead oxides, while anglesite in direct intergrowth is not affected (Skinner and McBriab 1958; Pring et al. 1990). Anglesite starts to decompose in air at temperatures above 880 °C (Sajadi 2011).

As described, the pseudomorphs are lanced by numerous cracks due to a volume reduction during CO_2 loss of cerussite of about 39%, if converted to minium.

In contrast to Wittern (1994), microscopic observations lead to the result that the typical red color of the samples is not caused by litharge but by fine-grained hematite distributed along cracks and fissures. The low firmness is most likely due to the conversion of low-quartz to high-quartz occurring at 573 °C and its reconversion (volume change ~5%).

Step III: Processes in the dump. After FS, material containing no or only little ore was thrown on a dump. Here, basic lead phases could form by the reaction of weathering fluids with lead oxides, which is proven by common replacement and overgrowth textures (cf. Figs. 1b, 1d, 1g, and 1h).

In principle, there are two possibilities (or a combination of both) where this water-lead oxide interactions can take place. (1) During dousing of the hot rock with water after the FS process or (2) during processes in the dump where meteoric and/or developing soil fluids react with lead oxides.

Fluid path models: Mode of formation of basic lead phases

In the following, geochemical fluid path models are presented to explain the occurrence of basic lead phases during FS, at slag dumps, and in areas with metallic lead pollutants (Model I). Also the occurrence of basic lead phases in contact to concrete is discussed (Model II). In addition, the stability diagrams were used to explore the conditions under which basic lead minerals can form in oxidation zones of ore deposits.

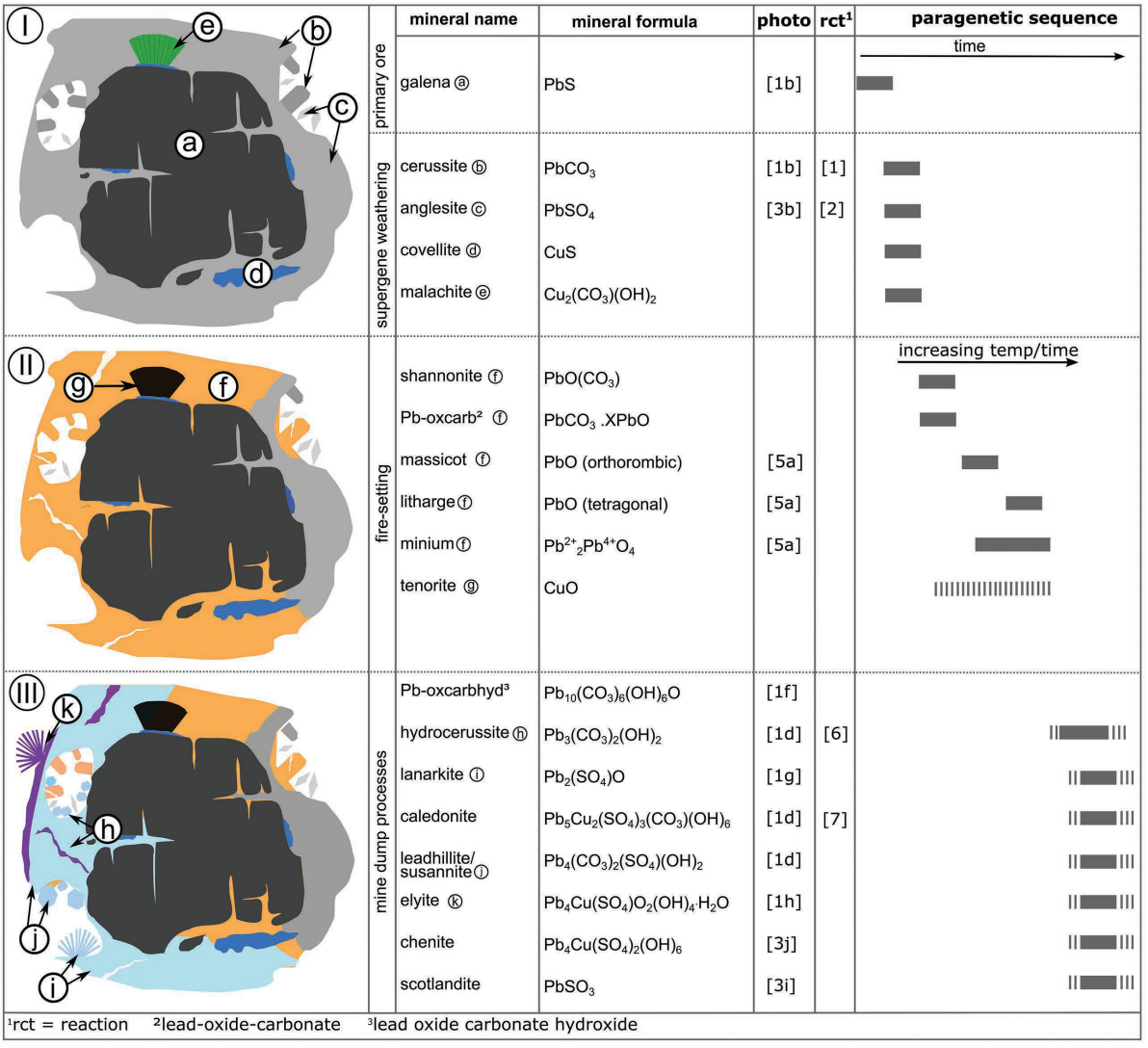

FIGURE 7. Three steps process of the FS assemblage with: (**I**) supergene weathering, (**II**) FS, and (**III**) mine dump processes. Additionally listed are sketches of each step, mineral names, mineral formula, representative photo (in Fig. 1), formation reaction mentioned in the text, and the paragenetic sequence.

Formation during FS, in contact to lead pollutants and slags (Model I). The basic lead phases of the FS assemblage are texturally closely related to lead oxides (see above). Also in other anthropogenically influenced environments like slag dumps and in contaminated soils, metallic lead alters to lead oxides (e.g., Lin et al. 1995; Lin 1996; Essington et al. 2004; Ma et al. 2007; Ettler et al. 2009a, 2009b; Li et al. 2015). Here, the lead oxides are directly related to basic lead phases like hydrocerussite (Lin 1996; Ma et al. 2007). If the lead oxides come into contact with meteoric fluids, protons are consumed and the pH rises (Eq. 4).

$$Pb^{4+}Pb^{2+}_2O_4 \text{ (minium)} + 6H^+ = 3Pb^{2+} + 3H_2O + 0.5O_2 \quad (4)$$

If lead carbonates or basic lead carbonates like cerussite (Eq. 5), hydrocerussite (Eq. 6), or caledonite (Eq. 7) precipitate additionally, CO_2 is consumed (see also Ma et al. 2007).

$$PbO \text{ (litharge)} + HCO_3^- + H^+ = PbCO_3 \text{ (cerussite)} + H_2O \quad (5)$$

$$3PbO \text{ (litharge)} + 2HCO_3^- + 2H^+ = Pb_3(CO_3)_2(OH)_2 \text{ (hydrocerussite)} + H_2O \quad (6)$$

$$5PbO \text{ (litharge)} + 2Cu^{2+} + HCO_3^- + 3SO_4^{2-} + H_2O + 3H^+ = Pb_5Cu_2(CO_3)(SO_4)_3(OH)_6 \text{ (caledonite)} \quad (7)$$

With PHREEQC it is possible to track the fluid evolution during these reactions (Model I) and evaluate the phase saturation during the evolution of the fluid chemistry. Note that this model is not designed to simulate processes at a specific locality, but rather to show general trends during the reaction of lead oxides with weathering fluids.

The FS products, slags, and lead pollutants are likely to interact with rainwater. For this reason, a rain water analysis

from Négrel and Roy (1998) was chosen and reacted with 1.5×10^{-4} M minium in 100 steps (path i and ii). During each reaction step, the phases anglesite, cerussite, hydrocerussite, lanarkite, litharge, minium, massicot, and leadhillite were allowed to precipitate if supersaturated. For the calculations a system closed to CO_2 was assumed, which is reasonable for microenvironments. For path ii the water was additionally reacted with 3×10^{-3} M galena to enrich the sulfur-poor rainwater with sulfur and slightly change the pH to lower values. This is reasonable since the investigated FS samples and many slags frequently contain sulfide relics (e.g., Ettler et al. 2001, 2009b). The resulting fluid paths are shown in Figure 8a, the appropriate saturation indices for phases reaching saturation (Si = 0) during progressive reaction with minium in Figure 8b. Due to the differences in lead/sulfur activity of the fluid path compared to the stability diagrams, the paths do not exactly plot on the borders of the stability fields.

In both models, the CO_2 partial pressure decreases from the starting value of $\log P_{CO_2} = -2.0$ and the pH value rises during progressive reaction with minium. Path i shows that in sulfur-poor systems under moderate pH (pH = 6.0), cerussite is the first stable phase. With progressive reaction, P_{CO_2} decreases and hydrocerussite becomes stable. In path ii (start pH = 5.7) cerussite and anglesite coprecipitate, followed by leadhillite. The path then ends in the triple point anglesite-leadhillite-lanarkite. Fluid paths i and ii explain why lead oxides are often overgrown/replaced by basic lead phases. Whether hydrocerussite, leadhillite, anglesite, or lanarkite are stable depends mainly on the availability of sulfur and the pH-value of the fluid. Higher-pH will favor lead carbonates and/or sulfcarbonates to precipitate. Additional Cu in the fluid can result in the precipitation of caledonite and/or linarite depending on the P_{CO_2} (see Figs. 6c and 6d).

The formation of basic lead minerals by the reaction with lead oxides is not restricted to artificial environments only. Alteration of primary metallic lead to lead oxides is also observed rarely in nature (e.g., Karup-Møller 1975).

Formation in contact to concrete (Model II). Artificially formed basic lead phases can also be found in contact with concrete. A paragenesis including hydrocerussite and elyite is described from the Clara mine, in the central Schwarzwald, SW Germany, where lead-bearing fluids come into contact with shotcrete (Kolitsch 2000; Markl 2015). Furthermore, Lee (2007) reports the stabilization of aqueous lead, liberated from lead contaminants during the reaction with cement by the formation

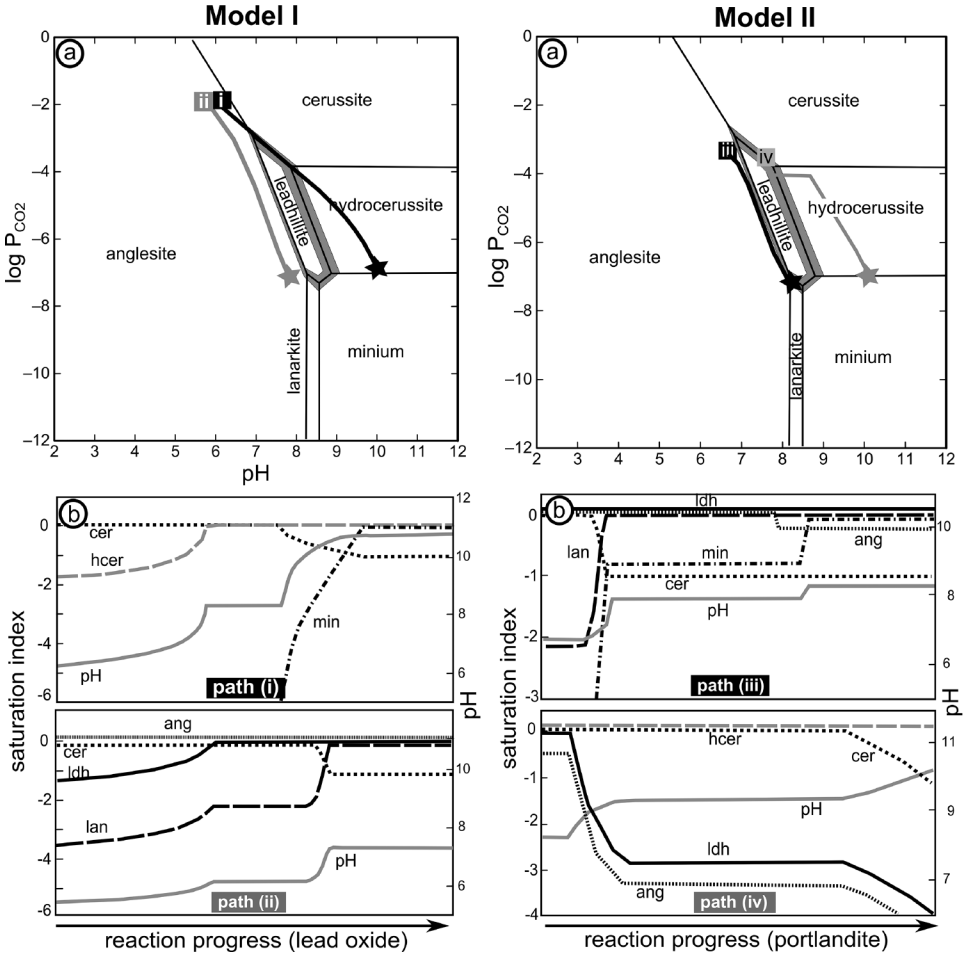

FIGURE 8. Fluid path models for the reaction with minium (model I) and portlandite (model II). (**a**) The evolving fluids i + ii for model I and iii + iv for model II plotted in a $\log P_{CO_2}$-pH diagram (Fig. 6). (**b**) The evolving saturation indices during progressive reaction, respectively.

of less soluble leadhillite and lead carbonate hydroxide hydrate [$3PbCO_3 \cdot 2Pb(OH)_2 \cdot H_2O$]. Reaction of water with concrete (portlandite) will rise pH values as follows (Eq. 8):

$$Ca(OH)_2 \text{ (portlandite)} + 2H^+ = Ca^{2+} + 2H_2O \quad (8)$$

Precipitation of calcite consumes CO_2:

$$Ca(OH)_2 \text{ (portlandite)} + CO_2 = CaCO_3 \text{ (calcite)} + H_2O \quad (9)$$

To track the fluid evolution during reaction of a fluid with concrete (Model II), a water analysis from the Clara underground mine from Bucher et al. (2009) was reacted with portlandite in a system closed to CO_2. The fluid was reacted with galena (in the model, similar to what is observed in the mine) to enrich it in lead. This modified water was then reacted with 9×10^{-4} M portlandite in 100 steps. During each reaction step, the phases anglesite, cerussite, hydrocerussite, lanarkite, leadhillite, massicot, and minium were allowed to precipitate if supersaturated.

The resulting fluid paths iii and iv are shown in Figure 8c, the appropriate saturation indices during progressive reaction with portlandite in Figure 8d. Path iv is additionally equilibrated with calcite to reach a slightly higher pH value and. In both fluid paths, the pH values rise and P_{CO_2} decreases during progressive reaction with portlandite.

On fluid path iii (starting pH of 7), first cerussite, anglesite, and leadhillite are stable. As P_{CO_2} decreases and pH rises, the assemblage anglesite plus leadhillite becomes stable and with progressive reaction additionally lanarkite. During the protracted reaction with portlandite, anglesite is not stable anymore and the assemblage lanarkite plus leadhillite becomes stable. The path then ends with precipitating minium, leadhillite, and lanarkite.

Fluid iv starts with a higher pH value of 8.0. This results in cerussite, hydrocerussite, and leadhilite being the stable phase assemblage at first. With proceeding reaction, leadhillite becomes unstable and the fluid will end up precipitating hydrocerussite. Both fluid paths show that basic lead phases can be formed during the reaction of a fluid with portlandite and that changes in pH, for example due to the dissolution of calcite, can result in different phase assemblages. Again, the pH-value of the starting fluid is important for the course of the fluid path. Higher pH-values and additional carbon added to the system by the dissolution of calcite will favor the precipitation of lead carbonates and sulfcarbonates (for more details about the aqueous speciation of the ions, see the PHREEQC input code in Appendix[1] B). Overall, the reaction with portlandite and the precipitation of basic lead phases drops the P_{CO_2} and increases the pH value in a system closed to CO_2. Again, if Cu is available, caledonite/linarite can precipitate (see Figs. 6c and 6d).

Wittern (1994) described the formation of $Ca(OH)_2$ due to heating of calcite at the FS location Glücksrad mine, Harz mountains, Germany. Such a reaction is unlikely at Badenweiler since calcite is lacking there. However, at the Glücksrad mine, $Ca(OH)_2$ could play an important role during basic lead phase formation.

Formation of basic lead minerals in natural environments. In rare cases, basic lead minerals form in oxidation zones of hydrothermal ore deposits such as Tsumeb, Namibia (Ingwersen 1990; Bowell and Clifford 2014); Leadhills, Lanarkshire, Scotland (Temple 1956); Tiger, Mammoth ore district, Arizona (Bideaux 1980; Abdul-Samad et al. 1982b), Caldbeck Fells, Cumberland, England (Cooper and Stanley 1997); Friedrich-Christian mine, Schwarzwald, Germany (Walenta 1991); Laquorre mine, Pyrenees, France (Asselborn 2012), and Göschenen, Uri, Switzerland (Stalder et al. 1998). The occurrence of basic lead minerals in such systems is not explainable by the reaction with lead oxides.

Formation of basic lead minerals in lead-bearing systems closed to CO_2 accompanied by the precipitation of cerussite is not possible. During precipitation of cerussite, CO_2 is consumed and the pH decreases (Eq. 10).

$$Pb^{2+} + HCO_3^- = PbCO_3 \text{ (cerussite)} + H^+ \quad (10)$$

Since the pH and HCO_3^- are related, the P_{CO_2} of a fluid will not decrease during cerussite precipitation in a closed system. Thus, the fluid will end up precipitating anglesite if the pH is sufficiently low. This is in contrast to the reaction with PbO where the pH increases during basic lead phase precipitation. Consequently, the basic lead mineral assemblage in the oxidation zones cannot be explained by e.g., weathering of galena in a "simple" closed system.

As Figure 6b shows, weathering under elevated temperatures does not necessarily require low CO_2 partial pressures to stabilize hydrocerussite, since the stability field shifts to higher P_{CO_2}. In nature, alteration/weathering of primary galena under elevated temperatures (about 30–50 °C) is known from Tsumeb and the Tiger ore deposit based on microthermometric studies on cerussite (Gilg et al. 2003; Boni et al. 2007). Indeed, the analyzed cerussite is not directly associated to basic lead minerals, but we assume that in parts of the deposit, where basic lead minerals occur (together with cerussite), similar temperatures were reached during their formation. At the Tiger ore deposit, cerussite is first replaced by leadhillite and/or hydrocerussite that are later again replaced by cerussite (Abdul-Samad et al. 1982b). This paragenetic sequence may indicate temperature fluctuations during oxidation of the deposit, for example due to discontinuous influx of meteoric fluids into a warm (geothermal) fluid system shifting the stability of cerussite and hydrocerussite to higher or lower P_{CO_2}.

Nobody has investigated the conditions of weathering in the Alpine fissures (e.g., Göschenen, Switzerland) yet, but it appears reasonable to assume oxidation during cooling of primary (i.e., metamorphic) fluids interacting with ore minerals upon exhumation. At Leadhills and the other localities with basic lead minerals, nothing is known about elevated temperatures during supergene processes, but it appears to be the only reasonable explanation for their formation to date.

In summary, the rarity of basic lead minerals in oxidation zones is probably caused by the lack of elevated temperatures during supergene processes in most oxidation zones. The occurrence of lanarkite, however, cannot be explained by elevated temperatures alone, since its stability field is not very *T*-dependent (cf. Fig. 6b). This is most probably the reason, why lanarkite is the rarest of the basic lead minerals discussed here. Consequently, additional processes have to be invoked to support lanarkite formation in nature. At much higher temperatures, Ettler et al.

(2005) report the minor occurrence of lanarkite in particles from lead smelting, which shows that lanarkite is principally stable under high-temperature conditions.

FS experiments

The FS experiments confirm the three step formation process predicted by the textures of the medieval sample material (cf. Fig. 7). Dousing the hot rock surface with water is not a necessary process for the formation of basic lead phases since the experimental FS material was cooled down in static air before it was brought in contact to a fluid phase. This, however, does not exclude that dousing with water additionally favors formation of basic lead minerals.

All experiments were conducted with water in contact to atmospheric CO_2. Under these conditions hydrocerussite is thermodynamically not stable (Essington et al. 2004). All CO_2-pressures of the experimental waters are higher (between $\log P_{CO_2}$ = –1.5 and –3.5) than needed for hydrocerussite precipitation ($\log P_{CO_2}$ = –3.7). The reason that still hydrocerussite occurs in all experimental setups leads to two different explanations. First, the thermodynamic data of hydrocerussite are not correct or, second, microenvironments on the lead oxide-water interface exist where the CO_2 partial pressures are low enough to stabilize hydrocerussite thermodynamically. The quality of the thermodynamic data of hydrocerussite has been discussed in Mercy et al. (1998 and references therein) and it appears that this explanation is not the one to choose here. Hence, basic lead phases can form in environments that are in contact to atmospheric CO_2. Consequently, in contrast to the process proposed e.g., by Essington et al. (2004), no closed or CO_2-depleted system for the external fluid is necessary to form hydrocerussite if lead oxides are available. The formation of hydrocerussite in microenvironments producing high pH and low P_{CO_2} was also proposed by Li et al. (2015). The same applies to the pH values of the experimental systems. Only four of six samples show pH values of the experimental waters that are high enough to stabilize hydrocerussite (pH > 7.7), but all experiments contained this phase. Hence, local equilibria play a major role in the formation of basic lead phases.

Ettler and Johan (2014) show in their long-term leaching experiments with slag from Pb ore processing that the lead concentration of the fluid is controlled by the precipitation of newly formed cerussite and anglesite in a system lacking lead oxides. In contrast, Pb activity in soil waters in environments with predominant lead oxides due to weathering of metallic lead, e.g. at shooting ranges (Li et al. 2015), is most probably controlled by hydrocerussite. Li et al. (2015) report that cerussite and hydrocerussite are more capable of forming a protective layer that prevents further weathering than lead oxides because of their lower solubility.

Calculated solubilities including the basic lead phases hydrocerussite, leadhillite, caledonite, lanarkite in addition to cerussite, anglesite, and litharge show that most basic lead phases except for lanarkite are less soluble than cerussite, anglesite, litharge under neutral to slightly basic pH conditions (Fig. 9).

In all of our experimental setups, lead oxides were in continuous contact with the weathering fluid. The analyzed waters can hence provide constraints on which phases control the availability of lead. For this reason the lead concentration determined in the experiments were plotted in the solubility diagrams and are compared to the different mineral solubilities. It is obvious that the lead concentrations are significantly lower than the solubility of litharge. All experimental setups show that lead concentrations are also below cerussite solubility. All analyses of the experimental setups plot near the hydrocerussite solubility. This indicates that the solubility of lead oxides like litharge is controlled by the precipitation of hydrocerussite in all of our experiments. The trend that the lead concentration are highest in the setups with the lowest pH-values is not surprising because of the increasing solubility of lead minerals at lower pH (Ma et al. 2007 and references therein).

The observation that less hydrocerussite was formed in experimental setup B (hence, at higher pH values than in setup A) was also observed by Ma et al. (2007) and is explained by the lack of protons required for basic lead mineral precipitation.

Finally, the experiments impressively indicate that crystallization of basic lead minerals is possible in short time periods, since first mineral growth was macroscopically visible after only a few hours.

Temperature range during FS

The temperatures reached during FS are unclear. Lead oxide stability and the melt compositions analyzed in the present study, however, provide constraints on the temperature range obtained. FS experiments of Willies and Weisgerber (2000) on simple bonefires lead to maximum temperatures of 500 to 700 °C during FS, but according to these authors, fires with access to flowing air easily reach higher temperatures.

The stability of the divalent lead oxides massicot and litharge is temperature-dependent: Massicot is stable at higher

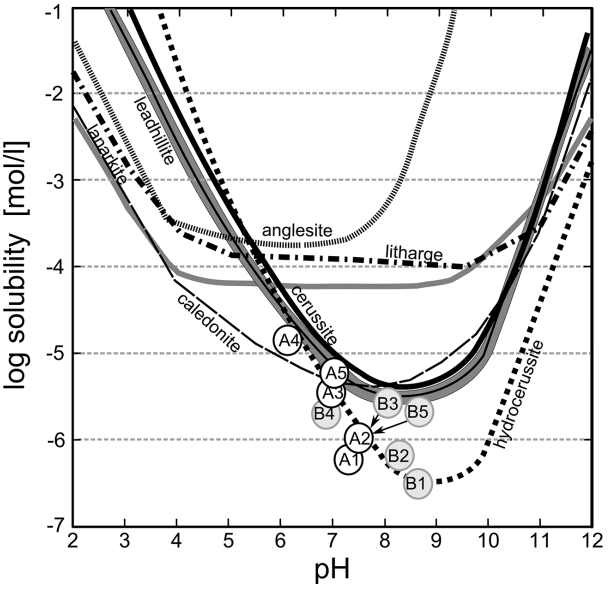

FIGURE 9. Diagram showing molar solubility of hydrocerussite, leadhillite, caledonite cerussite, anglesite, lanarkite, and litharge at pH 2–12. Water analysis of the experimental setup A1–5 and B1–5 are included as labeled symbols. The solubility of leadhillite includes the uncertainties regarding the solubility constants as gray range (see Methods section).

temperatures, the transformation litharge-massicot happens between 489 and 540 °C (Gavrichev et al. 2008). Experiments in static air show that minium forms during prolonged oxidation (370 °C) of massicot and litharge (Ciomartan et al. 1996). However, this transformation depends on the type of experimental atmosphere.

Minium and litharge are the predominant lead oxides occurring in the investigated samples. Massicot subordinately occurs as fine-grained aggregates. The predominance of litharge instead of massicot indicates that in most cases, temperatures did not exceed 540 °C. Although massicot is metastable at room temperature (e.g., Perry and Wilkinson 2007), transformation to litharge during cooling seems unlikely. In our experiments massicot is frequently occurring beside litharge, which is explained by the relatively high temperatures used for decarbonization of cerussite (650–800 °C).

Depending on thermal conductivity, the temperature gradient during FS is very large with high temperatures at the fire/rock interface and much lower temperatures only centimeters away in the rock (Willies and Weisgerber 2000). The occurrence of shannonite instead of pure oxide shows that temperatures in many samples were not sufficiently high for a complete decarbonization of cerussite (see also Pring et al. 1990). Experiments by Yamaguchi et al. (1980) show that shannonite starts to form from cerussite around 300 °C. About 440 °C are needed to complete the transformation to lead oxides (cf. Eqs. 3a–3c). In some samples, lead oxides, oxycarbonates, and unaffected cerussite appear side by side (cf. Fig. 1b), which implies a strong temperature gradient on a small scale. The experiments show that complete transformation of cerussite to lead oxides was possible in only 15 min.

In addition to the lead oxides/oxycarbonates, which indicate low temperatures below 500 °C during the FS process, the deterred melt provides important information on the maximum temperature reached. Melt was formed in a few cases and probably only in direct contact of blaze and rock. Although the FS experiments were conducted at relatively high temperatures of 700–800 °C, only a small amount of sample material shows partial melting.

To get an estimate of the minimum temperatures reached during partial melting, the bulk compositions of melt directly associated with crystal type II and I were reintegrated based on image analyses and EMPA data (see Fig. 4b, 4c, 4d). The bulk, crystal, and the former melt composition of MK-06 (almost pure Pb-Si-O melt) can be plotted into the experimental PbO-SiO_2 phase diagram of Smart and Glasser (1974) (see Figs. 10a and 10b). Both reintegrated bulk compositions (A+B) completely melt around 760 °C. The crystal compositions of crystal type I correspond well to the mineral alamosite (average chemical composition: $Pb_{1.01}Si_{0.95}O_3$; see Table 5). μ-XRD and Raman measurements, however, do not allow a distinct identification as alamosite. Small differences in composition (A) and (B) are easily explained by different portions of additional minor elements like iron or barium (cf. Table 4).

The composition of the Zn-rich crystal type II and the former melt of sample MK-08 are more complex as they include zinc as additional major element. They are plotted into the ZnO-PbO-SiO_2 phase diagram of Jak et al. (1997) (see Fig. 10c). The bulk compositions (C) and (D) are almost identical and entirely melt

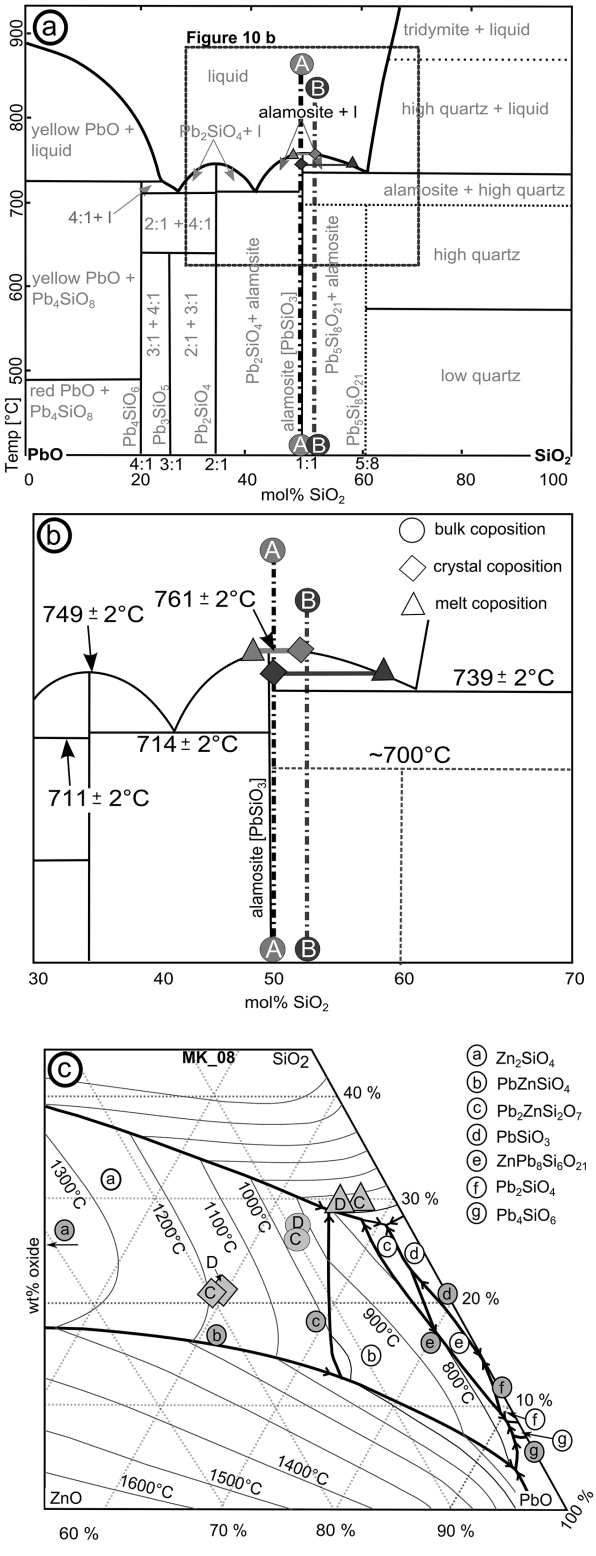

FIGURE 10. (**a** and **b**) Reintegrated bulk, crystal, and former melt compositions for sample MK-06 plotted in a binary PbO-SiO_2 system of Smart and Glasser (1974). (**c**) Reintegrated bulk, crystal, and former melt compositions of sample MK-08 plotted in a ternary ZnO-SiO_2-PbO system (Jak et al. 1997).

around 950 °C. The crystal composition is close to larsenite (average composition: $Pb_{0.85}Zn_{0.80}Si_{1.28}O_4$). Again the discrepancy in composition is most probably explained by additional elements.

IMPLICATIONS

This paper investigates the formation and stability of basic lead phases in different artificial and natural environments with a special focus on their occurrence during medieval fire-setting (FS). Since lead of natural and anthropogenic sources is one of the most widespread pollutants, a better understanding of the stability relations and formation conditions of supergene, low-temperature lead phases is of interest. The short-term experiments show that in environments where lead oxides predominate, the basic lead hydrocerussite is likely to control the availability of lead in aqueous systems, especially at neutral to slightly basic pH conditions. This is of interest for the evaluation of the toxic potential of lead-contaminated sites like medieval mine dumps and shows that relatively rare secondary phases may be important in some weathering environments and should be taken in account besides the more common ones. Long-term experiments have to confirm if the basic lead minerals have the potential to retain lead over long time periods.

The formation conditions of basic lead minerals in natural oxidation zones are not well understood. The stability diagrams presented in this contribution, show that weathering under elevated temperatures (between 35 and 75 °C) could play a crucial role for their formation.

Finally, the results presented provide a basic frame for mining archeologists unraveling FS at places where FS mining traces are missing. The results of the melt remnants offer the possibility to constrain temperatures reached during this widespread medieval mining method.

ACKNOWLEDGMENTS

We are grateful to T. Wenzel for his friendly assistance during EMP analyzes and discussion of the results. We thank M. Keuper for assisting during micro-Raman analysis, C. Berthold and N. Wichtner for their help during μ-XRD measurements, and S. Schafflick for the professional sample preparation. G. Stoschek and M. Marks for their help during water analyses. This work is a contribution of the r⁴ project "ResErVar—Ressourcenpotential hydrothermaler Lagerstätten der Varisziden" funded by the German Ministry of Education and Research (BMBF).

REFERENCES CITED

Abdul-Samad, F.A., Thomas, J.H., Williams, P.A., Bideaux, R.A., and Symes, R.F. (1982a) Mode of Formation of some rare copper (II) and lead (II) minerals from aqueous solution with particular reference to deposits at Tiger, Arizona. Transition Metal Chemistry, 7, 32–37.

Abdul-Samad, F.A., Thomas, J.H., Williams, P.A., and Symes, R.F. (1982b) Chemistry of formation of lanarkite. Pb_2OSO_4. Mineralogical Magazine, 46, 499–501.

Agricola, G. (1556) De re metallica libri XII, 931 p. Deutscher Verlag der Wissenschaften, Berlin (in German).

Anserment, S. (2012) Mines et minéraux du Valais, II. Anniviers et Tourtemagne, 374 p. Rossolis, Bussigny (in French).

Armstrong, J.T. (1991) Quantitative elemental analysis of individual micro particles with electron beam instruments. In K.F.J. Heinrich and D.E. Newbury, Eds., Electron Probe Quantitation, p. 261–315. Springer, New York.

Asselborn, E. (2012) Minéralogie de la France, 241 p. Teammedia GmbH, Grünewald (in French).

Berthold, C., Bjeoumikhov, A., and Brügemann, L. (2009) Fast XRD² microdiffraction with focusing X-ray microlenses. Particle & Particle Systems Characterization, 26, 107–111.

Bethke, C.M., and Yeakel, S. (2015) GWB Essentials Guide. Aqueous Solutions, 149 p. LLC Champaign, Illinois.

Bideaux, R.A. (1980) Famous mineral localities: Tiger, Arizona. Mineralogical Record, 11, 155–181.

Blanc, P., Lassin, A., Piantone, P., Azaroual, M., Jacquemet, N., Fabbri, A., and Gaucher, E.C. (2012) Thermoddem: A geochemical database focused on low temperature water/rock interactions and waste materials. Applied Geochemistry, 27, 2107–2116.

Boni, M., Terracciano, R., Evans, N.J., Laukamp, C., Schneider, J., and Bechstädt, T. (2007) Genesis of vanadium ores in the Otavi Mountainland, Namibia. Economic Geology, 102, 441–469.

Bowell, J.R., and Clifford, J.H. (2014) Leadhillite Tsumeb, Namibia. Rocks and Minerals, 89, 354–362.

Bucher, K., Zhu, Y., and Stober, I. (2009) Groundwater in fractured crystalline rocks, the Clara mine, Black Forest (Germany). International Journal of Earth Sciences, 98, 1727–1739.

Ciomartan, D.A., Clark, R.J.H., McDonald, L.J., and Odlyha, M. (1996) Studies on the thermal decomposition of basic lead (II) carbonate by Fourier-transform Raman spectroscopy, X-ray diffraction and thermal analysis. Journal of the Chemical Society, 3639–3645.

Cooper, M.P., and Stanley, C. (1997) Die Mineralien der Caldbeck Fells, Cumberland, England. Lapis, 22, 13–34 (in German).

Craddock, P.T. (1992) A short history of fire setting. Endeavour, 16, 145–150.

Downs, R.T. (2006) The RRUFF Project: an integrated study of the chemistry, crystallography, Raman and infrared spectroscopy of minerals. Program and Abstracts of the 19th General Meeting of the International Mineralogical Association in Kobe, Japan, 3-13.

Essington, M.E., Foss, J.E., and Roh, Y. (2004) The soil mineralogy of lead at Horace's Villa. Soil Science Society of America, 68, 979–993.

Ettler, V., and Johan, Z. (2014) 12years of leaching of contaminants from Pb smelter slags: Geochemical/mineralogical controls and slag recycling potential. Applied Geochemistry, 40, 97–103.

Ettler, V., Legendre, O., Bodénan, F., and Touray, J.C. (2001) Primary phases and natural weathering of old lead–zinc pyrometallurgical slag from Příbram, Czech Republic. The Canadian Mineralogist, 39, 873–888.

Ettler, V., Johan, Z., Baronnet, A., Jankovský, F., Gilles, C., Mihaljevič, M., Sebek, O., Strnad, L., and Bezdicka, P. (2005) Mineralogy of air-pollution-control residues from a secondary lead smelter: environmental implications. Environmental Science & Technology, 39, 9309–9316.

Ettler, V., Červinka, R., and Johan, Z. (2009a) Mineralogy of medieval slags from lead and silver smelting (Bohutín, Příbram district, Czech Republic): Towards estimation of hystorical smelting conditions. Archometry, 51, 987–1007.

Ettler, V., Johan, Z., Kříbek, B., Šebek, O., and Mihaljevič, M. (2009b) Mineralogy and environmental stability of slags from the Tsumeb smelter, Namibia. Applied Geochemistry, 24, 1–15.

Gavrichev, K., Bolshakov, A., Kondakov, D., Khoroshilov, A., and Denisov, S. (2008) Thermal transformations of lead oxides. Journal of Thermal Analysis and Calorimetry, 92, 857–863.

Geyer, O.F., and Gwinner, M.P. (2011) Geologie von Baden Württemberg, 627 p. Schweizerbart'sche Verlagsbuchhandlung, Stuttgart (in German).

Gilg, H.A., Hochleitner, R., Keller, P., and Struck, U. (2003) A fluid inclusion and stable isotope study of secondary oxidation minerals from the Tsumeb Cu-Pb-Zn deposit, Namibia: Proceedings ECROFI XI, Budapest, Hungary, June 5-7 (2003) Acta Mineralogica-Petrographica, Abstract Series, 78–79.

Graf, H.W. (1991) Die Grube Neue Hoffnung bei Bleialf/Eifel. Lapis, 16, 13–18 (in German).

Haupt, G. (1884) Die Stollenanlagen; Leitfaden für Bergleute und Tunnelbauer, 258 p. Julius Springer, Berlin (in German).

Ingwersen, G. (1990) Die sekundären Mineralbildungen der Pb-Zn-Cu-Lagerstätte Tsumeb. Namibia (Physikalisch-chemische Modelle), 233 p. Ph.D. thesis, University of Stuttgart, Stuttgart (in German).

Jak, E., Hayes, P.C., Degterov, S., Pelton, A.D., and Wu, P. (1997) Thermodynamic optimization of the systems PbO-SiO_2, PbO-ZnO, ZnO-SiO_2 and PbO-ZnO-SiO_2. Metallurgical and Materials Transactions B, 28, 1011–1018.

Karup-Møller, S. (1975) On the occurrence of the native lead, litharge, hydrocerussite and plattnerite within the Ilímaussaq alkaline intrusion in South Greenland. Neues Jahrbuch für Mineralogie, 37, 230–241.

Keim, M.F., and Markl, G. (2015) Weathering of galena: Mineralogical processes, hydrogeochemical fluid path modeling and estimation of the growth rate of pyromorphite. American Mineralogist, 100, 1584–1594.

Kirchheimer, F. (1976) Bericht über Spuren römerzeitlichen Bergbaus in Baden-Württemberg. Der Aufschluss, 27, 361–371 (in German).

Klockenkämper, R., (1996) Total-reflection X-Ray Fluorescence Analysis, 245 p. Wiley.

Kolitsch, U. (1997) Neufunde von Mineralen aus einigen Vorkommen der Vogesen, Frankreich: Triembach, Bluttenberg und Val d`Ajol. Der Aufschluss, 48, 65–91 (in German).

——— Eine durch Betoneinwirkung entstandene Paragenese von Blei-Verbindungen aus der Grube Clara im mittleren Schwarzwald. Der Erzgräber, 14, 48–53 (in German).

Kolitsch, U., and Tillmanns, E. (2003) The crystal structure of anthropogenic $Pb_2(OH)_3(NO_3)$ and a review of Pb-(O. OH) clusters and lead nitrates. Mineralogical Magazine, 67, 79–93.

Lee, D. (2007) Formation of leadhillite and calcium lead silicate hydrate (C-Pb-S-H) in the solidification/stabilization of lead contaminants. Chemosphere,

66, 1727–1733.
LGRB (2006) BW GÜK300: Geologische Übersichtskarte 1:300000 Ref. 92: Landesgeologie, Regierungspräsidium, Freiburg (in German).
Li, Y., Zhu, Y., Zhao, S., and Liu, X. (2015) The weathering and transformation process of lead in China's shooting ranges. Environmental Science: Processes & Impacts, 17, 1620–1633.
Lin, Z. (1996) Secondary mineral phases of metallic lead in soils of shooting ranges from Örebro County, Sweden. Environmental Geology, 27, 370–375.
Lin, Z., Comet, B., Qvarfort, U., and Herbert, R. (1995) The chemical and mineralogical behaviour of Pb in shooting range soils from central Sweden. Environmental Pollution, 89, 303–309.
Livingstone, A. (1993) Origin of the leadhillite polymorphs. Journal of the Russell Society, 5, 11–14.
Markl, G. (1991) Neufunde von der Grube Erzengel Gabriel im Schierengrund, oberes Einbachtal bei Hausach, Mittlerer Schwarzwald. Der Aufschluss, 5, 44–46 (in German).
——— (2015) Schwarzwald, Lagerstätten und Mineralien aus vier Jahrhunderten, Band 1 Nordschwarzwald und Grube Clara, 672 p. Bode, Lauenstein (in German).
Ma, L.Q., Hardison, D.W. Jr., Harris, W.G., Cao, X., and Zhou, Q. (2007) Effects of soil property and soil amendment on weathering of abraded metallic Pb in shooting ranges. Water, Air, and Soil Pollution, 178, 297–307.
Mercy, M.A., Rock, P.A., Casey, W.H., and Mokarram, M.M. (1998) Gibbs energies of formation for hydrocerussite [$Pb(OH)_2{\cdot}(PbCO_3)_2$(s)] and hydrozincite {$[Zn(OH)_2]_3{\cdot}(ZnCO_3)_2$(s)} at 298 K and 1 bar from electrochemical cell measurements. American Mineralogist, 83, 739–745.
Metz, R., Richter, M., and Schürenberg. H. (1957) Die Blei-Zink-Erzgänge des Schwarzwaldes, 277 p. Beihefte zum Geologischen Jahrbuch (29), Hanover (in German).
Négrel, P., and Roy, S. (1998) Chemistry of rainwater in the Massif Central (France): a strontium isotope and major element study. Applied Geochemistry, 13, 941–952.
Parkhurst, D.L., and Appelo, C.A.J. (1999) User's guide to PHREEQC (ver. 2)-A computer program for speciation, batch-reaction, one-dimensional transport, and inverse geochemical calculations. U.S. Geological Survey Water-Resources Investigations Report, 99-4259.
Perry, D.L., and Wilkinson, T.J. (2007) Synthesis of high-purity α- and β-PbO and possible applications to synthesis and processing of other lead oxide materials. Applied Physics A, 89, 77–80.
Pring, A., Birch, W.D., and Reller, A. (1990) An occurence of lead oxycarbonate ($PbCO_3{\cdot}PbO$) as a mine fire product at Broken Hill, New South Wales. Mineralogical Magazine, 54, 647–648.
Sajadi, S.A. (2011) A comparative investigation of lead sulfate and lead oxide sulfate study of morphology and thermal decomposition. American Journal of Analytical Chemistry, 2, 206–211.
Schlomann, C., and Steen, H. (1990) Neue Mineralfunde aus dem Bergbaugebiet von Badenweiler im Südschwarzwald. Lapis, 15, 13–20 (in German).
Schnorrer-Köhler, G. (1987) Die Minerale in den Schlacken des Harzes. Der Aufschluss. 38, 231–246 (in German).
——— (1988) Mineralogische Notizen IV. Der Aufschluss, 39, 153–168 (in German).
Schnorrer-Köhler, G., Standfuss, K., Standfuss, L. (1982) Neue Schlackenminerale aus Laurion. Der Aufschluss, 33, 459–462 (in German).
Skinner, B.J., and McBriab, E.M. (1958) Minium from Broken Hill, New South Wales. Mineralogical Magazine, 31, 947–950.
Smart, R.M., and Glasser, F.P. (1974) Compound formation and phase equilibria in the system $PbO\text{-}SiO_2$. Journal of the American Ceramic Society, 57, 378–382.
Stalder, H.A., Wagner, A., Graeser, S., and Stuker, P. (1998) Mineralienlexikon der Schweiz, 608 p. Wepf, Basel (in German).
Temple, A.K. (1956) The Leadhills-Wanlockhead Lead and Zinc Deposits. Transactions of the Royal Society of Edinburgh, 63, 85–113.
Treiman, A.H. (1999) Bad water: Origin of phoenicochroite-lanarkite solid solution, $Pb_2O(CrO_4SO_4)$, in Martian Meteorite EETA79001. Lunar and Planetary Science Conference, 30, 1124.
Walenta, K. (1991) Neufunde aus dem Schwarzwald; 4. Folge. Lapis, 16, 19–24 (in German).
Willies, L., and Weisgerber, G. (2000) The use of fire in prehistoric and ancient mining-firesetting. Paléorient, 26, 131–149.
Wittern, A. (1988) Eine typische Mineralparagenese durch Feuersetzen. Der Aufschluss, 39, 317–318 (in German).
——— (1994) Sekundärmineralien durch Feuersetzen in Oberschulenberg. Bönkhausen. Bleialf und Badenweiler. Der Aufschluss, 45, 36–42 (in German).
Wobrauschek, P. (2007) Total reflection X-ray fluorescence analysis—a review. X-ray Spectrometry, 36, 289–300.
Yamaguchi, J., Sawada, Y., Sakurai, O., Uematsu, K., Mizutani, N., and Kato, M. (1980) Thermal decomposition of cerussite ($PbCO_3$) in carbon dioxide atmosphere (0–50 ATM). Thermochimica Acta, 35, 307–313.
Young, B., Hyslop, E., Bridges, T., and Cooper, J. (2005) New records of supergene minerals from the Northern Pennine orefield. Transactions of the Natural History Society of Northumbria, 64, 211–214.

Manuscript received August 4, 2016
Manuscript accepted February 26, 2017
Manuscript handled by Sylvain Grangeon

Sehr geehrter Herr Keim,

gerne bestätigen wir Ihnen hiermit formlos, dass wir Ihnen die letzten eingereichten Autorenfassungen (vor Akzeptanz bzw. Freigabe zur Produktion an den Verlag) der folgenden beiden Artikel

https://doi.org/10.1127/njma/2017/0058
https://doi.org/10.1127/njma/2016/0002

zur Verwendung in Ihrer kumulativen Dissertation freigeben. Bitte verweisen Sie auf die Originalpublikation (DOI-Link). Die Dissertation wird auf der Bibliotheksseite der Uni Tübingen frei im Internet verfügbar sein.

Mit freundlichen Grüßen

Dr. A. Nägele

Auszug:

Author’s Retained Rights (Springer; Mineralium Deposita)

Author(s) retain following non-exclusive rights for the published version provided that, when reproducing the article or extracts from it the Author(s) acknowledge and reference first publication in the journal:

a) To reuse graphic elements created by the Author(s) and contained in the article in presentations and other works created by them;
b) They and any academic institution where they work at the time may reproduce the article for the purpose of course teaching (but not for inclusion in course pack material for onward sale by libraries and institutions);
c) To reproduce or to allow a third party Assignee to reproduce the article in whole or in part in any printed volume (book or thesis) written by the Author(s)

MINERALOGICAL SOCIETY OF AMERICA
3635 Concorde Pkwy Ste 500 • Chantilly VA 20151-1110 • USA
Tel: 1 (703) 652-9950 • Fax: 1 (703) 652-9951 • Internet: www.minsocam.org

January 24, 2018

Mr. Maximilian Keim
Eberhard Karls Universität Tübingen
Wilhelmstraße 56
DE-72074 Tübingen
Germany

E-Mail: max.keim@googlemail.com

Mr. Keim:

I received your e-mail message of 2018-01-24 requesting permission to reproduce the following article as supplemental material for your cumulative dissertation:

Maximilian F. Keim Bernd Gassmann Gregor Markl (2017) Formation of basic lead phases during fire-setting and other natural and man-made processes, *American Mineralogist* 102 (7): 1482-1500.

It is with pleasure that we grant you permission to reproduce this article for inclusion without cost and all subsequent editions of the work, its ancillaries, and other derivative works, in any form or medium, whether now known or hereafter developed, in all languages, for distribution throughout the world on the conditions that reference is given to the original publication of the Mineralogical Society of America.

Sincerely,

J. Alex Speer

J. Alexander Speer
Executive Director, MSA